INTEGRATED AIRBORNE AND GROUND GEOPHYSICAL INVESTIGATION OF MINERAL DEPOSITS IN PARTS OF MIDDLE-BENUE TROUGH, NIGERIA.

BY

ONUM, STEPHEN ADIKWU (B.Sc BSU., M.Sc FUTO)
20164139108

A THESIS SUBMITTED TO THE POSTGRADUATE SCHOOL

FEDERAL UNIVERSITY OF TECHNOLOGY, OWERRI

IN PARTIAL FULFILMENT OF THE REQUIREMENTS OF THE AWARD OF THE DEGREE OF DOCTOR OF PHILOSOPHY (Ph.D.) IN GEOPHYSICS

JULY, 2021

CERTIFICATION

This is to certify that the research "Integrated Airborne and Ground Geophysical Investigation of Mineral Deposits in parts of Middle-Benue Trough, Nigeria" was carried out by ONUM, STEPHEN ADIKWU (20164139108) in partial fulfillment of the requirements for the award of the degree of Doctor of Philosophy (Ph.D.) in Geophysics in the Department of Geology, School of Physical Sciences, Federal University of Technology Owerri, Imo State. Nigeria.

.....
DR. S.I. IBENEME
(Principal Supervisor)

23/06/2021
.....
DATE

.....
DR. C. N OKEREKE
(Co-Supervisor)

23-06-2021
.....
DATE

.....
DR. Y.E. OBIOHA
(Co-Supervisor)

24/06/2021
.....
DATE

.....
DR. A. I. OPARA
(Head of Department)

24/06/2021
.....
DATE

.....
PROF. C.C.Z AKAOLISA
(Dean, School of Physical Sciences)

6/7/2021
.....
DATE

.....
PROF. C.C EZE
(Dean, Postgraduate School)

.....
DATE

.....
PROF. O.A ANYIAM
(External Examiner)

15-6-2021
.....
DATE

DEDICATION

This work is dedicated to God Almighty the creator and giver of life.

ACKNOWLEDGEMENTS

My profound gratitude goes to God Almighty, whose banner over my life is love. I acknowledge the amiable lecturers and staff of the great department of Geology, and the School of Physical Sciences (SOPS), FUTO. Special Acknowledgement goes to my Supervisors, in the persons of Dr. S.I Ibeneme, Dr. C.N Okereke and Dr. Y.E Obioha. I acknowledge the indelible efforts of the Head of Department of Geology, in the person of Dr. A.I Opara, the Dean School of Physical Sciences, in person of Prof. C.Z Akaolisa and the Departmental PG Coordinator, in the person of Dr. C.N Okereke. My appreciation also goes to Prof. K.K Ibe, Prof. O.C Okeke, Prof. S.O Onyekuru, Dr. Ikoro, Dr. I. Njoku, Mr. Essien A.G, and all other members of staff for their support.

I acknowledge the Director General of Nigerian Geological Survey Agency (NGSA) Abuja, the person of Mr. A.N Nwegbu for giving me the postgraduate internship opportunity in the year 2018. And, the Deputy Director /Head of Geophysics (NGSA), the person of Mr. A.U Abba for his great impact in the cause of my postgraduate internship. My profound gratitude goes to Mr. Iduma Uche of KelmaGeodynamic Limited, Nigeria for his technical assistance.

I also cannot continue without acknowledging my Parents, most especially my mother Mrs. Comfort Adikwu, my lovely Siblings and Uncles who God has used to beautiful my life by all the morals and support they have always bestowed on me. Finally, I acknowledge all my friends and my wife to be, in person of Miss. Sunday Martha Enem for their support and prayers. I pray God reward you all according to his riches.

TABLE OF CONTENTS

LIST OF TABLES

LIST OF FIGURES

LIST OF PLATES

ABSTRACT

An enhanced interpretation was carried out to delineate the tectonics and subsurface structural trend in parts of the Middle-Benue Trough that lays between latitudes 7°30′–9°0′N and longitudes 9°00′–10°30′E as well as it implications for mineralization. The desk study stage involved the acquisition of Landsat 8 imagery, image processing (Atmospheric Correction, Colour Composite, Band Rationing, Principal Component Analysis) were applied and result shows imagery highlighting areas where concentration of minerals and assemblage of alteration minerals, as iron-bearing minerals, hydroxyl-bearing minerals and hydrated sulphates occur, discriminating altered from unaltered rocks. In order to validate the results, nine (9) High Resolution Aeromagnetic data used were subjected to various filtering operations, the residual magnetic map showed the difference in locations of high and low magnetic intensities and many crustal magnetization patterns with majorly NE-SW trending of low magnetic susceptibility, The RTE magnetic anomaly map shows both low and high magnetic frequencies representing points of low and high magnetic signatures respectively in the area with a shift of orientation of anomalies as observed. The highest magnetic susceptibility values ranged from 14.6 to 570.8 nT, Analytic Signal map show relatively high magnetic amplitude observed to be associated with the highlands are interpreted as the basement rocks, intermediate magnetic amplitude is observed to be associated with moderate elevations and is interpreted as sandstone and magnetic mineral (magnetite and hematite) enrichment areas; while low magnetic amplitude is associated with lowlands. The First Vertical Derivative, Second Vertical Derivative, Upward Continuation, TDR filter was applied. Maps displayed most structural feature of the area such as the faults, folds, contacts and to some extent the shape of some lithology. The interpreted geological map from aeromagnetic dataset shows the geologic units, structures, deformation intensity and OH bearing, ferrumagnetisation and ferruginization alteration zones. Two zones (Bangagala as Zone 1 and Ibi as Zone 2) were selected for further investigations based on the anomalous attributes of the zones and varying(moderate to high) deformation intensity across the study area. Ground magnetic survey, em-vlf, electrical resistivity and induced polarization were employed to further investigate magnetic depleted areas as well as the degree of conductivity and resistivity across the interpreted chargeable bodies resulting from segregation of hydrothermal fluid, leading to the separation of chargeable bodies of associated minerals (e.g. lead, quartz e.t.c). The three-dimensional voxel model was used to isolate chargeable bodies (potential mineralization) with chargeability >15msec which is regarded as anomalies of interest. The volume of the chargeable voxel was then computed and used for the probable reserve estimation. The estimated volume of chargeable body in zone 1(Bangagala) is 853,250 m^3 with nearest estimate of 2,730,400 tonnes and estimated value of $1.3Billion. While, the estimated volume of chargeable body in zone 2 (Ibi) is 502,310 $m^3$with nearest estimated of 1,607,392 tonnes and estimated values of $750Million.

Keywords**:** Fracture, Electromagnetic, Magnetic, Exploration, Induced Polarization, Mineral, and Hydrothermal.

CHAPTER ONE

1.1 Background Information

Minerals are the constituents of rocks, ores, and meteorites and with a few exceptions are the most stable chemical elements known to Man. Minerals are the foundation for the economic and industrial development of any nation. According to (Runge, 1996) and (Vogley, 1985) materials used by humans are derived from two major sources, namely; agriculture and mining; but mining alone accounts for about 70 percent of the total. In fact all metallic materials - without which no industrial or technological development can take place - are obtained through mining. Petroleum, bitumen and coal account for over 85% of materials for energy generation (Runge, 1996; Vogley, 1985) and these too, are obtained through mining. It is therefore obvious that the first step towards economic and technological development of a nation is the exploration, exploitation and processing of its mineral resources – solid and fuel. Although a nation may import minerals to fill these important needs, it is more economical if the minerals are sourced within the country. Since nations are not equally blessed with deposits of minerals by nature, it becomes important that in planning for her national economic development a nation should first give consideration to how much of mineral reserves she has.

A purposeful or detailed exploration of mineral deposits should provide information on the actual mode of occurrence of any identified mineral ore, its peculiar chemical and mineralogical composition, and the reserve. With this information in a country database, investment planning for national economic development becomes easier (Runge, 1996). The Nigerian economy is driven by oil and not by solid minerals like that of South Africa and few other African countries. Although several solid mineral occurrences have been identified in the country, these appeared to be either indicated or inferred as their actual mode of occurrence,

chemical or mineralogical composition, and reserves are not accurately known since no detailed exploration of these mineral deposits has been carried out. Investment planning with mineral deposits requires definite information about the composition and reserves of the ore.

Thus, it is always better for a nation to have proven reserves of her mineral deposits in her database. Detailed exploration to create proven mineral reserve database is a very expensive and risky investment, and thus is done systematically in stages. Such detailed exploration usually starts with a regional aerial survey for gravimetric, magnetic or geo-electric anomalies followed by ground truthing geological detailing. The modern Geographic Information System (GIS) with its versatile computer software, Global Positioning System and satellite imagery is especially very useful in modern exploration. These tools, with improved technology in modern exploration equipment and a well-planned field work will certainly ensure a less expensive detailed exploration of identified minerals in Nigeria.

Mining is one of the oldest economic activities in Nigeria dating back to prehistoric times when man crudely exploited iron and clay, and perhaps other metals for the production of his cosmetics, crude implements and utensils. The early European explorers, mainly German, Spanish and British, located and mined tin, galena, gold, and other minerals for export to their home countries. Records show that organized exploration activities in Nigeria commenced in 1903 and 1904 when the Secretary of State for Colonies inaugurated mineral surveys of the Southern and Northern Protectorates respectively (MSMD, 2010) The principal mineral occurrences discovered by the survey teams included lignite deposits at Asaba, lead-zinc ores at several locations, tin and columbite in the southeast, monazite, limestone and lead-zinc ores at Abakaliki district. Others were coal at Enugu, brine springs at Arufu and Awe, Galena in Jos area, iron ore deposits in Niger and Kwara districts and marble deposits in Jakura. Mining activity in controlled form, however, commenced in the country in 1915 with the production of coal at the Enugu mines. Nigeria was impressively sustained by agriculture and few solid

minerals known at the time, namely coal, tin, columbite and gold prior to the discovery of petroleum. Coal, for example, met fully the needs of our railway system and electricity supply while tin yielded substantial foreign exchange earnings for the nation. In addition, these minerals also offered employment opportunities and possibilities of development of indigenous technology in mining and minerals engineering (MSMD, 2010).

Although few solid minerals were known in the late colonial era and early independence days, by 1994 however, when the Nigerian government canvassed a

private sector-led economic revival programme in solid minerals, agriculture and manufacturing as a means of diversifying the nation's economy and the Ministry of Solid Minerals Development (MSMD) was created, improved geological data helped to identify about 34 solid minerals in Nigeria against the 37 indicated by the geological survey concluded in 1987. Thirteen (13) of these minerals are being actually mined, processed and marketed. They are coal, kaolin, baryte, limestone, dolomite, feldspar, glass sand, gemstones [haphazard],gold [in small quantities], iron minerals (MSMD,2010 and Akande, Horn, & Reutel, 1988). lead-zinc, tin and its associated mineral sand recently gypsum. The remaining twenty-one (21) minerals, though in demand are untapped (MSMD, 2010).

Investigations actually revealed that these mineral deposits are known and some are even being mined, yet their reserves and average compositions are not fully known thus resulting in huge economic loss. Systematic field mapping by Ministry of Mine and Steel Development (MMSD, 2010) reveals that the Cretaceous Middle-Benue Trough veins are located mainly in Akwana and Arufu. This mineralization is hosted in silicified limestone sequence which belongs to the Asu River Group (Akande *et al*., 1988). Dips of these veins are generally steep to vertical. Petrographic analysis of outcrop samples also shows that theVein constituents include galena, sphalerite, tetrahedrite, and occasionally native silver. At Azara, the veins are rich in barites with occasional cubic galena. Limestone wall rock at Arufu and Akwana is highly silicified, which

appears to be related to the mineralization processes as the intensity of the silicification decreases away from the vein (MMSD, 2010).

Several industrial minerals that are in great demands in the country are also observed to occur in specific area from the available mineral inventory in the country. Figure 1.0 shows suggested area for detailed investigation of Mineral Ore deposits mainly around the Benue trough to the eastern border with the Republic of Cameroun covering several states.

In this study, a detailed exploration of identified mineral deposits in parts of the Middle-Benue trough will not be as costly as searching for new mineral deposits because the presently known occurrences present patterns that will make such exploration less expensive by carrying out comprehensive reconnaissance study using nine (9) sheets of the newly acquired high resolution aeromagnetic data comprising of Kwolla 211, Shendam 212, Amar 213, Akiri 232, Ibi 233, Bantagi 234, Akwana (252), Wukari 253 and Donga 254 and Landsat 8 data covering about 27,225 km^2, which will provide the necessary background information of anomalous locations of interest with a ground follow-up of Magnetic, EM-VLF, Electrical resistivity and IP techniques as well as drilling for the confirmation of anomalous bodies.

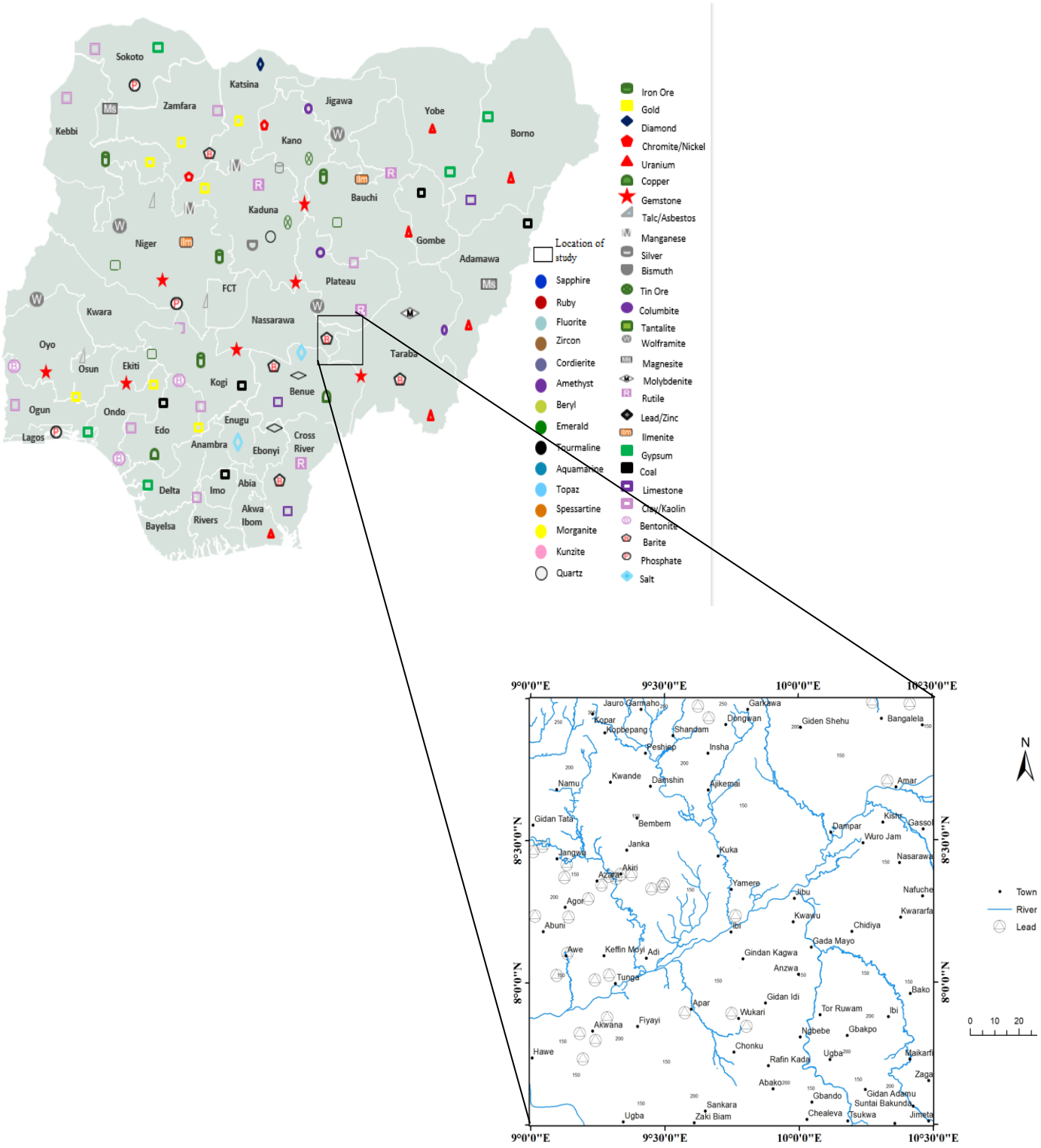

Figure 1.0: Mineral map of Nigeria (Modified after KPMG, 2017).

1.2 Statement of the Problem

There is paucity of information about mineral deposits within the Middle-Benue Trough when compared with the upper and Lower Benue Troughs. There has not been intensive research utilizing high resolution instruments within the Middle-Benue Trough to enable in-depth study and adequate cataloguing of the minerals within the study area.

Most research centered on structural analysis with little information on the stratigraphic deposition of sediments and their relationships to mineralization. As a result, the need to carry out a detail integrated geophysical research further unraveling the mineral potential of the Middle Benue Trough to improve on the information base of the Middle-Benue Trough.

1.3 Aim and Objectives of the Study

The main objective of this study is to carry out Integrated Airborne and Ground Geophysical Investigation of Mineral deposits in Parts of Middle-Benue Trough, Nigeria.

The specific objectives include:

1. To obtain composite images that can aid structural interpretations of the study area.
2. To generate an enhanced structural map using Landsat ETM and HRAM of the study area.
3. To delineate mineralized zones.
4. To determine the electrical conductivity and chargeability distributions as they relate to mineralization in the area.
5. To improve on the existing mineral map of the Middle-Benue Trough by delineating new mineralized zones.

6. To estimate reserves of mineral deposits in the area.

1.4 Justification of Study

It is true that Benue Trough has been studied by previous workers using geologic mapping, aeromagnetic and remote sensing techniques, but the Middle-Benue Trough has been relatively least studied using integrated approach.

The need to find an additional revenue source to augment those derived from hydrocarbons in the Niger Delta and ramp up the nation's mineral reserve as well as diversifying the economy has driven renewed government interest and activities in mineral deposits exploration across Nigeria.

1.5 Scope of the Study

This research is restricted to the geological interpretation of LANDSAT 8 OLI, High Resolution Aeromagnetics (HRAM) data, and ground follow up of Magnetic, EM-VLF and IP survey data that lies between latitudes 7°30′–9°0′N and longitudes 9°00′–10°30′Ecovering a total area of about 27,225 km^2 (Figure 1.1).

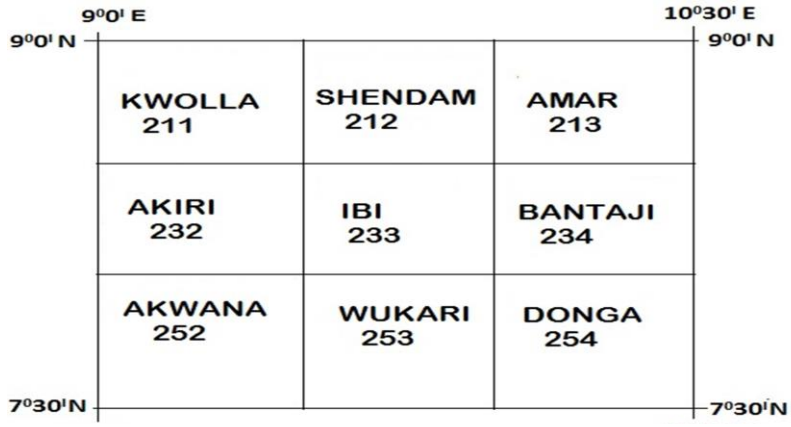

Figure1.1: Aeromagnetic sheets for the study area

CHAPTER TWO

LITERATURE REVIEW

2.1 Review of Related Literature

Following the release of the first aeromagnetic data collected over most parts of Nigeria by the Geological Survey of Nigeria (GSN) in 1974, attempts were made by early researchers to interpret the data both qualitatively and quantitatively. Studies involving the interpretation of aeromagnetic data over the Benue Trough have revealed the existence of block faulting and numerous intrusive bodies (Osazuwa *et al.,* 1981; Ajakaiye, 1981; Ofoegbu, 1984, 1985; Ofoegbu &Mohan, 1990; Ofoegbu & Onuoha, 1991). Various depth estimate techniques were applied to the data and results obtained showed that estimates of the thickness of sedimentary rocks obtained by different authors agree fairly well with each other. For example, Osazuwa *et al.* (1981) obtained a depth range of 0.9–4.9 km and 0.9–2.2 km in the northern Benue Trough from magnetic and gravity data respectively, while Nur (2000) combining two-dimensional spectral analysis and Hilbert transform magnetic data reported the existence of two main source depths in parts of the northern Benue Trough, with the deepest source lying between 1.5 and 2.25 km. In the southern Benue Trough, Ofoegbu (1984) found that the thickness of sediments varies between 0.5 and 7 km. Ofoegbu & Onuoha (1991) from the results derived from 2D spectral analysis identified the existence of two main source depths in parts of the southern Benue Trough, the deeper source lying at a depth of 1.3– 2.5 km, while the shallower depths were generally <250 m. Nearly all mineral deposits are related to some type of distortion of the lithosphere, and most theories of ore formation and concentration embody tectonic or deformational concepts (O'Leary *et al.,* 1976; Ananaba & Ajakaiye, 1987). Some lineament patterns have been expressed to be the most favourable structural conditions in control of various mineral deposits. They include the traces of major regional

lineaments, the intersection of major lineaments or both major (regional) and local lineaments, lineaments of tensional nature, local highest concentration (or density) of lineament, between en echelon lineaments, and lineaments associated with circular features.

Between 2005 and 2009, the Federal Ministry of Mines and Steel Development engaged the services of Fugro Airborne Surveys Limited, to acquire high-resolution data of 500 m line spacing and 80 m terrain clearance for most parts of Nigeria. The release of these data by the Nigerian Geological Survey Agency (NGSA) in 2010 coincided with the availability of high speed and robust computer programs like Oasis Montaj, making it increasingly possible to generate subtler results and more detailed information.

Pabalelo, Bokani, Elisha, Boniface, & Thato (2021) research on integrated use of induced polarization and electrical resistivity imaging methods to delineate zones of potential gold mineralization in the Phitshane Molopo area. The 2D IP/ERI measurements were acquired along ten 300 m long profiles trending northeast southwest, with 15 m line separation and 7.5 m electrode spacing. Thereafter, we inverted the data using the standard Gauss-Newton optimization method to produce 2D and 3D models. Based on a combination of IP and resistivity results, we identified distinct lithological units comprising the mineralized and non-mineralized zones. High chargeability (≥6.86 mV/V) and high resistivity (≥641 Ωm) anomalies were attributed to the presence of disseminated sulfides or gold-bearing quartz and/or carbonate veins that obliquely crosscut (east west trend) the banded iron formation (BIF) units and the intensely silicified BIF units, respectively. Zones exhibiting a combination of low to intermediate chargeability (1.0-6.86 mV/V) and low to intermediate re-sistivity (1.4-641 Ωm) are likely non-sulfidized zones with little/no gold mineralization in the study area. The integrated use of IP and ERI methods was successful in delineating zones that are likely to be hosting disseminated sulphides and/or potentially gold-rich zones in the Phitshane Molopo area, Kraaipan Greenstone Belt.

Koné, Nasr, Traoré, Amiri, Inoubli, Sangaré, & Qaysi (2021) worked on Geophysical Contributions to Gold Exploration in Western Mali utilizing Airborne Electromagnetic Data and ground follow up. Result showed trends similarity for different orders of conductivity. They allowed for characterizing resistance and conductive structures with prevalent N-S and NE-SW directionalities. Conductive structures are strongly related to known Artisanal Mining Sites (AMS). They coincide with tourmaline sandstones and quartz-albite veins, which are both often artisanally recognized as indicators of gold mineralization in Western Mali. Field observations show that resistance structures correspond to felsic rocks. These structures can bear gold only when silicified and they have spatial relations with Artisanal Mining Sites (AMS) within the Kenieba area. This study shows the efficiency of electromagnetic methods to characterize Birimian structures in relation to the gold mineralization in Kedougou-Kenieba Inlier (KKI).

Ouchchen, Said, Driss, Mohamed, Kevin, Abdelhalim, Fatima, & Bouchra (2021) in Structural interpretation of the Igherm region (Western Anti Atlas, Morocco) from an aeromagnetic analysis: Implications for copper exploration. Aeromagnetic data were analyzed, constrained by geological and ore deposit mapping to investigate possible regions within the Igherm inlier region of the Anti-Atlas in western Morocco that are favorable for more detailed copper exploration. The aeromagnetic data were investigated by creating reduction to the pole (RTP), upward continuation and tilt-angle anomaly maps. Additionally, depths to magnetic susceptibility sources were estimated using three-dimensional Euler deconvolution and tilt-angle depth methods. The RTP map indicated several anomalous regions where magnetic maxima can be related to Paleoproterozoic and Neoproterozoic metamorphic and volcanic rocks located between the uplifted regions in the northern portion of the Igherm inlier region. The western portion of the study area is characterized by short wavelength, NE-trending magnetic maxima that are related to Pan-African orogeny volcanic

units. Derivative maps indicate that the majority of the lineaments are NE-trending probably related to post Pan-African rifting. However, there are several NW- and E-trending lineaments related to the Variscan orogeny. The depths of the sources of these lineaments range between 100 m and 5200 m, with the deeper depths mainly trending toward the northeast. Using the derivative analysis, RTP, magnetically determined depth estimates and the nature of known copper deposits in the region (e.g., Tizert deposit), several regions were determined to be favorable for more detailed mineral exploration. These regions are located along the edges of Proterozoic uplifts where paleobasins containing Basal Series sediments have been affected by mainly NE-trending faults that act as conduits for deeper magmatically formed ore-rich fluids.

Araffa, (2021) worked on Geophysical Data for Mapping Structural Features and Hydrothermal Alteration Zones in Basement Rock of Egypt in two case studies; the first case study at the southern part of Sinai (El Regeita area) where geological, remote sensing, and geophysical data were used to explore copper ore mineral in three alteration zones. The result of the integrated studies indicates that the study area no. 1 is dissected by a NE-SW trending fault zone and that El Regeita copper mine is located on the fault zone and this area includes six dykes (magnetic bodies) of NE–SW, N–S, and NW–SE trends. The second case study located at the south Eastern Desert (Wadi El Beidda Area). In this area different tools are used for gold exploration such as geology geochemistry and geophysical techniques. The results of interpretation of different techniques indicate that the study area no. 2 contain different ore bodies at depth ranges from 30–60 m and these ore bodies coincidences with the alteration zones dissecting the study area of NW–SE trends.

Nndanduleni & Abera (2021) worked on the Identification of potential targets for kimberlite exploration using satellite imagery and map combination approach in the Lesotho Kimberlite Province. The study focuses on processing and integration of evidential map layers

(geomorphic features, linear structures and kimberlite indicator minerals). Result revealed major orientations of the mapped linear structures are NW-SE and ENE-WSW. These trends are found to be associated with known kimberlite pipes in the area. In addition, the known kimberlite pipes appear as depressions as delineated using the SRTM DEM image. Furthermore, the ASTER image pixels associated with the localities of most kimberlite pipes were mapped as kimberlite indicator minerals.

Olawale, Ahmed & Mousa (2021) carried out Mapping hydrothermal alteration mineral deposits from Landsat 8 satellite data in Pala, Mayo Kebbi Region, Southwestern Chad. The different image attribute extracting techniques, spectral enhancement ability, pixel classification methods have been applied on the Landsat 8 OLI satellite image data to map geological features and spatial distribution of hydrothermal alteration zones, which have been recorded to be associated with gold mineralization in the Pala, Mayo Kebbi region of southwestern Chad. Radiometric calibrated, noise filtered and image enhanced Landsat 8 OLI data were subjected to colour composite, band rationing and crosta analyses in order to enhance spectral reflectance and compositional information, create colourful multispectral images which enable the mapping of desired spectral bands into principal component images for the purpose of accentuating salient information needful to delineate hydrothermal alteration zones within the study area. Composite ratios 4/2-6/7-6/5 indicate relative spatial distribution of iron-oxide in the southeast while clays and hydroxyl minerals occur in the west and northwestern part of the study area. The eigenvectors and eigenvalues for hydroxyl minerals from the crosta analysis indicate highest loadings of opposite signs (-0.721498 & 0.649465; bands 6 & 7) in PC3, representing ‘’H’’ image. The eigenvectors and eigenvalues for iron-oxides on the other hand present highest loading of opposite signs (0.895721 & -0.443283; bands 2 & 4) in PC4, representing the “F” image. The white coloured pixels within the bright reflections generated from Crosta composite image of H, H+F & F in RGB

delineate hydrothermal alteration zones. The plot of delineated zones of hydrothermal alteration on the Landsat 8 true colour indicate spatial distribution of the alteration areas within the host greenstone belt belonging to the Precambrian Goueygoudoum series and they plot mainly along major structural features, suggesting structural control. Field control revealed that some areas delineated by band rationing as hydrothermal alteration zones appear to be the result of intense weathering. Accordingly, we recommend that remote sensing delineation of hydrothermal alteration zones should be checked by a relevant ground-observation based control procedure.

Tuşa, Khodadadzadeh, Contreras, Rafiezadeh, Fuchs, Gloaguen, & Gutzmer (2020) estimated mineral abundance in drill-core samples collected from Bolcana porphyry copper-gold deposit by employing hyperspectral short-wave infrared (SWIR) data and scanning electron microscopy-based image analyses using a mineral liberation analyzer (SEM-MLA). Machine learning algorithms were executed to combine the two data types and upscale the quantitative SEM-MLA mineralogical data to drill-core scale. Quasi-quantitative maps over entire drill-core samples were acquired.

Sekandari, Masoumi, Beiranvand, Muslim, Rahmani, ... , & Aminpour (2020) used Landsat-8, Sentinel-2, ASTER, and WorldView-3 spectral imagery for exploration of carbonate-hosted Pb-Zn deposits in the Central Iranian Terrane (CIT). For the processing of the satellite remote sensing datasets, band ratios and principal component analysis (PCA) techniques were adopted and implemented. Fuzzy logic modeling was applied to integrate the thematic layers produced by image processing techniques for generating mineral prospectivity maps of the study area. The spatial distribution of iron oxide/hydroxides, hydroxyl-bearing and carbonate minerals and dolomite were mapped using specialized band ratios and analyzing eigenvector loadings of the PC images. Subsequently, mineral prospectivity maps of the study area were generated by fusing the selected PC thematic layers using fuzzy logic modeling. The

most favorable/prospective zones for hydrothermal ore mineralizations and carbonate-hosted Pb-Zn mineralization in the study region were particularly mapped and indicated. Confusion matrix, field reconnaissance and laboratory analysis were carried out to verify the occurrence of alteration zones and highly prospective locations of carbonate-hosted Pb-Zn mineralization in the study area. Results indicate that the spectral data derived from multi-sensor remote sensing satellite datasets can be broadly used for generating remote sensing-based prospectivity maps for exploration of carbonate-hosted Pb-Zn mineralization in many metallogenic provinces around the world.

Shirmard, Farahbakhsh, Beiranvand, Muslim, Müller, & Chandra (2020) integrated selective dimensionality reduction techniques such as PCA, ICA, and minimum noise fraction (MNF) for mineral exploration using ASTER satellite data. These techniques were applied on specific subsets of the advanced spaceborne thermal emission and reflection radiometer (ASTER) spectral bands for mapping gossans and hydrothermal alteration zones, such as argillic, propylitic, and phyllic zones. The fuzzy logic model was used for integrating the most rational thematic layers derived from the transformation techniques, which led to an efficient remote sensing evidential layer for mineral prospectivity mapping. The results showed that ICA was a more robust technique for generating hydrothermal alteration thematic layers, compared to the other dimensionality reduction techniques. The capabilities of this technique in separating source signals from noise led to improved enhancement of geological features, such as specific alteration zones. In this investigation, several previously unmapped prospective zones were detected using the integrated hydrothermal alteration map and most of the known hydrothermal mineral occurrences showed a high prospectivity value. Fieldwork and laboratory analysis were conducted to validate the results and to verify new prospective zones in the study area, which indicated a good consistency with the remote sensing output. This study demonstrated that the integration of remote sensing-based alteration thematic layers derived from the

transformation techniques is a reliable and low-cost approach for mineral prospectivity mapping in metallogenic provinces, at the reconnaissance stage of mineral exploration.

Zhang, Ding & Carranza. (2020) worked on 3D Mineral Exploration Targeting with Multi-dimensional Geoscience Datasets, Tongling Cu(au) District, China. A 3D district-scale geological model was constructed from multiple geoscience datasets. Secondly, multi-level (0 m, −300 m, −600 m, −900 m, −1200 m) exploration criteria were extracted by spatial analyses. Thirdly, the weights-of-evidence method, discrete smooth interpolation, and ordinary kriging interpolation were used to integrate multi-level exploration criteria including two-dimensional (2D) surface geochemical and remote sensing data into a 3D posterior-probability model. Finally, the concentration-area and concentration-volume fractal methods were used to define posterior-probability thresholds to outline 2D and 3D targets, respectively. The results indicated that the integrating performance of ordinary kriging interpolation is better than that of discrete smooth interpolation in 3D posterior-probability modeling. The whole procedure yielded a series of high-potential Cu(-Au) targets. The methodology discussed here can be used in other magma-skarn districts in the world.

Jackisch, Lorenz, Kirsch, Zimmermann, Tusa, Pirttijärvi ...., & Savolainen (2020). integrated drone-borne photography, multi- and hyperspectral imaging, and magnetics data for mapping a carbonatite-hosting outcrop in Siilinjärvi, Finland. Structural orientations and lithological units are deduced based on high-resolution, hyperspectral image-enhanced point clouds. Unmanned aerial system (UAS)-based magnetic data allow an insight into their subsurface geometry through modeling based on magnetic interpretation. A geologic map is resulted discriminating between the principal lithologic units and distinguishes ore-bearing from waste rocks. Schodde (2020) worked on Geophysical signatures of the Ni-Cu-PGE mineralization in the Stillwater West property, Stillwater Complex, southern Montana, USA

Induced Polarization (IP) survey and pointed out that geophysics play a growing role in the exploration for mineral deposits under cover and at greater depths (> 500 m).

Martín-Crespo, Gómez-Ortiz & Martín-Velázquez (2020) presented the results of the geo environmental characterization of La Matildes river bed, affected by mine tailings in the Cartagena–La Unión district, Murcia (southeast Spain) using geophysical and geochemical techniques. Two electrical resistivity imaging (ERI) profiles were carried out to obtain information about the thickness of the deposits and their internal structure. The geochemical composition of borehole samples from the riverbed materials shows significantly high contents of As, Cd, Cu, Fe, Pb, and Zn being released to the environment. Results demonstrated that surface extraction in three open-pit mines have changed the summits of Sierra de Cartagena–La Unión and rock and metallurgical wastes have altered the drainage pattern and buried the headwaters of ephemeral channels.

Stephen *et al.* (2020) worked on high resolution airborne magnetic data of some regions of Southeast Nigeria were analyzed to map structures controlling mineralization. First and second vertical derivatives, upward continuation, source edge detection, analytical signal, Centre for Exploration Targeting (CET) and standard Euler deconvolution operations were done to delineate the spatial distributions and depths to the different magnetic sources. The enhanced maps showed major and minor magnetic anomaly centres in the Lower Benue Trough (LBT) and Ikom-Mamfe Rift (IMR) characterized by thin (151–745 m) sedimentation. Also, within these areas there exist some isolated pockets of intermediate depths (745–1634 m) occurring in the neighborhood of these magnetic anomalies. The Calabar Flank (CF) characterized by minor remnants of post-Cretaceous intrusions has sedimentation of over 6126 m in some locations. The 2000 m upward continued TMI map revealed the existence of major deep-seated weak zones believed to have originated during the rifting episode connected with the formation of the Benue Trough. The abundance of

intrusive bodies in the LBT and IMR render these parts of the study area unattractive for hydrocarbon exploration. Nevertheless, they possess high base metal mineralization potential while CF is a favorable site for hydrocarbon search.

Bolouki, Ramazi, Maghsoudi & Sohrabi (2019) investigated a remote sensing-based application of Bayesian networks for epithermal gold potential mapping in Ahar-Arasbaran area, NW Iran. Landsat Enhanced Thematic Mapper+ (Landsat-7 ETM+), Landsat-8, and ASTER datasets were used to detect hydrothermal alteration zones associated with epithermal gold mineralization using band ratio, relative absorption band depth (RBD) and PCA techniques. The Bayesian network classifier was used to synthesize the thematic layers of hydrothermal alteration zones. Many new potential zones of epithermal gold mineralization were identified in the Ahar-Arasbaran region.

Cyril, (2019) worked on Delineation of High-Resolution Aeromagnetic Survey of Lower Benue Trough for Lineaments and Mineralization and results of the interpretation shows that the study area is dominated by four to five lithology as proven by the total magnetic intensity image, reduction to equator, residual magnetic intensity map, analytic signal image. From the upward continuation maps, it can be concluded that the subsurface geology has regional trend of NE–SW and E-W direction. The interpreted subsurface lineaments trend in three major directions which are NE-SW, ENE-WSW and NW-SE direction as seen on the tilt angle derivative and second vertical derivative. The total depth estimation to the top of magnetic sources for the study area as shown on the spectral plot ranged from 0.279 km (27.9 m) to 2.64 km for shallower and deeper sources respectively.

Sawuta, Ayanninuola, Udensi & Ogwola (2019) in Estimation of Magnetic Depth to Source Using High Resolution of Aeromagnetic Data of Parts of Upper Benue Trough, North Eastern Nigeria was carried out using Source Parameter Imaging (SPI) and Standard Euler Deconvolution methods for the purpose of estimating the sedimentary thickness of the study

area for hydrocarbon maturation or accumulation. The polynomial fitting with order one method was applied in the regional–residual separation. Further analysis was conducted on the residual map. The SPI results revealed a maximum sedimentary thickness of 4908.178m while Standard Euler Deconvolution results also revealed a depth of 4050.1 m. Therefore, the highest sedimentary thickness of the study was found around Wafango, Dong and Lau region of the study area with shallow thickness of 741.108m to 1162.154m around Biliri, Tula and Kaltungo down to Lankoviri in Southern region of the study area. Consequently, the highest sedimentary thickness of about 4908.17 m from SPI and 4050.1 m from Standard Euler deconvolution is sufficient enough for hydrocarbon maturation or accumulation. These areas with maximum sedimentary thickness may be subjected for further geophysical investigation like seismic reflection/refraction, so as to affirm its hydrocarbon potential.

Okwesili, Johnson & Igwe (2019) carried out Spectral analysis and source parameter imaging of aeromagnetic data of Lafia and Akiri Areas, Middle Benue Trough, Nigeria. Aeromagnetic data were used and spectral analysis and source parameter imaging were used for the quantitative interpretation of the data. The total magnetic intensity (TMI) contour map obtained from gridding of the data ranging from -39.5 to 100.0 nT was separated into regional and residual contour maps; it was done by polynomial fitting to produce the residual aeromagnetic intensity contour map. The residual intensity varies from -78.9 to 55.0 nT while the regional intensity varies from -39.18 to 39.84 nT. Depth results obtained from spectral analysis revealed two depth sources: the shallower magnetic source bodies and the deeper magnetic source bodies. The depth of shallower magnetic sources ranges from 0.557 to 1.261 km, with an average depth value of 0.899 km, whereas the depth of deeper magnetic sources varies from 2.419 to 5.732 km with an average depth value of 4.105 km. The SPI depth result ranges from -0.5638 km (shallow magnetic bodies) to 5.8381 km (deep lying magnetic bodies). The two methods showed depth estimation within the same range. The sedimentary

thickness obtained from the different methods indicates the possibility of hydrocarbon accumulation if other conditions for hydrocarbon generation are satisfied.

Zoheir, El-Wahed, Pour & Abdelnasser (2019) utilized Landsat 8-Operational Land Imager (OLI), ASTER, PALSAR and Sentinel-1 satellite data coupled with field and microscopic investigations to unravel the setting and controls of gold mineralization in the Wadi Beitan–Wadi Rahaba area in the South Eastern Desert of Egypt. Band ratios, RBD and mineralogical indices were used to extract the representative pixels form Landsat 8-OLI and ASTER bands. Lineaments were manually and automatically extracted from PALSAR and Sentinel-1 data. The data fusion approach was used and showed no particular spatial association between gold occurrences and certain lithological units but indicates a preferential distribution of gold–quartz veins in zones of chlorite–epidote alteration overlapping with high-density intersections of lineaments. A priority map with zones defined as high potential targets for undiscovered gold resources were generated for the Wadi Beitan–Wadi Rahaba area in this study.

Sun, Khan & Shabestari (2019) integrated ground-based hyperspectral imaging and geochemistry data for resource exploration and exploitation of sediment-hosted disseminated Gold at the Goldstrike District, UT, USA. Ground-based hyperspectral imaging was applied to study a core drilled in the Goldstrike district covering the basal Claron Formation and Callville Limestone. The integration of remote sensing and geochemistry data helped to identify an optimum stratigraphic combination of limestone above and siliciclastic rocks below in the basal Claron Formation, as well as decarbonatization, argillization, and pyrite oxidation in the Callville Limestone, that are related with gold mineralization.

Pour, Park, Park, Hong, Muslim, Läufer, ..., & Rahmani (2019) utilized Landsat-8, ASTER and WorldView-3 multispectral remote sensing imagery for prospecting copper-gold mineralization in the Northeastern Inglefield Mobile Belt (IMB), Northwest Greenland at

regional, local, and district scales. Hydrothermal alteration minerals such as iron oxide/hydroxide, Al/Fe-OH, Mg-Fe-OH minerals, silicification (Si-OH), and SiO_2 mineral groups were mapped using directed principal components analysis (DPCA) technique, Linear spectral unmixing (LSU) and adaptive coherence estimator (ACE) algorithms. Several high potential zones for Cu-Au prospecting were identified in the IMB, Northwest Greenland, including (i) the boundaries between the Etah metamorphic and meta-igneous complex rocks and sedimentary successions of the Franklinian Basin in the Central Terrane, (ii) orthogneiss in the northeastern part of the Cu-Au mineralization belt adjacent to Dallas Bugt, and (iii) the southern part of the Cu-Au mineralization belt nearby Marshall Bugt.

Opara, Odumosu, Akaolisa, Onyekuru, Emberga, & Onu (2018) worked on Basement Depth Re-Evaluation and Structural Kinematic Analysis of Part of the Middle Benue Trough using High Resolution Aeromagnetic Data and results of the 2-D spectral analysis of the aeromagnetic data revealed a two depth source model with the depth to the magnetic basement having an average depth of 3.90km. This deeper magnetic layer is probably associated with the magnetic rocks of the basement and different levels of deformation associated with it such as faults, folds and fractures. The shallower magnetic sources with an average depth of 0.70 km could be attributed to near surface basement features within the sedimentary pile. Structural analysis of the HRAM data revealed major faults which are believed to be associated with the intrusive bodies within the Southeastern part of the study area. The delineated linear features correlated well with the position and orientation of the paleo-structures in the area. These features further offsets the migmatite blocks originally trending in the NE-SW direction causing them to change orientation towards an E-W alignment. The results of this study revealed that the Gboko fault is a normal fault with the adjoining sub-basins strike-slipped to the left (sinistral). These observations were further interpreted in terms of the theory of block deformation and structural kinematic analysis.

Ojonugwa, Ezeh & Chinwuko (2018) Integration of Aeromagnetic Interpretation and Induced Polarization Methods in Delineating Mineral Deposits and Basement Configuration within Southern Bida Basin, North-West Nigeria. Spectral analysis method was used in delineating the depth to magnetic basement and model prominent magnetic anomaly. Analysis of Induce Polarization data were used in delineating the potential fractures zones of mineralization. Visual inspection of the magnetic anomalies and first vertical derivative maps reveals that the area is highly faulted with major faults trending East-West (E-W) and minor ones Northeast-Southwest (NE-SW) directions. The qualitative interpretation results of both the resistivity and chargeability pseudo sections reveal potential fractures zones trending East-West (E-W) and the depth to the anomalous body ranges from (0.3-2.5 km) with average overburden thickness of 2.1 km. Two depth source models were interpreted using Discrete Fourier Transform method (spectral analysis) namely; the shallower sources which range from 0.45 to 1.49 km and the deeper ones which range from 1.81 to 3.24 km. The quantitative interpretation of the aero magmatic data, depict that the average sedimentary thickness ranges from (2.3-3.2 km) and the average depth to the Curie isotherm in the area is 24.76 km. The result also shows that the Curie temperature isotherm within the basin is not a horizontal level surface, but is undulating. The regional average results for both geothermal gradient and heat flow across the study area are 23.07 o C/km and 57.66 W/m 2 respectively. Based on the computed sedimentary thicknesses (2.3-3.2 km), the geothermal gradient (22.27 and 37.00 o C/km.) and the prevalent fractures, the possibility of hydrocarbon accumulation in the northern and southeastern part of the study area is feasible whereas other parts of the study area with low sedimentary thicknesses will favour magnetic mineral deposits such as the prevalent ooilitic iron ore deposits at Agbaja and Kotonkarifi axes.

Baranwal, Rønning, Gautneb, Larsen, Ofstad & Brönner (2018) in integrated interpretation of airborne and ground geophysical data for graphite exploration in Northern

Norway shows correlation of low magnetic anomalies and low apparent resistivity obtained. These data are noticed from already known areas with abundant graphite and from new sites with exposed graphite at the surface. Based on this correlation, new potential areas for graphite deposits are identified and refined for further follow up and detail investigation using ground geophysical methods and core drilling to confirm the deposits and whether it is economical.

Eze & Adaora (2018) carried out ground magnetic survey to investigation Lead-Zinc ore presence in Edor area of Cross River State, Nigeria. Magnetic-intensity profiles were made along seven profile lines over the target area. All the magnetic lows match in position with aeromagnetic lows which have been associated with Pb-Zn mineralisations in the area. It was therefore concluded that the Pb-Zn mineralisation is depicted by magnetic lows.

According to Thiabaut (2017) research on Orman gold prospect in Mondulkiri province Cambodia. The aim of the research was to develop a new approach in the implementation of the minimum gradient support regularization operator, applied to a time-domain induced polarization problem. The resistivity and induced polarization data were acquired during the geophysical campaign in Mondulkiri Province, Cambodia, on the largest known gold resource of the country. The deposit was an Intrusion Related Gold system, characterized by polarizable sulphides minerals. Four long profiles were realized on the contact zone between a magmatic intrusive and the hosting sediment formations, which is a zone of interest concerning gold mineralization.

Kasidi & Lazarus (2017) who worked on the analysis of aeromagnetic data over Middle Benue Trough and its adjourning basement terrain using Source Parameter Imaging (SPI) in Oasis montaj version 8.2 indicates that, the depth to magnetic sources in adjourning basement varies between 0.2 km to1.7 km. The depth to magnetic source at the middle of the study area which made up of the Cretaceous sediments of middle Benue varies between 4 km to 6 km. The shallow depth at the adjourning basement could be as a result of basic intrusive

rocks of the basement terrain, while the deeper sources at the middle of the study area that made up of cretaceous sediments of middle Benue, could be due to rifting of the Benue Trough. From the results obtained the adjourning basement terrain could be a potential site for mineral exploration while, the sedimentary section belonging to the middle Benue Trough could be a potential site for petroleum exploration

Onwuegbuchulam, Ikoro, Nwugha & Okereke (2016) used Electromagnetic method (VLF-EM) in mapping fracture/conductive zone around Auchi Southeastern, Nigeria. Three profiles were taken along the roads from Auchi to Igara, Auchi to Fugar and Auchi to Uloke using Abem Wadi Terrameter. Plots of the profiles were carried out using computer software (Excel) and contouring using Surfer 10 to delineate the fractured/conductive zones. The values range from 0.3 to 22.5 Siemens. Areas of low conductivity values indicate highly massive resistive rocks while Areas of high conductivity indicates the sedimentary terrain/ host rock or mineralized zones. The area is sparsely (few) fractured. Along profile A, two fractured zones were identified with conductivity values of 7.6 to16.8 Siemens between 100m (7.146 ^{o} N, 6.195oE) to 400m (7.150 ^{o} N, 6.200 ^{o} E) and 420m to 460m with conductivity value range of 11.0 to 22.5 Siemens. For profile B, one fractured zone was identified and a stretch of massive intrusive from 7.099 o N and 7.102 o N and 6.357 o E to 6.364 o E, with conductivity range of 0.9-5.2 Siemens at points 400m and 520m-1000m. Profile C has identifiable fractured zones at 900m-1100m with conductivity of (35-50) Siemens. The intrusive/ host rock conductivity values of (0.3-8.7) Siemens located at 380m to 880m 7.156 ^{o} N and 6.308 ^{o} E, 1100m to 2000m, 7.148 o N and 6.3295 o E. A total of five conductive zones were observed.

Leandro, Cesar, & George (2016) carried out a research on geophysical modeling of manganese deposit using induced polarization method in Itapira Brazil. The geophysical survey consisted on 10 lines of Induced Polarization Tomography using a Wenner-

Schlumberger array, with an along line electrode separation of 10 m for all lines. The IP data were modeled through commercial inversion software to generate 2D section models of chargeability. In order to create a 3D visualization model of chargeability, the 2D inversion models were then combined and interpolated in order to create a 3D visualization model. The 3D model revealed two independent ore bodies in both surface and subsurface, characterized for high chargeability (up to 20mV/V), instead of a single elongated orebody as suggested by the lateritic surface in the field. In addition, the model showed that the orebodies are elongated perpendicular to the area main structural trend and the regional alignment of the lateritic occurrences, which can bring new ideas in terms of local exploration strategies for manganese in this context.

Zhang, Meng & Sai (2016) applied geophysical methods to gold prospecting in Loulitou district, Jiadong Peninsula eastern China. The research was based on analyzing previous geological data, some geophysical methods, such as high magnetic measurement, DC resistivity combined profiles, induced polarization (IP) survey, were applied to constrain the distributions of the stratum, structure and magmatic rocks as well as ore-controlling factors in the Loulitou district, Jiaodong Peninsula. The interpretation of surface and underground IP data were used to guide ground prospecting. Through the geophysical methods employed, several possible favorable abnormal locations for concentration of ore-bearing sulfides were distinguished and several locations for gold prospecting were verified by drilling.

Victor, Onwuemesi & Aniwetalu (2015) in the high VLF anomalies delineation from Ishiagu area, in the SW part of Lower-Benue Trough yielded a high conductivity contrast result well-suited for Pb-Zn mineralization and the geologic information of the area. KHF filtering techniques were integrated and applied in the VLF data interpretation of the Ishiagu area and results of strong EM induction were detected, probably indicating the presence of

Pb-Zn deposits. Current density maps also revealed the inferred mineralized veins' trends in NW–SE direction with their subordinates in N–S direction and this conforms the tensional tectonic deformations of Cenomanian episode in the Lower-Benue Trough.The broad tipper responses in the northern part of the survey area indicate deeper sources while the sharp tipper responses observed in the central part indicate shallow sources in correspondence to the NE trending anticlinal axis.

Brigo Mining Company Ltd. (2015) carried out Electromagnetic and Induced Polarization Exploration around Wase and result revealed that the Interpreted EM conductive bodies occur within the magnetic lineament corridors and have high IP chargeability values. Therefore, proposed target testing via drilling to be carried out on some of the interpreted conductors.

Opara, Onyewuchi, Selemo, Onyekuru, Ubechu, Emberga, ..., & Nosiri (2014b) in the interpretation of the structural and tectonic features of Ugep and Environs, Calabar Flank, Southeastern Nigeria. Various image and data enhancement and transformation routines were carried out on the aeromagnetic and Landsat data to delineate the residual from the regional anomalies. The study revealed a dominant NE-SW structural trend in the area under study. The presence of a long lineament located around Iko Anwari, southwest of Ugep is interpreted as a tectonic escarpment. Also the major drainage in the study area: the Cross and the Ukpom rivers shows evidence of being structure controlled owing to the high density witnessed around. It is believed that this feature represents the boundary between the lower Benue trough and the Niger delta. Several clusters of circular magnetic anomaly closures with different amplitudes which occur especially in the northeastern half of the area were interpreted to be lithological variations of mafic–ultramafic inclusions within granodioritic batholiths. Similarly, the distribution of mafic and felsic rock forming minerals were correlated to the positive and negative second vertical derivative anomalies around the basement complex area. There also seem to be a correlation of the interpreted lineaments with

areas of primary mineralization in the study area. Result of the 2-D spectral analysis revealed a two layer depth model. The depth to the deeper magnetic source bodies (D 2) ranges between 1.299km and 3.136km, with an average of 2.289km. The depth to shallower magnetic source bodies (D 1) ranges between 0.035km and 1.285km, with an average of 0.746km. Alagbe & Sunmonu (2014) in Interpretation of Aeromagnetic Data from Upper Benue-Trough, Nigeria Using Automated Techniques have equally revealed a complete architect of the basement rocks in the area. The study showed the area to be a fractured zone and rifting structures is often good sites for mineralization.

Ogah & Jatau (2014) worked on aeromagnetic interpretation of Otukpo. The data was digitized, processed and interpreted for anomalies and causes of anomalies in the area. The airborne magnetic survey provided information about folding; the differential uplift of basement resulting from magmatic intrusions, gave rise to drape folds in the overlying sediments. Airborne anomaly indications have clearly defined large igneous bodies. These intrusive rocks of intermediate basic composition occur in the Santonian and Albian shales. Two layers of sedimentary features were observed. The average thickness for the first and second observed layers is 0.37km and 1.8km respectively. The Basement depth ranges from 3 to 8.2km. Calculated magnetic susceptibility contrast of the area was 0.073- 1.71 electromagnetic units. Areas of geological interest which are exploration targets were delineated. They include areas of broad magnetic intensity anomaly closures, which are zones of structural displacement associated with deep seated basement, areas of magmatic intrusions, dyke spots, fractures and fault zones. These structural studies may yield clues to the location of concealed mineral deposits

Ogunmola, Ayolabi & Olobaniyi (2014) in Lineament Extraction from SPOT 5 and NigeriaSat-X Imagery of the Upper Benue Trough, Nigeria. Several digital image enhancement techniques such as general contrast stretching and edge enhancement were

applied to the NigeriaSat-X and SPOT 5 image in ERDAS IMAGINE 9.2 after which structures were mapped out on-screen using ArcMap 10. The Digital Elevation Model (DEM) of the Trough was also used to enhance geomorphic features. The analysis carried out on the images revealed that lineaments are abundant in the Upper Benue Trough and they can be subdivided into four major trends, NE–SW, NW–SE, W–E and N–S in order of abundance and range in length from about 300 m to 26 km. Several faults were also mapped out within the Basin such as a sinistral fault around Bakoreji village in Bauchi, a dextral fault close to Kalmai town in Gombe and a dextral fault close to Wong in Taraba. It was discovered that some of the sites where minerals such as lead and zinc ores are being mined occur in the zones of high lineament density. The study shows the capability of the DEM, SPOT 5 and NigeriaSat-X images for lineament/structural interpretations.

Nwosu & Onuba (2013) carried out Evaluation of the Magnetic Basement Depth Over Parts of Middle Benue Trough Nigeria. The regional field was modeled with a first order polynomial and the residual field regarded as an error between the model and the data using the polifit program. The residual data was contoured into a map and the preliminary qualitative analysis on it revealed areas of low frequency anomaly probably related to deep seated bodies which are areas of thicker sediment; and areas of high frequency anomaly for shallow seated bodies. Then profiles were then taken along these most prominent anomaly closures of the map and labeled profile OO', NN', WW',BB' and AA' respectively for the purpose of depth determination. The Maximum slope techniques employed using an empirical constant of 1.82 estimated an average depth of 3.66km for the deep magnetic basement and an average of 0.80km for the shallow depth. The half slope technique also employed using an empirical constant of 0.63 estimated an average depth of 3.74km for the deep magnetic source. The results obtained with this method compares favorably with that obtained through spectra analysis for the area. Predominant NE-SW trend in the orientation of the magnetic

contour closures were equally found within the study area which is an attribute of the Pan – African Orogeny trends. The significance of this result is that, this study area with an average depth to basement of 3.70km and the oldest geological formation being marine sediment of Albian age, may be promising for hydrocarbon accumulation if other conditions are met.

Jatau & Nandom (2013) carried out structural interpretation of aeromagnetic data and Landsat imagery over the Middle Benue Trough. The aeromagnetic and Landsat data were subjected to various image and data enhancement and transformation routines. Results of the study revealed lineaments with trend directions in the N-S, NE-SW, NWSE and E-W directions, with the NE-SW trends been dominant. The depths to basement within the trough were established to be at 1.8, 0.3 and 0.8km, as shown from the spectral analysis plot. The Source Parameter Imaging (SPI) plot generated showed the centralsouth/ eastern portion of the study area as being deeper in contrast to the western-south-west portion. The basement morphology of the trough was interpreted as having parallel sets of micro-basins which could be considered as grabens and horsts in agreement with the general features interpreted by early workers.

Likkason, Sing & Samaila (2013) utilized spectra matching applied to the aeromagnetic anomaly data of the Middle Benue Trough, Nigeria. The performances of the radial spectrum and matched filtered output of the field were compared. Results from the plot of log radial spectrum against the frequency numbers indicate five discernable linear segments giving depths corresponding to magnetic layers ranging from 20.62 km (highest) to 0.26 km (lowest). Results from the spectral matching yielded three dipole equivalent source layers at 0.89, 4.33, and 18.22 km, giving two corridor bands. With the sensed magnetic discontinuities at depths of 18.10 to 20.50 km (from ground level), the temperature gradient probably over the area lies between 28.80 and 25.40°C/km for the Curie temperature of 520°C. Finally, we have computed the angular spectrum of the field over this area. It is found that the angular spectrum

in the mid and high frequency bands shows two peaks at 62° and 145°. Also there are peaks corresponding to the direction of polarization and the rectangular tapered window used in the analysis.

Oha, Onuoha, Nwegbu & Abba (2014) worked on high resolution airborne magnetic data of parts of the southern Benue Trough were digitally processed and analyzed in order to estimate the depth of magnetic sources and to map the distribution and orientation of subsurface structural features. Enhancement techniques applied include, reduction to pole/equator (RTP/RTE), first and second vertical derivatives, horizontal gradients and analytic signal. Results from these procedures show that at least 40% of the sedimentary basin contain shallow (<200 m) magmatic bodies, which in most cases are intermediate to mafic intrusive and hyperbysal rocks, and may occur as sills, dikes or batholiths. Magnetic lineaments with a predominant NE–SW trend appear to be more densely distributed around the basement rocks of the Oban Hills and metamorphosed rocks around the Workum Hills. 3D standard Euler deconvolution and Source Parameter Imaging (SPI ^{TM}) techniques were employed for depth estimation. Results from the two methods show similar depth estimates. The maximum depth to basement values for 3D Euler and SPI are 4.40 and 4.85 km with mean depths of 0.42 and 0.37 km, respectively. Results of 2D modeling of magnetic profiles drawn perpendicular to major anomalies in the study area reveal the existence of deep seated faults which may have controlled the emplacement of intrusive bodies in the basin. The abundance of intrusive bodies in the study area renders this part of the southern Nigerian sedimentary basins unattractive for petroleum exploration. However, the area possesses high potential for large accumulation of base metal mineralization.

Anudu Onwuemesi & Awajiokan (2012) carried out analysis of aeromagnetic data over Wamba and its adjoining areas in north-central Nigeria. Regional- residual separation was applied to a total aeromagnetic intensity contour map to produce a residual aeromagnetic

intensity contour map. The rose diagram of the orientations or azimuth direction of the structural lineaments delineated on the maps depicted major trends being NE-SW, NW-SE and NNESSW (Pan-African trends) with minor NNW-SSE and E-W trends (pre-Pan-African trends). Depths to the magnetic source bodies were estimated using Peter's (half-slope) method, indicating two depth source models. The deeper sources ranged from 0.88km to 3.15km and had -32nT to -225nT magnetic intensity, whereas the shallower sources ranged from 0.23km to 0.76km and had -10nT to 20nT magnetic intensity. The deeper sources were most likely due to intra-basement basic intrusive bodies underlying the sediment-covered marginal areas of the Benue Trough. The sedimentary cover in the area was generally low and therefore not likely to favour hydrocarbon generation.

Okereke, Onu, Ibe, Selemo, Opara, Ikoro, Ibeneme & Oha (2012) results from Analysis of Landsat and Aeromagnetic Data for Mapping of Linear Strutures: A Case Study of Yola Area, Upper Benue Trough, Nigeria. The landsat imagery generated was processed using ILWIS 3.2 Academic and Erdas imaging softwares. The structural trend is predominantly in the NE-SW direction. The drainage pattern is dendritic which is indicative of lithological, structural and topographic differences and also indicative of alluvial rocks, which is typical of the geology of the area that consists mainly of sedimentary rocks. Areas of topographic heights averaging about 500m are potential region for groundwater assessment. These areas agree with areas in the lineament map where the lineament density is high. It was observed that these regions have a lot of lineaments crossing each other which is indicative of groundwater availability. Results of the magnetic data revealed two depths: a shallow layer of magnetization with depths ranging from 0.223km to 0.934km with an average depth of 0.546km while the deeper layer of magnetization has its depths ranging from 1.233km to 4.013km with an average depth of 2.788km. The depths show that the basin is good for mineral prospecting and not favourable

for hydrocarbon prospecting. The dominant trend of the magnetic data is the NE-SW direction which agrees with the landsat data.

Onuba, Chinwuko, Onwuemesi, Anakwuba & Nwokeabia (2012) in Discrete Fourier Transform analysis of Aeromagnetic data over parts of Upper Benue Trough and Southern Chad Basin, Nigeria. The results show that two depth sources were obtained in the study area; the deeper sources range from 1.5 - 2.5 km while the shallower sources range from 0.5 - 1.4 km. The depths to magnetic basement are increasing in the northeastern direction and they range from 0.5 to 2.5 km. Four major regional faults trending in NE-SW direction were delineated. These faults conform to the trend of the Benue Trough and possibly suggest that the two basins are of similar origin. However, based on the computed sedimentary thickness (0.5-2.5km) and temperature at depth (81-115^{0}C), the possibility of hydrocarbon generation in the northeastern part of the study area is feasible.

Fon, Che & Suh (2012) applied electrical resistivity and chargeability data on a GIS platform in delineating auriferous structures in a deeply weathered lateritic terrain, Easter Cameroon. Exploration for primary gold in tropical settings is often problematic because of deep weathering and the development of a thick soil cover. The research presented the results of both chargeability and resistivity surveys carried out over the Belikombone hill gold prospect (14°00' - 14°25'E,5°25' - 6°00'N) in the Betare Oya area (eastern Cameroon), where previous soil sampling had identified gold anomalies. IP (Induced Polarization) chargeability and resistivity data combined, identified irregular anomalous zones trending NE-SW. The trend was consistent with the attitude of most auriferous quartz veins exposed in artisanal pits and parallel to the regional shear zone system and foliations. The high resistivity anomalies correspond to quartz veins while the relatively high IP anomalies correspond to low sulphide ± gold concentrations in the quartz veins. Modeling IP-chargeability and resistivity data prepared as contours and 3D maps, culminated to the development of an inferred, irregular

and discontinuous mineralized body at depths of up to 95 m. The size and shape of this mineralized body can only later be tested by drilling to ascertain the resource.

Shirzaditabar, Bastani & Oskooi (2011) worked on Imaging a 3D geological structure from HEM, airborne magnetic and ground ERT data in Kalat-e-Reshm area, Iran. The data set includes helicopter electromagnetic (HEM), airborne magnetic and ground electrical resistivity measurement. Occam approach was used to invert the HEM data to model the resistivity using a layered earth model with fixed thicknesses. The algorithm is based on a nonlinear inverse problem in a least-square sense. The algorithm was tested on a part of an HEM dataset acquired with a DIGHEM helicopter EM system at Kalat-e-Reshm, Semnan in Iran. The area contains a resistive porphyry andesite that is covered by Eocene sedimentary units. The results are shown as resistivity sections and maps confirming the existence of an arc like resistive structure in the survey area. The resistive andesite seems to be thicker than it is indicated in the geological maps. The results are compared with the reduced to the pole (RTP) airborne magnetic anomaly field data as well as with two ground resistivity profiles. We found reasonable correlations between the HEM 1D resistivity models and 2D models from electrical resistivity tomography (ERT) inversions. A 3D visualization of the 1D models along all flight lines provided a useful tool for the study of spatial variations of the resistivity structure in the investigation area.

Obi, Okereke, Obei & George (2010) carried out depth estimates based on 'SAKI' modeling, power spectrum, and horizontal gradient magnitude and observed that sediment thickness range between1.0 and 4.0 km.Wijns (2009); Tsiboah & Grant (2009); Meyer, De Waele & Monoury (2010) and Chaturvedi, Lo¨tter, CJagannadha, ... , & Rai (2010, 2012) gave insight into how EM can play an important role in outlining the geology to assist in the mineral exploration process. Combrinck, Botha & Hutchins (2009b) gave an example of geological and structural mapping of a covered area in Namibia, and Finn, Cameron & Hutchins (2010)

describe how regional AEM can be used to assist in mapping overburden thickness that can then be used to guide subsequent exploration programs.

Onyedim, Awoyemi, Ariyibi & Arubayi (2006) investigated the morphology of the basement beneath the pile of the sediment in the parts of the middle Benue trough, Nigeria. His work resulted in the delineation of the twelve major fault segments which divide the basement rocks into discrete blocks. Thus, he interpreted the boundaries between the segmented basement blocks, as high angle faults, some of which may be shear zone.

Okereke & Ananaba (2006) generated a regional magnetic field intensity map from aeromagnetic data of partly Lower Benue Trough and Niger Delta. The produced regional map showed prominent features and major tectonic trends lineaments in the NE-SW direction which when compared with those indicated on the tectonic map of Africa suggested a linear extension of the Chain and Charcot fracture zones into the continental part of Nigeria which is a further confirmation of the ongoing speculation.

Ikpokonte & Ajayi (2003) used a preliminary interpretation of shallow regional structures deduced from ground magnetic data over the Eastern part of the Lower Benue Trough (confluence) area, Nigeria to investigate the anomalies found in the regions. They postulated that the NE-SW trending anomalies in the region could possibly be associated with the basement ridges which occur within and are parallel to the general trend of the Benue Trough. The gravity anomaly models on the profiles they produced also show that these ridges may also be intruded in places by intra-basement basic bodies. Thus they arrived at a conclusion that the Lower Benue trough was underlain by basic intrusive under uplifted basement at its north and south margins and under the deep basin. As such, the basement of this basin is irregular and forms a step fault at the margins and sub-basins at the depth.

Al-Zoubi, Awin & Ziah (2003) carried out geophysical investigation at the central part of Wadi Araba area Jordan to delineate fractures/veins and locate mineralization zones using Gravity,

Magnetic, Electromagnetic and induced Polarization technique. It was found that the alteration zones in the study area align along NNW-SSE and NW trends. This alteration zone probably host significant mineralization which needs further exploration to determine the extent of mineralization.

The Isiagu lead-zinc deposits were investigated using the Electrical resistivity and self-potential methods by Isife, Obasi & Balogun (2000). They found out that shallow water table was about 20m from the surface and that this depth approximately corresponded with the depth of the ore-body. Electrical measurements also showed that structural elements that controlled mineralization in Isiagu area are joints and fractures.

Ernst Schetselaar & Eric De Kemp (2000) shows that Combined data from Potential Fields Magnetic data from standard regional airborne surveys and TM multispectral satellite sensors can be used to give reasonable predictions of general bedrock classes. In this area 76 % accuracy can be expected for supracrustal verses othogneiss terrain classification. The TM data shows spectral contrast related to compositional variations between lithologies within the two structural levels that can be used to predict the basement and cover relationships. Misclassification of basement and cover in the TM data is likely due to spectral contrast both within the cover stratigraphic sequence, as well as lateral variations within individual units.

In some cases, electromagnetic methods cannot be used to discover ore bodies directly, but the ore deposits may be associated with some type of geological structures which can sometimes be detected or mapped electromagnetically.

There are a limited number of case histories involving EM methods published by academics. Another study interpreted Induced Polarization (IP) effects in EM data at the El Arco porphyry copper deposit (Flores & Peralta-Ortega , 2009). Inverting for the chargeability and relaxation time of the polarization, it was observed that the locations where the chargeability was high were

in good agreement with the locations of high sulphide volume and veinlet (rather than disseminated) mineralization.

Ananaba & Ajakaiye (1987) made a lineament density map of Nigeria using 30 Landsat frames. The lineament density map has been compared with the primary mineral occurrences map and results shows good correlation between the areas of high lineament density and the areas where the occurrences of most primary minerals and also this correlation suggests that primary mineralization is tectonically controlled.

This study aims at utilizing remote sensing data, the newly acquired high resolution airborne magnetic data and ground follow up data acquisition to generate more detailed information on the structural framework and distribution of mineral deposits in the Trough.

2.2 Theoretical Framework

2.2.1 Magnetism of the Earth

The Earth may be divided into three parts *i.e* crust, mantle and core. The core of the Earth may also divide into two parts that is the molten outer core and the solid inner core. The core of the Earth is the main provider of heat energy in the Earth. Inglis (1955) pointed out that, it is impossible at present for determine the types of convectional motion in the molten core. Reeve (2005) indicated that the movement of the charged electric particles within the molten core produces a magnetic field around the Earth after several theoretical and experimental studies. This magnetic field enveloping the Earth give rise to the magnetic features of the various rocks found within or on the surface of the Earth. The flow of these electrical charges successfully creates a huge electromagnet (Clark & Emerson, 1991).

2.2.2 Nature of the Geomagnetic Field

The Earth‟s magnetic field within or at the surface of the Earth is produced from the molten outer core (Rivas, 2009). The Earth's magnetic field is made up of three parts (Telford *et al.*, 1990) namely;

1. The major field, which differs comparatively gradually and originates within the Earth.

2. The minor field (compared to the major field), which differs rather quickly and of external origin.

3. The spatial variations of the major field which are usually lesser than the major field, are almost the same in time and place, and are brought by local magnetic anomalies within the Earth′s crust. These are the areas of interest in magnetic surveying.

The compass needle aligns itself in the direction of magnetic field of the Earth when hanged freely at any position on the surface of the Earth. This alignment creates an angle between the magnetic and geographic north (Kearey *et al*., 2002).

Almost 90% of the geomagnetic field can be characterized by the field of a theoretical magnetic dipole at the Earth′s centre subtended at an angle of about 11.5° to the rotation axis (Kearey *et al*., 2002)

The Earth’s Magnetic Field If an unmagnetized steel needle could be hung at its centre of gravity, so that it is free to orient itself in any direction, and if other magnetic fields are absent, it would assume the course of the total geomagnetic field, a direction which is usually neither horizontal nor in- line with the geographic meridian (Telford *et al*., 1990).

The compass needle direction when hanged freely at any position of the Earth gives the direction of the geomagnetic field. The direction can be specified in terms of declination, the

angle between the true north and the horizontal and the direction of the total field. The field magnitude is proportional to the maximum torque exerted on the compass needle by the field.

The geomagnetic field to which the compass needle is reacting seems to be caused by complex interactions between the Earth's hot, liquid, metal outer core as it rotates and convection with it, generating circular current at the core-mantle boundary.

The Earth's magnetic field sources vary in nature and place. The dynamo action of the molten core produces the most extreme field recorded at the equator is in the range 30,000 nT whiles the poles record a range of 60,000 nT (Kono & Schubert, 2007). Whitham (1960) indicated that the magnetic elements are illustrated in Figure 2.1. The declination “D” is taken positive or negative depending on the deviation east or west of the geographic north. So declination can be defined as the angle the geographic north makes with the magnetic north of the Earth. Following Figure 2.1 in which the magnetic field is vertical plane, it is passing through the total magnetic force “T”. Hence, the magnetic field of the Earth at every position on the surface of the Earth “V” and “H” are vertical and horizontal components of “F”

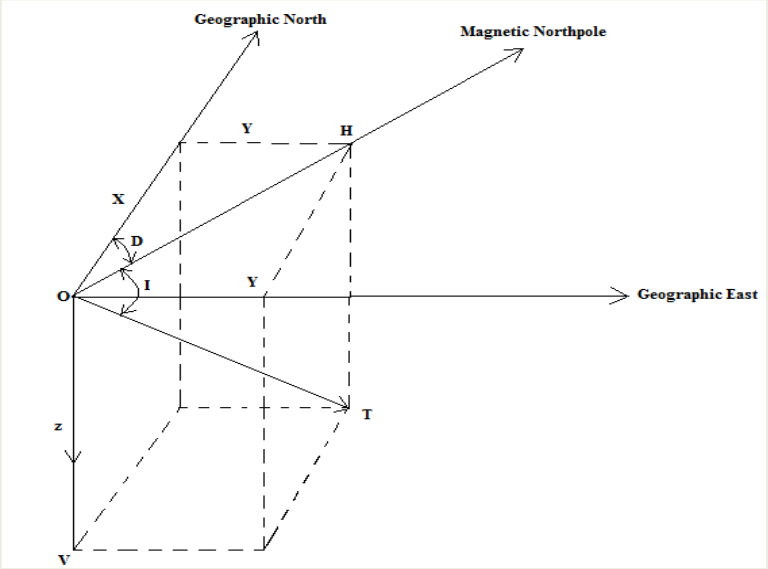

Figure 2.1: Vector representation of the geomagnetic field at any place on the Northern Hemisphere (Whitham, 1960).

These magnetic elements can be related as follows:

$$H = T \cos I \qquad 2.1$$

$$V = T \sin I \qquad 2.2$$

2.2.3 Maxwell's Equations

The universe of classical electrodynamics begins with a vacuum containing matter solely in the form of electric charges, possibly in motion, and electric and magnetic fields. We can detect the presence of these fields by the forces they exert on a moving point charge q.

Maxwell′s equations provide the curl and divergence of the electric fields and magnetic fields in terms of other things.

The universe we are operating in comprises an infinite vacuum containing electrical charges, represented by a local density **ρ**, which may be moving, and hence generating electric current,represented by a local current density **J**. The equations in vector form are:

$$A\ X\ E = \frac{-\partial(B)}{\partial(t)} \qquad 2.3$$

$$A.E = \frac{\rho}{e_o} \qquad 2.4$$

$$AXB = \mu_o(J + \epsilon_o \partial_t E) \qquad 2.5$$

$$A.B = 0 \qquad 2.6$$

where ρ is measured in (coulomb/m^3), **J** is also measured in (ampere/m^3), μ_o is permeability of vaccum (4π x 10^{-7} henries/m), e_o is capacitivity of vaccum ($1^{07}/ 4\pi c^2$ farads/m), **B** is in teslas and **E** is in volt/m.

2.2.4 Magnetism of Rocks and Minerals

Most rock-forming minerals are non-magnetic. Only a few magnetic minerals, that include magnetite (Fe_3O_4), ilmenite ($FeTiO_3$) and pyrrhotite (FeS), significantly affect the magnetization field of the particular area. Magnetic rocks contain these minerals, usually in small quantities.

Because subsurface temperatures increase with depth, substantial magnetization can occur only above certain depths. In areas with relatively high geothermal gradients, the maximum depth of magnetization is shallower than it is in areas with lower geothermal gradients.

Most sedimentary rocks contain negligible quantities of magnetic minerals, and are therefore non-magnetic. Most basic igneous rocks, on the other hand, have high magnetic susceptibilities, while acid igneous rocks and metamorphic rocks can have susceptibilities ranging from negligible to extremely high (Reeves, 1989; Petersen, 1990; Reynolds, 1997).

Below the Curie temperature is when the magnetic features of rocks can exist. This temperature varies for different rock types but ranges from 550^{o}C to 600^{o}C. Present day geothermal studies have indicated that Curie point can be reached at depths 30 to 40 km beneath the Earth. Based on these assumptions, it is estimated that all crustal rocks are very potent to carry magnetic features. Reeves (1989) suggested that the upper part of mantle has no magnetic properties hence the bottom of the Earth′s crust may be effective depth where magnetic sources can be found.

Magnetic materials can be grouped on the basis of their behavior when placed in an external field (Telford *et al.,* 1990). Many materials have equal numbers of electrons spinning and orbiting in opposite direction so that, in absence of some external magnetic field, their effects cancel out. If a magnetic field is applied, the electron orbits are very slightly disturbed electromagnetism induction. This very slightly weakens the field inside the material giving a minute magnetic effect called diamagnetism. Diamagnetism is independent of the temperature. Diamagnetic materials include quartz, feldspar, calcite, graphite, salt. The diamagnetic substances have negative magnetic susceptibilities (Reynolds, 1997).

The paramagnetic materials have unbalanced electrons so that the individual atoms or molecules act like very tiny magnets. In the absence of an external magnetic field these molecular magnets are arranged at random, giving no resultant magnetic effect to the material as a whole but if a magnetic field is applied the molecular magnetic becomes partially aligned with it thus increasing its strength. This is small effect is called paramagnetism. With

paramagnetic materials which have positive values of magnetic susceptibilities. The total magnetic intensity will be bigger than the original magnetic field. Examples of such materials include pyroxene, olivine, pyrite, and biotite (Reynolds, 1997).

Strong paramagnetic materials such as iron, nickel and cobalt are said to be ferromagnetic. With ferromagnetic materials, there is almost a perfect arrangement of their domains. Ferromagnetic materials have all their magnetic dipoles aligned hence there is a magnetization of high effect being produced. With anti-ferromagnetic materials such as hematite its adjacent magnetic dipoles are opposite to the direction of magnetization hence produces zero magnetization effect. Materials such as magnetite, ilmenite show very strong magnetization effect and its domains align themselves in the direction of applied external field (Reynolds, 1997).

2.2.5 Magnetic Susceptibility

The degree to which a material can be magnetized in an applied external field is a physical parameter known as magnetic susceptibility (Dalan, 2006). In geology, magnetic susceptibility is one characteristic of a mineral type. Its measurement gives us information about the type and quantity of minerals present in the sample. The measure of magnetization is solely characterized by the amount and composition (shape and size) of iron oxide in the rocks (Dearing, 1994; Wemegah *et al*., 2009).

The magnetic susceptibility effectively is the magnetization effect divided by the applied magnetic field. If the magnetic field is **H** (A/m) and the magnetization is **M** (A/m), the magnetic susceptibility is

$$K = X_V = \frac{M}{H} \quad 2.7$$

Where x_v is volume of susceptibility

Although susceptibility has no units, to rationalize its numerical value to be compatible with the SI or rationalized system of units, the value in c.g.s. equivalent units should be multiplied by 4 (Clark, 1997).

Reynolds (1997) indicates that most sedimentary rocks contain negligible quantities of magnetic minerals, and are therefore non-magnetic. Most basic igneous rocks, on the other hand, have high magnetic susceptibilities, while acid igneous rocks and metamorphic rocks can have susceptibilities ranging from negligible to extremely high. Magnetic susceptibility is a trace parameter of rocks, because the percentage of magnetic minerals is usually one percent or less, even in basic igneous rocks. Slight differences in iron oxide content of a mineral can cause large magnetic susceptibility variations. Remke *et al.* (2004) also pointed out that the amounts of iron oxides in rocks are influenced by the parent rock, age of rock and weathering processes.

2.2.6 Remanent and Induced Magnetism

There are two components involved in a rock's magnetization that is remanent magnetism and induced magnetism. Remanent magnetism also known as the permanent magnetism is the type which when the applied field is removed, still remains in the rock. Materials that belong to ferromagnetic and ferromagnetic retain their magnetism even when the external field is taken away. Rock magnetization usually takes place mostly at the shallow depths

because there is an increment in temperature towards the centre of the Earth (typically < 50 km depth) (Clark & Emerson, 1991). Furthermore, remanent magnetization can occur when the arrangement of the magnetic domains are locked in the presence of a weak geomagnetic field.

During cooling the magnetic domains are locked up at specific curie points owing to significant change in crystal growth. These thermo, chemical, and detrital remanent magnetizations are little and influence only the most sensitive magnetic sensors (Remke *et al.,* 2004). Primary remnant magnetization is acquired by the cooling and solidification of an igneous rock from above the Curie point (of the sources of magnetic minerals) to normal surface temperature (TRM) or by detrital remnant magnetization (DRM). Secondary remnant magnetization, such as chemical, viscous or post-depositional remnant magnetization, may be acquired later on in the rock′s history (Reynolds, 1997). The magnetization effect, M divided by the applied effect; H gives the magnetic susceptibility of the rocks. This explains best induced magnetization (Remke *et al.,* 2004)

2.2.7 Magnetization at Low Magnetic Latitudes

Close to the magnetic equator of Earth, the ambient magnetic field is almost horizontally oriented approximately north-south, and has a field intensity of between 25000 and 40000 nT, about one-half the intensity at the magnetic poles. The magnetic equator lies within 10^{o} of the Earth′s geographic equator. The decreased equatorial field intensity causes local magnetic anomalies at low latitudes to have smaller magnitudes than those produced by similar structures at high latitudes. The north-south orientation of the horizontal inducing field means that a long north-south striking magnetic structure may show no anomaly at all, except at the south and north termination of the structure (Beard & Goitom, 2000). On the other hand, the outcome can be generally reviewed this way; magnetic

readings are high along and near a line that goes through a magnetic object in the direction of the field of the Earth; magnetic readings are low in all other locations. Additionally, at very low latitudes, typically between 10^{o} inclinations, the amplitude correction for north-south trending features unduly intensifies noise and alters difference in the magnetic susceptibilities from originating magnetic sources in different directions from the external field. There are always complications with magnetic dataset interpretations because of the asymmetric anomalies produced by symmetric causative rocks mostly located anywhere on the Earth apart from areas closer to the magnetic poles (Rajagopalan, 2003).

2.2.8 Rock Alteration

Alteration is a deformation of rock when hot fluids moves from high pressure areas to low pressure areas. Along the Earth′s surface alteration of rocks may occur during chemical weathering which is the supergene alteration (Appiah, 1991). Shanks (2010) explained that the reaction of hydrothermal liquids and rocks brings about a deformation called hydrothermal alteration. Hydrothermal alteration can occur as results of isochemical activities such as metamorphism, and characterized by mineralogical variations, or it can be metasomatic and result in major element addition or removal.

The deformation of magnetic minerals is significant to remember when it comes to the explanations of magnetic anomalies. Mineral deposits are mainly controlled by wall rock alteration next to hydrothermal veins by the hot liquids (Appiah, 1991).

The alternation may range from simple recrystallization to the addition, removal or rearrangement of chemical components. The nature of the alteration products depend upon, the character of the original rock, the character of the invading fluid, which defines

such factors as pH, vapour pressure and the degree of hydrolysis and the temperature and pressure at which the reactions took place (Studemeister, 1983).

The potassic alteration zone associated with oxidized, magnetic felsic intrusions is often magnetite-rich. This is commonly observed for Au-rich porphyry copper systems (Sillitoe, 1979). However, contact metamorphism of hydrothermally altered, demagnetized igneous rocks for instance by dike injection may produce secondary magnetite. Deformation of the wall rock can bring about recrystallization, color transformations and permeability changes. The edges of a vein or close to an igneous contact are recrystallized to form carbonate rocks. The permeability of the undeformed rocks is lesser than the recrystallized rock signifying that some ores may be transported following a complex wave of recrystallization. Wall rocks alteration is an important exploration tool, the alteration brings around many deposits which are extensive and much easier to locate than the ore bodies (Appiah, 1991).

2.4 Lithology, Structure and Magnetism

In the natural environment, magnetic minerals are pervasive and occur in every kind of rocks *i.e* rocks, sediments and soils. These magnetic minerals have the magnetic dipoles locked the direction of the Earth‟s magnetic field during the formation of the rock (Harrison *et al.,*2007).

Plummer *et al*. (2001) grouped structures into two. The first is the brittle structures which resulted in the brittle-elastic breakdown of rocks long-ago. Joints and faults formed part of this broad type of structures. The second type is ductile structures which conserves the main viscoplastic alteration of rock all the way through the geological time. Examples of such structures include the folds and metamorphic foliations.

Isolated magnetic anomalies, generally circular or oval in plan and several hundred meters across, and with amplitude of tens to hundreds of nanoteslas, may arise from accumulation of magnetite and pyrrhotite, which may be associated with economic grades of copper, lead, zinc, silver, gold and others (Plummer *et al.*, 2001).

Grant (1985) pointed out that sedimentary rocks are usually non-magnetic. The analysis of geophysical data suggests that sources of magnetic bodies must located beneath the bottom of the sedimentary rocks. Sedimentary rocks like sandstone, dolomite, limestone etc have low magnetic features hence the outcome anomalies of the magnetic values are extremely small in amplitude. Due to this characteristic nature of sedimentary rocks it is sometimes difficult to detect such formations using airborne surveys (Langenheim *et al.,* 2000). Very little or no magnetic influence is experienced or detected within the Precambrian metasedimentary sequences. The only exemption is a slight lithologic part which is mainly made up of an iron rich metachert. Igneous and plutonic rocks demonstrate a broad range of magnetic features (Plummer *et al.*, 2001). On the other hand, metavolcanic formations, gabbros and several intrusive formations can generate strong magnetic anomalies (Langenheim *et al*., 2000). The Precambrian metavolcanic formations produce magnetic susceptibility values ranging from 2 for meta-rhyolite to 8000 for metabasalt multiplied by 10^{-6} SI units (Langenheim *et al*., 2000). The crust of the Earth is mainly dominated by metamorphic rocks and has a broad range of magnetic susceptibilities. They produce composite sample of magnetic anomalies. The rocks with highest magnetic anomalies are Itabiritics followed by metabasic rocks. On the other hand, regions of felsic dominated rocks such as granitic/gneissic series produce weak magnetic anomalies on a comparatively smooth background (Grant, 1985).

2.4 Theory of Aeromagnetic Survey

Aeromagnetic survey is a well-known type of geophysical survey carried out using a magnetometer aboard or towed behind an aircraft. They are widely used during mineral exploration. The principle is analogous to a magnetic survey carried out with a hand-held magnetometer, but permits much larger areas of the earth's surface to be covered quickly for regional reconnaissance. The aeromagnetic geophysical method plays an eminent role when compared with other geophysical methods in its rapid rate of coverage and low cost per unit area explored. The aircraft typically flies in a grid-like pattern with height and line spacing determining the resolution of the data (and cost of the survey per unit area).

As the aircraft (typically a helicopter) flies, the magnetometer records tiny variations in the intensity of the ambient magnetic field due to the temporal effects of the constantly varying solar wind and spatial variations in the earth's magnetic field, the latter being due both to the regional magnetic field, and the local effect of magnetic minerals in the earth's crust. By subtracting the solar and regional effects, the resulting aeromagnetic map shows the spatial distribution and relative abundance of magnetic minerals in the upper levels of the crust. Different rock types differ in their content of magnetic minerals; hence, the magnetic map allows a visualization of the geological structure of the upper crust in the subsurface, particularly the spatial geometry of bodies of rock and the presence of faults and folds.

2.4.1 Applications of Aeromagnetic Data

Aeromagnetic survey is a supportive geophysical method in mapping subsurface bedrock geology (lithology) and structures due to variations in magnetic susceptibility of rocks (Gunn, 1997). According to Reeves *et al.* (1997), where the bedrock geology cannot be mapped due to thick jungle, swamp, deep weathering or sand cover, aeromagnetic data can

give information on the hidden geology using methods of inference that are similar to those used in photo geological interpretation (such as enhancement filters). One of the main goals for the use of the magnetic data is to delineate geological structures and to some extent delineate lithology (Gunn, 1997) by gridding and applying enhancement tools.

Rocks of the study area showed different aeromagnetic responses that can be related to their lithology and tectonic activities that have resulted in the geological structures (e.g. folds, faults and fractures) in the area. Linear features (geological structures) associated with the volcanic rocks, sandstones and shale are observed as moderately low and low magnetic signature.

2.4.2 Aeromagnetic Data Processing

Data processing of the aeromagnetic data is primarily aimed at methodically separating the local anomalies from regional magnetic anomalies and for enhancement of these anomalies. Numerous analytical processes and methods are used for analysis of aeromagnetic data. They include: filtering and convolution of aeromagnetic data, reduction to pole, regional- residual separation and depth estimation analysis. These techniques are discussed in details for a better understanding.

2.6 Enhancement Techniques

Usually, the original total magnetic intensity grid is visually difficult to observe and interpret the various structures. A variety of enhancement techniques when applied to geophysical data tends to improve the data quality on the basis of mathematical principles. Mathematical enhancements filters which include reduction to the pole, analytical signal, vertical

derivative, etc are extremely helpful in developing near surface geological features except that their restrictions are based on the value of the data and extra reasons like the angle the Earth′s magnetic axis makes with the horizontal.

2.5.1 Filtering of Aeromagnetic Map

Filtering is a way of separating signals of different wavelength to isolate and hence boosts any anomalous feature with a certain wavelength. The rule of thumb is that the wavelength of an anomaly divided by three or four is approximately equal to the depth at which the body producing the anomaly is buried. Thus filtering can be used to enhance anomalies produced by features in a given depth range. Traditional filtering can be either low pass (Regional) or high pass (Residual). Thus the technique is sometimes referred to as Regional-Residual Separation. Band pass filtering isolates wavelengths between user-defined upper and lower cut-off limits. In geophysical exploration, not every signal may be of interest thus; there is always a need for filtration processes. Near surface or shallow anomalous sources usually produce relatively short wavelength disturbance.

Practically, in the manual digitization of aeromagnetic map, certain short-wavelengths are removed to allow a pass of longer wavelength disturbances of lower wave numbers. This is known as a low-pass filter. The irregularities in aeromagnetic maps are removed by low pass filtering, which thus produces a smoother map than the original. Alternatively, the filter in the Fourier domain is designed to eliminate longer wavelengths and pass shorter ones. This is called a high pass filter. Wavelength filtering is a major consideration in selection of anomalies. In studying a large-scale crustal structure, a low pass filter is employed as small local bodies are of less interest. Similarly, in the investigation of anomalies due to shallow crustal sources, a high pass filtering is employed.

2.5.2 Reduction to the Pole (RTP)

Reduction to the Pole transformation is a tool that corrects for the offset between the locations of anomalies and their sources that is a consequence of the vector nature of the Earth's magnetic field. To apply the reduced-to-pole transformation correctly, one must assume that the total magnetizations of most rocks in the study area align parallel or anti-parallel to the Earth's main field. This approach makes it possible to determine from the observed total field the position and depth of the pole that has the magnetic effect equivalent to that of an external source with the inclined magnetization. This technique transforms induced magnetic responses to those that would arise where the sources are placed at the magnetic pole (vertical field).

Pole reduction is difficult at low magnetic latitudes, since N-S bodies have no detectable induced magnetic anomaly at zero geomagnetic inclination. Pole reduction is not a valid technique where there are appreciable remanence effects. Reduction to pole of magnetic data served as an auxillary method of qualitative analysis. This allows us to have a pseudo magnetic map where the magnetization vector of the rocks and the measured total field both are in vertical direction. The contribution of remanent magnetization is supposed to be irrelevant.

2.5.3 Regional- Residual Separation

Regional magnetic features are believed to be caused by the properties of materials deep within the earth or due to the dipole field of the earth. The methods employed in the isolation of the background field from survey data have been discussed extensively in various geophysical literatures. These methods involve either visual and or graphical procedures or

analytical methods such as least squares fit.The mapped potential field data are the sum of the effect of all sources causing a magnetic anomaly. The problem in applied geophysics is to eliminate or reduce to the lowest, the effects of deep-seated, non-commercial sources with as little distortion of the resultant anomaly as possible. A geophysical anomaly is typically composed of a broad spectrum of frequencies, each frequency being characterized by specific amplitude. The anomalies of interest may be corrupted by multi-frequently "noise" consisting of regional trends, instrument drift, uninteresting geologic variation, etc. If the frequently content of both anomaly and noise is known, and there is no spectral overlap between them, then a filter of interest would be designed to eliminate the noise effects.

2.5.4 Polynomial Fitting

Polynomial fitting is a purely systematic method which involves matching of the regional field with a low order polynomial surface to produce the residual features as random errors. The system is based on statistical theory. The regional trend is represented by a straight line or generally by a smooth polynomial curve. The polynomial is fitted by the method of the least squares. But, it should be well noted that this method has its inherent drawbacks:

1. The higher the order of the polynomials, the better it fits the observations.

2. The ludicrous extreme when the order of the polynomial is less than the number of the observations, the curve then passes perfectly through all the data points but geologically has no meanings.

A curve fitted by least squares must pass through the mean of the magnetic values, so that the residual anomalies are divided equally between positive and negative values. Each residual anomaly is flanked by anomalies of opposite sign, which are due to the same anomalous mass

that caused the central anomaly; and so they have no significance of their own. In practice, the polynomial is rarely extended beyond the second orders.

2.5.5 Upward continuation of the potential Field.

Upward continuation is a filter operation, which smoothens the original data by attenuation of short wavelength anomalies relative to their long wavelength counterparts. In space, the upward continuation operation is a 2D convolution process given by the integral equation (Bhattacharyya, 1976).

$$\phi'(x,y) = \int_{-\infty}^{\infty}\int_{-\infty}^{\infty} f(\alpha,\beta)\phi(x-\alpha, y-\beta)d\alpha d\beta \qquad 2.8$$

Ø´(x,y) is the input data, Ø(x,y) is the output data and f(α,β) is the filtering function.

In order that a filtering function can be useful, it must be of finite extent, if f(x,y) becomes zero for |x|=|X| and |y|=|Y| then equation (2.8) can be replaced by

$$\phi'(x,y) = \int_{-X}^{X}\int_{-Y}^{Y} f(\alpha,\beta)\phi(x-\alpha, y-\beta)d\alpha d\beta \qquad 2.9$$

Convolution in the space domain is equivalent to multiplication in the frequency domain. In order to arrive at the spectrum of the output, the spectrum input is multiplied by the spectrum of the filtering function. Denoting the Fourier transform of a function by the corresponding capital letter, with a frequency argument and taking the Fourier transform of Equation (2.8). Thus we have:

$$Ø\,´(f_x,f_y) = F(f_x,f_y)\, Ø(f_x,f_y) \qquad 2.10$$

Where f_x and $f_y$are the angular frequencies along x and y axes respectively, From the results of the potential theory, the upward continuation of the potential functionØ(x,y,0) in a source free region to a height(h) above the plane Z=0

$$\phi'(x,y,h) = \int_{-\infty}^{\infty}\int_{-\infty}^{\infty} \frac{h\phi(\alpha,\beta,0)d\alpha d\beta}{2\pi\sqrt{[(x-\alpha)^2+(y-\beta)^2+h^2]^3}} \qquad 2.11$$

Comparing equation (2.11) and (2.8), and realizing that the convolution integral are commutation, allows recognition of equation (2.11) as a two dimensional convolution and hence a filtering operation. The potential function Ø(x, y, 0) is operated upon by the filtering function f_u (x,y,h) in order to arrive at Ø(x,y,h) where

$$f_u(x,y,h) = \frac{h}{2\pi\sqrt{(x^2-y^2+h^2)^3}} \qquad 2.12$$

The theoretical frequency response of a true upward continuation operator may be obtained by the Fourier transform solution of the integral

$$f_u(f_x,f_y,h) = \int_{-\infty}^{\infty}\int_{-\infty}^{\infty} \frac{he^{-2\pi i(f_x x+f_y y)}}{2\pi\sqrt{(x^2+y^2+h^2)^3}}dxdy \qquad 2.13$$

Solution of this equation by gamma functions yields

$$F_u(f_x,f_y,h) = e^{-2\pi h\sqrt{(f_x^2+f_y^2)}} \qquad 2.14$$

Transformation from space domain to the frequency domain provides a fast and convenient way in which otherwise complicated numerical filtration operations on magnetic fields can be performed.

2.5.6 Depth Estimation

Interpretation of depth to magnetic source estimation is very complex and when done accurately can be used to plan drill holes to test magnetic and non-magnetic targets and to prepare accurate budget and plan exploration program. The depth to the top of the magnetic source is useful in finding sedimentary succession and also for locating major structures in the basement rocks. At times most anomalies that arise from the basement are due to lithological changes rather than structural features. In some geological conditions, the depth to the bottom of the magnetic source is believed to correspond to the Curie temperature. (Reeve, 2005).

Depth estimation techniques in the past involved the use of contours, stretched histogram, pseudo-colour compositions and first vertical derivative data. Now, exciting suite of new generation depth estimation tools and products are being used. The tools include;

1. Spectral analysis
2. Improved naudy automatic model
3. Traditional and extended euler deconvolution
4. Philip's method
5. Matching filter depth separation and slicing
6. Complex amplituide and instantaneous phase
7. Magnetic coherence map
8. Analytical signal
9. Vertical derivatives, continuation, pass and directional filters
10. Powerful visualization and hard copy composition language and tools

The methods listed above are used to locate the contacts and also to estimate the sources depth. They are based on the transformation of the potential field anomalies into special functions that form gradient peaks and ridges over the sources. The maxima peak values are located directly above the magnetic contact depending on the assumed geometry model used (Chukwuka, 2016).

2.5.7 Spectral Analysis

Trifonova *et al.* (2006) has used this model to prove the average depths to the tops of magnetized bodies with success. One principal result of Spector and Grant's analysis is that the expectation value of the spectrum for the model is the same as that of a single body with the average parameters for the collection (Okubo *et al*., 1985).

In polar coordinates (S, ψ) in frequency space, this spectrum has the form

$$F(S,\psi) = 2\pi JA\,[(N + i\,(L cos\psi + M\,sin\psi)] \times [n + i\,(l cos\psi + m sin\psi)]$$

$$\times\, sinc(\pi sa cos\psi)\; sinc(\pi sb sin\psi)$$

$$\times \exp(-2\pi is\,(x_o\, cos\psi + y_o sin\psi))$$

$$\times [\exp(-2\pi s z_t) - \exp(-2\pi s z_b) \qquad 2.15$$

Where

$J = magnetization\ per\ unit\ volume$;

$A = average\ cross - sectional\ areas\ of\ the\ bodies$;

$L, M, N = direction\ cosines\ of\ the\ geomagnetic\ field$;

$l, m, n =$ *direction cosines of the average magnetization vector a and b* $=$ *average body* $x -$ *and* $y -$ *directions,*

$x_0 and\ y_0 = average\ body\ x -$ *and* $y -$ *centre locations and*

$$z_t and\ z_b = average\ depths\ to\ the\ top\ and\ bottom\ of\ the\ bodies,$$

$$and\ where\ sinc(x) = \frac{sinx}{x}$$

Estimation of the bottom depths could be approached in two steps (Bhattacharyya & Leu, 1975 and 1977): firstly, finding the centroid depth $z_0$and secondly, determine the depth to the top z_t. The depth to the bottom (inferred CPD) is calculated from these values:

$$z_b = 2z_0 - z_t \qquad 2.16$$

The terms involving $z_t$and $z_b$can be recast into a hyperbolic sine function of $z_t$and $z_b$plus a centroid term. At very long wavelengths, the hyperbolic sine tends to unity, leaving a single term containing z_0, the centroid. At somewhat shorter wavelengths, the signal from the top dominates the spectrum and an estimate of the depth to the top can be obtained (Okubo *et al*. 1985). If we begin with the centroid, at very long wavelengths (compared to the body dimensions), the terms involving the body parameters ($a, b, and\ z_b - z_t$) may be approximated by their leading terms, to yield

$$F(S,\psi) = 4\pi VJA\ [(N + i\ (Lcos\psi + M\ sin\psi)] \times [n + i\ (lcos\psi + msin\psi)]$$

$$\times \exp(-2\pi is\ (x_o\ cos\psi + y_o sin\psi))$$

$$\times \exp(-2\pi s z_0) \qquad 2.17$$

Where

$$V = is\ the\ average\ body\ volume.$$

Equation 2.17 can be recognized as the spectrum of a dipole.

In effect, the ensemble average at these very low frequencies is that of a random distribution of point dipoles. What follows, therefore, is independent of the details of the body parameters (prisms, cylinders or whatever), provided that the dimensions in all directions are comparable. The method of Okubo *et al.* (1985) was used in estimating $z_0$from Equation 2.17:

If $F(S,\psi) = \frac{1}{s}(S,\psi)$

First, average the square amplitude of Gover an angle in the frequency plane

$H^2(s) = \frac{1}{2\pi}\int_{-\pi}^{\pi} |G(S,\psi)|^2 d\,\psi$

Then $H(s)$ has the form

$H(s) = A\exp(-2\pi s z_0)$

If F satisfies Equation 2.17, where A is a constant. Hence,

$\ln H(s) = \ln A\exp(-2\pi s z_0)$ 2.18

holds. The centroid depth $z_0$can now be estimated by least-squares fitting $\ln H(s)$ with a constant and a term linear in s.

The second step is the process of estimating the depth to the top. For this purpose, we return to Equation (2.16) and assume that a range of wavelengths can be found for which the following approximations hold:

$\sin c(\pi\pi a\cos\psi) \approx 1$

$\sin c(\pi\pi a\sin\psi) \approx 1$

And

$\exp(-2\pi s a z_b) \approx 0$

For these approximations to be valid, the bodies must in general be large in depth compared to their horizontal dimensions. However, if the distribution of horizontal body dimension is very broad, a similar effect will be produced by variability in terms corresponding to the horizontal body dimensions.

If the above approximation holds, the spectrum reduces to the form

$$F(S,\psi) = 2\pi VJA\,[(N + i\,(Lcos\psi + M\,sin\psi)] \times [n + i\,(lcos\psi + msin\psi)]$$

$$\times \exp(-2\pi is\,(x_o\,cos\psi + y_o sin\psi))$$

$$\times \exp(-2\pi sz_t) \qquad 2.19$$

Which is very similar to Equation 3, except for a factor of s. Equation 2.19 is in fact the spectrum of a monopole.

Estimation of $z_0$is therefore done using

$$K^2(s) = \frac{1}{2\pi}\int_{-\pi}^{\pi} |F(S,\psi)|^2 d\,\psi \qquad 2.20$$

From which

$$K(s) = B\exp(-2\pi sz_t)$$

Follows, where B is a sum of constants independent of s, then from

$$\ln K(s) = \ln B\exp(-2\pi sz_t) \qquad 2.21$$

And fit $\ln K(s)$with a constant and a term linear in s.

The reliability of this method has been proven in many cases (e.g. Okubo, 1994; Trifonova *et al*., 2006). Fast Fourier transform (FFT) estimates Fourier components between zero frequency and the Nyquist limit imposed by the grid cell size. The Nyquist frequency is the highest frequency (short wavelength) that is possible to measure given a fixed sample interval (Yawsangratt, 2002). It is defined by the expression,

$$N = \frac{1}{(2\Delta x)} \qquad 2.22$$

Where $\Delta x$is the sampling interval.

2.6 Aeromagnetic Data Interpretation

Aeromagnetic datum is interpreted qualitatively and quantitatively;

2.6.1 Qualitative Interpretation

Qualitative interpretation involves the description of the survey results and the explanation of the major features disclosed by a survey in terms of the types of possible geological formations and structures that give rise to the evident anomalies. The qualitative interpretation of a magnetic anomaly map begins with a visual inspection of the shapes and trends of the major anomalies. Typically, some geological information is available from outcrop evidence within the survey area (or nearby) and very often the role of the geophysical data is to extend this geological knowledge into areas where there is no outcrop information (i.e. extrapolation from the known to the unknown) or to extend mapped units into the depth dimension (i.e. to help add the third dimension to the mapped geology).

After delineation of the structural trends, a closer examination of the characteristic features of each individual anomaly is carried out. These features are:

i. The relative locations and amplitudes of the positive and negative contour parts of the anomaly,

ii. the elongation and aerial extent of the contours and

iii. the sharpness of the anomaly as seen by the spacing of contours

Accordingly, the following items are taken in considerations during qualitative interpretation of the aeromagnetic map:

1. In sedimentary regions, mainly where the basement depth exceeds 1.5 km, the magnetic contours are normally smooth and variations are little, reflecting the basement rocks rather than the near surface features (Telford *et al*., 1998). The magnetic relief observed over sedimentary basin areas is virtually always controlled more by the lithology of the basement than by its topography (Dobrin & Savit, 1988).

Meanwhile, in regions where igneous and metamorphic rocks predominate, usually exhibit complex magnetic variations.

2. Changes in the magnetization of basement rocks a mile or more deep may result in magnetic anomalies up to several thousand gammas (nT) in magnetic readings at the surface. The density of contour lines often provides a useful criterion for indicating structures. The closer the contours, i.e., the greater the gradients, the shallower, in general, is the source. Any abrupt change in the spacing over an considerable distance implies a discontinuity in depth, possibly a fault (Dobrin, 1983).

3. The magnetic anomalies of large areal extent reflect a deeper source than small-size anomalies.

4. Often, a well-defined boundary between zones with considerable different degrees of magnetic relief can denote the presence of a major basement fault (Dobrin & Savit, 1988).

2.6.2 Quantitative Interpretation

This involves making numerical estimates of the depth and dimensions of the sources of anomalies and this often takes the form of modeling of sources which could, in theory, replicate the anomalies recorded in the survey. In other words, conceptual models of the subsurface are created and their anomalies calculated in order to see whether the earth-model is consistent with what has been observed. The model parameters are then attuned in order to obtain a better conformity between observed and calculated anomalies.

2.7 Theory of Remote Sensing

Remote sensing is the acquisition of information about an object or phenomenon without making physical contact with the object and thus in disparity to on the site observation. It refers to the activities of recording, observing, and perceiving (sensing) objects or events in far-away (remote) places.

In modern usage, remote sensing in general refers to the use of aerial sensor technologies to detect and classify objects on Earth by means of propagated signals (e.g. electromagnetic radiation). It may be split into active remote sensing (when signal is first emitted from aircraft or satellites) or passive (e.g. sunlight) when information is merely recorded. The output of a remote sensing system is usually an image representing the scene being observed. A further step of image analysis and interpretation is required to extract useful information from the image. Depending on the scope, remote sensing may be broken down into:

1. Satellite remote sensing; when satellite platforms are used,
2. Photography and photo grammetry; when photographs are used to capture visible light,
3. Thermal remote sensing; when the thermal infrared portion of the spectrum is used,
4. Radar remote sensing; when microwave wavelengths are used, and
5. LIDAR remote sensing; when laser pulses are transmitted toward the ground and the distance between the sensor and the ground is measured based on the return time of each pulse.

The applications of remote sensing includes archaeology, agriculture, cartography, civil engineering, meteorology and climatology, coastal studies, emergency response, forestry, geology, geographic information systems, hazards, land use and land cover, natural disasters, oceanography, water resources, and so on.

2.7.1 Principles of Electromagnetic Radiation

Remote sensing takes one of the two forms depending on how the energy is used and detected. Passive remote sensing systems record the reflected energy of electromagnetic radiation or the emitted energy from the earth, such as cameras and thermal infrared detectors. Active remote sensing systems send out their own energy and record the reflected portion of that energy from the earth's surface, such as radar imaging systems.

Electromagnetic radiation is a form of energy with the properties of a wave, and its major source is the sun. Electromagnetic spectrum is solar energy traveling in the form of waves at the speed of light (denoted as *c* and equals to 3.108 ms^{-1}). The waves propagate through time and space in a manner rather like water waves, but they also oscillate in all directions perpendicular to their direction of travel. Electromagnetic waves may be characterized by two principal measures: wavelength and frequency. The wavelength λ is the distance between successive crests of the waves. The frequency μ is the number of oscillations completed per second. Wavelength and frequency are related by the following equation:

$$C = \lambda \, . \, \mu \qquad 2.17$$

The electromagnetic spectrum, despite being seen as a continuum of wavelengths and frequencies, is divided into different portions by scientific convention (Figure 2.3). Major divisions of the electromagnetic spectrum, ranging from short-wavelength, high-frequency waves to long-wavelength, low-frequency waves, include gamma rays, x-rays, ultraviolet (UV) radiation, visible light, infrared (infrared) radiation, microwave radiation, and radiowaves.

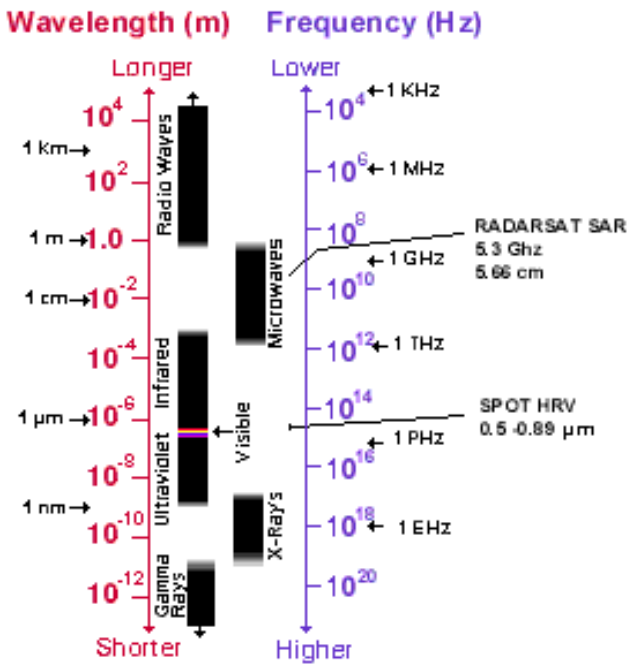

Figure 2.2: The electromagnetic spectrum showing the spectral bands

The visible spectrum, commonly known as the *rainbow of colors* we see as visible light (sunlight), is the portion of the electromagnetic spectrum with wavelengths between 400 and 700 billionths of a meter (0.4–0.7 µm). Although it is a narrow spectrum, the visible spectrum has a great utility in satellite remote sensing and for the identification of different objects by their visible colors in photography.

The infrared spectrum is the region of electromagnetic radiation that extends from the visible region to about 1 mm (in wavelength). Infrared waves can be further partitioned into the near-infrared, mid-infrared, and far-infrared spectrum, which include thermal radiation.

Microwave radiation has a wavelength ranging from approximately 1 mm to 30 mm. Microwaves are emitted from the earth, from objects such as cars and planes, and from the atmosphere. These microwaves can be detected to provide information, such as the

temperature of the object that emitted the microwave. Because their wavelengths are so long, the energy available is quite small compared with visible and infrared wavelengths.

2.7.2 Characteristics of Remotely Sensed Data

Data collected by these remote sensing systems can be in either analog format (e.g., hardcopy aerial photography) or digital format (e.g., a matrix of "brightness values" corresponding to the average radiance measured within an image pixel). Digital remote sensing images may be input directly into a GIS for use; analog data also can be used in GIS through an analog-to-digital conversion or by scanning. More often, remote sensing data are first interpreted and analyzed through various methods of information extraction in order to provide needed data layers for GIS. The achievement of data collection from remotely sensed imagery needs an understanding of four basic resolution characteristics, namely, spatial, spectral, radiometric, and temporal resolution.

i. Spatial Resolution

This term referred to the number of pixels utilized in construction of digital image. It is a measurement of the minimum distance between two objects that will allow them to be distinguished from one another in an image and is a function of sensor altitude, detector size, focal size, and system configuration. Spatial resolution for aerial photography is measured in resolvable line pairs per millimeter, while for other sensors; it refers to the dimensions (in meters) of the ground area that falls within the instantaneous field of view of a single detector within an array or pixel size.

ii. Radiometric resolution

It portrays how well the differences in brightness in an image can be perceived. It refers to the sensitivity of a sensor to incoming radiance. Coarse radiometric resolution would record a

scene using only a few brightness levels, that is, at very high contrast, whereas fine radiometric resolution would record the same scene using many brightness levels.

iii. Temporal resolution

This is the amount of time it takes for a sensor to return to a previously imaged location. Therefore, temporal resolution has a significant inference in change detection and environmental monitoring. Many environmental phenomena constantly change over time, such as vegetation, weather, forest fires, volcanoes, and so on.

2.7.3 Remote Sensing Instrumentation

The most common types of remote sensor are radiometers, Multispectral Scanners, spectrometers, and film camera. The first two convert radiation (photons) emanating from each surface target into electrical signals whose magnitudes are proportional to the spectra radiances in the intervals (bands) sensed. The surface is usually sampled successively, as by a mirror scanning from side to side while the sensor moves forward on its platform. Each pixel provides the collective radiation from the material within it to the record as a single discrete quantity so that the converted signal is a measure of the combined ground target variation from one successive pixel area to the next.

The airborne imaging spectrometer developed by the Jet propulsion laboratory uses a slit to pass radiation from the ground onto a multi-linear array Charge Coupled Detector (CCD) to sense successive area along a moving track. The film camera differs from the sequential sensor types in that it allows the radiation from all surface targets sensed at the same instant to strike the film (recorder) simultaneously in their correct positions as determined by the optics of the system.

Remote sensing as a technology refers to the acquisition of data and derivative information about object, classes or materials located at some distance from the sensors by sampling radiation from selected region (Wave bands) of the electromagnetic (EM) spectrum for sensors mounted on moving platforms (e.g. aircraft and satellites) operating in or above the earth's atmosphere, the principal sensing regions are in the visible, reflected near- infrared, thermal infrared, and microwave radar regions of the EM spectrum. The particular wavelength (or frequencies) detectable by visible infrared sensors depend in large measure on the extent to which the waveband radiation is absorbed, scattered, or otherwise modified by the atmosphere ("Windows of transparency" concept). The radiation measured from space platform is usually secondary in that it is reflected or emitted energy generated from molecular interaction between incoming radiation (irradiant) and the earth material being sensed. Common primary energy sources included the sun or active radiation - generating devices such as radar, sensed thermal radiation from the earth's surface results from internal heat source and the heating effect of solar radiation. Because most material absorbs radiation over the sensed parts of the Enhanced Thematic Mapper spectrum, only fraction of the incoming radiation are returned to the sensor. Layer of a negative on development are yellow, magenta and cyan, being sensitive to blue, green, and red light respectively. However, when producing a "colour composite" from individual waveband images are needed to make a Multispectral colour composite (Campbell, 2007).

Colour composite photographs can be produced by passing white light successively through a primary colour filter and each respective black and white transparency after all three images are superimposed and registered to one another on a colour sensitive film. The red band activates red colour on the film if projected through a red filter. Light tones (clear in a transparency) representing red objects pass red-filtered high onto the film while screening out blue and green filters. The resulting composite is a natural colour photograph. When an

infrared band transparency is projected through a red filter, and red and green bands through green and blue filters, respectively, vegetation, in particular, which is highly reflective (very bright) in the infrared, moderately reflective in the green and low in the red because of absorption of red light by chlorophyll, will appear red in the colour composite (little blue and almost no green contribution). Thus, in a false-colour composite, red is almost always a reliable indicator of vegetation (Campbell, 2007).

A set of Multispectral images is produced by breaking the image-forming radiation into discrete spectral intervals through the use of waveband filters (or other light dispersion or selection devices). If a surface material has high reflectance or remittance in some given interval, it will be recorded as a light (bright) tone on a position film-based image conversely, a dark tone represents a low reflectance or emittance. Because the same material normally has varying value of reflectance or emittance in different spectral regions, it will produce some characteristic gray level (on film) in the image from each particular waveband. Different materials give rise to different gray levels in any set of waveband images, thus creating the varying tonal patterns that spatially define classed, objects or features. Multispectral images of the same scene are characterized by different tonal levels for the various classes from one band to the next (Campbell, 2007).

2.7.4 Application of Landsat Satellite

Landsat data has a wide range of applications which has been proved undoubtedly to be of benefit to humanity. These applications are listed below:

i. **Geology:** It is used for recognition of rock types,mapping of major geology units, revising geology maps, mapping igneous intrusions, mapping land forms, search for surface guides to mineralization, mapping linears.

ii. **Environment:** Monitoring surface mining and reclamation, mapping and monitoring of water pollution (e.g. tracing oil spills and pollutants), determination of effects of natural disasters and monitoring environmental effects of man's activities (e.g. Lake Entrophication, defoliation etc).

iii. **Agriculture, Forestry and Range Resource:** Discrimination of vegetative types; crop types, timber types, range vegetation, determination of range readiness and biomass, determination of vegetation stress, determination of soil conditions and assessment of grass and forest fire damage.

iv. **Land Use and Mapping**: Classification of land uses, cartographic mapping and map updating, separation of urban and rural categories (Monitoring urban growth), regional planning, mapping of transportation networks and mapping of land – water boundaries.

v. **Water Resources:** Determination of water boundaries and surface water area and volume,mapping of floods and flood plains, determination of a real extent of snow and snow boundaries, determination of water depth and determination of irrigated fields.

2.7.5 Remote Sensing Data Analysis and Interpretation

Remotely sensed data can be used to extract thematic and metric information, making it ready for input into GIS. Thematic information provides descriptive data about earth surface features. Themes can be as diversified as their areas of interest, such as soil, vegetation, water depth, and land cover. Metric information includes location, height, and their derivatives, such as area, volume, slope angle, and so on. Thematic information can be obtained through visual interpretation of remote sensing images (including photographs) or computer based digital image analysis. Metric information is extracted by using the principles of photogrammetry.

1. Photographic/Image Interpretation and Photogrammetry

Photographic interpretation can be defined as the process of examining aerial photographs/images for the purpose of identifying objects and judging their significance (Colwell, 1997). The activities of aerial photo/image interpreters may include: Detection/identification, measurement, and problem solving.

In the process of detection and identification, the interpreter identifies objects, features, phenomena, and processes in the photograph and conveys his or her response by labeling. These labels are often expressed in qualitative terms, for example, *likely, possible, probable,* or *certain.* The interpreter also may need to make quantitative measurements. Techniques used by the interpreter typically are not as precise as those employed by photogrammetrists. At the stage of problem solving, the interpreter identifies objects from a study of associated objects or complexes of objects from an analysis of their component objects, and this also may involve examining the effect of some process and suggesting a possible cause.

The elements used commonly in photographic/image interpretation: tone/color, size, shape, texture, pattern, shadow, and association. Tone/color is the most important element in photographic/image interpretation.

i. **Tone** is the specific quality of brightness, deepness, or hue of a tint, or shade of a color. It refers to each discernible variation from white to black and is a record of light reflection from the land surface onto the film. The more light received, the lighter is the image on the photograph.

ii. **Colour** is the property possessed by an object of producing different sensations on the eye as a result of the way it reflects or emits light. It refers to each distinguishable variation on an image produced by a multitude of combinations of hue, value, and chroma.

iii. **Size** is the relative extent of something; a things overall dimensions or magnitude; It provides another important clue in discrimination of objects and features. Both the relative and absolute sizes of objects are important. An interpreter also should judge the significance of objects and features by relating to their background.

iv. **Shape** is the external form or characteristic of something. The shapes of objects/features can provide diagnostic clues in identification. It is worthy to note that human-made features often have straight edges, whereas natural features tend not to.

v. **Texture** is the frequency of change and arrangement in tones. The visual impression of smoothness or roughness of an area often can be a valuable clue in image interpretation. For example, water bodies typically are finely textured, whereas grass is medium and brush is rough, although there are always exceptions.

vi. **Pattern** is the spatial arrangement of objects. It is the regular arrangement of objects that can be diagnostic of features on the landscape. Human-made and natural patterns are often very different. Pattern also reveals a great deal of information about the lithology and structural patterns in an area.

vii. **Shadow** relates to the size and shape of an object. Geologists like low-sun-angle photography because shadow patterns can help to identify objects. Steeples and smoke stacks can cast shadows that can facilitate interpretation.

2. Digital Image Pre-processing

In digital analysis of remotely sensed data, the basic elements of image interpretation, although developed initially based on aerial photographs, also should be applicable to digital images. However, most digital image analysis methods are based on tone or color, which is represented as a digital number (i.e., brightness value) in each pixel of the digital image. As multisensor and high spatial resolution data have become available, texture has been used in image classification, as well as contextual information, which describes the association of

neighboring pixel values. Before main image analyses take place, preprocessing of digital images often is required. Image preprocessing may include detection and restoration of bad lines, geometric rectification or image registration, radiometric calibration and atmospheric correction, and topographic correction.

Geometric correction and atmospheric calibration are the most important steps in image preprocessing. *Geometric correction* corrects systemic and nonsystematic errors in the remote sensing system and during image acquisition (Lo & Yeung, 2002).

It commonly involves;

i. D*igital rectification,* a process by which the geometry of an image is made planimetric, and

ii. R*esampling,* a process of extrapolating data values to a new grid by using such algorithms as nearest neighbor, bilinear, and cubic convolution.

iii. Accurate geometric rectification or image registration of remotely sensed data is a prerequisite, and many textbooks and articles have described them with details (e.g., Jensen, 2005).

3. **Image Enhancement and Feature Extraction**

Image-enhancement methods can be roughly grouped into three categories: contrast enhancement, spatial enhancement, and spectral transformation. They are applied to enhance visual interpretability of remotely sensed data as well as to facilitate subsequent thematic information extraction.

i. ***Contrast enhancement*** involves changing the original values so that more of the available range of digital values is used, and the contrast between targets and their backgrounds is increased (Jensen, 2005).

ii. ***Spatial enhancement*** applies various algorithms, such as spatial filtering, edge enhancement, and Fourier analysis, to enhance low- or high-frequency components, edges, and textures.

iii. ***Spectral transformation*** refers to the manipulation of multiple bands of data to generate more useful information and involves such methods as band rationing and differencing, principal components analysis, vegetation indices, and so on.

Feature extraction is often an essential step for subsequent thematic information extraction. Many potential variables may be used in image classification, including spectral signatures, vegetation indices, transformed images, textural or contextual information, multitemporal images, multisensor images, and ancillary data. Because of different capabilities in class separability, use of too many variables in a classification procedure may decrease classification accuracy (Price *et al*., 2002). It is important to select only the variables that are most effective for separating thematic classes. Selection of a suitable feature extraction approach is especially necessary when hyperspectral data are used. This is so because the huge amount of data and the high correlations that exist among the bands of hyperspectral imagery and because a large number of training samples is required in image classification. Many feature-extraction approaches have been developed, including principal components analysis, minimum-noise fraction transform, discriminant analysis, decision-boundary feature extraction, nonparametric weighted-feature extraction, wavelet transform, and spectral mixture analysis (Neville *et al*., 2003; Rashed *et al*., 2001).

4. Image Classification

The objective of image classification is to assign all pixels in the image to particular classes or themes (e.g., water, forest, residential, commercial, etc.) and to generate a thematic "map." Image classification uses spectral information represented by digital numbers in one or more spectral bands and attempts to classify each individual pixel based on the spectral information. The former

refers to the categories of interest that the analyst is actually trying to identify from the imagery, and the latter refers to the groups of pixels that are uniform (or near alike) with respect to their brightness values in the different spectral channels of the data. Generally, there are two approaches to image classification: supervised and unsupervised classification.

i. ***Supervised*** **classification:** here, the analyst identifies in the imagery homogeneous representative samples of different cover types (i.e., information classes) of interest to be used as training areas. Each pixel in the imagery then would be compared spectrally with the training samples to determine to which information class they should belong. Supervised classification employs such algorithms as minimum-distance-to-means, parallelepiped, and maximum likelihood classifiers (Lillesand *et al*., 2008).

ii. **U*nsupervised*** **classification**: here, spectral classes are first grouped based solely on digital numbers in the imagery, which then are matched by the analyst to information classes. The objective is to group multiband spectral response patterns into clusters that are statistically separable. Thus, a small range of digital numbers (DNs) can establish one cluster that is set apart from a specified range combination for another cluster (and so forth). The logic or steps involved in the two methods of classification can be grasped from these flow diagrams:

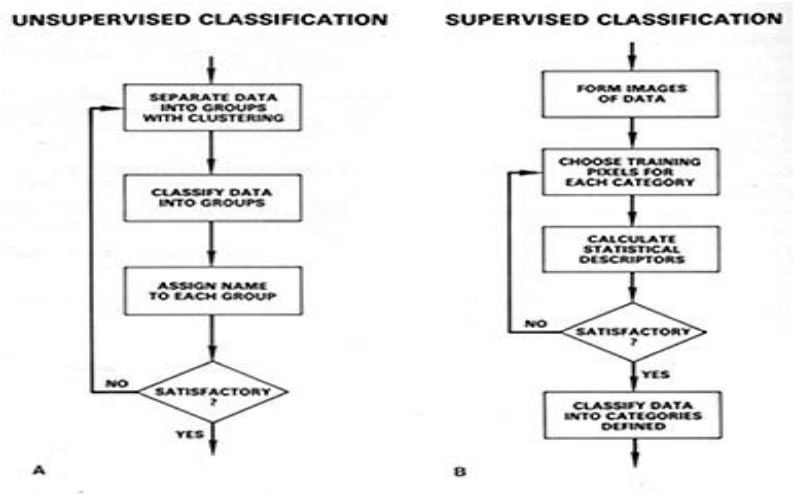

Figure 2.3: Flow Diagrams (a) Supervised and (b) Unsupervised Image Classification

2.8 General Principles of Resistivity Surveying.

The principle of the resistivity method is that when current is passed into the earth through electrodes, any subsurface variation in the conductivity alters the current flow which in turn affects the distribution of the electric potential (Telford *et al.*, 1990). It is usually possible to obtain information about the distribution of subsurface materials from measurements of electric potentials made at the surface (Telford *et al*., 1990).

When current is introduced to subsurface materials (rocks), the amount of current absorbed or rejected is dependent on the nature of the material encountered in the subsurface and hence, we can infer the type of material offering such response to the passage of electrical current using typical resistivity models Telford *et al.,* (1990). All resistivity methods employ artificial source of current which is introduced into the ground through point electrodes. It is therefore possible to determine an effective or apparent resistivity of the subsurface material after measuring the potential at other electrodes in the vicinity of the current flow. The resistivity of rocks is strongly influenced by the presence of groundwater which acts as an electrolyte. This is especially important in porous sediments and sedimentary rocks and also in fractured basement rocks. The general principle involves passing current into the subsurface using two electrodes. The lines of current flow adapt to the surface resistivity pattern so that the potential difference between surfaces can be measured where they intersect the ground surface.

Mineral grains comprised of soils and rocks are essentially nonconductive, so the resistivity of soils and rocks is governed primarily by the amount of pore water and the arrangement of the pores. Generally, since the resistivity of a soil or rock is controlled primarily by the pore water conditions, there are wide ranges in resistivity for any particular soil or rock type, and resistivity values cannot be directly interpreted in terms of soil type or lithology (Telford *et al*., 1990).

Subsurface materials exhibit a very large range of electrical resistivity values. Fresh rock is generally a poor conductor of electricity. The electrical properties of most rocks are governed to a

large degree by the amount of water filling the gaps between the mineral grains as well as the amount of salt dissolved in the water. Pure water has a very low electrical conductivity whereas sea water is a good conductor; owing to the high level of dissolved salts (such as sodium chloride) it contains (Telford *et al*., 1990).

The summary of properties that may affect the resistivity of a soil includes: -

i. Porosity.
ii. Permeability.
iii. Water content.
iv. Mineral composition.
v. Salinity of the water.

For conduction in electrolytic conducting medium, there is an aqueous solution of common salt in the rock pore spaces. For such materials that have water-bearing rocks, the resistivity depends on:

1. The amount of water present in the pores.
2. The salinity of water content and
3. The distribution of water in the pore space.

It is noteworthy that conduction is temperature – dependent. Extreme temperatures affect the electrical resistivities of rocks. For instance, very high temperature can lead to the evaporation of water from the pore space, leading to higher concentration and therefore higher conductivity. Similarly, low temperatures can lead to the freezing of the water in the pore spaces leading to low conductivity. Average temperature will increase the mobility of the ions thereby leading to good conductivity (Telford *et al*., 1990).

The actual dependence of conductivity on temperature is given by the relationship

$$\rho_t = \frac{\rho_{to}}{1 + \mu(t - t_0)} \qquad 2.23$$

Where ρ_t= resistivity measured at a reference temperature

t = ambient temperature

μ = temperature coefficient of resistivity

t_0 = temperature at the surface.

The potential about a single current electrode is developed from two basic considerations.

They are: -

1. Ohm's law and
2. Divergence theorem.

Consider a continuous current, I, flowing in an isotropic homogenous medium. If j, is the current density in A/m^2, the current density and electric field intensity, $\bar{E}$ are related as follows:

$$\bar{E} = \rho\, j \qquad 2.24$$

Where ρ = resistivity.

The electric field is the gradient of a scalar potential i.e

$$\bar{E} = -\nabla U = -\partial U/\partial r \qquad 2.25$$

Where U is a potential function.

If charge is conserved, using the divergence theorem,

$$\nabla \cdot j = 0 \qquad 2.26$$

Unless there is a source or sink in a given chunk of material, the current going in must equal the current leaving.

Considering (2.24) and (2.25)

$\nabla . j = \nabla . \bar{E}/\rho$ 2.27

Substituting (2.25) into (2.27)

We have that $\nabla . j = 1/\rho \nabla . (\nabla . U)$ 2.28

But from vector and tensor analysis, the divergence of the gradient of the potential is the Laplacian of such a function.

Thus, equation (2.28) reduces to

$\nabla . j = 1/\rho \nabla^2 U = 0$ 2.29

This follows that either $\rho = 0$ or $\nabla^2 U = 0$

In a homogenous medium, ρ is independent of coordinate axes, therefore

$$\left.\begin{array}{l} \rho \neq 0 \\ \nabla^2 U = 0 \end{array}\right\} \quad 2.30$$

Equation (2.30) implies that electric field potential distribution for direct current flow in a homogenous medium satisfies Laplace's equation.

For a current I introduced into an infinite homogenous medium at a point, potential at any distance, r, from the source is only a function of r.

Hence, Laplace equation reduces to

$\frac{\partial^2}{\partial r^2} = \frac{2}{r}\frac{\partial U}{r^2} = 0$ 2.31

The general solution is $U = A - B/r$ 2.32

Boundary conditions for the equation;

At infinite distances, as $r \rightarrow \infty$, $A = 0$

$$=> U = -B/r \quad 2.33$$

But at any point r, j is given by

$$j = -1/\rho \partial U/\partial r \quad 2.34$$

But $\partial U/\partial r = -B/r^2$

$$j = 1/\rho\ B/r^2 \quad 2.35$$

But the total current flowing out of a spherical surface of radius r is given by

$I = j.\ A$

$= 4\pi r^2.\ B/\rho\ r^2$

$B = I\rho/4\pi = Ur$

This implies that $U = I\rho/4\pi r$ 2.36

For semi – infinite homogenous earth, total current, I, flowing out of the hemisphere is given by

$$I = 2\pi r^2.j \quad 2.37$$

Therefore, the earth is assumed to be a hemispherical equipotential surface of area $2\pi r^2$. The electric field lines around a source electrode, which supplies current to the ground is radially outward. Around a sink electrode where current flows out of the ground, the field lines are radially inward as shown below.

Input electrode (Input current I)

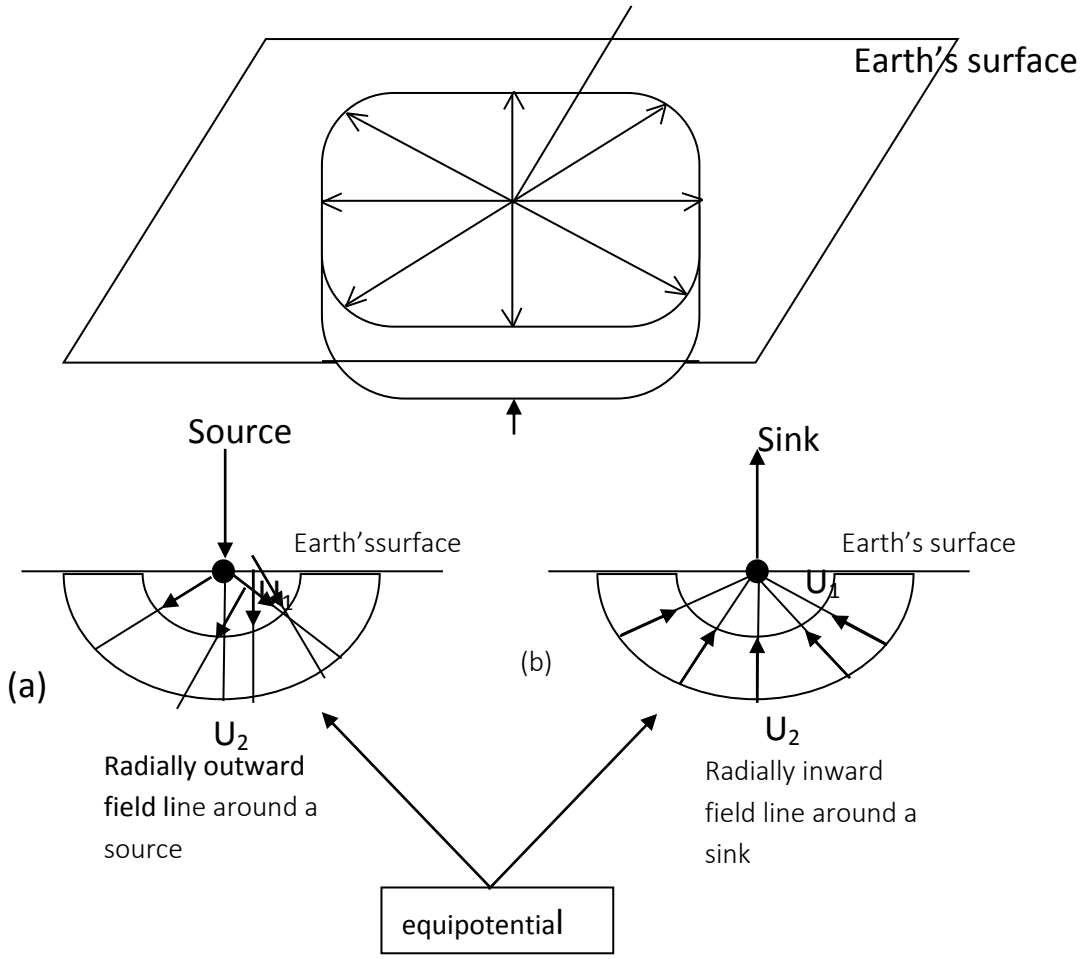

Figure 2.4: Hemispherical equipotential surface of area $2\pi r^2$

From (2.31), the equation of potential distribution in a homogenous earth is given as

$$U = I\rho /2\pi r \qquad 2.38$$

But in practice, we have current going in at one point and leaving from another point as shown below

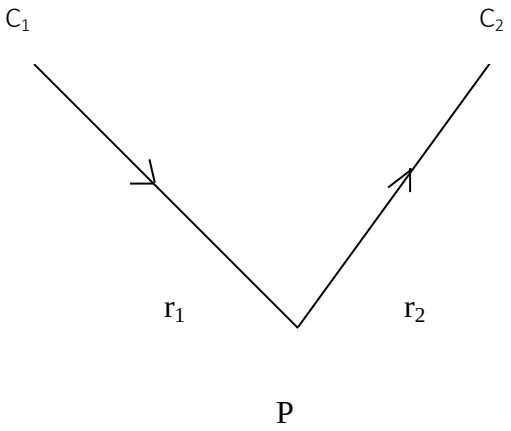

Figure 2.6: Current source and sink for a bipolar arrangement.

Therefore, the potential at any point due to this bipolar arrangement is given by

$$U = \frac{I\rho}{2\pi}\left[\frac{1}{r_1} - \frac{1}{r_2}\right] \qquad 2.39$$

Where r_1 and r_2 are the distances of the points from the source and sink respectively.

2.8.1 Field Measurement of Resistivity.

The measurement consists of four electrodes. The arrangement is made up of a pair of potential electrodes, P_1 and P_2 and a pair of current electrodes, C_1 and C_2. The current electrodes act as source and sink while the potential electrodes act as detection electrodes. The general set-up is shown below.

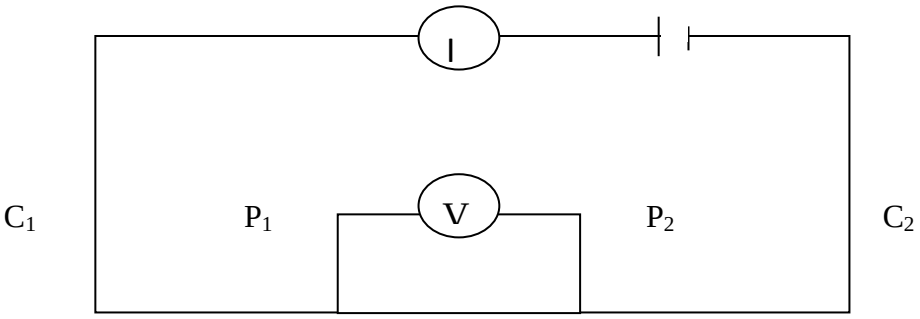

Figure 2.5: General electrode configuration for resistivity measurement.

In practice, the physical quantities measured are the current, I, flowing between the two current electrodes, and the potential difference, V, between the two potential electrodes.

Using equation (2.39),

The potential at P_1 due to current from C_1 and C_1 is given by

$$U_1 = \frac{I\rho}{2\pi}\left[\frac{1}{C_1P_1} - \frac{1}{C_2P_1}\right] \qquad 2.40$$

Similarly, the potential at P_2 due to current source C_1 and C_2 will be

$$U_2 = \frac{I\rho}{2\pi}\left[\frac{1}{C_1P_2} - \frac{1}{C_2P_2}\right] \qquad 2.41$$

Then, the potential difference $\Delta U = U_1 - U_2$

$$= \frac{I\rho}{2\pi}\left[\frac{1}{C_1P_1} - \frac{1}{C_2P_1} - \frac{1}{C_1P_2} + \frac{1}{C_2P_2}\right] \qquad 2.42$$

Where $G = \left[\frac{1}{C_1P_1} - \frac{1}{C_2P_1} - \frac{1}{C_1P_2} + \frac{1}{C_2P_2}\right]$

This follows that $\Delta U = I\rho\frac{G}{2\pi}$ 2.43

Where G is called the geometric factor and represents the effect of electrode spacing. From equation (25), $\rho = \frac{2\prod\Delta U}{IG}$

But, $\rho = \frac{\Delta U}{I}$ = Resistance, R

Thus, $\rho_a = \frac{2\prod r}{G}$ 2.44

Where ρ_a is known as the apparent resistivity.

2.8.2 The Concept of Apparent Resistivity.

For a homogenous earth, R, G, and ρ are constant. But in the field, in homogeneity exists either laterally or vertically. The resistivity thus changes either by changing the electrode separation or

transferring the whole arrangement to an entirely new location. The values of resistivity obtained depend upon the spacing and the geometry of the four electrodes as well as upon the surface geometry. Hence, the values of the resistivity obtained are apparent. The apparent resistivity is affected by material at increasingly greater depths as the electrode spacing is increased. Because of this effect, a plot of apparent resistivity against electrode spacing can be used to indicate vertical variations in resistivity.

2.8.3 Electrode Configuration

Before discussing the various electrode arrays, it is necessary to consider what is actually measured by an array of current and potential electrodes. The measured quantity is known as the apparent resistivity of a zone in the vicinity of electrode array. Only in the case of homogenous ground is the apparent resistivity value equivalent to the actual resistivity.

A number of electrode spreads have been used in resistivity at various times. Some of them are discussed below.

i. **Wenner Array**.

The Wenner arrangement is one of the most common electrode arrangements for resistivity measurements. In this array, the electrodes are uniformly spaced. The potential difference is normally measured from the separation between adjacent electrodes equally spaced.

From the equation for apparent resistivity, we obtain the apparent resistivity due to Wenner as

$\rho_{a(w)} = 2\pi aR$.

The Wenner electrode spread is shown below.

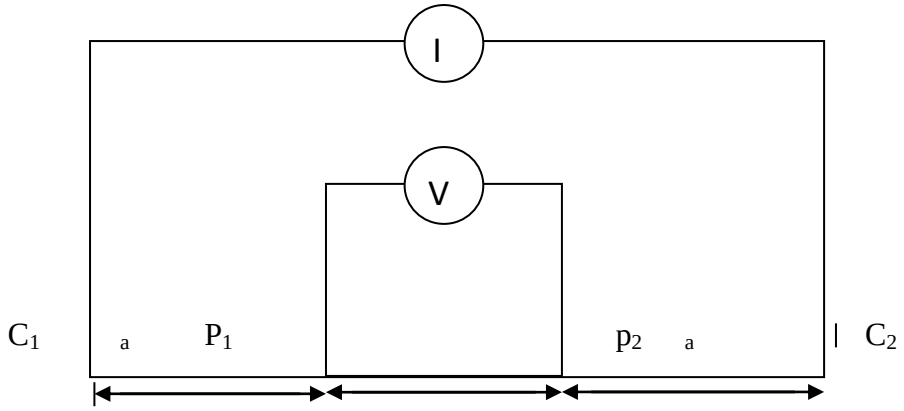

Fig. 2.6: Wenner electrode configuration.

ii. **The Schlumberger Array**

The Schlumberger electrode configuration was employed for the soundings. It measures potential gradient approximately. The potential electrodes (P_1 and P_2) are placed so close to each other as to approximate a dipole.

$P_1P_2 << C_1C_2$

In actual fact, $C_1C_2 \geq 5\ P_1P_2$.

Using the equation for apparent resistivity,

$$\rho_a = \frac{2\prod r}{G}$$

We obtain the apparent resistivity due to Schlumberger array as

$$\rho_{a(s)} = л\left[\frac{a^2}{b} - \frac{b}{4}\right]R \qquad 2.45$$

or $\rho_{a(s)} = KR$

where $K = л\left[\frac{a^2}{b} - \frac{b}{4}\right]$

a = half current electrode spread (AB/2)

b = potential electrode spread

iii. **Dipole Array**

It is used for deep penetration. The current electrodes are usually well separated from the potential electrodes.

The dipole electrode array is shown below

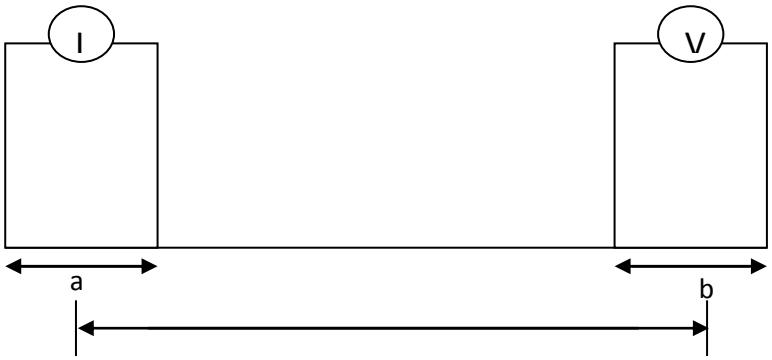

Fig. 2.7: The dipole electrode configuration.

Table 2.1: Array advantages and disadvantages

Array	Advantages	Disadvantages
Wenner	Easy to calculate ρ_a in the field Less demand on instrument sensitivity	All electrodes are moved during each sounding Sensitive to local shallow variations Long cables for large depths
Schlumberger	Fewer electrodes to move at each sounding needs shorter potential cables	Can be confusing in the field Requires more sensitive equipment Long Current cables
Dipole-dipole	Cables can be shorter for deep soundings	Requires large current Requires sensitive instruments

2.8.4 Resistivity Method Field Procedures

Regardless of the electrode spacing employed there are only two basic procedures in resistivity work. The procedure to be adopted depends on whether the interest is in resistivity variation with depth or with lateral extent. The two methods are discussed below.

i. Electrical Drilling.

This is also known as Vertical Electrical Sounding. Since the fraction of total current which flows at depth varies with the current electrode separation, the field procedure is to use a fixed centre with an expanding spread. Both Wenner and Schlumberger array are suited to this technique, but the Schlumberger array has certain advantages.

This method is useful in determining the depth of overburden and resistivity of flat – lying sedimentary beds. It is necessary to carry out the procedure at several locations in an area, even

when the main interest may be in lateral exploration, in order to establish proper electrode spacing for lateral search.

ii. **Electrical Profiling**.

Electrical profiling (or mapping), is particularly useful in mineral exploration where the detection of isolated bodies of anomalous resistivity is required. Any of the electrode arrangements may be used, the selection depending mainly on the field situation. This method is however not suitable in water exploration, but is useful in reconnaissance surveys in structural prospecting for contacts, dykes, faults and fissured zones.

2.8.5 Applications of the Electrical Resistivity Method.

The general applications of the resistivity method are two in number.

1. To detect areas where subsurface materials have abnormally high or low resistivity compared to the surrounding.
2. To estimate depth to subsurface boundaries separating layers of different resistivities and to estimate their resistivity values.

Other main applications include:-

i. To locate and map sand and gravel deposits.
ii. Hydrogeophysical studies.
iii. Mineral exploration.
iv. Pollution plume studies.
v. To determine depth to basement/bedrock.
vi. To map buried stream channels.
vii. To map regional variation in soil layer.
viii. To map geothermal anomalies.

ix. To map archaeological sites.

x. To map salt water and fresh water locations.

xi. To locate fractures and faults.

xii. To determine extent of salt water intrusion.

xiii. To identify areas of potentially unstable ground.

xiv. Utilized in dam stability analysis.

2.9 Electromagnetic Methods

Electromagnetic (EM) surveys as used by the minerals industry are chiefly a type of active geophysical method, i.e. they use artificially created electromagnetic fields. The measurement of naturally occurring EM fields is less common (see online Appendix 4 for a description of these methods). Surveys are conducted from the air (airborne electromagnetics), on the ground surface, and in drillholes (downhole electromagnetics; DHEM). Although primarily used as an exploration tool, there is increasing use of EM in-mine, the intention being to map an ore body accurately prior to, and during, mining to reduce the amount of delineation drilling required. The basic aim of EM surveying is to map spatial variations in electrical conductivity with the data presented in the form of pseudo-maps, cross-sections or volumes showing the conductivity variations in a continuous form. The data may also be used to infer the location of a 'target', i.e. a discrete zone of conductivity approximated by some simple shape.

2.9.1 Principles of Electromagnetic Surveying

The EM method is based on the principle of Faraday's Law of Electromagnetic Induction which states that the magnitude of the induced emf (ε) in volts (V) is proportional to the rate of change of the magnetic field (ψ) experienced by the coil, i.e. it depends on how fast the magnetic field changes. The induced emf is given by;

$$\varepsilon = -\frac{d\psi}{dt} \qquad 2.42$$

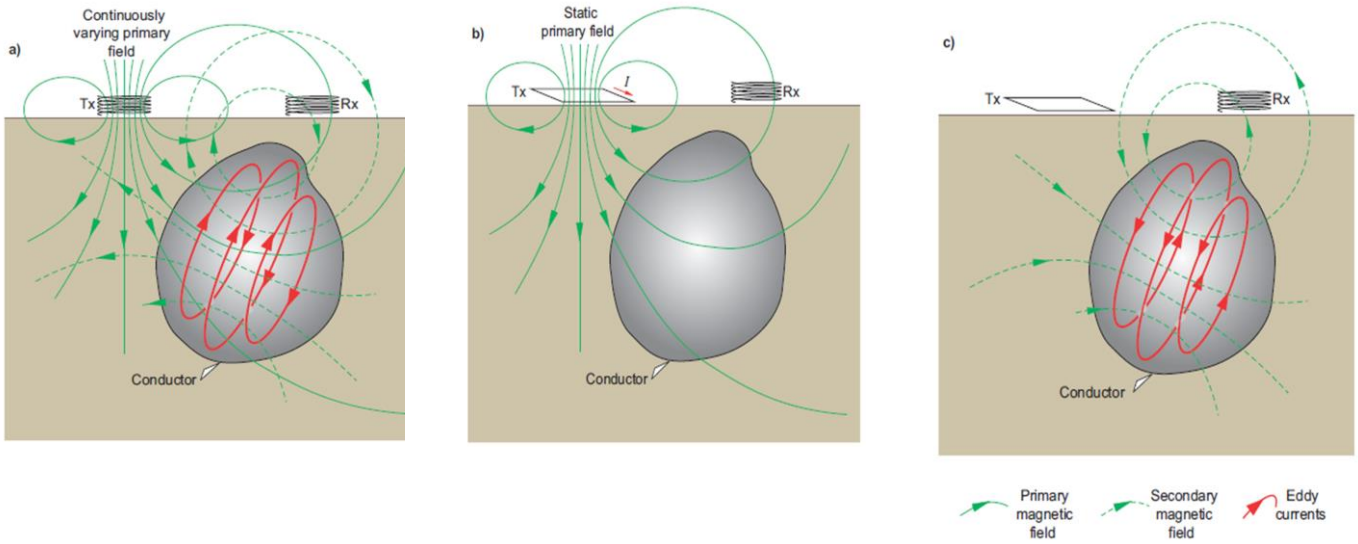

Figure. 2.8: Schematic illustration of an EM system used for geophysical investigations. Adapted from Grant & West (1965).

(a) The frequency domain case of a continuously varying primary field. The Diagram shows the situation for a primary field increasing in strength, so the secondary field has the opposite direction to oppose the change. (b) The time domain case with a steady-state primary field shown before turn-off. (c) Induced eddy currents and their secondary field following turn-off. To oppose the change when the primary field is turned off, the secondary field (broken lines) is detected by the receiver (Rx), which is either a coil, shown here, or a magnetic sensor.

In accordance with Faraday's Law (Eq.3), when the time-varying magnetic field intersects electrically conductive material eddy currents are induced within it. The eddy currents have a magnetic field associated with them, the secondary magnetic field, which is detected by the receiver (Rx). Properties of the secondary field provide information about the conductor.

We initially describe the EM method in general terms of the two fundamental categories of EM measurements: frequency domain and time domain measurements. This is followed by descriptions of creating the primary field, the induction and behaviour of induced eddy currents

and, finally, the detection and characterisation of the resulting secondary magnetic field. Based on these fundamental concepts, aspects of EM surveying are then described: specifically, the system geometry and system signal. Systemgeometry refers to the types of transmitter and receiver used and the relative positions and orientations of their antennae. System signal is the nature of the time variations in the primary field and the way the secondary field is characterised. These parameters determine the effectiveness of the EM system in detecting particular discrete conductors, mapping variations in a wide range of conductivity and resolving shallow and deep targets.

2.9.2 Very Low Frequency (VLF) Surveys

Governments with naval forces have established a grid of tall high-powered transmitters, up to 1000 watts, that broadcast a signal field in the 15 to 28 KHz frequency range. These broadcast fields propagate thousands of miles over the Earth's surface and are essentially uniform in the atmosphere. For the purpose of this survey we make use of the closest Transmitter which is in South Africa. Due to the power of this transmitter, the signals penetrate into the ground to depths of several hundred feet. Because of the high material properties contrast at the ground/air interface, the signals are refracted down into the ground at steep angles. Since the Earth is relatively less homogeneous than the atmosphere, the EM flux crowds into zones of higher conductivity and rarefies in zones of higher resistivity. A VLF receiver tuned to the frequency of a VLF transmitter, traversed across the Earth's surface, will exhibit high signals over conductive water-bearing fracture zone, for example, and a low strength signals over the resistive portions of the crystalline rock mass. Any linear conductive body, in addition to water-bearing fractures, can also be detected by VLF methodology. For the purpose of this study we look for evidences of structures (fractures; faults and joints) based on the variation in conductivity of the area.

CHAPTER THREE

MATERIALS AND METHODS

3.1 Materials

3.1.1 Field Equipment's

The following equipment's were used for field work: -

i. **OVERHAUSEER MAG/VLF**: The MAG/VLF is a lightweight, portable instrument with integrated GPS and a versatile design for both ground magnetic and VLF-EM data acquisition.

ii. **ABEM SAS 1000 TERRAMETER:** To be used for electrical resistivity and IP data acquisition.

iii. **Global Positioning System (GPS):** This is an instrument that operates as a function of space satellites. It gives the longitudinal and latitudinal position of the area. It also gives the height above mean sea level of a particular area.

iv. **Compass:** Was used for profile dip and strike measurements.

3.1.2 Data Processing/Interpretation software

The processing of data was carried out with the following software packages: -

i. Oasis Montaj (10.1)

ii. GeoMatica

iii. ArcGIS (10.5)

iv. Res2Dinversion.

v. 3DMine

3.2 Aeromagnetic Data Source

The aeromagnetic maps for the study were obtained from the Geological Survey of Nigeria (NGSA). The data were acquired and compiled by FAIREY SURVEYS LTD during an airborne geophysical survey in 2011. Unlike the data acquired in 1974 by the Geological Survey of Nigeria (at nominal flight height of 152.4 m, along N-S flight lines that were spaced at 2 Km interval), which will not yield much deductions, because the data only represent anomalies greater than 4km (twice spatial sample interval, because of aliasing effect) and the interpretation techniques used were ancient. This data is high resolution. The nominal flight height of 76m along N-S flight lines spaced at 500m interval using advanced equipments with higher resolution. The geomagnetic gradient was removed from the data using the International Geomagnetic Reference Field (IGRF). In this study, the digitizing process followed the basic acquired data along flight lines drawn on the map and the obtained data were shown as coloured filled contour maps. The data made in form of contoured maps on a scale of 1:100,000.

In order to aid in determining the structural makeup within the Middle-Benue trough and how these structures can be used to locate regions favorable for more detailed exploration for mineral deposits. Aeromagnetic data were analyzed using first vertical derivative, analytical signal, tilt derivatives, reduction to the Equator, upward continuation. The approximate depths to the magnetic susceptibility sources were obtained using the tilt derivatives. The resulting magnetic anomaly maps are used to further define the structural and geological framework of parts of the Middle-Benue Trough, and thus aid in predicting regions that would host additional ore deposits. This analysis helped in narrowing exploration areas to those with a better chance of containing ore deposits.

3.2.1 Aeromagnetic Data Analysis

Interpretation of the aeromagnetic survey data aims to map the surface and subsurface regional structures (e.g., faults, contacts, bodies and mineralization). Aeromagnetic data are mostly analyzed in these processes Aeromagnetic data, filtration (upward and/ or downward continuation, Reduction to pole, vertical derivatives, etc), Regional - Residual Separation, Depth estimation analysis and Source Parameter Imaging.

i. Regional-Residual Separation

The distinction between the regional and residual is somewhat arbitrary but the regional component can be thought of as the response of bodies large and/or deep compared with respect to the study area and, therefore, not readily interpretable within the bounds of the study area. To separate the regional field, a regional (or *low pass*) filter could be multiplied point-by point with the spectrum where low wave numbers are passed, high wave numbers rejected, with an approximately Gaussian *roll-off* between them to minimize *ringing* (also known as Gibb's phenomena) when the output is reverse-transformed to the space domain. The complement of the low-pass regional filter is the *high pass* or *residual* filter. The residual grid may be obtained either by applying such a filter in the wave number domain, or by subtracting the regional field from the original data grid. In practical cases, the residual filter would usually be designed to roll-off again at wave numbers corresponding to noise so that noise could be eliminated simultaneously. The filter then becomes a *band-pass* filter, retaining only information from a range of wave numbers considered important for the study of the residual anomalies at hand.

For this study the aeromagnetic data, the regional gradients were removed by polynomial fitting, this involved fitting a plane surface to the data by using multi-regression least squares analysis. The expression obtained for the regional field T(R) is given as:

$$T(R) = 76122.158 + 0.371x\ 0.248y \quad (3.1)$$

where x and y are units of spacing. The regional field values are subtracted from the observed data to obtain the residual anomaly values. The technique is carried out on the aeromagnetic data of the study area to produce the first to fourth residual and regional trend surfaces.

ii. **Reduction to Pole**

The reduction to pole filtering process removes the effect of the earth's magnetic field by way of a gross shift of the observed magnetic readings. The procedure is nothing more than a correction factor applied across the study area to remove the non-vertical magnetic component (the earth's magnetic field) and leave only the vertical component (causative body) in its correct spatial position. The RTP was performed on the digitized aeromagnetic data of the study are via fast Fourier filtering in Oasis Montaj 6.4 program in order to remove the dipolar nature of the magnetic field.

iii. Continuation Filtering

A potential field measured on a given observation plane at a constant height can be recalculated as though the observations were made on a different plane, either higher (upward continuation) or lower (downward continuation). The equation of the wave number domain filter to produce *upward* continuation is simply:

$$F(\omega) = e^{-h\omega} \qquad 3.2$$

Where h is the continuation height. This function decays steadily with increasing wave number, attenuating the higher wave numbers more severely, thus producing a map in which the more regional features predominate.

The equation of the wave number domain filter to produce *downward* continuation is

$$F(\omega) = e^{h\omega} \qquad 3.3$$

This is a curve which is zero at zero wave number and increases exponentially at higher wave numbers, thus emphasizing the effect of shallow sources - and noise! Noise removal is thus an essential first step before downward continuation, and continuation depths should not exceed real source depths. Some careful experimentation is usually necessary to obtain acceptable results (Reeves, 2005).

An upward continuation filtering of 100m, 500m and 800m were done on the aeromagnetic data to enhance the target anomalies.

iv. **Magnetic Depth Estimation**

Often one of the most useful pieces of information to be obtained from aeromagnetic data is the *depth* of the magnetic source (or rock body). Since the source is usually located in the so-called 'magnetic basement' (i.e. the igneous and metamorphic rocks lying below the -assumed non-magnetic - sediments), this depth is also an estimate of the thickness of the overlying sediments. Sufficient depth estimates from a large number of magnetic sources allow the depth of the basement to be contoured and this is then a rough isopach map of the sediments.

For this reason, several methods have evolved in the early days of magnetic interpretation simply to estimate the depth of sources from their anomalies without reference to any specific source models

The methods of magnetic depth estimation were employed in this study, they include, Spectral Methods and 3D Euler Deconvolution Method.

v. Spectral Analysis

One of the main researches on magnetic anomaly maps is to estimate depth of the buried objects resulting the anomaly. In interpretation of magnetic anomalies by means of local power spectra,

there are three main parameters to be considered. These are depth, thickness and magnetization of the disturbing bodies. It is necessary to define the power spectrum of a magnetic anomaly in relation to the average depth of the disturbing interface. The method of using spectral analysis in depth determination is based on the principle that a magnetic field measured at the surface can therefore be considered the integral of magnetic signatures from all depths. The power spectrum computes the thickness of the sedimentary basin and that of the crustal Moho depth (Spector & Grant, 1970). This same technique can be used to attempt identification of the characteristic depth of the magnetic basement, on a moving data window basis, merely by selecting the steepest and therefore deepest straight-line segment of the power spectrum, assuming that this part of the spectrum is sourced consistently by basement surface magnetic contrasts. A depth solution is calculated for the power spectrum derived from each grid sub-set, and is located at the Centre of the window. Overlapping the windows creates a regular, comprehensive set of depth estimates.

The logarithm of the power of the signal at each wavelength can be plotted against wavelength, regardless of direction, to produce a power spectrum. A potential field grid may be considered to represent a series of components of different wavelength and direction. Most approaches used involve Fourier transformation of the digitized aeromagnetic data to compute the energy (or amplitude) spectrum. This is plotted on the Logarithmic scale against frequency. The plot shows the straight line segments which decrease in slope with increasing frequency. The slopes of the segments yield estimates of depths to magnetic sources. The application of spectral analysis to the interpretation of aeromagnetic anomalies is now sufficiently well established (Spector & Grant, 1970; Hahn *et al*., 1976).

Given a residual magnetic anomaly map of dimension L×L digitized at equal intervals, the residual intervals, the residual total intensity anomaly values can be expressed in terms of double Fourier series expansion:

$$T(x,y)=\sum_{n=1}^{N}\sum_{m=1}^{M}P_m{}^n\cos(\frac{2\pi}{L})(nx+my)+Q_m{}^n\sin[(\frac{2\pi}{L})(nx+my)] \quad 3.4$$

Where: L - dimension of the block, $P^n{}_m$and $Q^n{}_m$- Fourier amplitude and

N, M - number of grid points along the x and y directions respectively.

Equation (3.4) can be combined into a single partial wave thus:

$$p_m^n\cos[(\frac{2\pi}{L})(nx+my)]+Q_m^n\sin[(\frac{2\pi}{L})(nx+my)]=C_m^n\cos[(\frac{2\pi}{L})(nx+my)-\delta_m^n \quad 3.5$$

Where $(P_m^n)^2+(Q_m^n)^2=(C_m^n)^2$ 3.6

and δ_m^n is the appropriate phase angle.

Each (C_m^n) is the amplitude of the partial wave.

The frequency of this wave is given by: $F_m^n=\sqrt{n^2+m^2}$ is called the frequency of the wave. Similarly, using the complex form, the two dimensional Fourier transform pair may be written (Bath, 1974)

$$G(U,V)=\int_{-\infty}^{\infty}\int_{-\infty}^{\infty}g(x,y)e^{-j(ux+vy)}dxdy \quad 3.7$$

$$g(x,y)=\frac{1}{4\pi^2}\int_{-\infty}^{\infty}\int_{-\infty}^{\infty}G(U,V)e^{-j(ux+vy)}dxdy \quad 3.8$$

Where u and v are the angular frequencies in the x and y directions respectively.

G (u,v) when broken up into its real and imaginary parts is given by

$$G(u,v)=P(u,v+jQ(u,v) \quad 3.9$$

The energy density spectrum or simply the energy spectrum is

$$E(u,v)+|G(u,v)|^2=P^2+Q^2 \quad 3.10$$

$$f(tx; ty; tz) = t^n f(x; y; z) \quad 3.11$$

It can be shown that, the following equation, which is known as Euler's homogeneity relation can be satisfied:

$$x\frac{\delta f}{\delta x} + y\frac{\delta f}{\delta y} + z\frac{\delta f}{\delta z} = nf \quad 3.12$$

In geophysics, the function f(x,y,z) can have the general functional form:

$$f(x, y, z) = \frac{G}{r^N} \quad 3.13$$

Where $r^2 = (x - x_0)^2 + (y - y_0)^2 + (z - z_0)^2$, N a real number (1, 2, 3...) and G a constant (independent of x, y, z). Many simple point magnetic sources can be described by equation (3.13), with (x_0; y_0; z_0) the position of the source whose field F is measured. The parameter N is dependent on the source geometry, a measure of the fall-off rate of the field and may be interpreted as the structural index (SI). Clearly equation (3.13) is homogeneous and thus N is equivalent to -n in Euler's equation (3.12).

Considering potential field data, Euler's equation can be written as:

$$(x - x_0)\frac{\delta T}{\delta x} + (y - y_0)\frac{\delta T}{\delta y} + (z - z_0)\frac{\delta T}{\delta z} = N(B - T) \quad 3.14$$

With B the regional value of the total magnetic field and (x_0; y_0; z_0) the position of the magnetic source, which produces the total field T measured at (x; y; z).

Thompson (1982) showed that simple magnetic and gravimetric models are consistent with Euler's homogeneity equation. Thus 3-D Euler Deconvolution provides an excellent tool for providing good depth estimations and locations of various magnetic sources in a given area, assuming that appropriate parameter selections are made (Reid, 1990).

The 3D Euler process is a fast method for obtaining depth and boundary solutions of magnetic sources for large areas in aeromagnetic surveys. Though it is a general advantage of the

Euler Deconvolution method, that it is applicable to all geologic models and that it is insensitive to magnetic remanence and geomagnetic inclination and declination, an initial assumption of the source type has to be made (Reids, 1990; Thompson, 1982). Dependent upon the potential source type, a structural index is chosen. This structural index is also a measure of the distinctive fall-off rate of the geologic feature. Table 3.1 summarizes the structural indices (SI) for given geologic models. The number of infinite dimensions describes the extension of the geologic model in space.

Table 3.1: Structural Indices for Simple Magnetic Models Used For Depth Estimations by 3D Euler Deconvolution (Reids, 1990; Thompson, 1982).

Geologic Model	**Number of Infinite Dimensions**	**Magnetic Structural Index**
Sphere	0	3
Pipe	1 (z)	2
Horizontal cylinder	1 (x-y)	2
Dyke	2 (z and x-y)	1
Sill	2 (x and y)	1
Contact	3 (x,y,z)	0

The significance of the location and depth estimates obtained by 3-D Euler Deconvolution is given by the specificity of the chosen parameters like the grid cell size, window size, structural index, chosen depth uncertainty tolerance, etc. The selection of the grid cell size should be based on the grid spacing and the wavelength of the anomalies to be analyzed, as the software Geosoft Oasis Montaj allows a square window size of up to 20 grid cell units. If the wavelengths of the anomalies are significantly longer or shorter than the window size, the 3D Euler method does not

yield appropriate results. On the other hand, the limiting distance from the centre of the algorithm window, in which solutions are still recorded, should be chosen with respect to the wavelength of potential anomalies.

In general, 3D Euler Deconvolution yields results for each window position; therefore, it is necessary to eliminate solutions with high uncertainties. A reliable tool for the limitation of results is the specification of a threshold value for depth and horizontal uncertainties. Geosoft Oasis montaj reports the depth and location uncertainties as percentage of the depth below the recording sensor position. As matter of principle, low SI values are associated with source bodies which give rise to low gradients, thus depth estimation solutions with low SI values have high uncertainties. The data quality determines the general level of uncertainty, so an examination of the recorded solutions will define the selection criteria.

The results of the Euler method are displayed in ordinary maps as point solutions combining the location (position of solution) and the depth (colour range). Given the choice of an appropriate structural index, 3D Euler Deconvolution will lead to a clustering of solutions, which can be interpreted. A vertical pipe structure will for example be shown as a cluster of solutions around a specific point, whereas an elongated dyke structure will be recognized as a linear trend of solutions. Another approach to limit the solutions obtained by the Euler method is the Located Euler 3D method, which, unlike the Standard Euler method, tests and limits grid locations before calculating depth estimations by Euler deconvolution.

vi. Source Parameter Imaging (SPI)

The Source Parameter Imaging (SPI TM) is a technique using an extension of the complex analytic signal to estimate magnetic depths. This technique developed by Thurston & Smith (1997, 1999) sometimes referred to as the local wavenumber method is a profile or grid-based method for estimating magnetic source depths, and for some source geometries the dip and

susceptibility contrast. The method utilizes the relationship between source depth and the local wavenumber (k) of the observed field, which can be calculated for any point within a grid of data via horizontal and vertical gradients Thurston & Smith (1997). The depth is displayed as an image. The original SPITM method (Thurston & Smith, 1997) works for two models: a dipping thin dike and a sloping contact. The local wave number has maxima located over isolated contacts, and depths can be estimated without assumptions about the thickness of the source bodies. Solution grids using the SPI technique show the edge locations, depths, dips and susceptibility contrasts. The local wave number map more closely resembles geology than either the magnetic map or its derivatives. The SPI method requires first- and second-order derivatives and is thus susceptible to both noise in the data and to interference effects. The SPI method (Thurston & Smith, 1997) estimated the depth from the local wave number of the analytic signal. The analytic signal A1(x,z) is defined by Nabighian (1972) as

$$A_{1(X,Z)=}\frac{\partial M(X,Z)}{\partial X}-j\frac{\partial M(X,Z)}{\partial Z} \qquad 3.15$$

Where M(x,z) is the magnitude of the anomalous total magnetic field, j is the imaginary number, and z and x are Cartesian coordinate for the vertical direction and the horizontal direction perpendicular to strike, respectively. Nabighian (1972) showed that the horizontal and vertical derivatives comprising the real and imaginary parts of the 2D analytical signal are related as follows:

$$\frac{\partial M(X,Z)}{\partial X}\Leftrightarrow -j \qquad 3.16$$

Where ⇔ denotes a Hilberts transform pair. The Local wavenumber k_1 is defined by Thurston & Smith (1972) to be

$$K_1=\frac{\partial \tan^{-1}\left(\frac{\left[\frac{\partial M}{\partial Z}\right]}{\left[\frac{\partial M}{\partial X}\right]}\right)}{\partial X} \qquad 3.17$$

The analytic signal defined by Nabighan (1972) uses the Hilbert transform pair in equation 18. The Hilbert transform and the vertical derivative operators are linear, so the vertical derivative of (18) will give the Hilbert transform pair,

$$\frac{\partial^2 M(X,Z)}{\partial Z \partial X} \Leftrightarrow -j\frac{\partial^2 M(X,Z)}{\partial^2 Z} \qquad 3.18$$

This enables us to define an analytic signal based on second- order derivatives, $A_2(x,z)$ where

$$A_2(x,z) = \frac{\partial^2 M(X,Z)}{\partial Z \partial X} \Leftrightarrow -j\frac{\partial^2 M(X,Z)}{\partial^2 Z} \qquad 3.19$$

This gives rise to a second –order local wave number k_2, where

$$K_2 = \frac{\partial \tan^{-1}\left(\frac{\left[\frac{\partial^2 M}{\partial^2 Z}\right]}{\left[\frac{\partial^2 M}{\partial X \partial Z}\right]}\right)}{\partial X}. \qquad 3.20$$

This first and second – order local wavenumbers are used to determine the most appropriate model and depth estimate of any assumption about a model.

Nabighian (1972) gives the expression for the vertical and horizontal gradient of a sloping contact model as

$$\frac{\partial M}{\partial X} = 2KF_C \sin d \ \frac{h_c \cos(2I-d-90)+x\sin(2I-d-90)}{h_c^2+x^2} \qquad 3.21$$

$$\frac{\partial M}{\partial z} = 2KF_C \sin d \ \frac{x \cos(2I-d-90)+x\sin(2I-d-90)}{h_c^2+x^2} \qquad 3.22$$

Where K is the susceptibility contrast at the contact, F is the magnitude of the earth`s magnetic field (the inducing field), c = 1 – cos2isin2α, α is the angle between the positive x-axis and the magnetic north, I is the ambient- field inclination, tan I = tani/ cosα, d is the dip (measured from the positive x- axis), h_c is the depth to the top of the contact and all trigonometric argument are in degrees. The coordinate system has been defined such that the origin of the profile line (x=0) is directly over the edge. The expression for the magnetic – field anomaly due to a dipping thin sheet is

$$M(x,z) = 2KF_C w \sin\frac{h_t \sin(2I-d) - x\cos(2I-d)}{h_t^2 + x^2} \quad 3.23$$

(Reford, 1964), where w is the thickness and ht is the depth to the top of the thin sheet. The expression for the magnetic- field anomaly due to a long horizontal cylinder is

$$M(x,z) = \frac{2KFS\sin I\left(h_h^2 - x^2\right)\cos(2I-180) + 2xh_h\sin(2I-d)}{\sin I(h_h^2 + x^2)^2} \quad 3.24$$

where S is the cross – sectional area and h_h is the depth to the expression for the centre of the horizontal cylinder.

Substituting (23), (24), (25), (26) into the expression for the first- and second order local wavenumbers, we obtain after some simplification, a remarkable result:

$$K_1 = \frac{(n_k+1)h_k}{h_k^2 + x^2} \quad 3.25$$

$$K_2 = \frac{(n_k+2)h_k}{h_k^2 + x^2} \quad 3.26$$

Where n_k is the SPI structural index (subscript k=c, t or h), and n_c =1 and n_h =2 for the contact, thin sheet and horizontal cylinder models, respectively.

3.3 Remote Sensing Data Source

For the purpose of the present study, we used cloud-free levelled, terrain corrected, Landsat 8 remote sensing data, obtained from the U.S. Geological Survey Earth Resources Observation and Science centre (EROS); (http://earthexplorer.usgs.gov). The image was acquired on the 10th of November 2017 (Path/Row 184/53) with the map projection UTM zone 33 N and WGS-84 datum. This period was preferred in order to avoid atmospheric hygrometry and dust, respectively characterized by high levels during the rainy (June – September) and the dry (March – May) seasons. The Landsat-8 data were recorded via two types of sensors; namely, Operational Land Imager (OLI) and the Thermal Infrared Sensor (TIRS) (Table 3.2). The OLI gathered information

through a nine-band push-broom sensor (eight bands at 30 m and one panchromatic band at 15 m ground pixel size), while the TIRS collects data in two long wavelengths of thermal infrared bands of 100 m spatial resolution.

Table 3.2: Landsat 8 instrument bands

Band#	Band name	Wavelength (μm)	Spatial resolution (m)
1	Coastal aerosol	0.43 - 0.45	30
2	Blue	0.45 - 0.51	30
3	Green	0.53 - 0.59	30
4	Red	0.64 - 0.67	30
5	Near Infrared (NIR)	0.85 - 0.88	30
6	Shortwave Infrared (SWIR) 1	1.57 - 1.65	30
7	Shortwave Infrared (SWIR) 2	2.11 - 2.29	30
8	Panchromatic	0.50 - 0.68	15
9	Cirrus	1.36 - 1.38	30
10	Thermal Infrared (TIRS) 1	10.60 - 11.19	100
11	Thermal Infrared (TIRS) 2	11.50 - 12.51	100

3.3.1 Methods of Landsat 8 processing

Images generated through remote satellite sensors are often affected by distortions resulting from solar and atmospheric effects as well as distortion associated with differences in sensor's calibration. Radiometric calibration and atmospheric corrections were applied to the bands 2

– 7 using Environment for Visualizing Images (ENVI) software package. Less emphasis were placed on bands 1, 8 and 9 which are not very relevant for mineral exploration since most of the hydrothermal alteration minerals have their signatures in the Visible Near Infrared (VNIR) and Shortwave Infrared (SWIR) regions of electromagnetic spectrum. Radiometric calibration assisted in converting the DN pixel values to spectral radiance and then to reflectance quantities. Other data /image enhancement techniques such as colour composite, Band Rationing (BR) and crosta analysis were employed to accentuate specific hydrothermal alteration properties, especially to increase the contrast between the hydrothermally altered rocks and unaltered rocks that host them. Composition of three colour bands (red, green, and blue) or RGB created a colourful multispectral image which could either be true colour or false colour. True colour normally results when composite of visible bands of the spectrum is involved, while false colour composite (FFC) image result when non-visible bands are involved Several colour composites of the study area were created from the combination of various bands displayed as RGB and employed to discriminate different geological features.

Band rationing, a technique which divide the digital numbers i.e. the brightness values corresponding to the peaks of high and low reflectance curve of one band by that of another band in order to improve the contrast and enhances compositional information while suppressing unwanted information, thus, allowing the highlight of some geological features that cannot be seen in raw data was employed in this study. Based on the spectral reflectance and position of the absorption bands of the mineral or mineral assemblages, band rationing of 4/2 (iron-oxides), 6/7 (hydroxyl and clay minerals) and 6/5 (ferrous minerals) (Ali &Pour 2014; Pour & Hashim 2015) was carried out on the processed and enhanced Landsat 8 data and subsequently employed to map of iron oxides, clay minerals and ferrous minerals, respectively and thereafter used to map the relative spatial distribution and concentration of these alteration minerals.

Crosta analysis apt at reducing the number of spectral bands input for Principal Component Analysis (PCA) in order to increase the chances of identifying desired spectral bands, so that they are unequivocally mapped into only one of the principal component images was applied to discriminate hydrothermally altered minerals. The Feature-orientated Principal Components Selection (FPCS) based on the examination of PCA eigenvector loadings was used to decide which of the principal component images will concentrate information directly related to the theoretical spectral signatures of specific targets and thus assign dark or bright pixels in the relevant principal component image to the target (Loughlin, 1991).The magnitude and sign of eigenvector loadings (eigenvalues) define the spectral properties of vegetation, rocks and soils and therefore determine the statistical variance mapped into each PC. The spectral signature of iron oxides and hydroxyl bearing minerals were obtained from the USGS spectral library. Based on this spectral library, bands 2, 4, 5, and 6 of Landsat 8 OLI were selected to highlight the spectral response of iron-oxide bearing minerals while bands 2, 5, 6 and 7 were used to enhance hydroxyl-bearing (clay) minerals. Actually, iron oxides do not display specific diagnostic features in the SWIR while clays minerals are sensitive to the spectral region covered by Landsat 8 OLI bands 6 and 7(Ducart *et al.*, 2016). The eigenvector values of bands 4 and 2 as well as 6 and 7 were further examined to determine the PC that best represents iron-bearing and hydroxyl minerals, respectively. Furthermore, band ratio and colour composite following the procedure proposed by Sabin (1999) is used to enhance alteration zones discrimination. Actually, Sabin (1999) and Ali & Pour (2014) demonstrated the effectiveness of RGB combination of band ratios 4/2, 6/7, 6/5 for lithological and alteration zones mapping. Following this false colour composite, 4/2 ratio enhances iron oxide areas in bright red colour, 6/7 ratio significantly delineate clay and hydroxyl rich areas while 6/5 band ratio delineates ferrous minerals rich blue areas.

3.4 Location of the Study Area

The area of study is the Middle Benue Trough and it cuts across parts of four (4) states (Benue, Nassarawa, Plateau, and Taraba) within latitudes $7^0 30'–9^0 00'$N and longitudes $9^0 00'– 10^0 30'$E as shown in Figure 3.1.

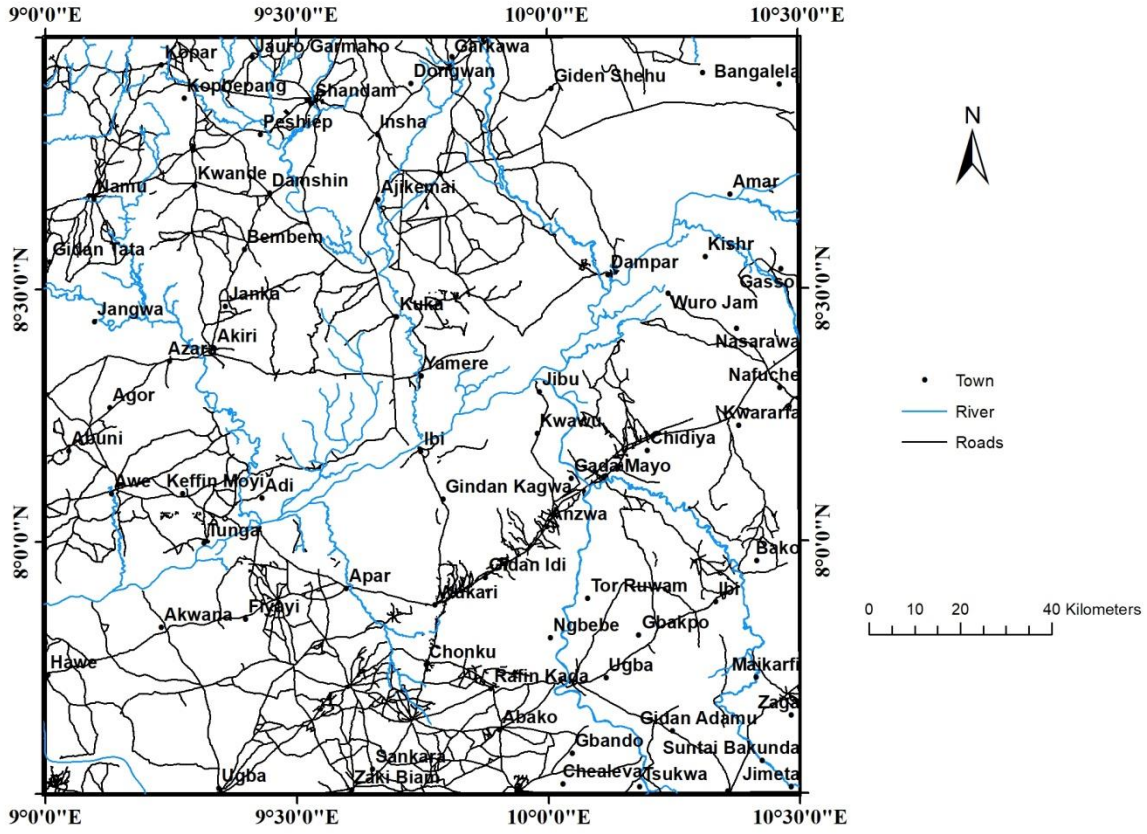

Figure 3.1: Location/Accessibility Map of the study area

3.5 Digitized Elevation Map (DEM)

The digitized elevation map that shows the highlands and lowlands in the study area is displayed in Figure 3.2. The elevation ranges from 61.2 to 859.8 m with a mean value of 460.5 m. On the average, a greater portion of the area falls within low lands (VL in Figure 3.2) which coincide with the River Benue and its river channels. Geologically lowland falls within the

Central Benue Trough, while the highlands fall within the Northern and Eastern Nigerian Massif of the study area.

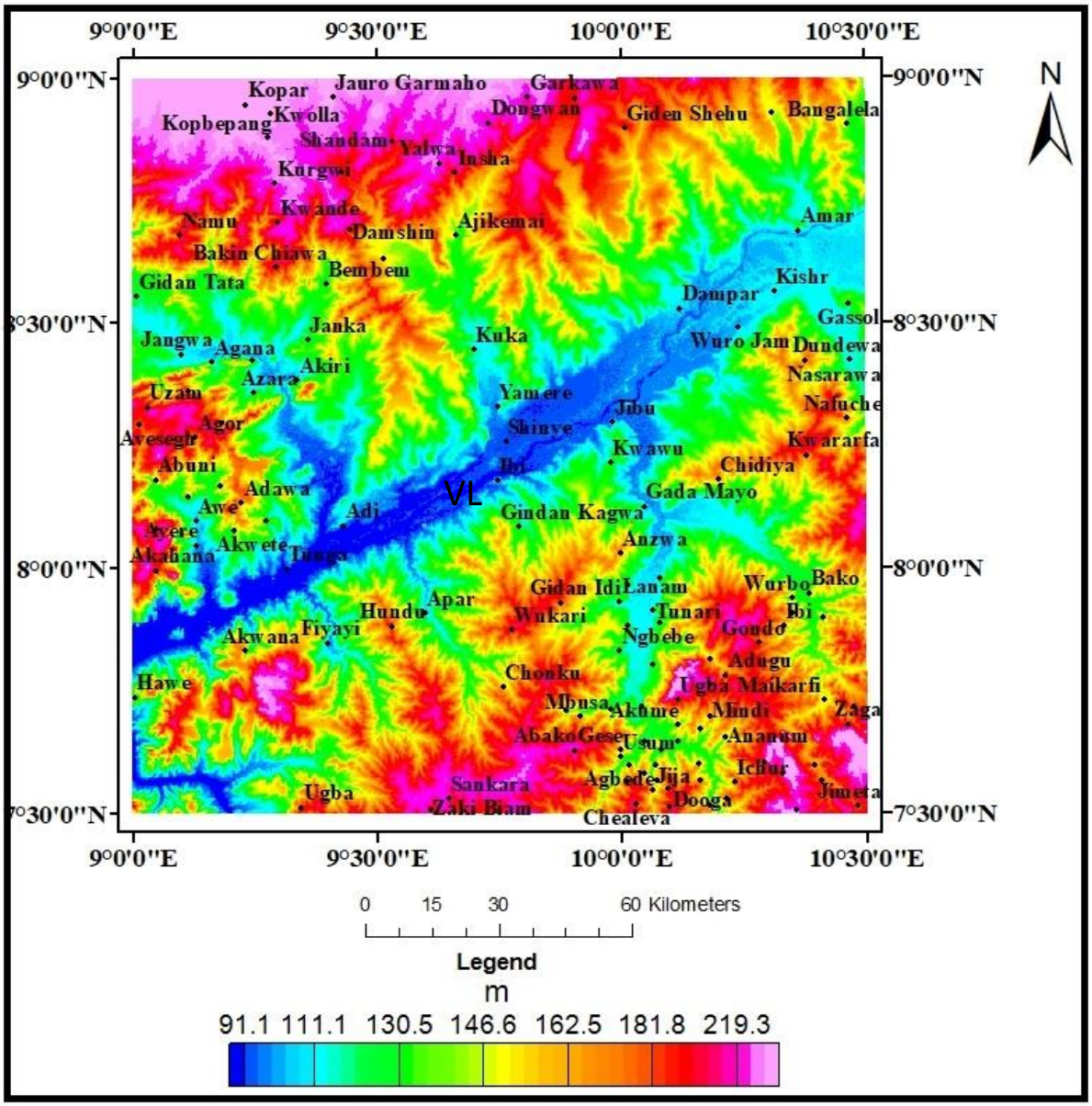

Figure 3.2: Digital Elevation Map of the area

The high elevations shown at the south eastern part of the area are partly associated with the banded granite, New Basalt and porphyritic granite (red to magenta in Figure 3.2). The relatively low elevations (green in Figure 3.2) coincided with the shale and sandstone units of the Central Benue Trough and the very lowland (VL) (blue in Figure 3.2) coincides with the alluvium

and river banks. The lowland is interpreted to serve as a control of the major river (River Benue) having a NE SW trend and based on its topography, its interpreted to have a SW directional flow.

3.6 Geology of the Study Area.

The Middle Benue Trough, Nigeria, is part of the Benue Trough of Nigeria. The Benue Trough is approximately 1,000-km northeast-southwest trending intra-cratonic rift structure that extends from the northern limit of the Niger Delta to the southern margin of the Chad Basin and is partitioned geologically and geomorphologically into Lower, Middle, and Upper Benue Troughs (Figure 3.3). It is resting unconformably upon the Precambrian Basement of Nigeria. The Middle Benue is the near linear parts of the basin while the Lower Benue Trough, which shifts SW, includes two main structural units: the $N6^0E$ trending Abakaliki Anticlinorium that is flanked by the Anambra Syncline trending $N3^0E$ (Grant, 1971). Many models have been proposed for the origin of the Benue Trough (King, 1950; Stoneley, 1966; Wright, 1968; Grant, 1971; Burke & Dewey, 1974; Thiessen *et al*., 1979; Mascle *et al*., 1986; Benkhelil, 1989; Nurnberg & Muller, 1991).

All agreed that the origin of the Benue Trough is related to the continental separation of Africa and South America. The lithological units of the Middle Benue Trough have been detailed by (Offodile, 1976). The oldest sediments of the Middle Benue belong to the Asu River Group: a mixture of shale and siltstones of marine origin, and lava-flows, dykes, and sills overlie the Basement complex rocks. The youngest sediment is the Maastrichtian Lafia Formation. A sediment of interest is the Agwu Formation. The Coniacian Agwu Formation consists mainly of black shale, sandstones, and local seams of coal. Around the Obi/Lafia area, this formation is coal-bearing and has been shown to fall within the oil window (mature) rich in organic matter. It could, therefore, be the source of significant quantities of hydrocarbons (HC) in the deeper portions of the basin (Obaje, 2000). The Lafia/Obi coal is also known to have moderate sulphur

content and so making it favourable for the production of solid fuel for metallurgical process and its high volatibility content makes it disposed of for use as coking coal (Ehinola *et al*., 2000).

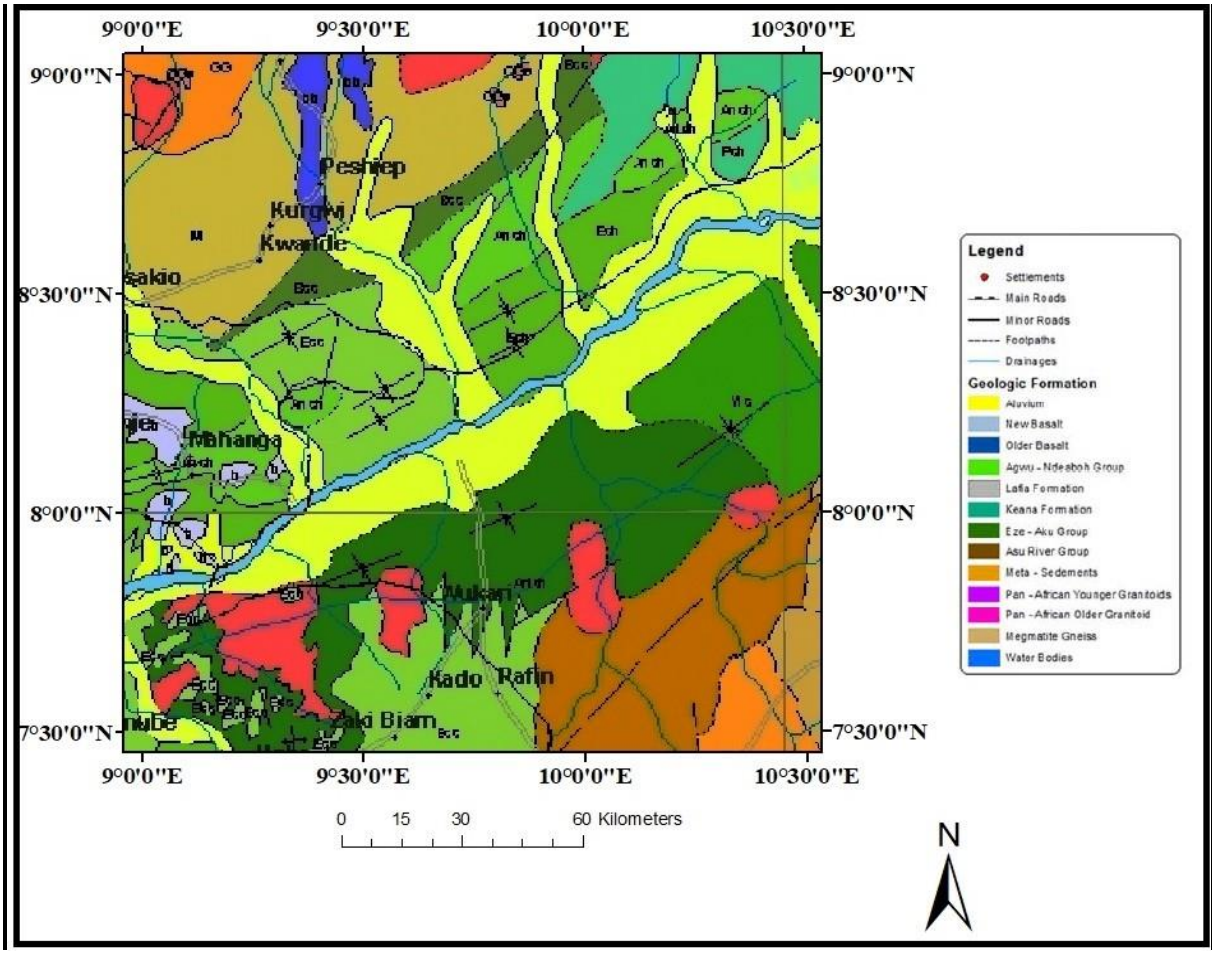

Figure 3.3: Geological map of the study area (Modified after NGSA, 2010**)**

The lead-zinc copper –barite deposits in the Benue Trough resulted from the hot basinal fluids leached metals from arkosic sediments and later precipitated them as metal sulphides in Cenomanian fractures of the Asu River Group (Akande *et al*., 1988).

A model by Akande *et al*., 1988 suggests that the primary ore target should be the Asu River Group sediments in which the metal ore bodies are stratabound. (Figure 3.4)

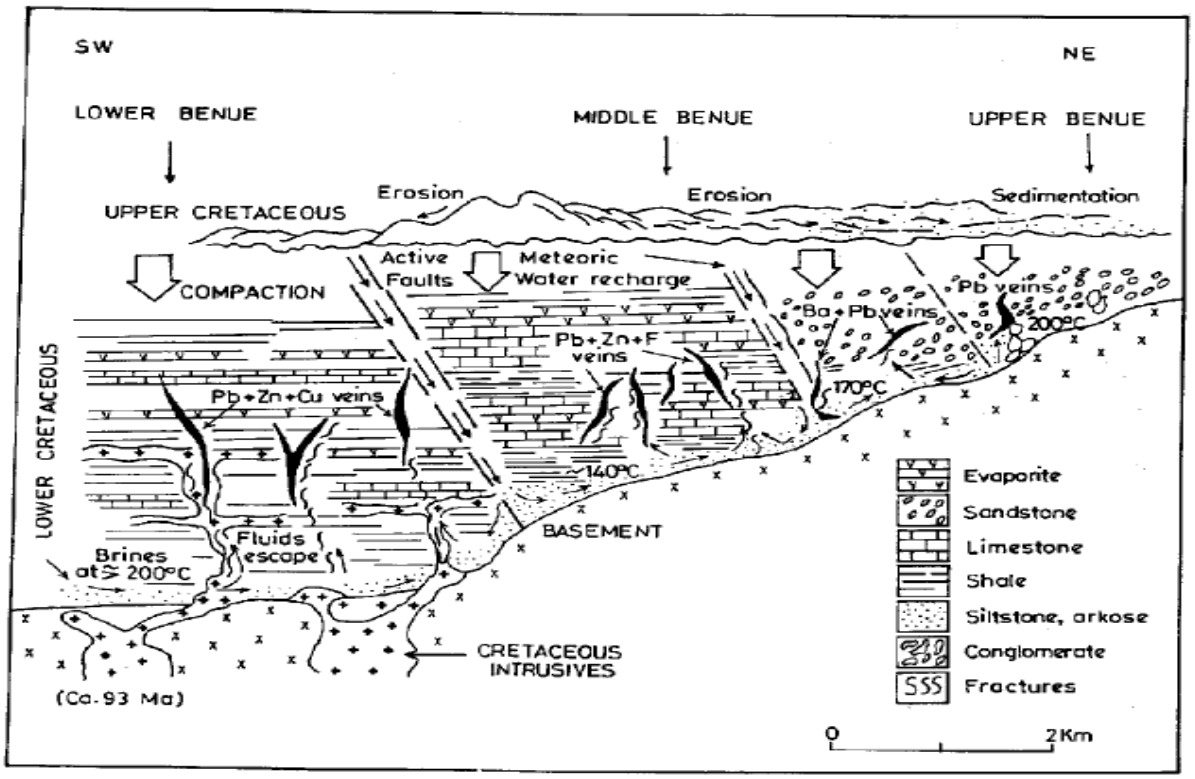

Figure 3.4: Genetic model for the evolution of the lead –zinc copper –barite deposits in the Benue Trough. (Modified after Akande et al.,1988).

3.7 Design of Survey

i. Numbering of stations

The ground survey was carried out on a rectilinear grid of 200m apart and position of 10m intervals (stations) in relation to the position of the base point.

ii. Numbering of transverse

Transverse was number according to their distance and approximate direction from the base point along the base line. Stations on the transverse are number according to their distance and

approximate direction from the base. The base line was positioned so that it lies along or parallel to the structure being investigated

3.8 Research Methods Workflow

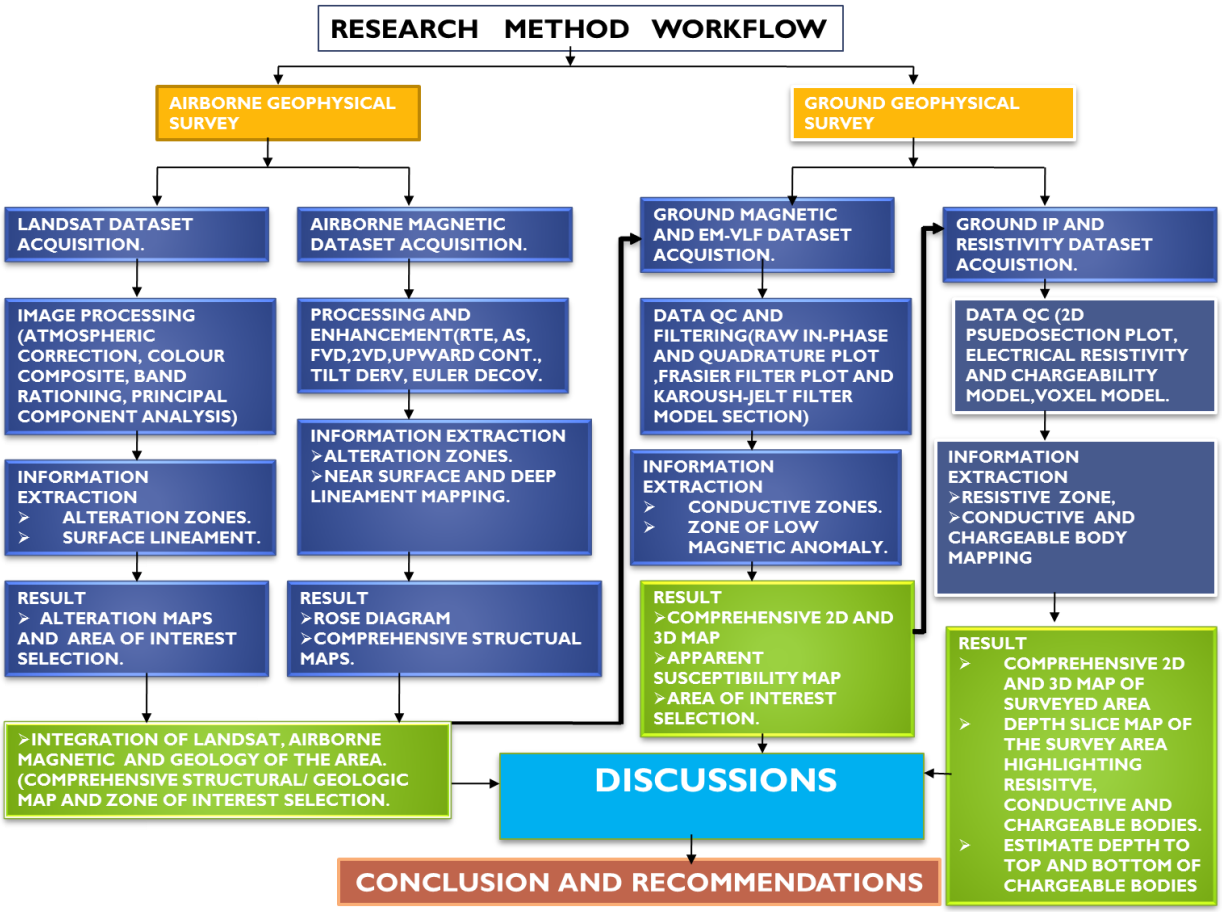

Figure 3.5: Research Workflow

CHAPTER FOUR
RESULTS AND DISCUSSION

In this chapter, the results that were obtained from remote sensing imagery, high-resolution aeromagnetic as well as ground magnetic, EM-VLF and IP survey within the study area is presented. These results were analyzed, computed and combined with regional and local geological data. The combination of the extracted information allowed defines targets and zones possibly associated with mineralization occurrences in the study area.

4.1 Results

4.1.1 Landsat 8 OLI Results

4.1.1.1 Single Band Combinations

Single band combinations were applied in a first approach, in order to analyze the study area and visually interpret the multispectral imagery. Using Landsat 8 Operational Land imager imagery, six bands (B2, B3, B4, B5, B6 and B7) were available to produce different band combinations, some of them enhancing relevant features for mineral exploration.

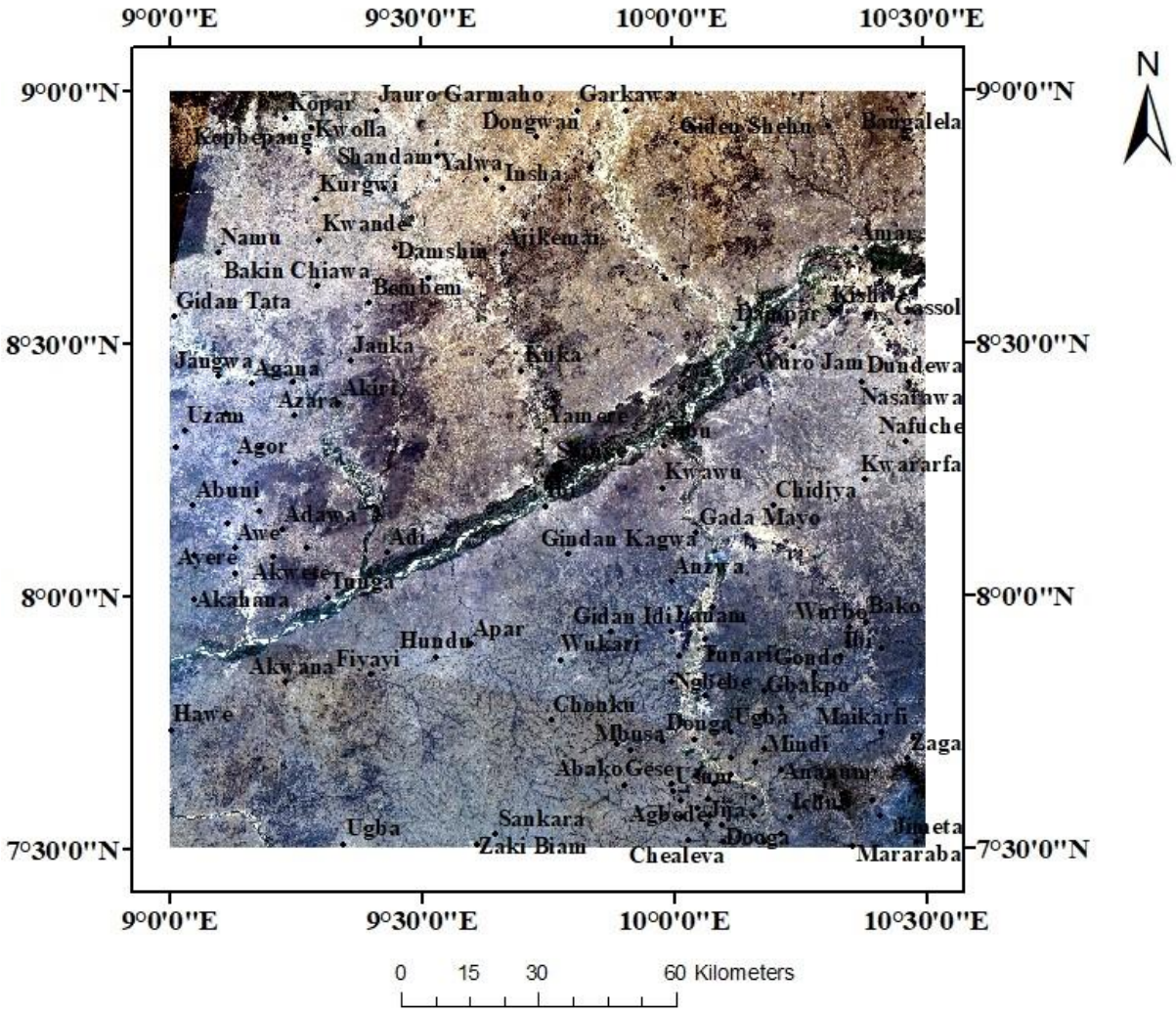

Figure 4.1: True Colour image. RGB combination of bands 4, 3, 2. Green colour represent vegetation, brown represents soil or rock and blue represents water.

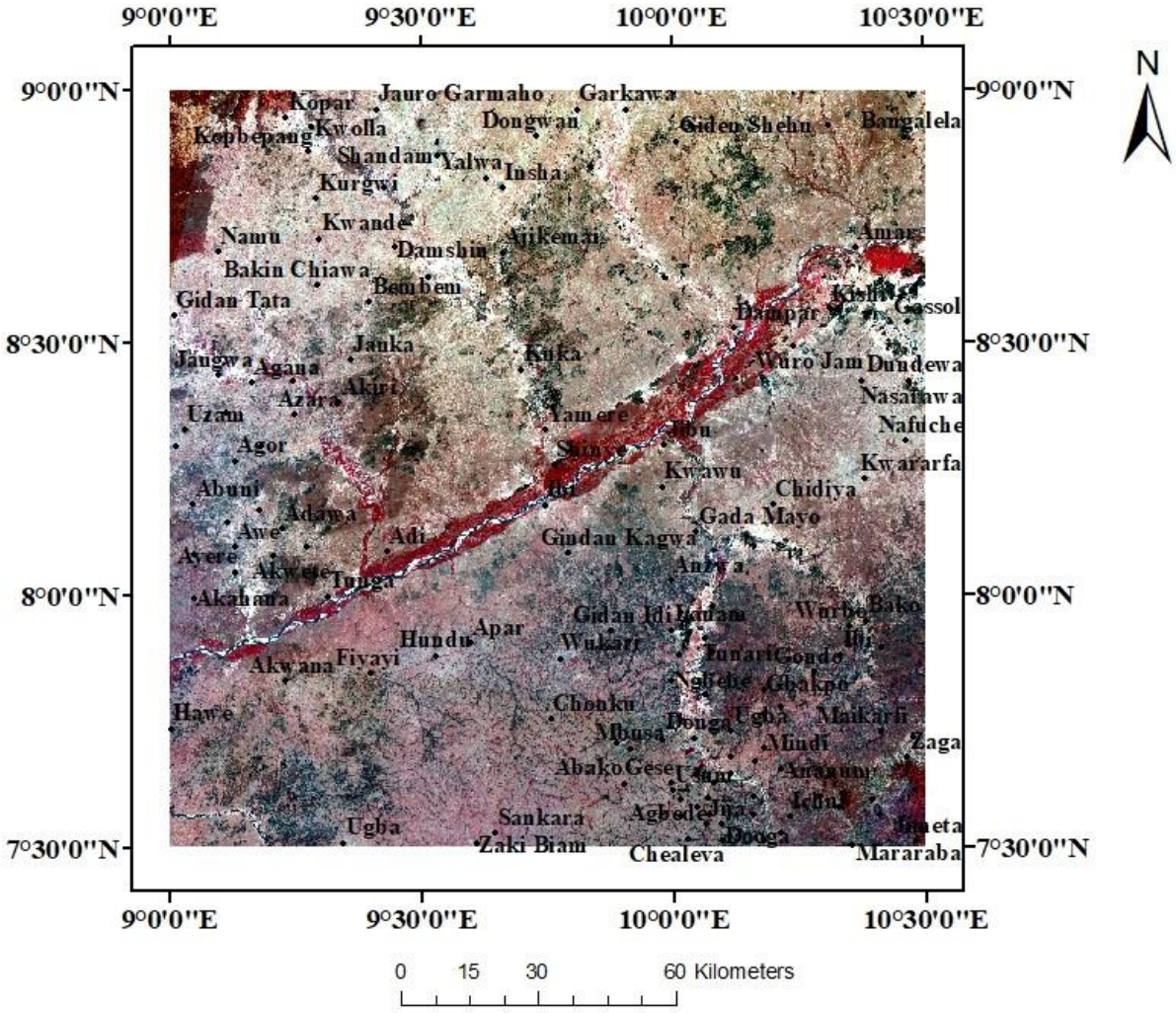

Figure 4.2: False Colour Composite. RGB combination of bands 5, 4, 3. Red colour represents vegetation, black represents water and rock or soil are represented by greyish colour. This RGB combination highlights the boundaries between vegetated and outcrop areas.

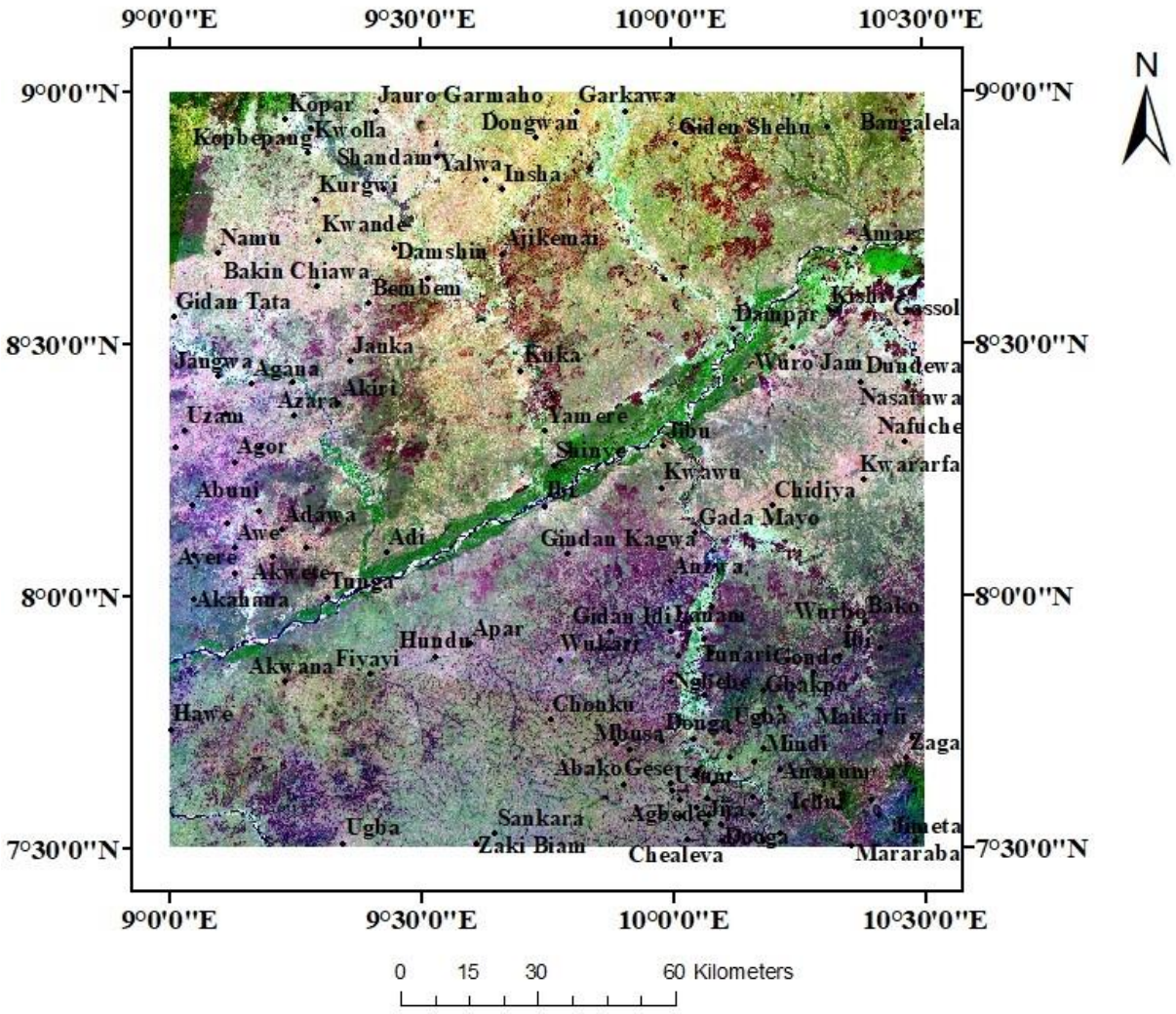

Figure 4.3: RGB combination for bands 7, 5, 2. Enhanced image where outcrops are represented in shades of orange and red, Vegetation in light green and water in black.

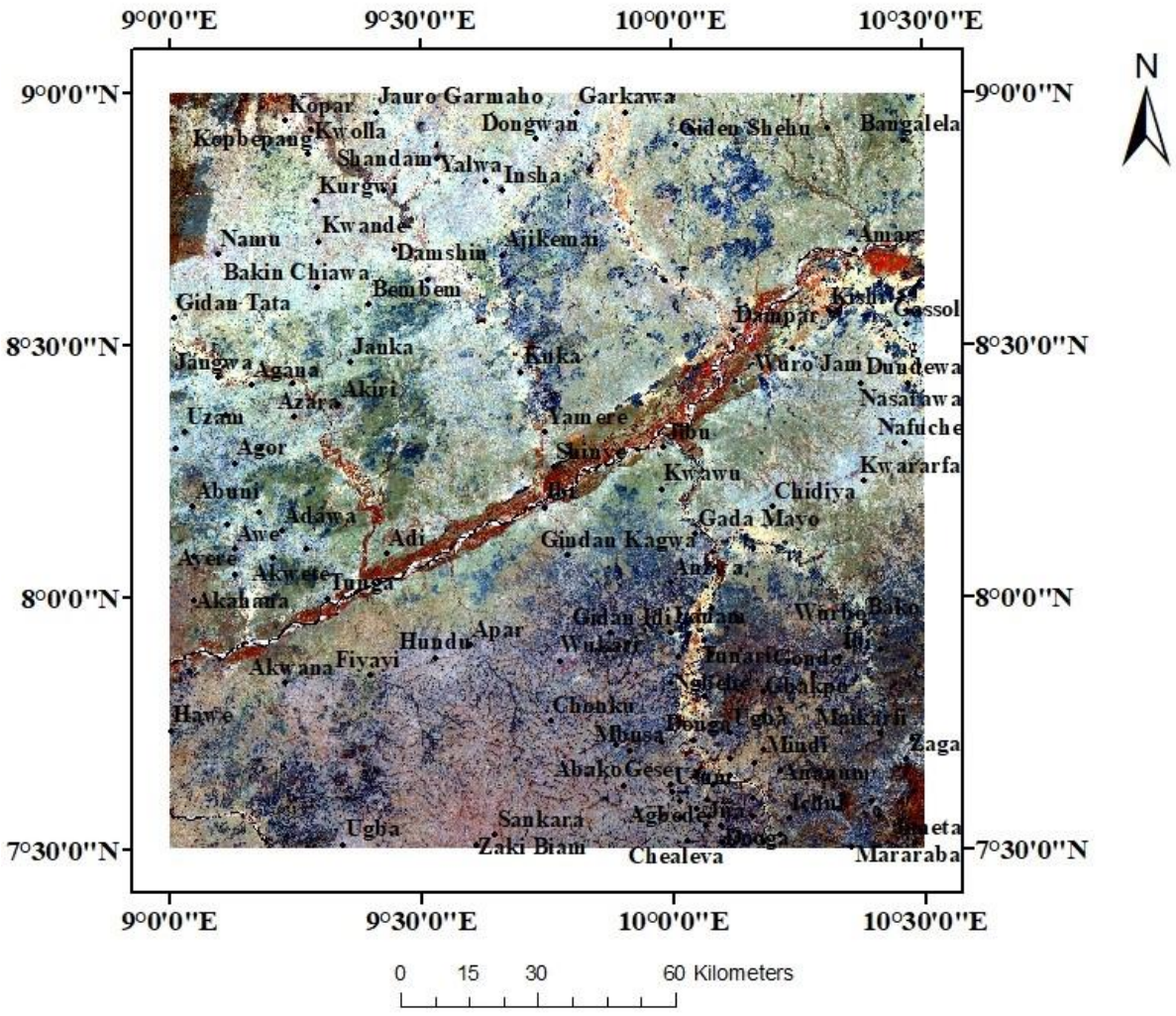

Figure 4.4: RGB combination for bands 5, 6, 7. In this image vegetated areas appear in orange colour, outcrops in light blue and water in black. Some hydrothermal altered rocks can be identified as blue.

4.1.1.2 Band Ratio

Band Ratio Images enhancing hydrothermal altered rocks using band ratios with distinctive reflection features were produced. This corresponds directly to minerals associated with this alteration and represents surface expression for auriferous deposits. Thus, it was applied on the ratio of Landsat 8 OLI band 4 over band 2, to highlight areas with abundant iron oxide bearing minerals, as brighter pixels (Figure 4.5).

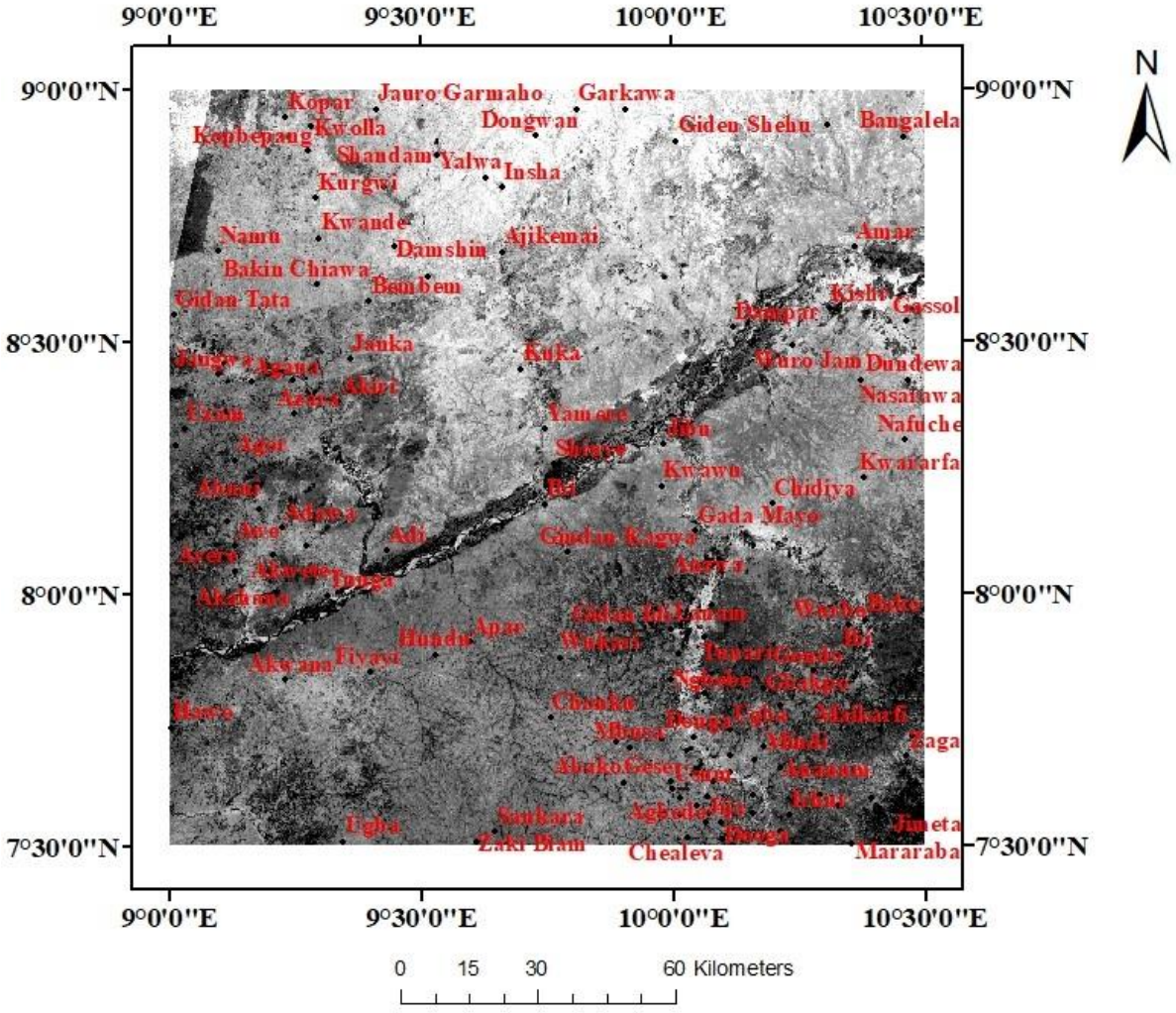

Figure 4.5: Landsat 8 band ratio 4/2 image reveals areas where iron minerals (hematite, goethite, limonite, etc.) are abundant as shown in bright tones.

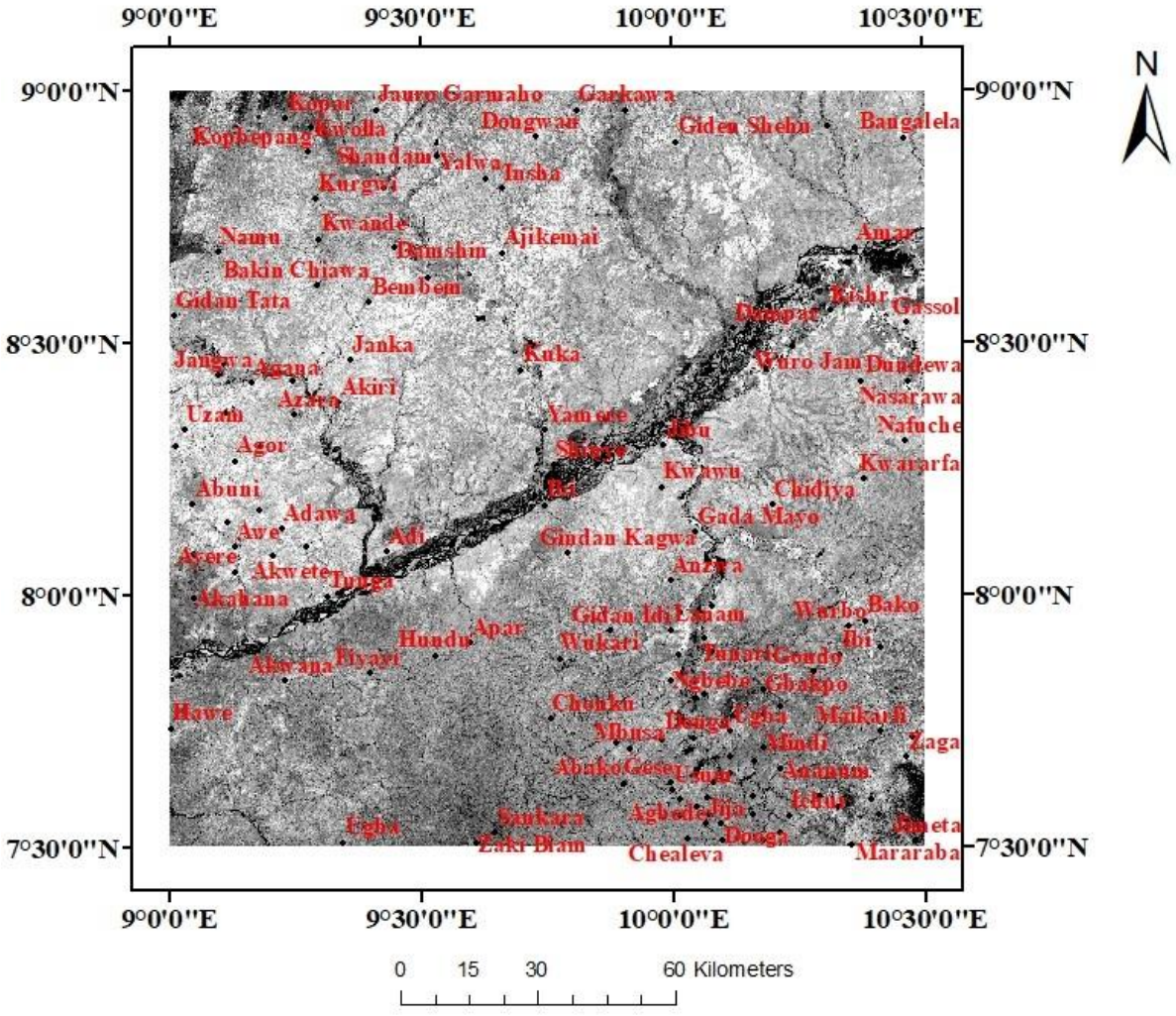

Figure 4.6: Landsat 8 band ratio 6/5 image discriminates ferrous minerals with bright tone.

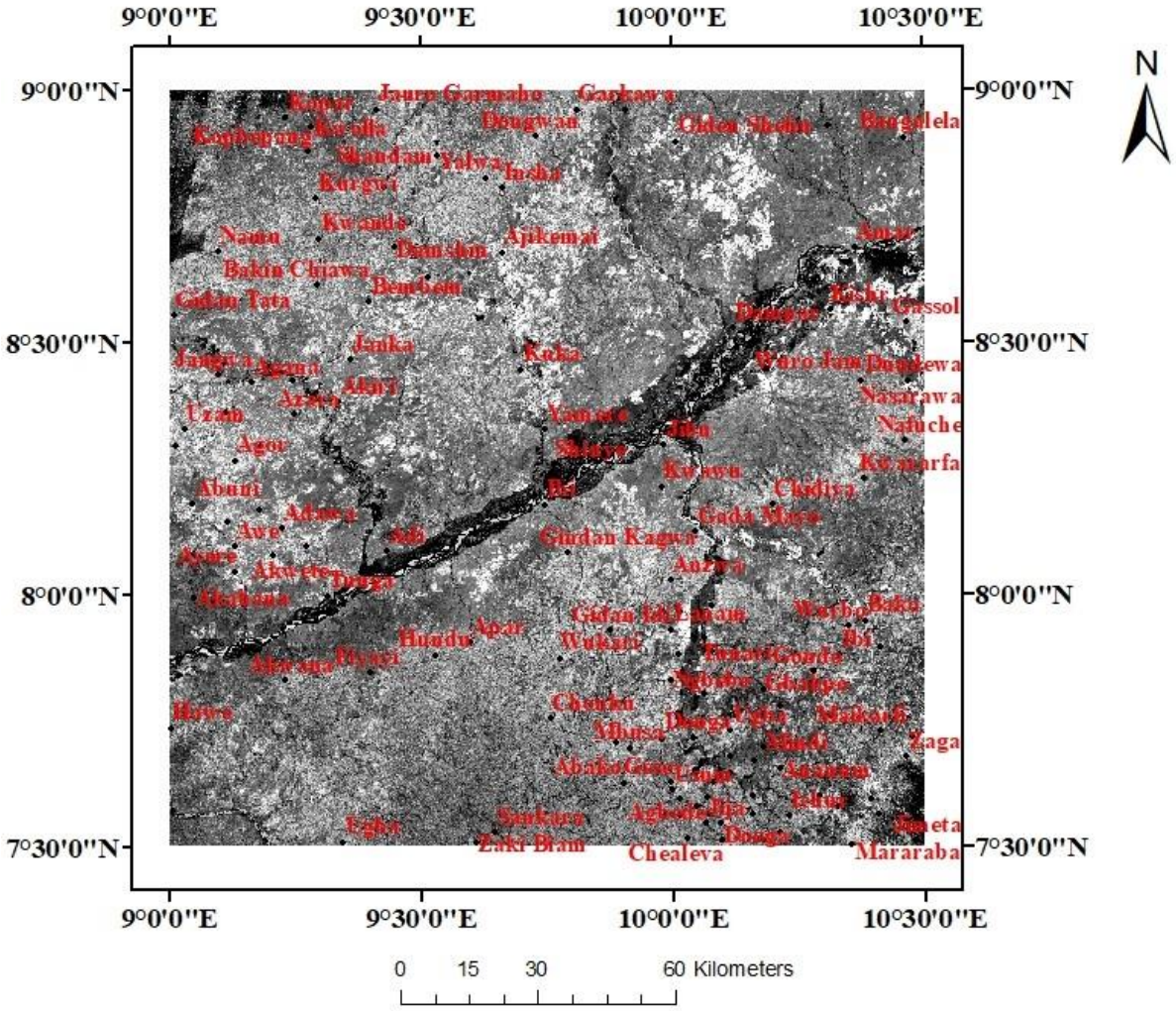

Figure 4.7: Landsat 8 band ratio (7/5) image reveals clay minerals, as illite, kaolinite and montmorillonite, in bright tones.

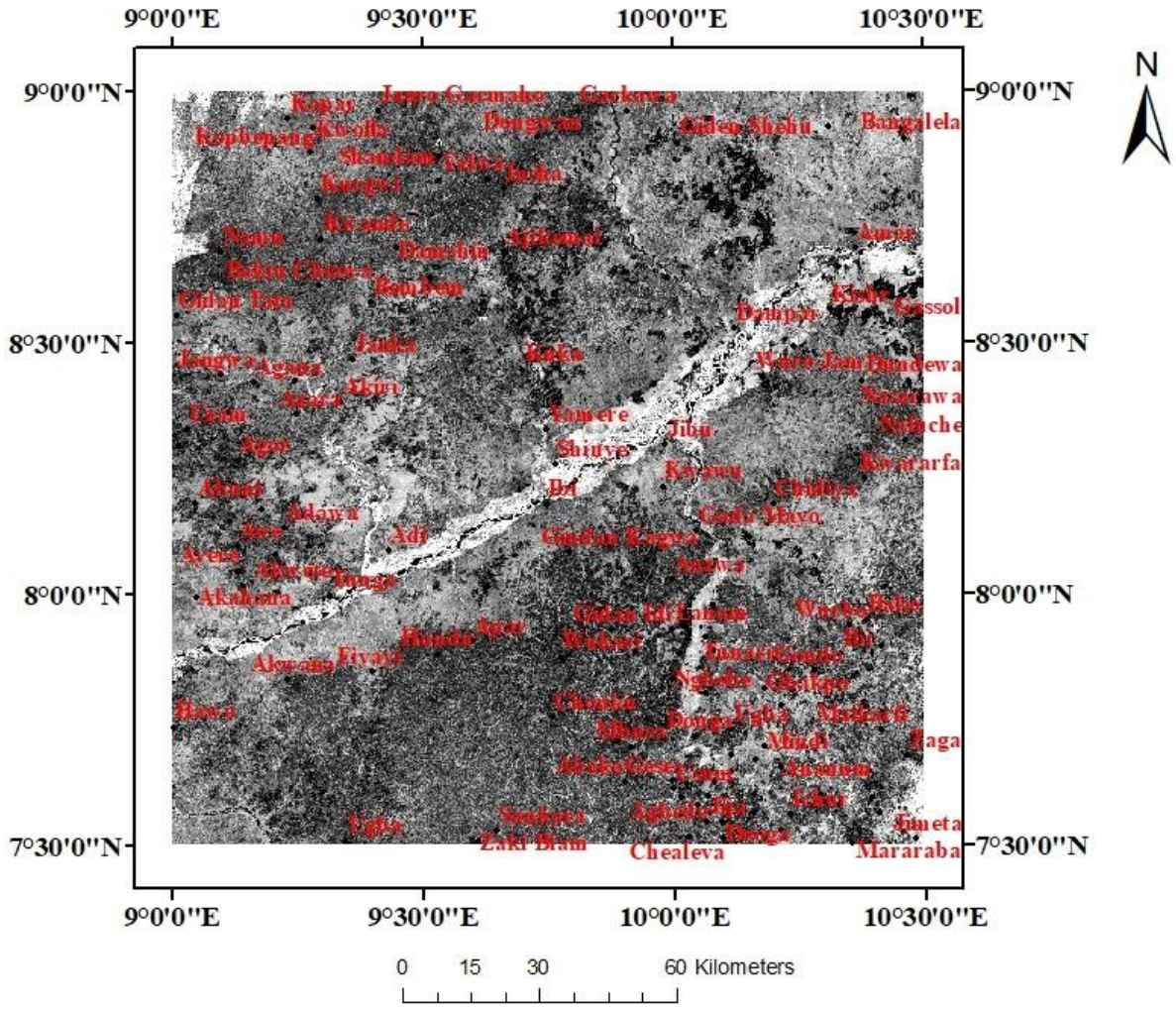

Figure 4.8: Landsat 8 band ratio 6/7 image shows alunite and hydrothermal clay minerals in bright tones.

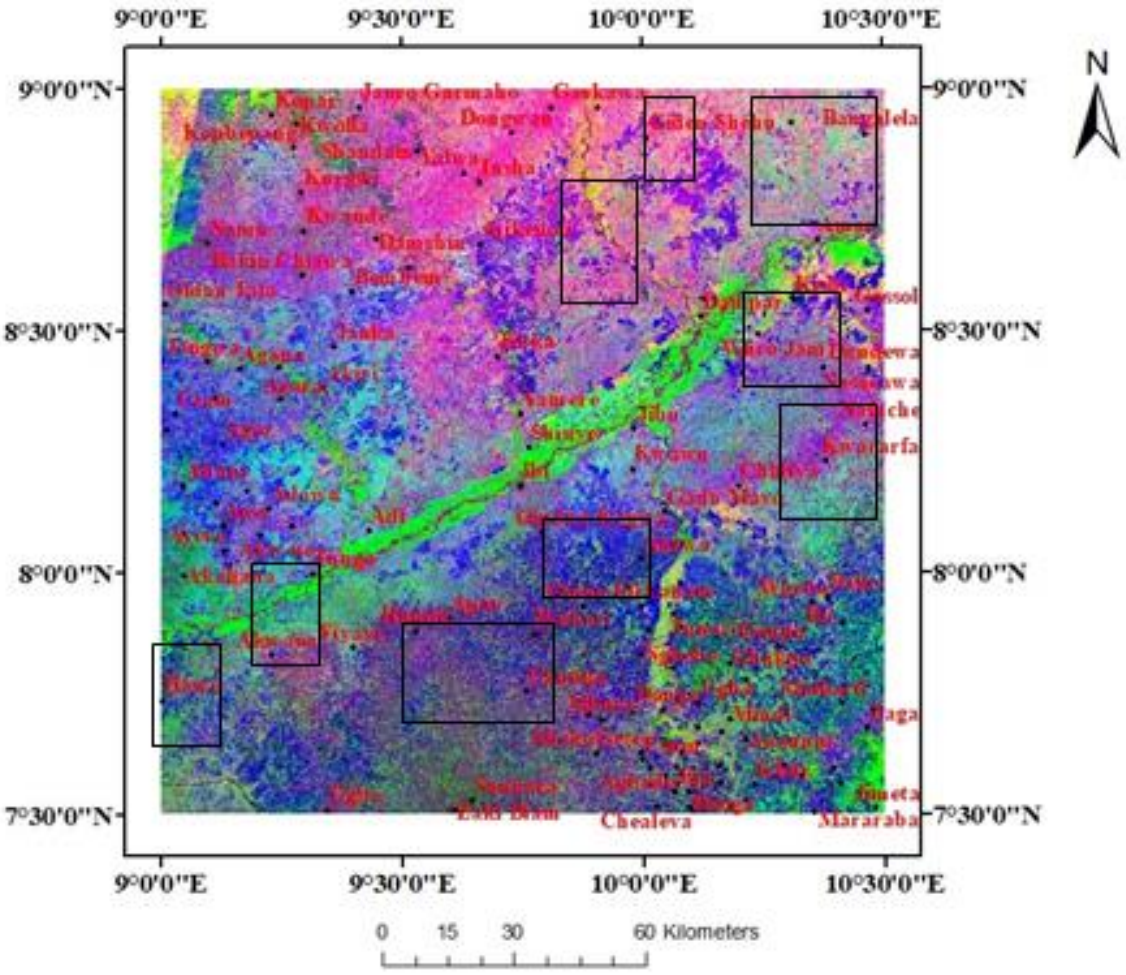

Figure 4.9: Sabin's ratio image (4/2, 6/7, 6/5). Outcrops are represented in light blue-yellow colour, vegetation in blue and water in dark green. Strong yellow represents buildings and other human constructions and light green represents altered rocks.

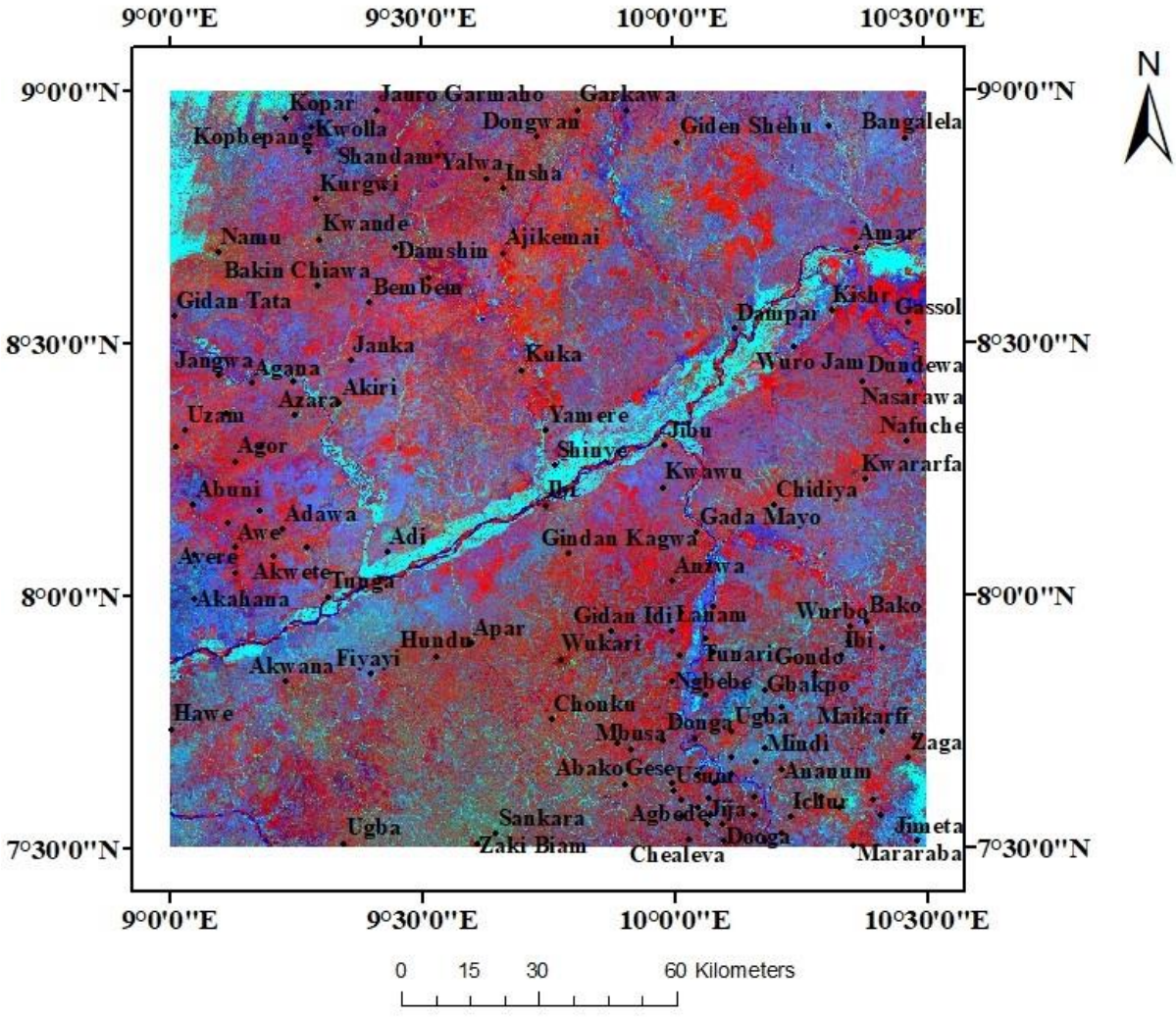

Figure 4.10: Kaufmann ratio (7/5, 5/4, 6/7). This band ratio combination highlight metasediments as dark green and granite outcrops are represented as rose, vegetation as light blue and water as red. Some red areas can be related to hydrothermal alterations.

4.1.1.3 Principal Component Analysis (PCA)

Firstly, this analysis was applied to the six Landsat 8 bands (2, 3, 4, 5, 6, and 7) that output an eigenvector matrix, represented in Table 5. This result allowed identifying which PC contains more useful spectral information from Landsat 8 bands which has much higher contrast than the original bands.

Table 4.1 - Eigenvectors and eigenvalues of PCA on Landsat 8 imagery.

	PC1	PC2	PC3	PC4	PC5	PC6
BAND 2	0 ,33541	0,44101	0,47773	0,53674	0,17977	0,37997
BAND 3	0,32237	0,31849	0,27952	0,08211	0,11697	0,83432
BAND 4	0,30589	0,34953	0,05763	0,66891	0,42059	0,39573
BAND 5	0,60051	-0,73032	0,29534	0,10042	0,07808	0,05112
BAND 6	0,45833	0,01101	0,63896	0,43077	0,44251	0,01313
BAND 7	0,34545	0,22004	0,44139	0,24917	0,75841	0,01221
EIGENVALUES	0,06686	0,00279	0,00102	0,00004	0,00002	0
ERCENTOFEIGEN VALUES	**94,5305**	**3,9425**	**1,4443**	**0,0549**	**0,0227**	**0,0051**
ACCUMULATIVE OFEIGENVALUE	94,5305	98,473	99,9173	99,9722	99,9949	100

The sign and magnitude of eigenvector loadings in each PC correspond to the spectral properties of surface materials such as rock, vegetation, and soils (Crosta & Moore, 1989)

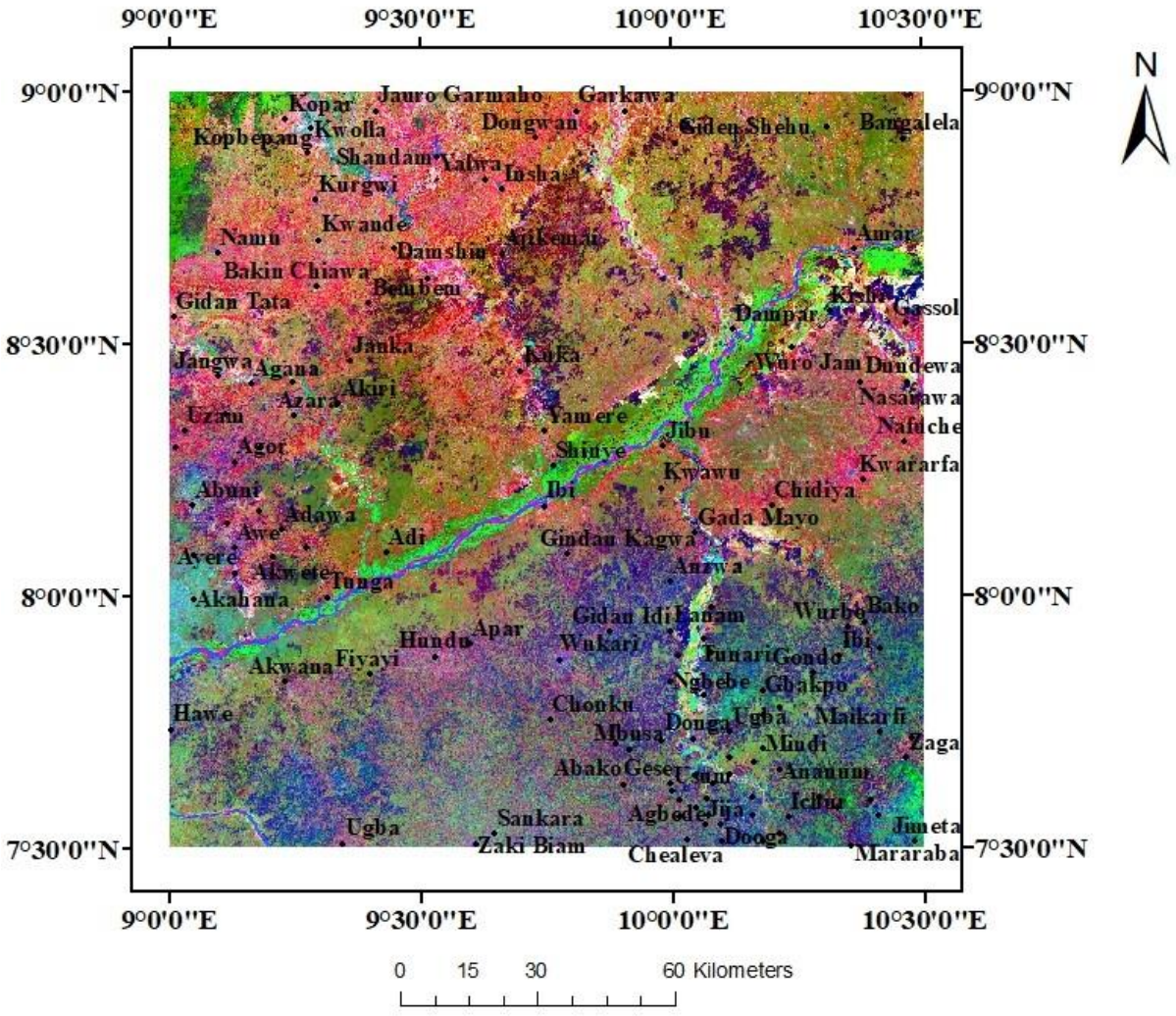

Figure 4.11: RGB colour combination of Principal Component Analysis 1, 2, 3 components. Green-yellow colours represent outcrops, vegetation in purple, water as light blue and metasediments as blue.

From the Landsat analysis, an alteration map (Figure 4.11) was produced. The alteration map represents the map of thermally altered rocks of interest within the Central Benue Trough.

4.1.2 Aeromagnetic Results

In order to determine the structural makeup within the parts of the Middle-Benue trough and how these structures can be used to locate regions favorable for more detailed exploration for mineral deposits, aeromagnetic data were analyzed using first vertical derivative, analytic signal, reduction to the Equator, upward continuation and tilt derivatives,. The resulting magnetic anomaly maps are used to further define the structural and geological framework of parts of the Middle-Benue trough and thus aid in predicting regions that would host additional ore deposits. This analysis helped in narrowing exploration areas to those with a better chance of containing ore deposits.

The result from the airborne magnetic survey are presented and discussed in this section. Interpretation of these images was carried out visually to identify the individual lithologies and delineate geological structures. Anomalous high magnetic zones and low magnetic areas suspected to have resulted from underlining rocks were delineated. To improve the available geological map and reduce the level of its subjectivity, a qualitative interpretation of the bedrocks from the available geophysical datasets was performed. This process involved comparing the existing geology map with that generated from a GIS environment and making inference to structure and geology.

4.1.2.1 Total Magnetic Intensity (TMI) Map

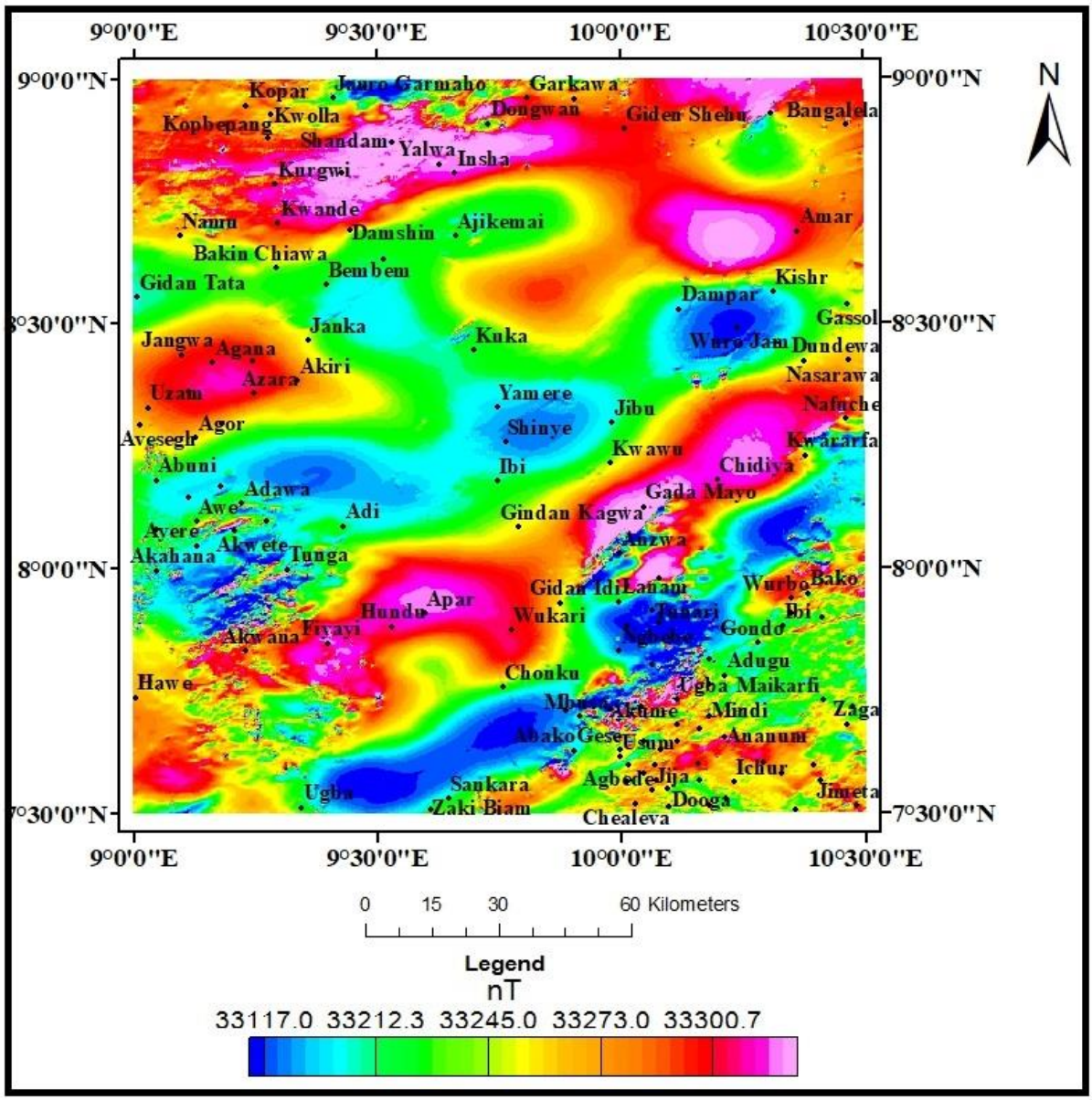

Figure 4.12: Total Magnetic Intensity, RMI grid map.

4.1.2.2 Residual Magnetic Intensity, RMI

The residual magnetic data was gridded with a 100 m grid space to show the spatial distribution of magnetic anomaly. The amplitude of a magnetic anomaly is directly proportional to magnetization which depends on magnetic susceptibility of the rocks (Gunn, 1997).

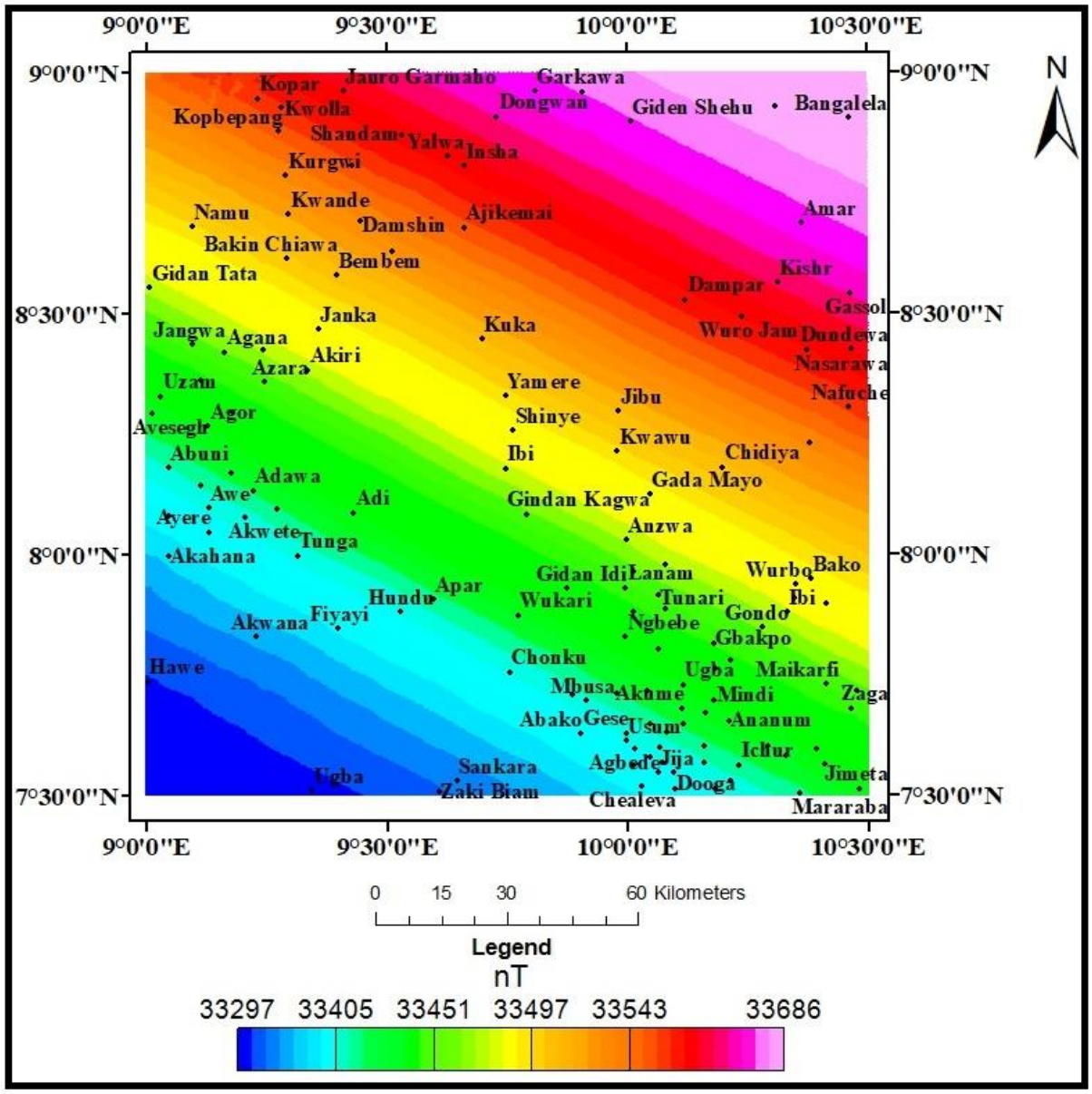

Figure 4.13: Regional Magnetic Intensity, RMI grid map.

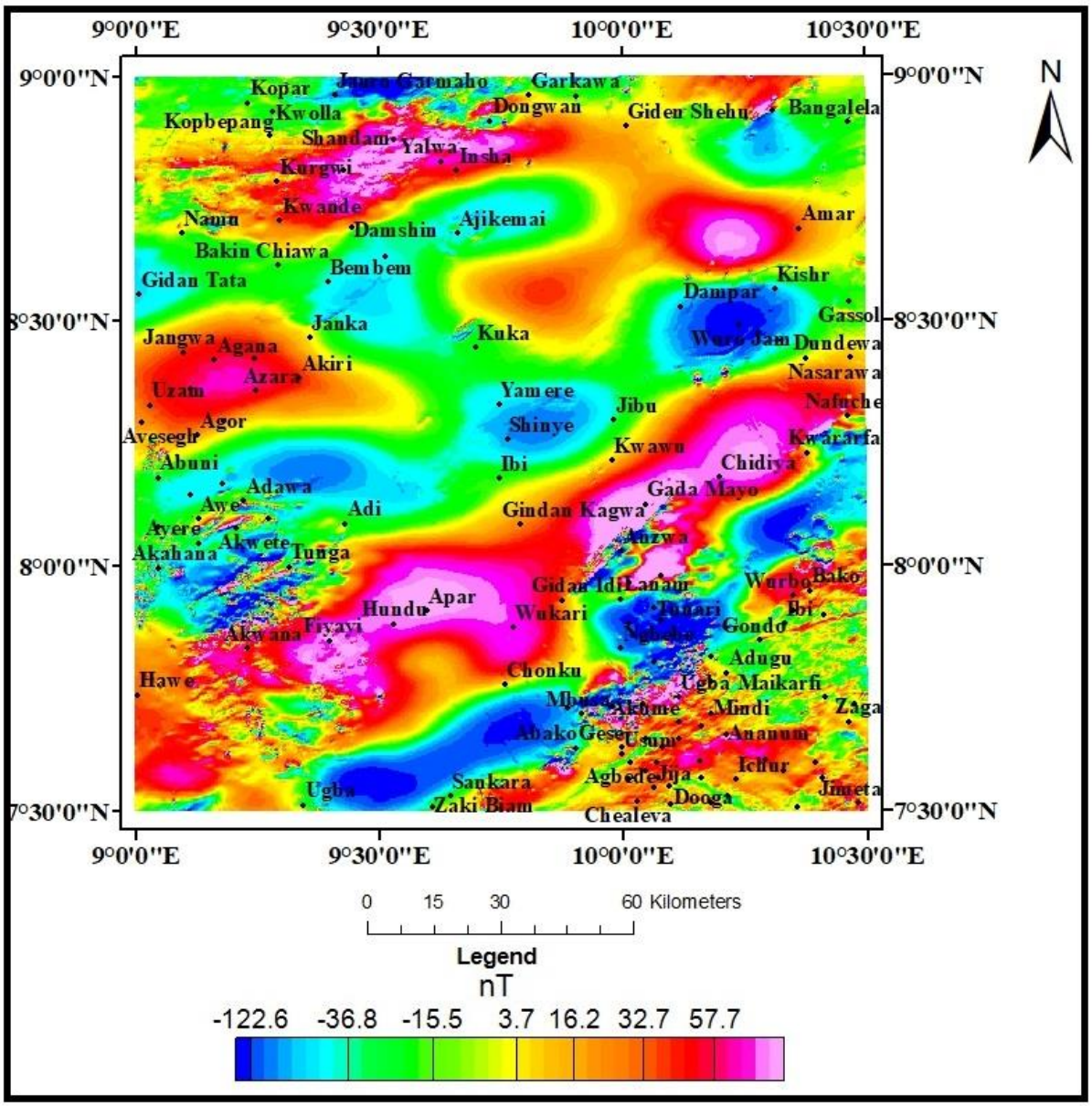

Figure 4.14: Residual Magnetic Intensity, RMI grid map.

4.1.2.3 Reduction to the Equator (RTE)

Reduction to Equator, RTE filter was applied to the RMI grid in order to locate the observed magnetic anomalies directly over the magnetic source bodies that caused the anomaly. It was also applied to remove the influence of magnetic latitude on the residual anomalies. The RMI grid was transformed into reduction to the Equator (RTE) grid using the 2D-FFT (Fast Fourier Transform) filter in Geosoft Oasis Montaj software. The parameters used for the transformation are an inclination of -9.8^{o} and declination of -1.9^{o} which represent the mean value for the area.

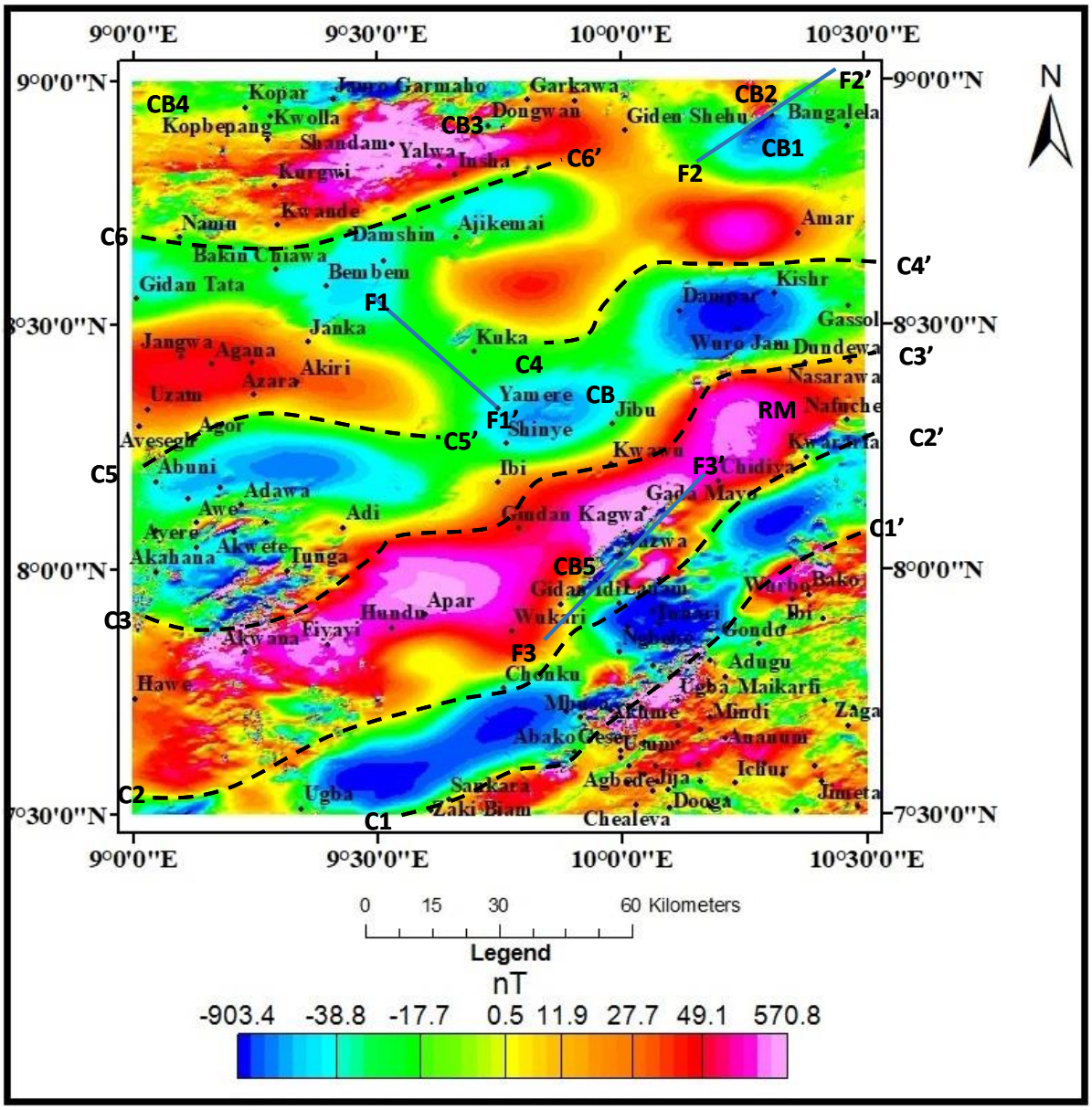

Figure 4.15: Reduction to the Equator (RTE) image using an inclination of -9.8^{o} and declination of -1.9^{o}

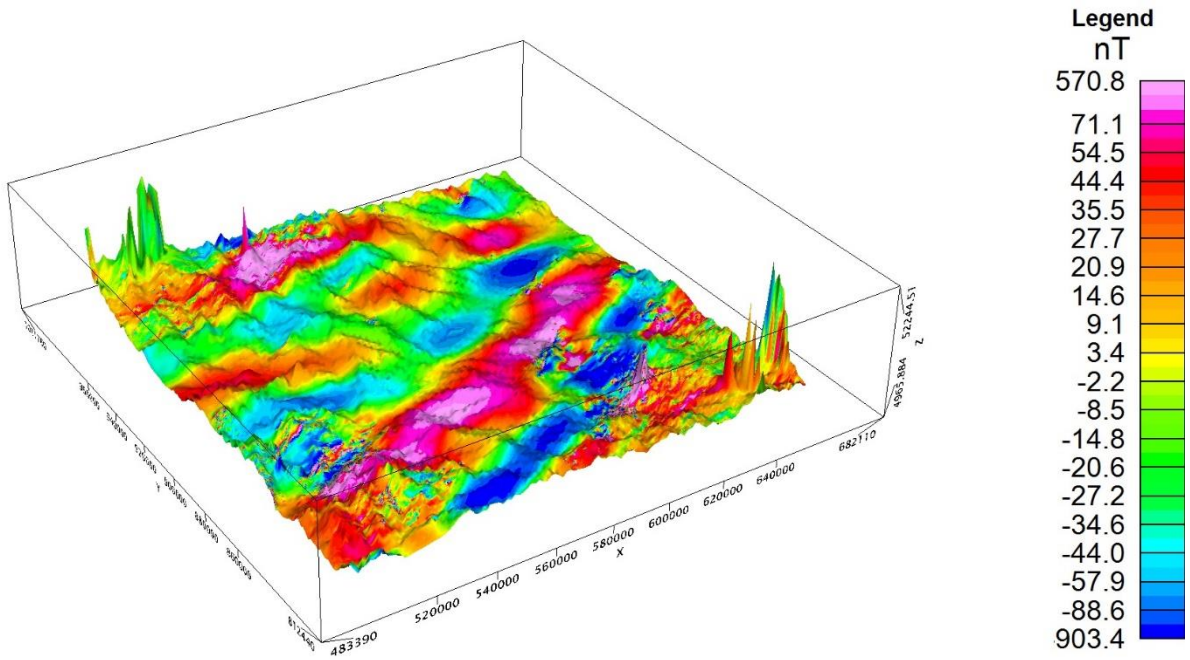

Figure 4.16: RTE image drape over DEM viewed in 3D (Red - high magnetic signature and blue-low magnetic signature)

4.1.2.4 Analytic Signal

To know the source positions of the magnetic anomaly regardless of direction and remnant magnetization in the sources effect that is mostly associated with the reduce to pole or equator, the analytical signal filter was applied to the RMI grid. The significant characteristic of the analytical signal, AS is that it is independent of the direction of the magnetization of the source. Moreover, the amplitude of the analytical signal can be related to the amplitude of magnetization. Asadi & Hale (1999) used the analytical signal of total magnetic intensities to delineate intermediary magmatic rocks in the Takab area of Iran.

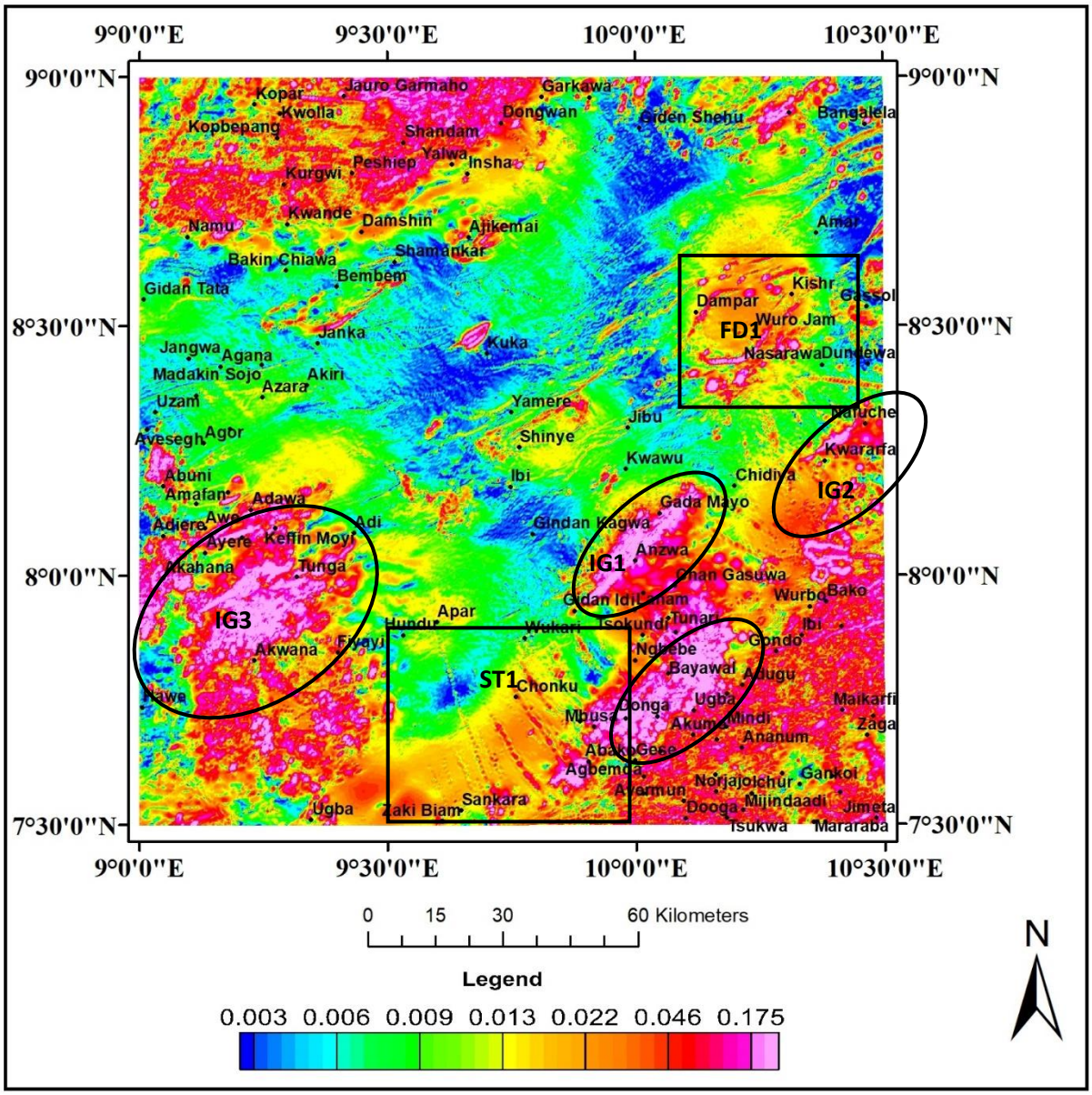

Figure 4.17: Analytic signal image of residual magnetic intensity

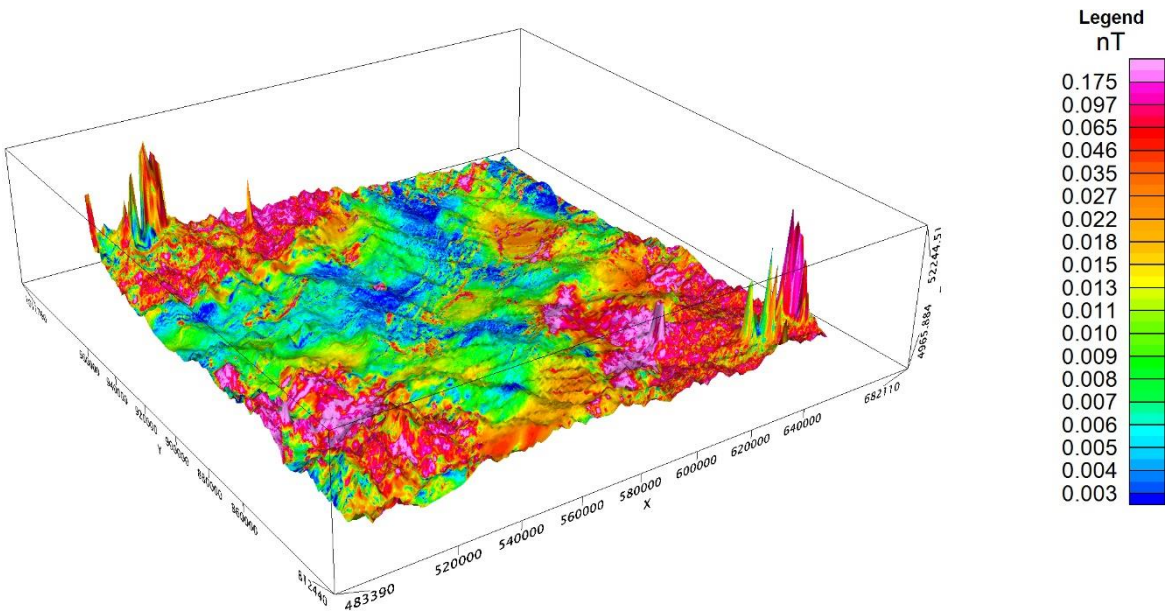

Figure 4.18**:** Analytic signal image draped over DEM viewed in 3D

4.1.2.5 First Vertical Derivative (FVD)

The First Vertical Derivative (FVD) and second vertical Derivative (SVD) transforms are the only transforms of this type that are routinely generated because, the higher the order the greater is the relative amplification of higher frequencies and greater too is the risk of accentuating noise to an unacceptable degree.

For the purpose of this work, the FVD and SVD were calculated, where the first vertical derivative can be used as an alternative to a residual display, and the SVD's ZERO CONTOUR represents the point of inflexion on the original anomaly curve which approximates the locations of edges of the causative bodies, provided that the bodies are shallow and have vertical sides. Recall that second vertical derivative (SVD) transform is a mathematical transform based on Laplace`s equation. It has the effect of accentuating the shorter wavelength (shallower source) components at the expense of longer wavelength (generally deeper) features.

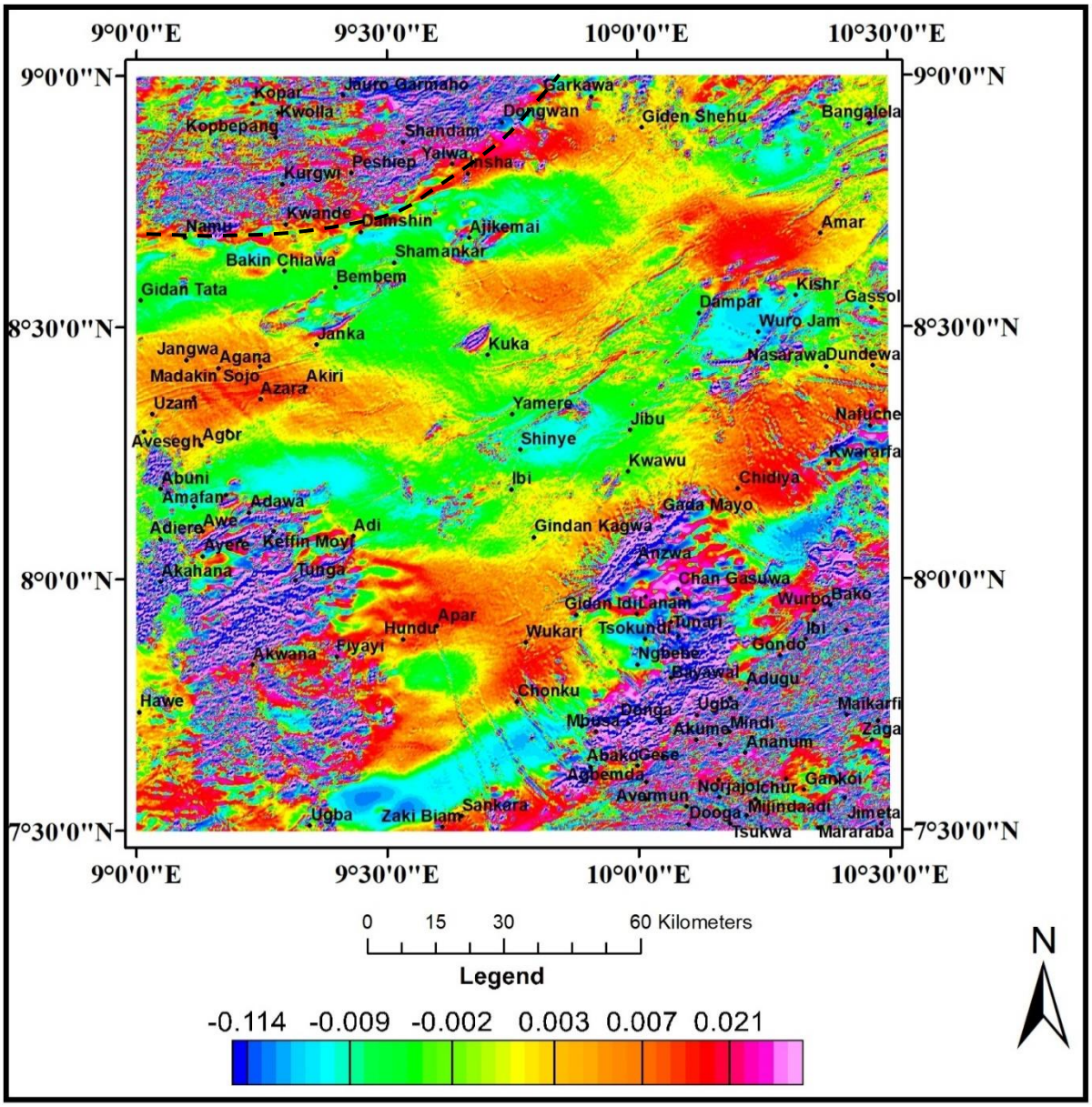

Figure 4.18a: First Vertical Derivative map of the RTE grid colour shaded map

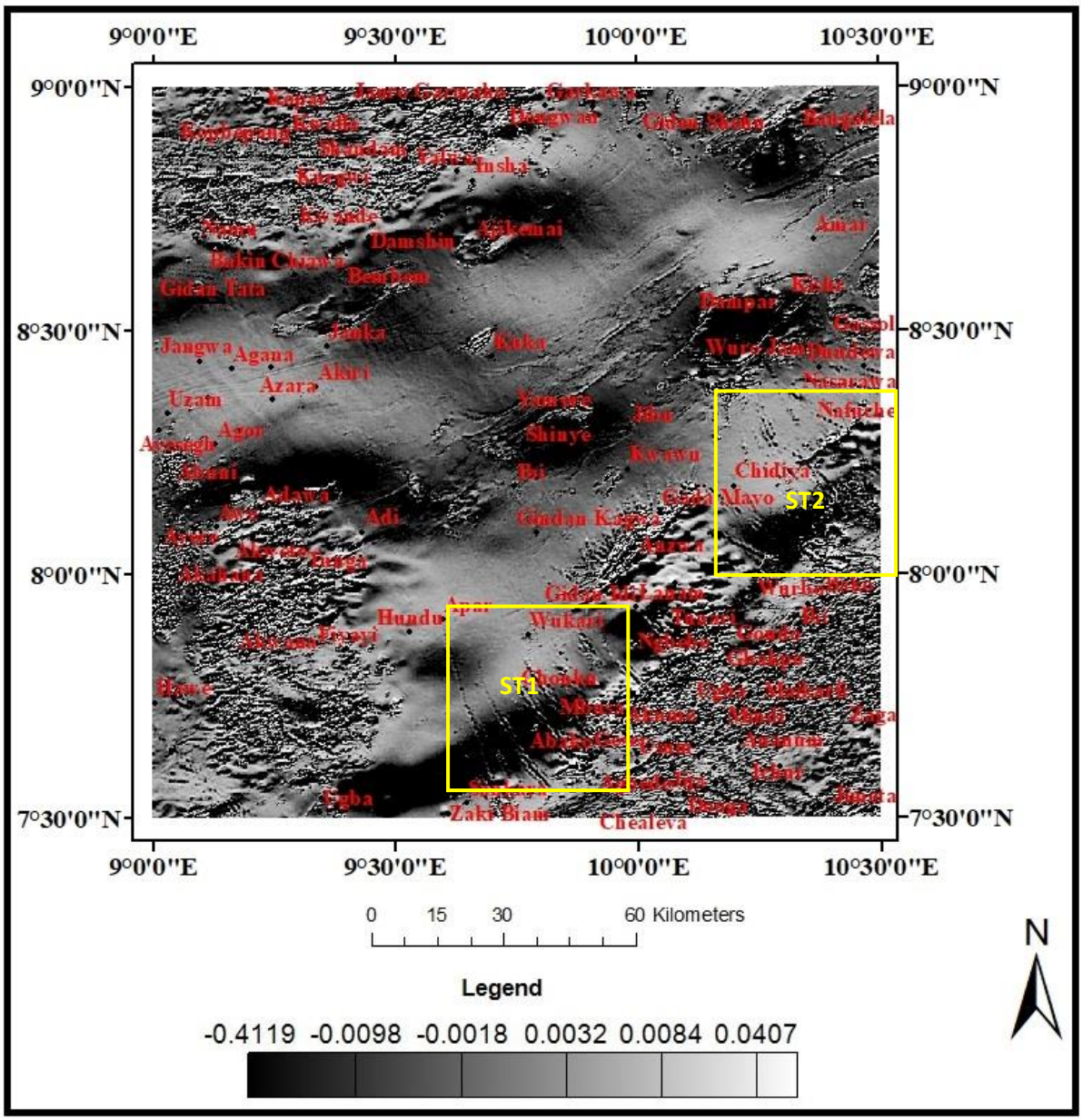

Figure 4.18b: First Vertical Derivative map of the RTE grid grey scale map

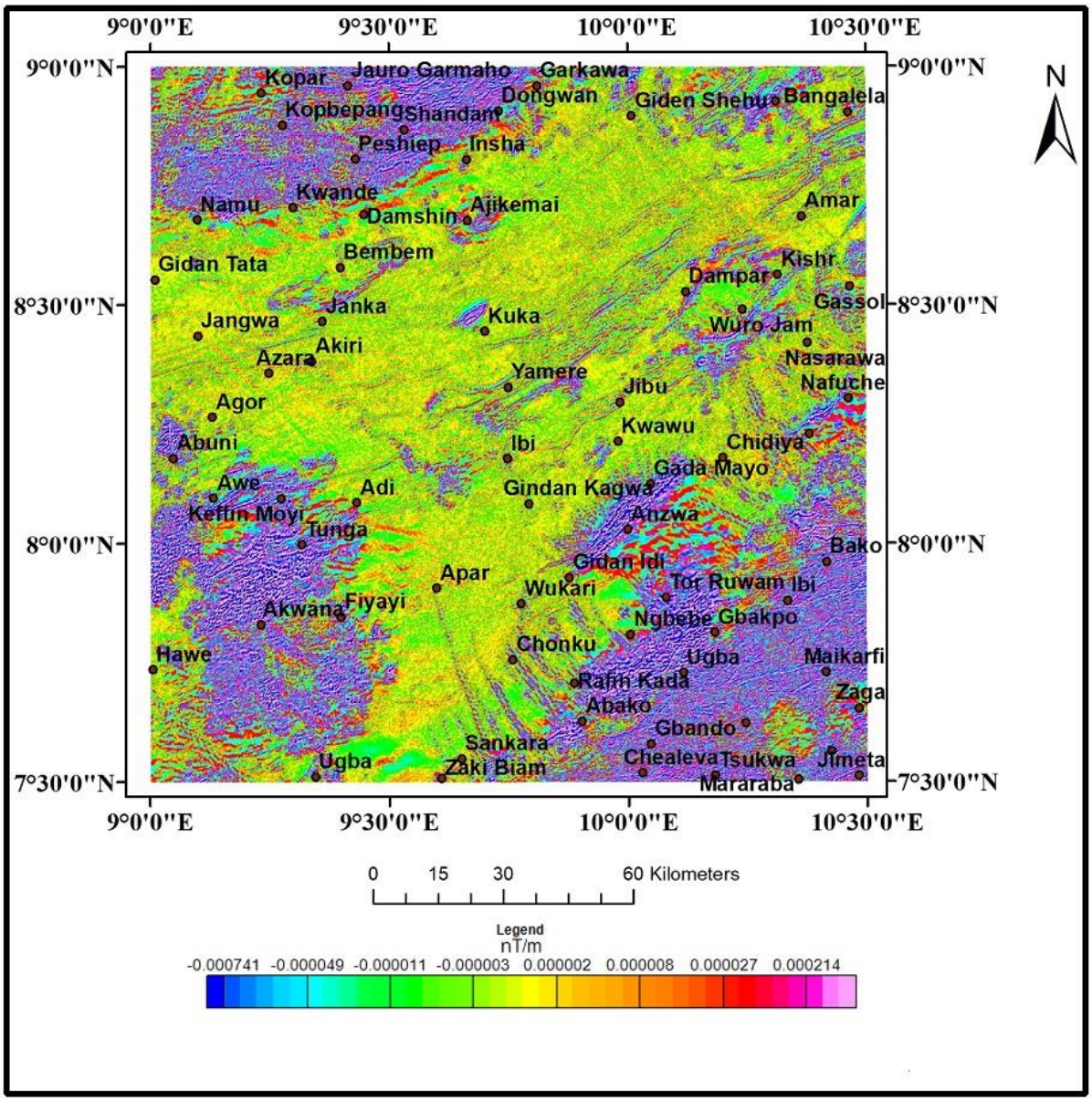

Figure 4.18c: Second Vertical Derivative map of the RTE grid grey scale

4.1.2.6 Upward Continuation

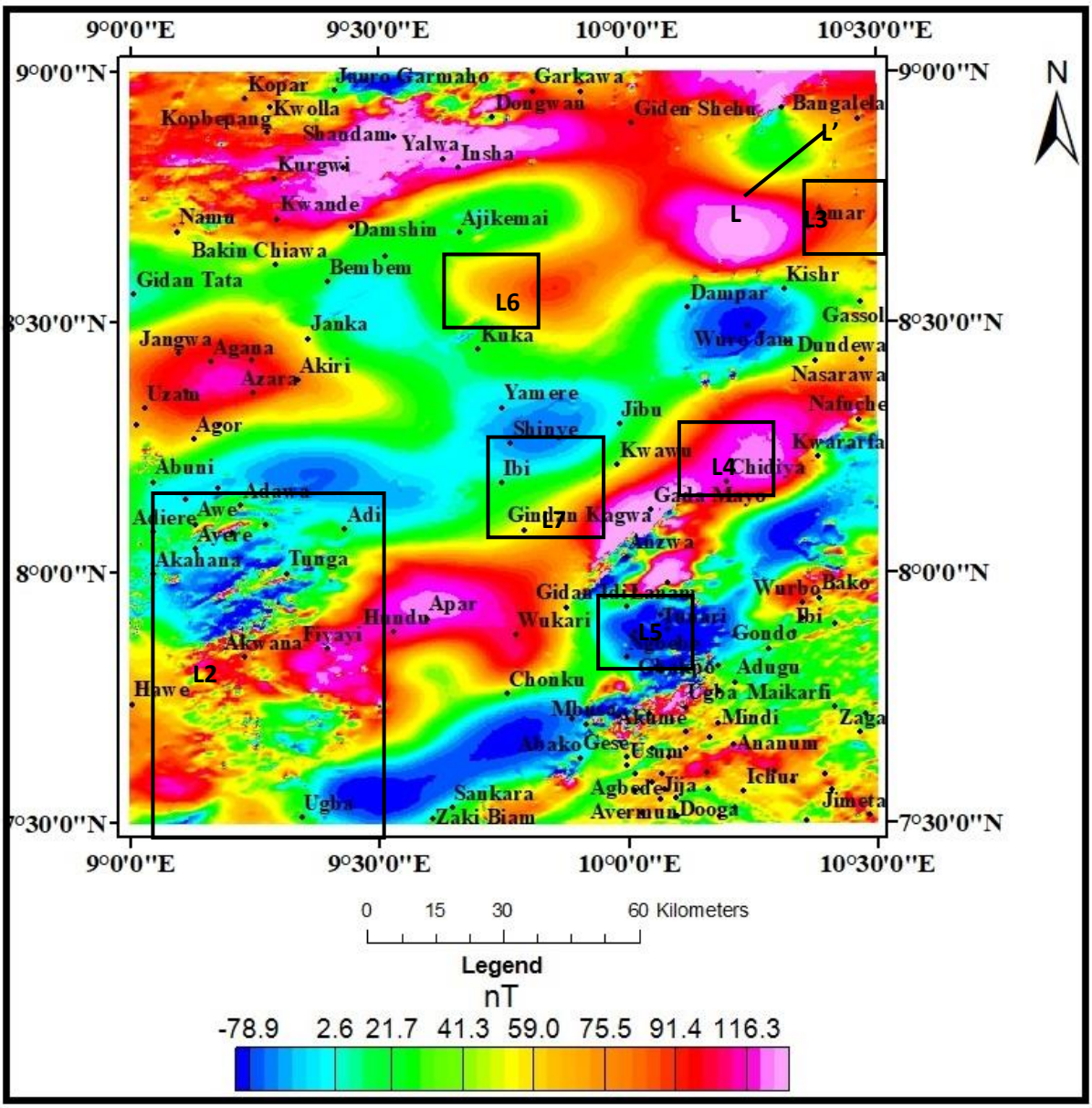

Figure 14.19a**:** RTE (grid) Continued Upward to 100 m

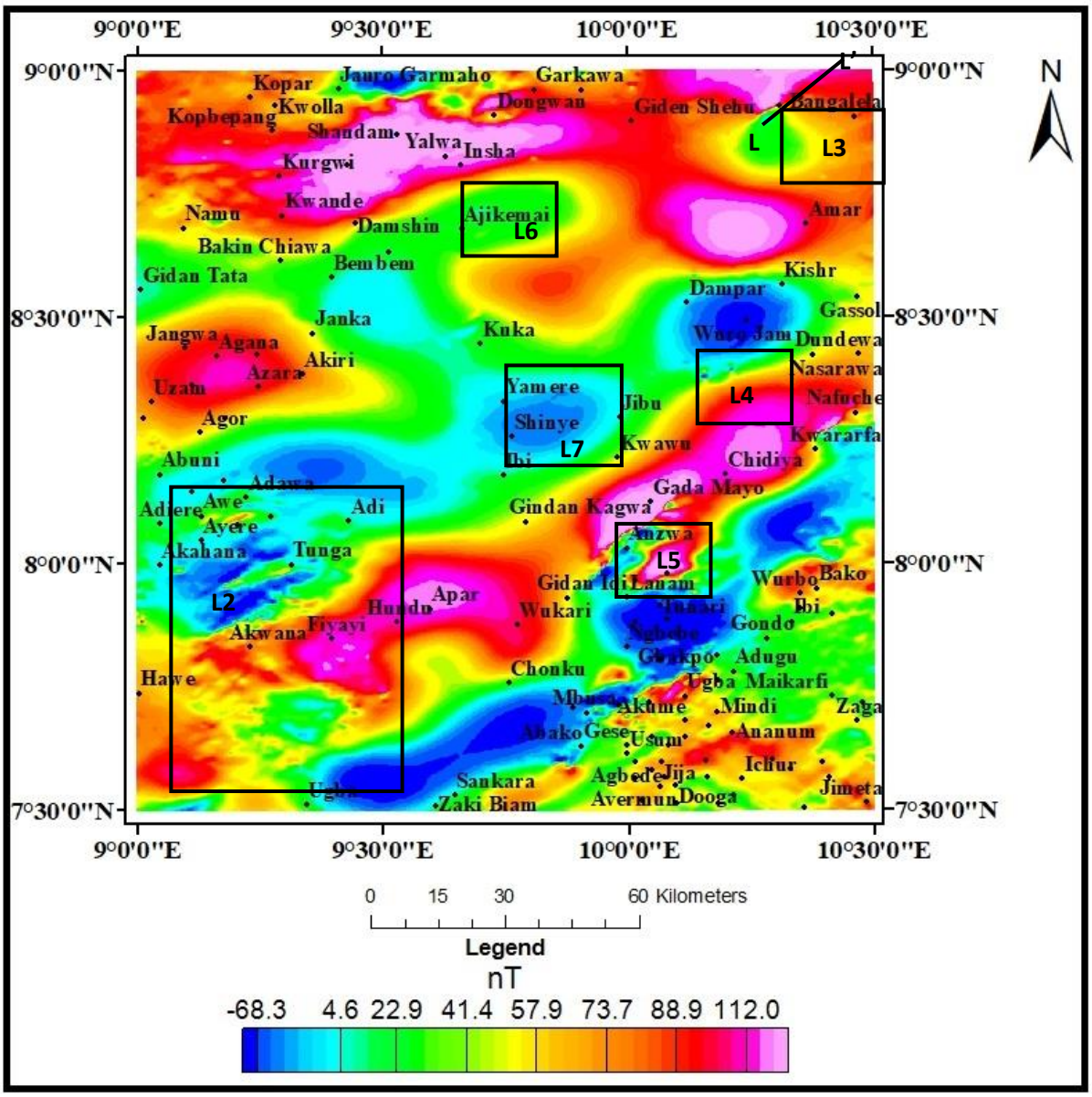

Figure 14.19b**:** RTE (grid) Continued Upward to 500 m

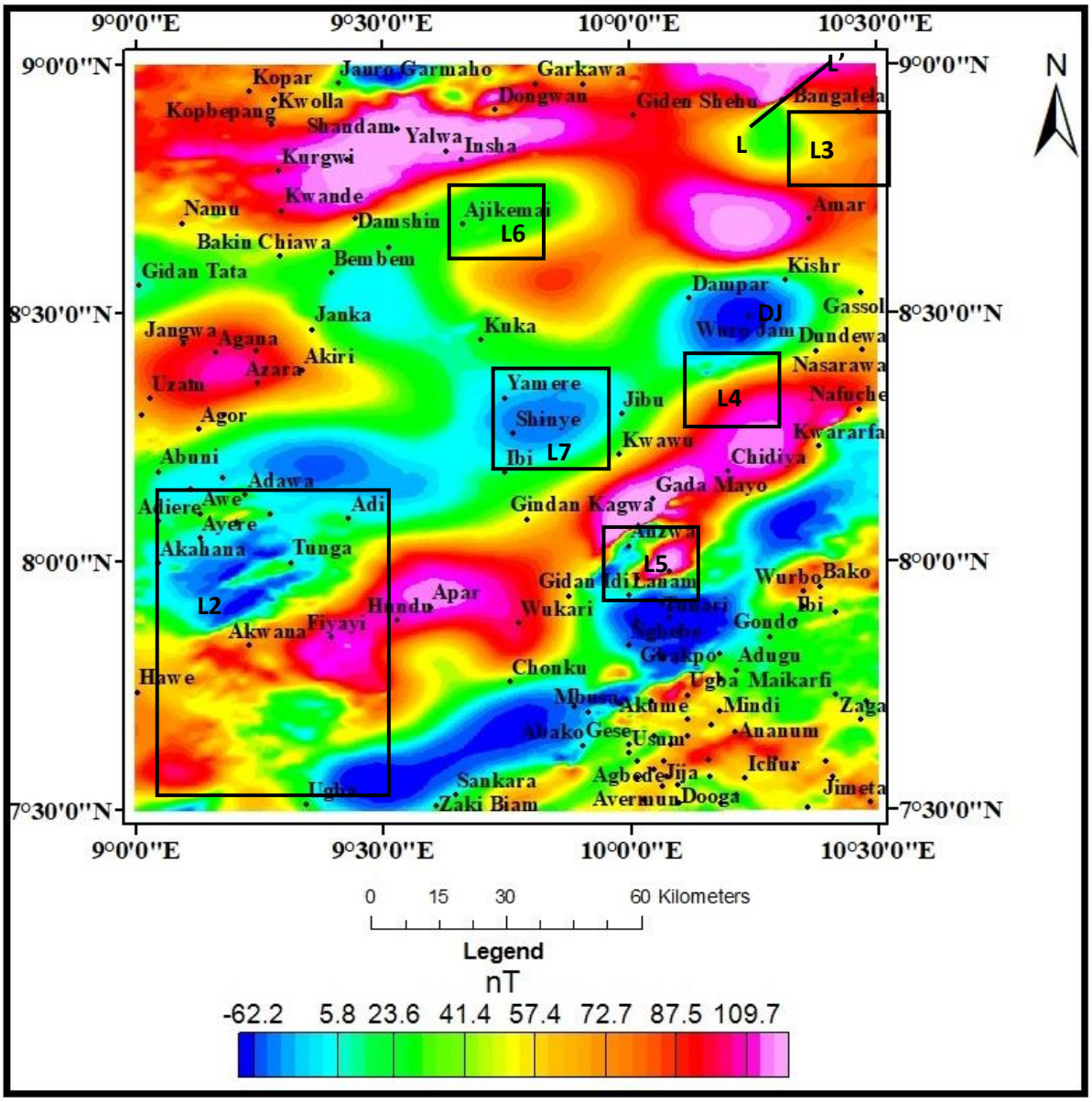

Figure 4.19c: RTE (grid) Continued Upward to 800 m

4.1.2.7 Tilt Derivative

To determine structures (faults and folds), the contacts and edges or boundaries of magnetic sources, and to enhance both weak and strong magnetic anomalies of the area, the TDR filter was applied to both the RMI and the RTE grid. The angle derivative filter attempts to place an anomaly directly over its source. Verduzco *et al.* (2004) showed in their work that tilt derivative filter performs an automatic-gain-control (AGC) filter which tends to equalize the response from both weak and strong anomalies, hence, providing an effective way to trace out along striking anomalies. Tilt angle derivative (TDR) of RMI locates the edges of formations, especially at shallow depths by using the theory that the zero contours are the edges of the formation (Salem *et al.,* 2007).

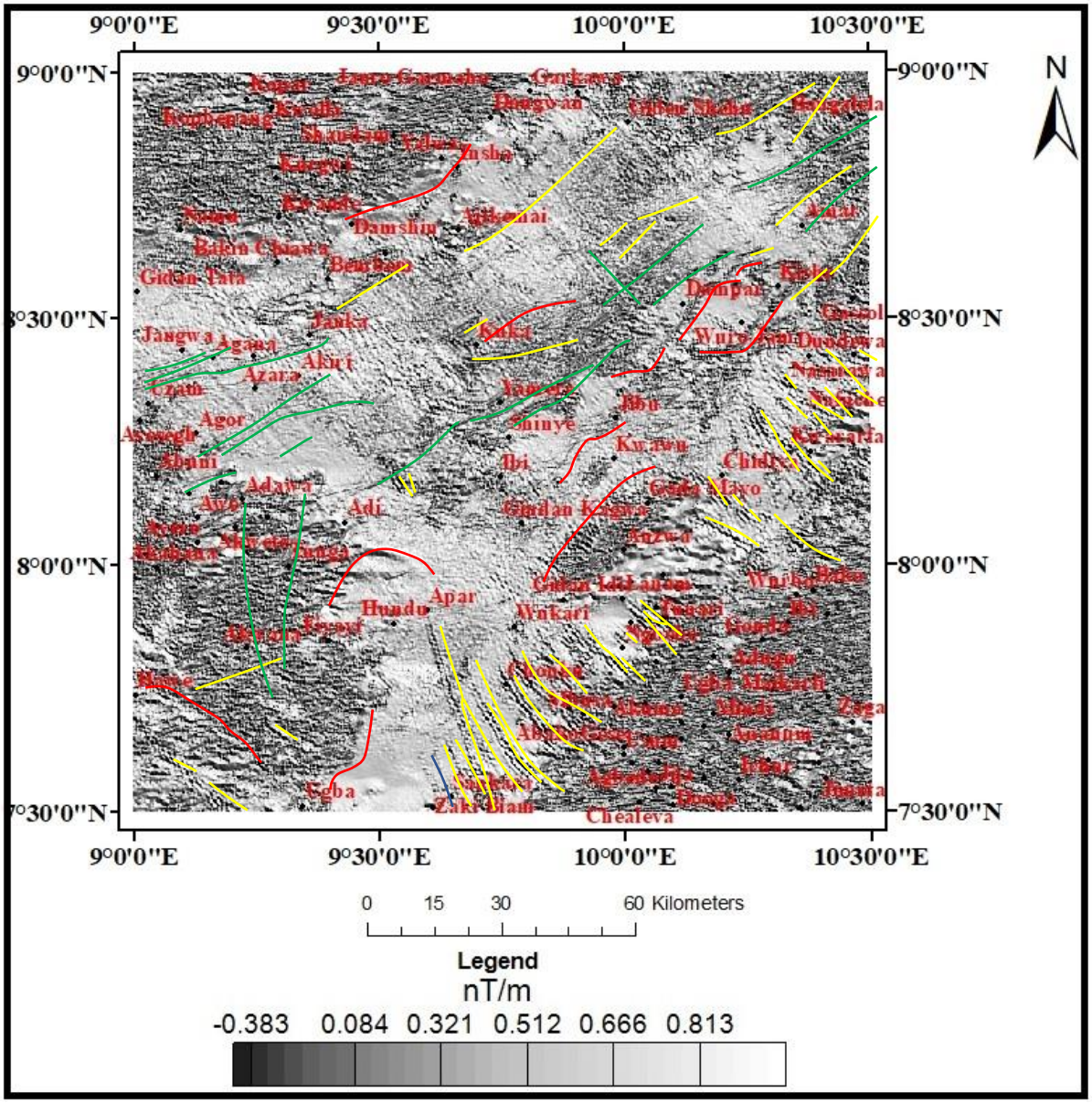

Figure 4.20a: Tilt derivative, TDR colour grey scale map

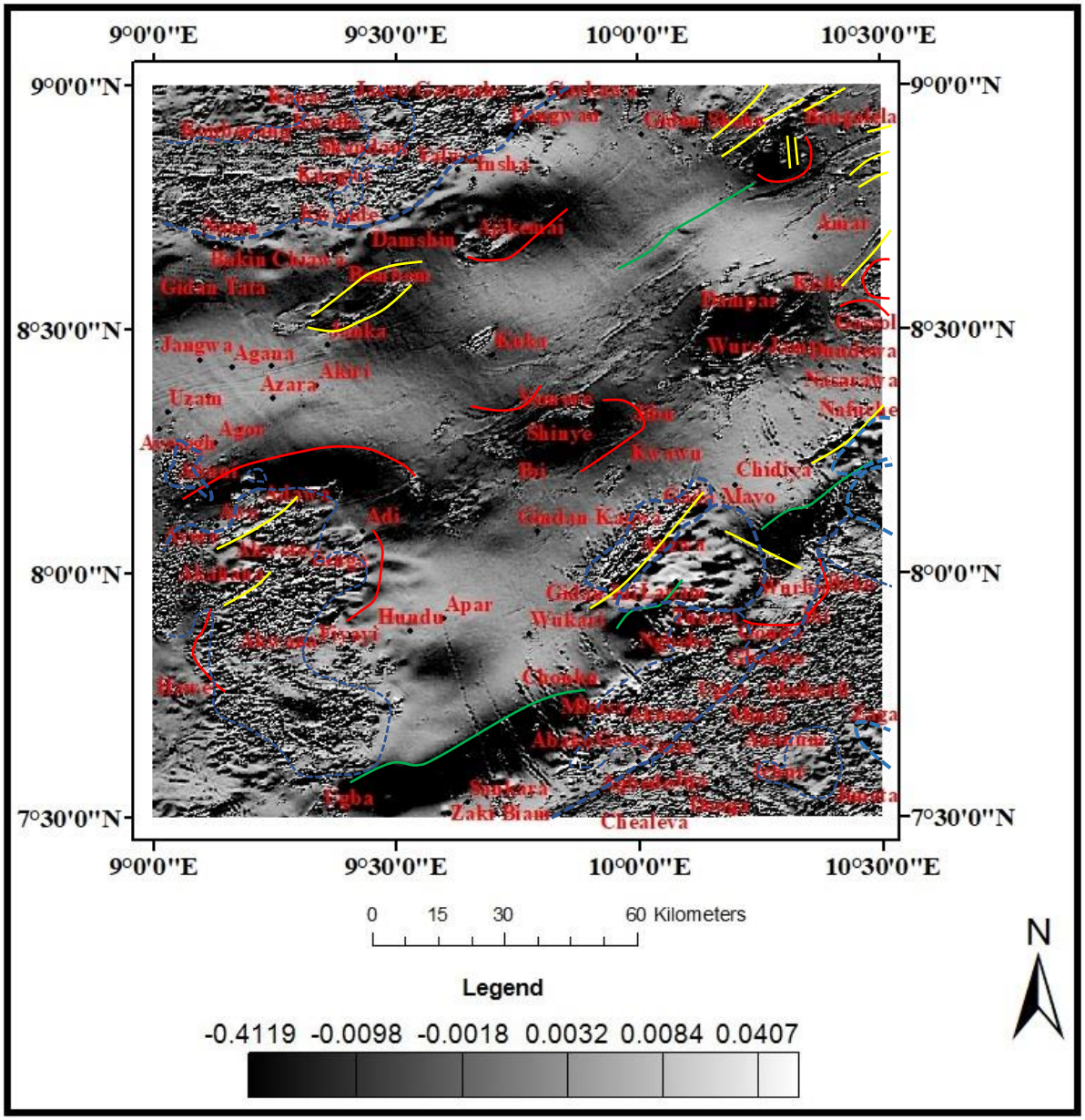

Figure 4.20b: First Vertical Derivative map of the RTE grid grey scale map

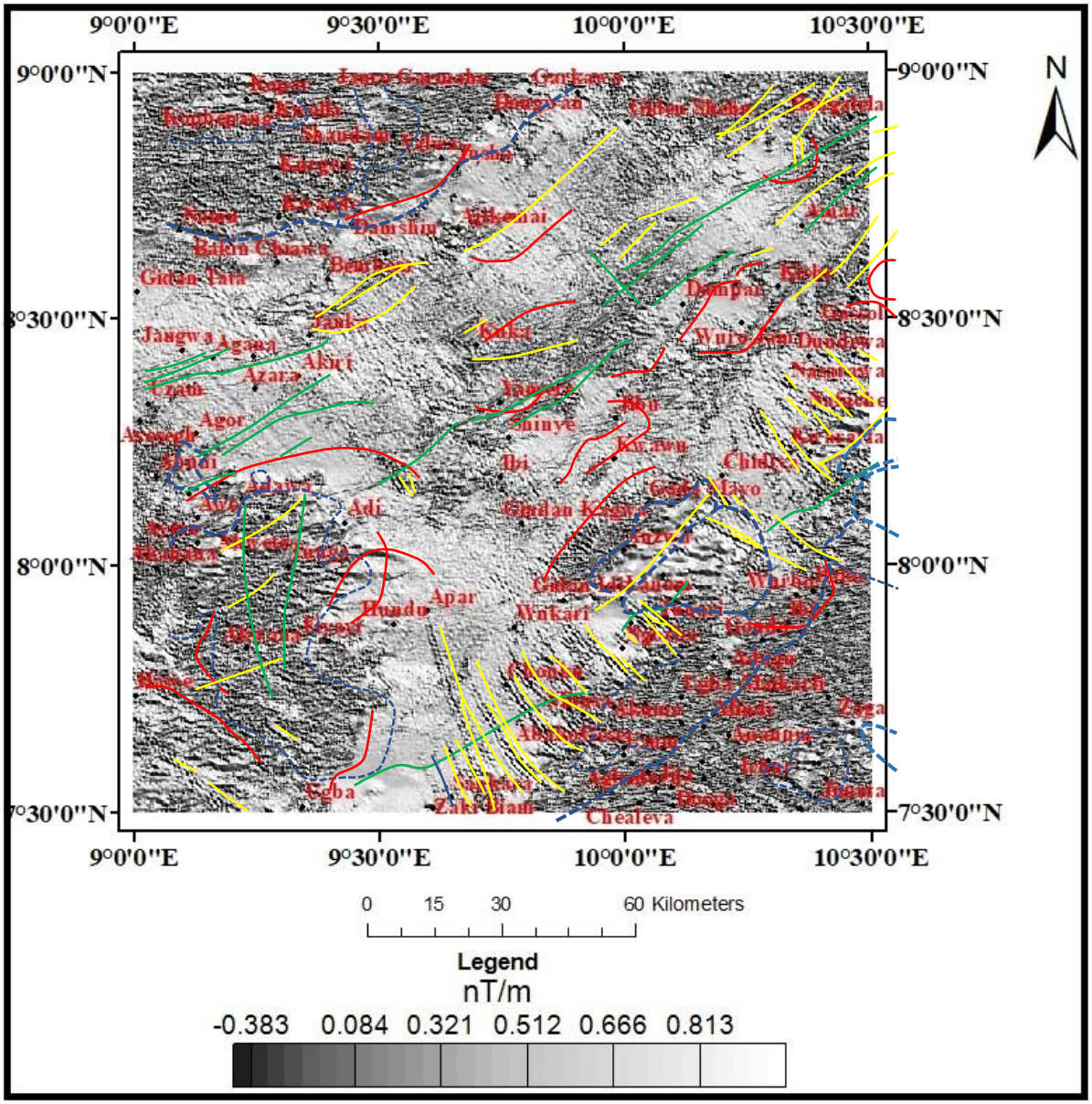

Figure 4.20c: Interpreted fault, folds and contacts superimposed on the TDR image displayed in greyscale

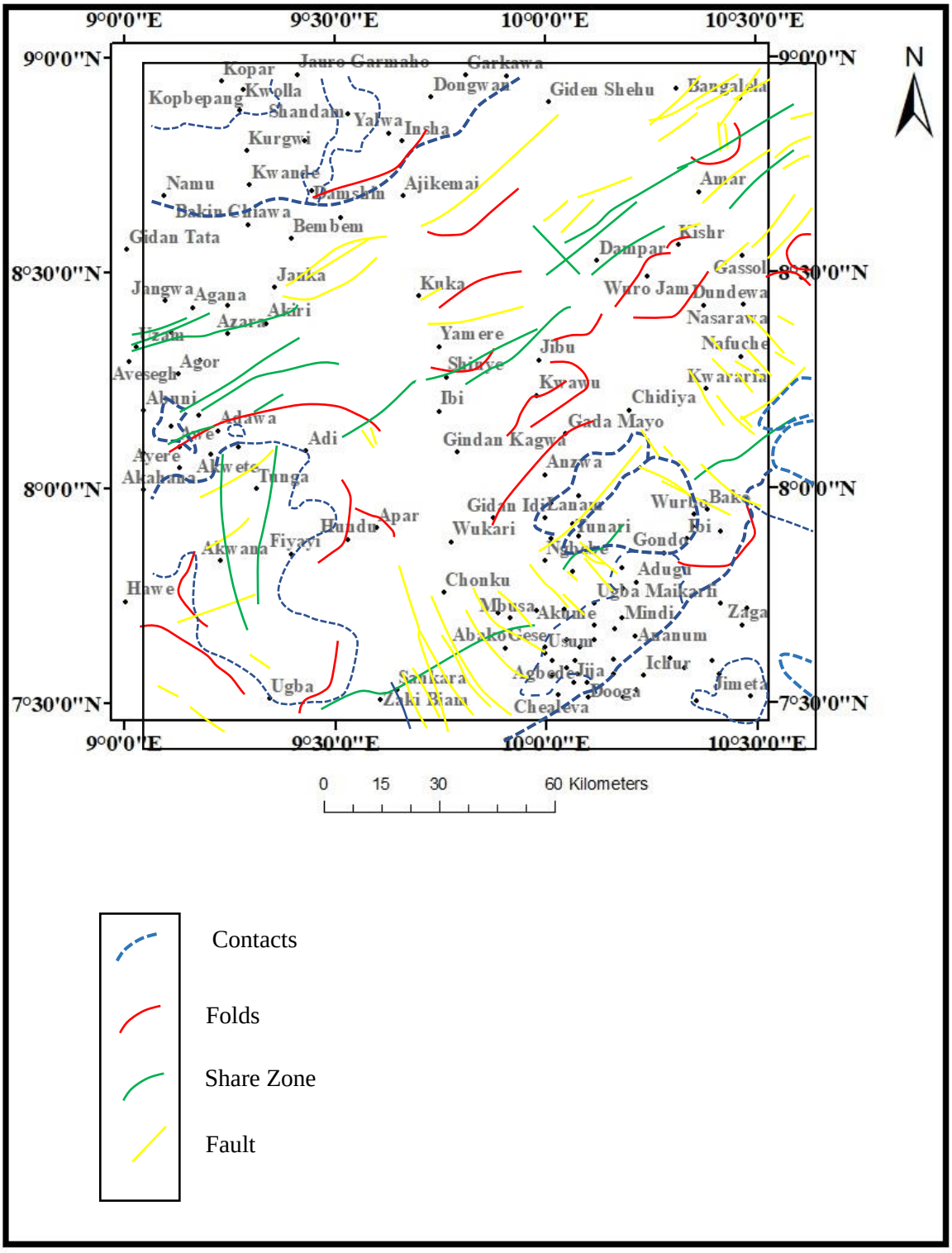

Figure 4.21: Interpreted structural map from the aeromagnetic dataset

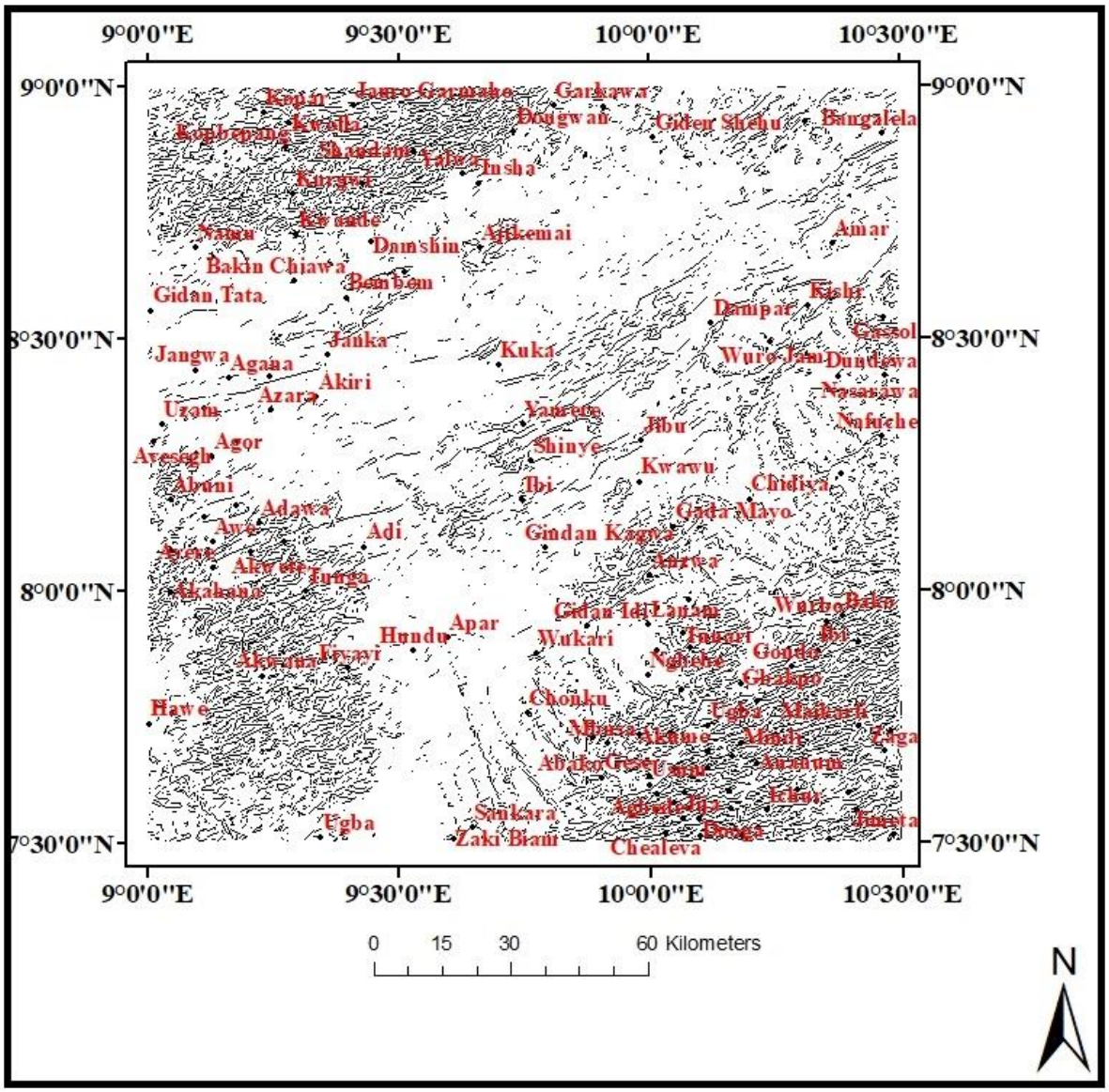

Figure 4.22a: Lineament Map of the Study Area

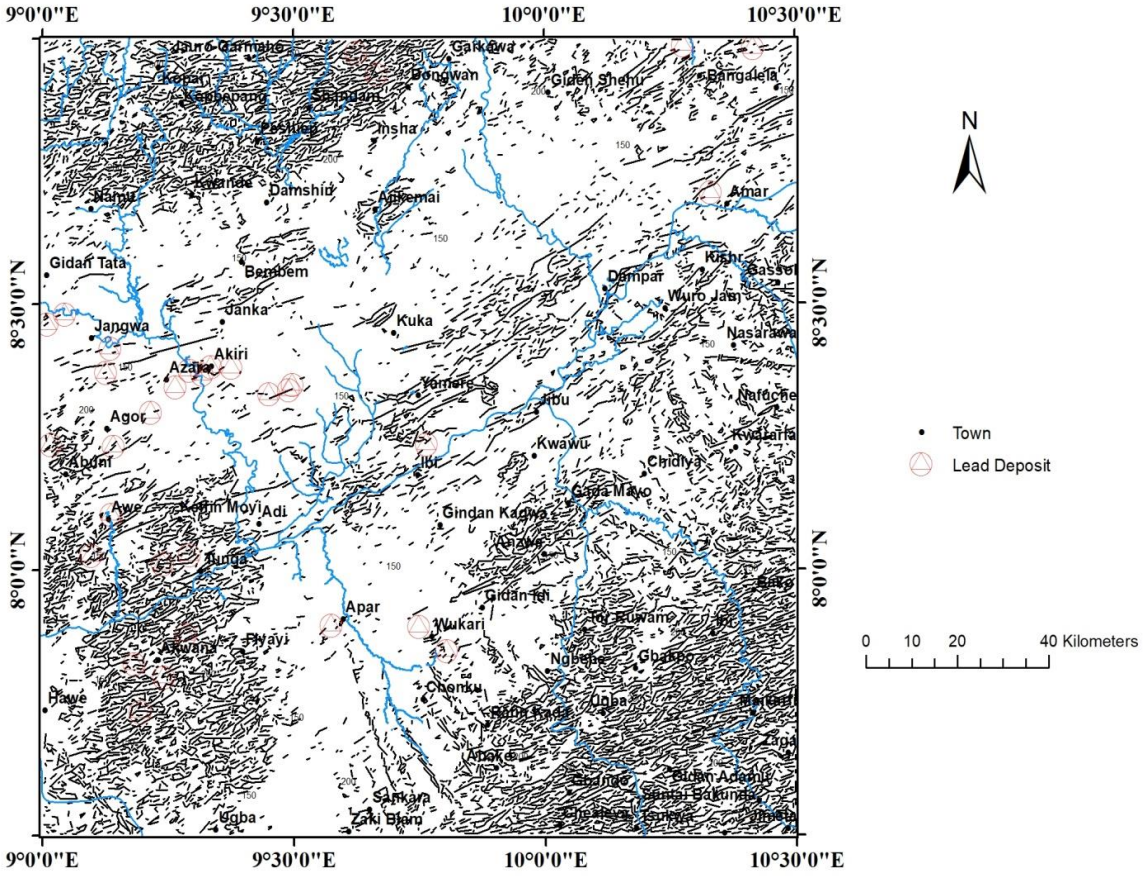

Figure 4.22b: Superimposed Location, Lineament and Mineral Map of the Study Area

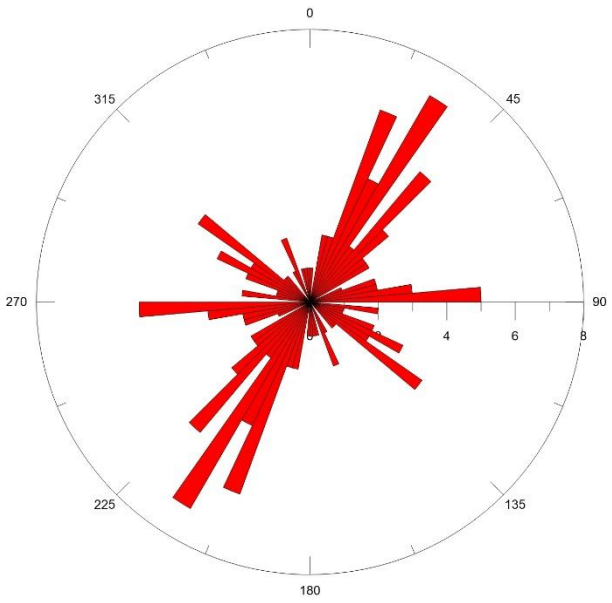

Figure 4.23: Rose Diagram of the Study Area

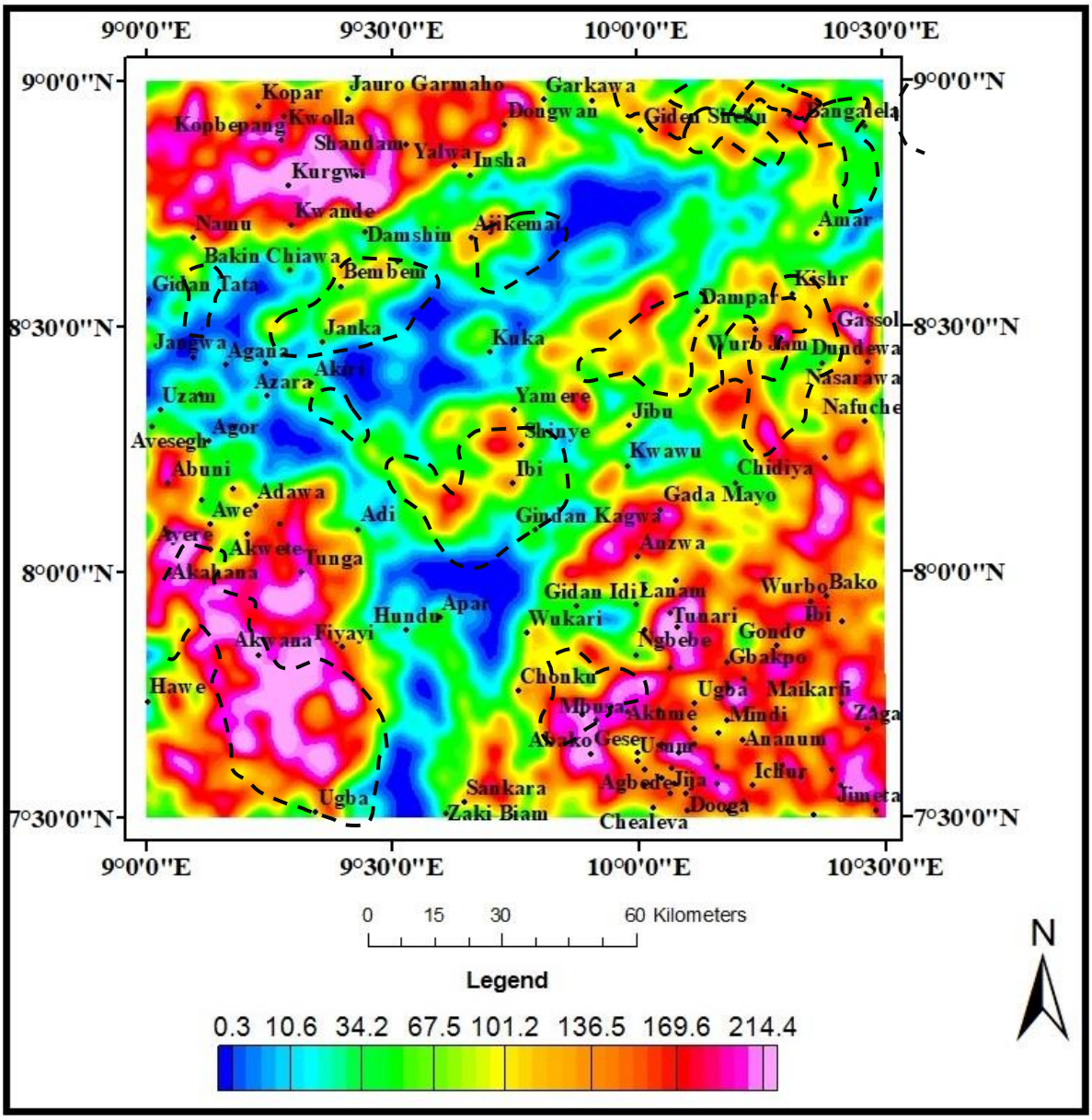

Figure 4.24: Lineament Density Map of the Study Area

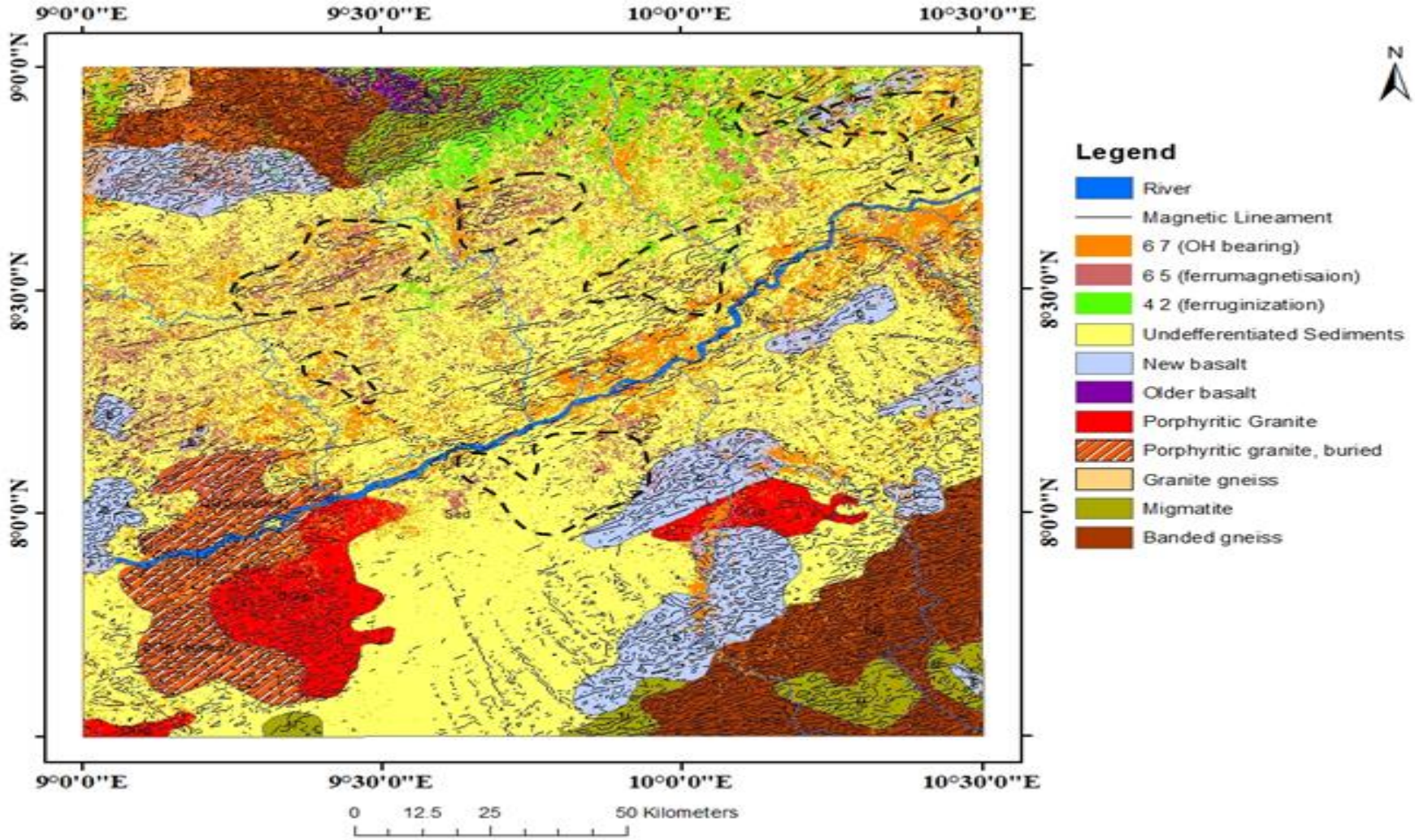

Figure 4.25: Interpreted geologic map from aeromagnetic and Landsat dataset (Adopted after NGSA 2006)

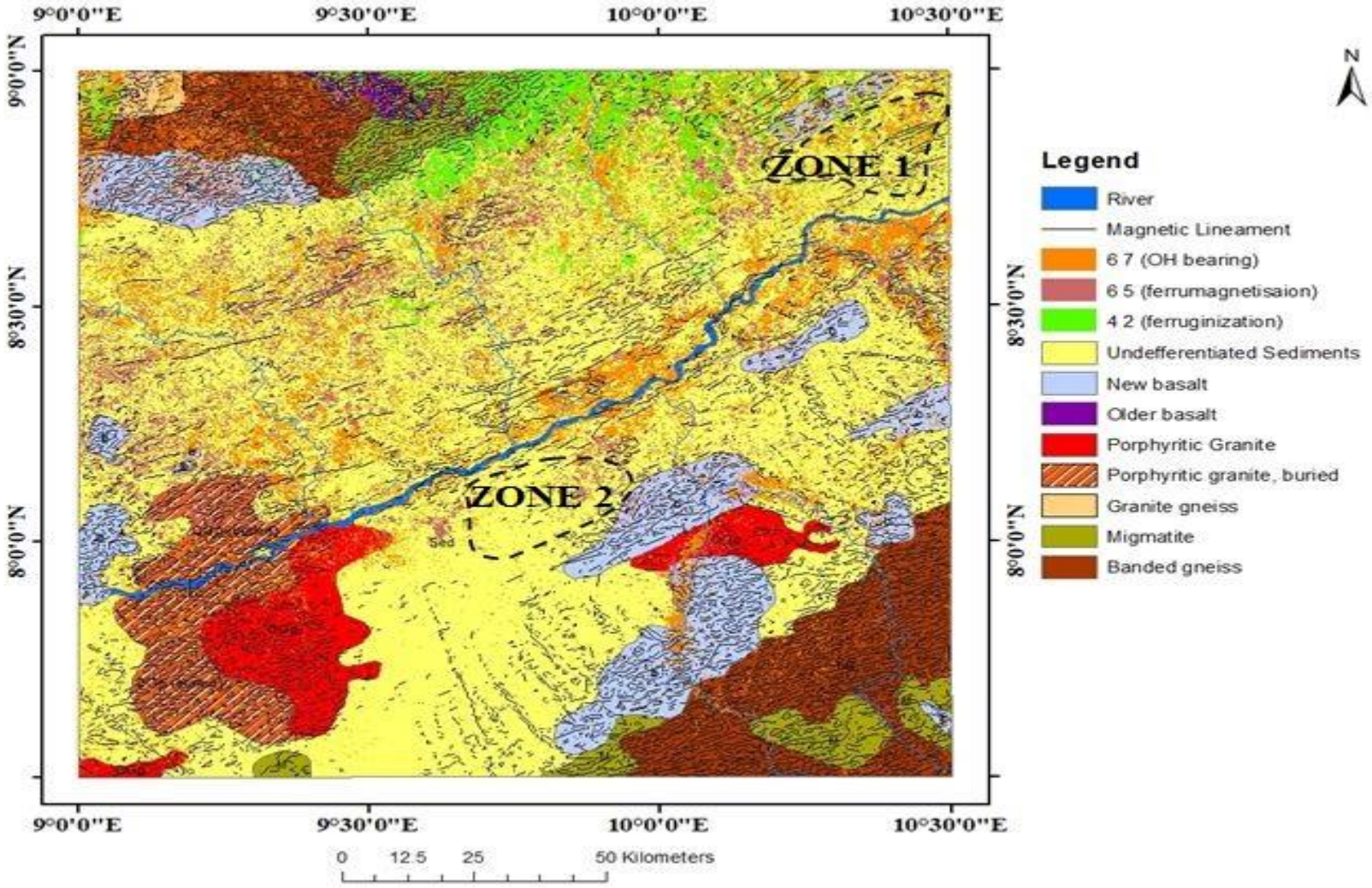

Figure 4.26: Selected Zones of interest for further investigation (Adopted after NGSA 2006)

Based on the interpreted geology, structures and alteration anomalies, two zones (zone 1 and zone 2) were selected for further investigation (Figure 4.26).

The interpreted geological map (Figure 4.25) from aeromagnetic dataset shows the geologic units, structures, deformation intensity, ferrumagnetisation and ferruginization alteration mapped.

4.1.3 Ground Magnetic Survey Results (Zone 1)

i. Technical Specifications of the Surveys

The Total magnetic field measurement was taken at 10m station interval along a profile stretching 3000m in length. The data was acquired in real time by using GPS receivers that were part of the magnetometer consoles at 3m height clearance and 200m profile spacing and the traditional stop and measure mode was used during data acquisition as it provides full sensitivity obtainable with a proton magnetometer (Appendix). The diurnal corrections were done by using a GSM-19 Base Station that recorded values of the total magnetic field every 10 seconds throughout the day. The final database was geo-referenced to the WGS-84, UTM-Zone 32N datum. The area selected for base station was magnetically quiet, hence, free from moving automobiles and is not close or on top of any major outcrop (Appendix ii).

Table 4.2: Magnetic Survey Equipment

MAGNETOMETER	SPECIFICATIONS	GPS POSITIONING
ROVING UNITS	GEM GSM19-W V 7.0 Overhauser Effect Proton procession Sampling Rate: 2.0 s Resolution: 0.01 nT Absolute Accuracy: 0.2 nT Gradient Tolerance:10 000 nT/m Sensor Height: ≈1.8 m	NOVATEL OEMV-1 Compatibility: (CDGPS, SBAS, DGPS, OMNISTAR) L1 –Lband& SBAS signal tracking - X, Y Precision: ≈ 1 m
BASE STATION	GEM GSM19 Overhauser Effect Proton Procession Resolution: 0.1 nT Absolute Accuracy: 0.2 nT Reading Interval: 10 s	NOVATEL OEMV-1 Compatibility: (CDGPS, SBAS, DGPS, OMNISTAR) L1–Lband& SBAS signal tracking - X, Y precision: ≈ 1 m

Table 4.3: Local Projection Parameters

Datum	WGS84
Name	UTM, Zone 32N
Ellipsoid	WGS84
Inverse flattening	298.25722
Type	Transverse Mercator
Central meridian	9.0
Latitude of origin	0^0 N
False Easting	500,000 m
False Northing	0 m
Scale factor	0.9996

ii. Magnetic Data Processing

1. **Total Magnetic Field:** The daily-recorded values of the total magnetic field taken by the roving units were corrected for diurnal drift and then checked for quality control before being merged into the final database. Gridding of the values was based on a nondirectional kriging algorithm, where each grid cell is given a weight and preferential interpolation direction based on a geo statistical analysis of the entire dataset; the objective being to highlight the different strikes and structural trends that are to be found

in the survey area. The grid cell size was set to 20 m and the maximum interpolation distance to 250 m. The results are presented as a colour contour map at a 1/7000 scale.

2. **Total Magnetic Field Reduced to Equator:** The shape of a magnetic anomaly profile is a direct function of the inclination and declination of the ambient magnetic field at any given point on Earth. The reduction to equator is used in order to alleviate the shortcomings of the variation of inclination and declination as one gets farther from the magnetic poles: 90° inclination and zero declination at the magnetic poles as well as 0° inclination and variable declination at the magnetic equator. In order to simplify the interpretation of the magnetic data, the total magnetic field values were reduced to pole, whilst using inclination and declination values of -8.3 °N and -0.9°E respectively for the area. This type of processing is more efficient for N/S striking structures and/or spherical *orebodies*.

3. **Polynomial Tilt Filter:** The purpose of this type of filter is to eliminate the long wavelength signatures and thus facilitate the discrimination of close or even superimposed anomalies. This filter also increases the noise level, which limits the use of higher order derivatives (n=2 for example). The vertical derivative is used to delineate the contacts between large-scale magnetic domains because its value is zero over vertical contacts.

4.1.3.1 Digital Elevation Map

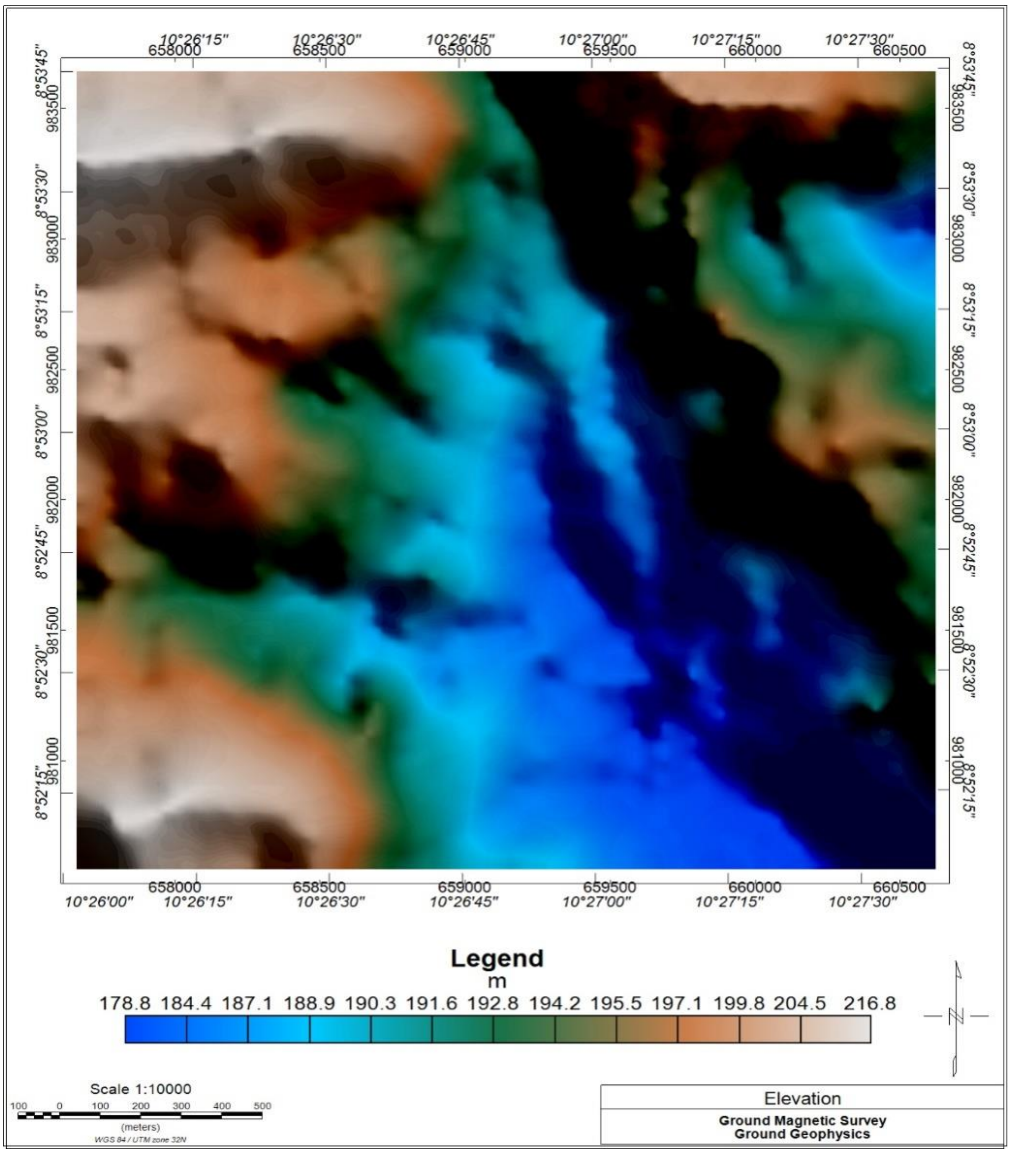

Figure 4.27: 3D surface DEM of study area

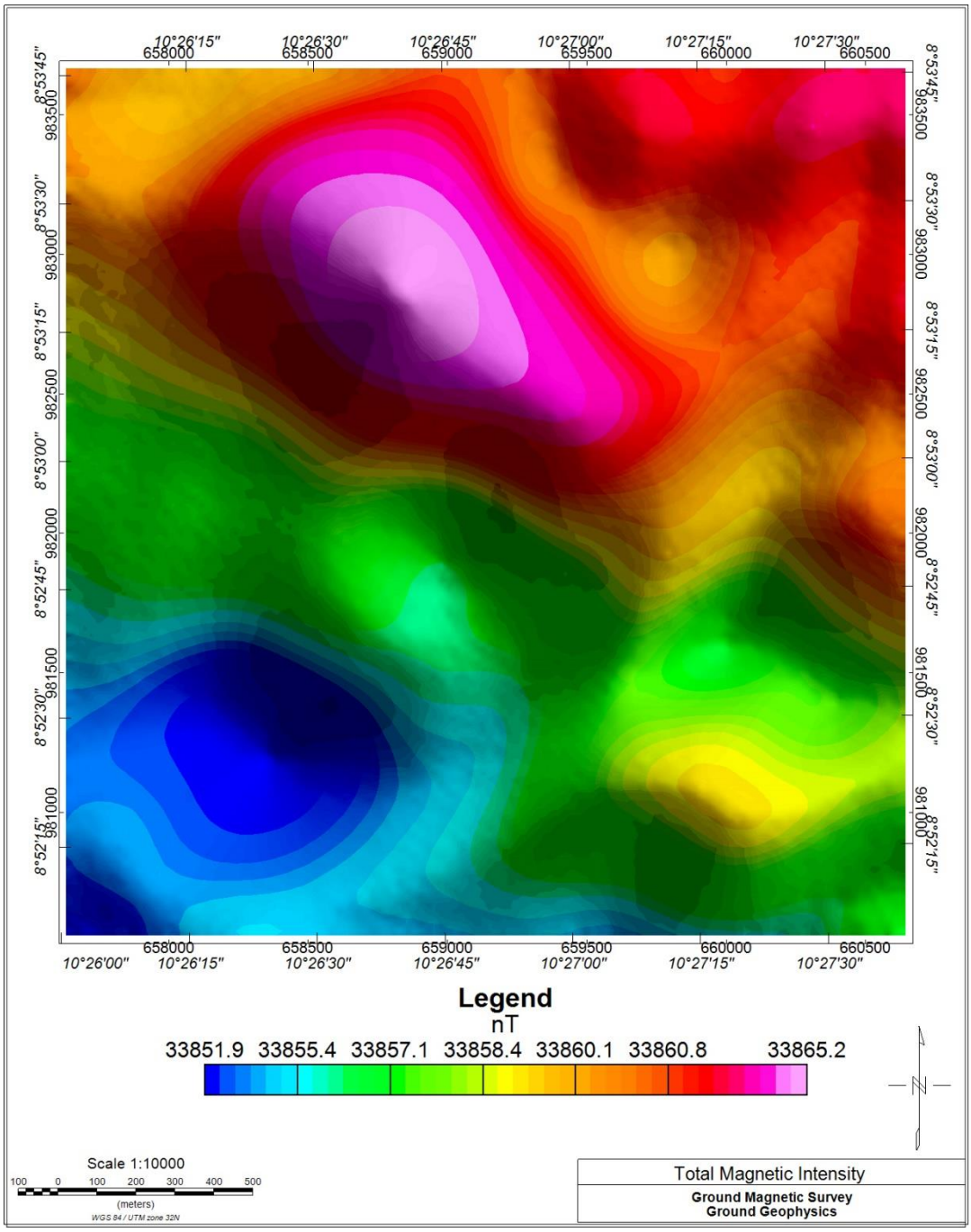

Figure 4.28: Observed Magnetic Intensity Map from ground magnetic survey

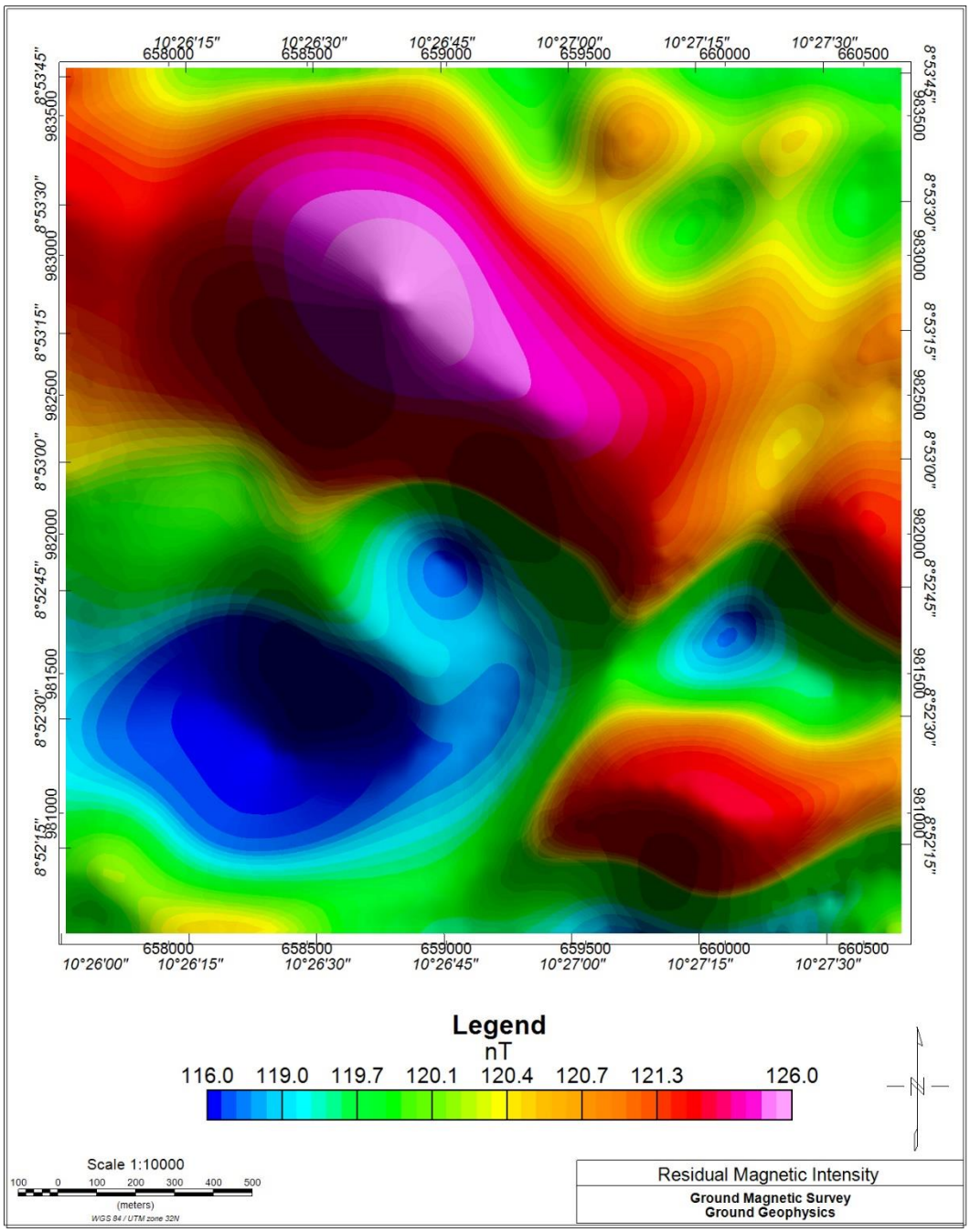

Figure 4.29: Residual Reduced to Equator magnetic intensity map from ground magnetic survey

4.1.3.2 Analytic Signal Map

At low magnetic latitudes like Nigeria where the RTE filter has trouble, the analytic signal filter becomes very useful (Milligan & Gunn, 1997). The analytic signal filter which is independent of the direction of magnetization is used as a type of RTE filter to remove the effect of remanence by maximizing the edges of magnetized bodies (MacLeod *et al.*, 1993).

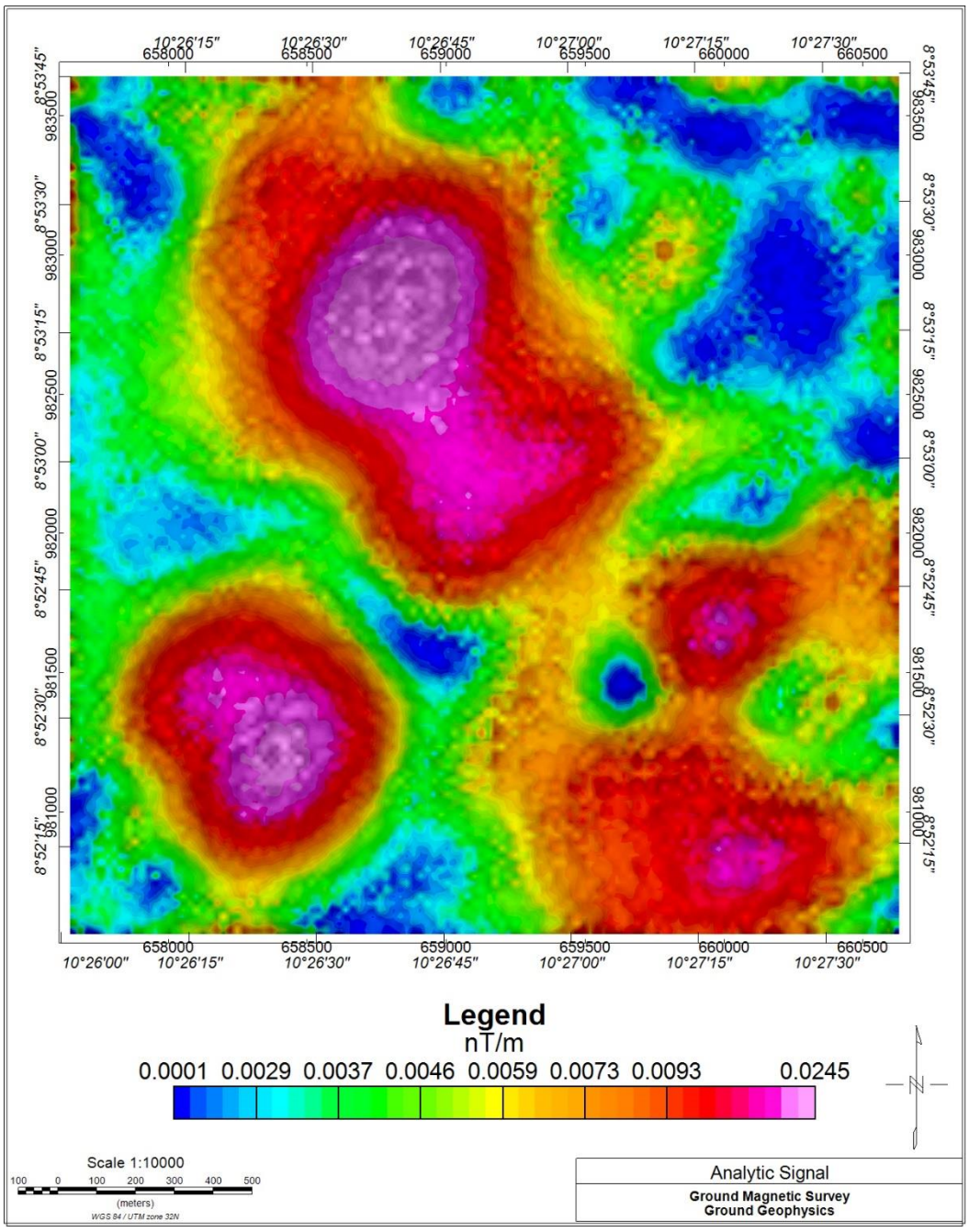

Figure 4.30: Analytic Signal map from ground magnetic survey

4.1.3.3 First Vertical Derivative Map

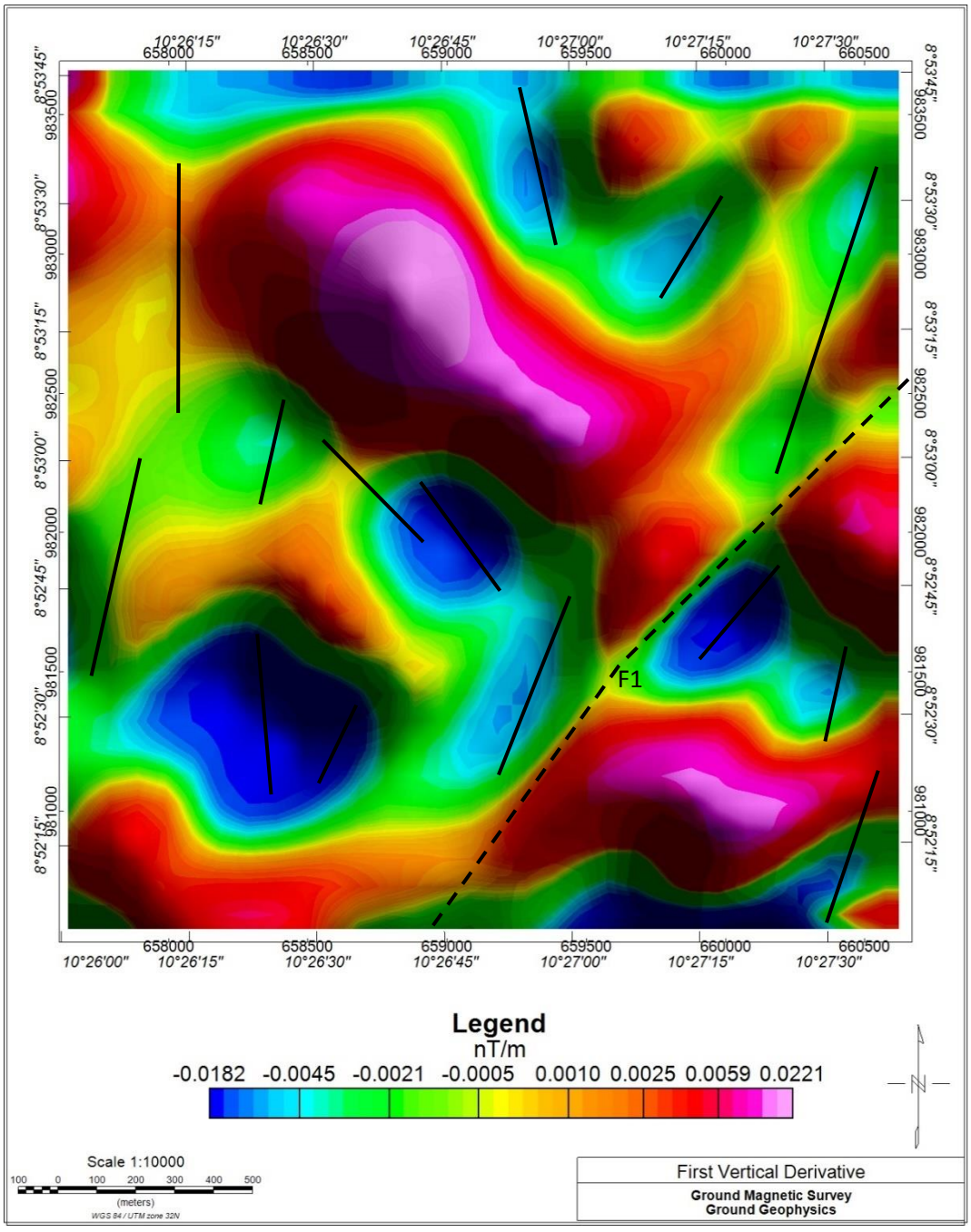

Figure 4.31: First Vertical Derivative map in greyscale

4.1.3.4 Apparent Susceptibility Analysis

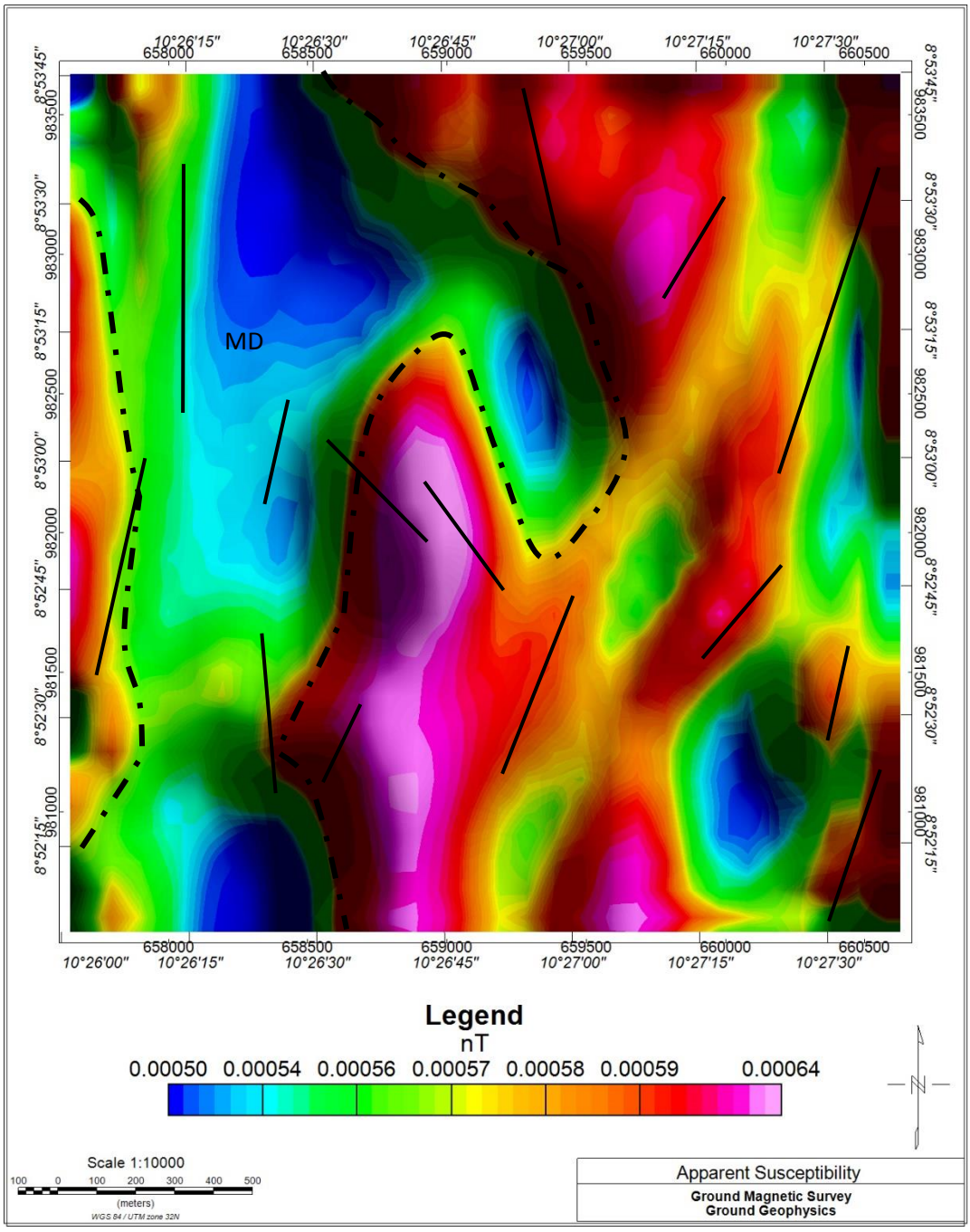

Figure 4.32: Apparent Susceptibility map

Figure 4.33: Faulted Shale (UTM zone 32: Lat 982403, Long 658025)

4.1.4 Ground Electromagnetic Very-Low Frequency (EM-VLF) Results

In carrying out the EM survey, we used the VLF method. Reading was taken in every 10 metres along the profile of 3km width and covered a total of 300 stations (Appendix ii). The instrument measures this field strength and phase displacement around a fracture zone or any conductive body in the rocks (Telford *et al*., 1990). It detects the ratio (in percent) between the vertical and the horizontal components. The VLF transmitter HWU located in La Blanc, France, operating at a frequency of 18.3 kHz with co-ordinates 46N37-001E05 was selected as the source for the entire VLF survey because it

provided a field which is approximately perpendicular to the direction of the strike of the envisaged geological structure beneath the ground surface.

1. VLF-EM Data Processing

VLF data collected using GEM systems GSM-19W Overhauser and processed using the Geosoft Oasis Montaj and KHFFILT software. Results were interpreted and compared to the interpreted magnetic structures data for mapping of conductive faults.

i. Raw Data Profiles

The raw data for each frequency was plotted for each line surveyed. No filtering or smoothing of the raw data was done.

ii. Fraser Filter Profile

Raw data was run through the Fraser filter. This filter transforms In-Phase cross overs and inflections into positive peak anomalies (Fraser, 1969). In-Phase inflections and cross overs usually plus to minus, while Quadrature responses are negative to positive giving a negative peak anomaly when the Fraser Filter is applied. VLF anomalies were selected based on their location and other pertinent information from the Fraser Filter profile.

iii. K-H Profiles

Raw Data was run through the Karous-Hjelt (K-H) filter. The filter is applied to obtain a section of current density. The higher values are generally associated with conductive structures (Karous, Hjelt 1983). Conductive zones are red/yellow while resistive zones are blue, this is shown on the Karous-Hjelt model profile as red. A depth scale is found on the left side of the model profiles.

Generally, VLF analysis is on the bases that the higher the in-phase values of the anomaly, the greater the conductivity of the underlying structures in relation to the surrounding rock. Some of the anomaly peaks are sharp and of high intensity while others are broad and of lower intensity. Suspected mineralized veins, were delineated on the gridded survey area using characteristic coincidence of positive inflections on filtered in-phase anomaly and were further interpreted on current density maps (Becken & Pedersen, 2003). With poor conductivity of the host geologic formation of the area, it is therefore logical to interpret the VLF-EM anomalies caused by the mineralized veins.

4.1.4.1 Profile Line 1

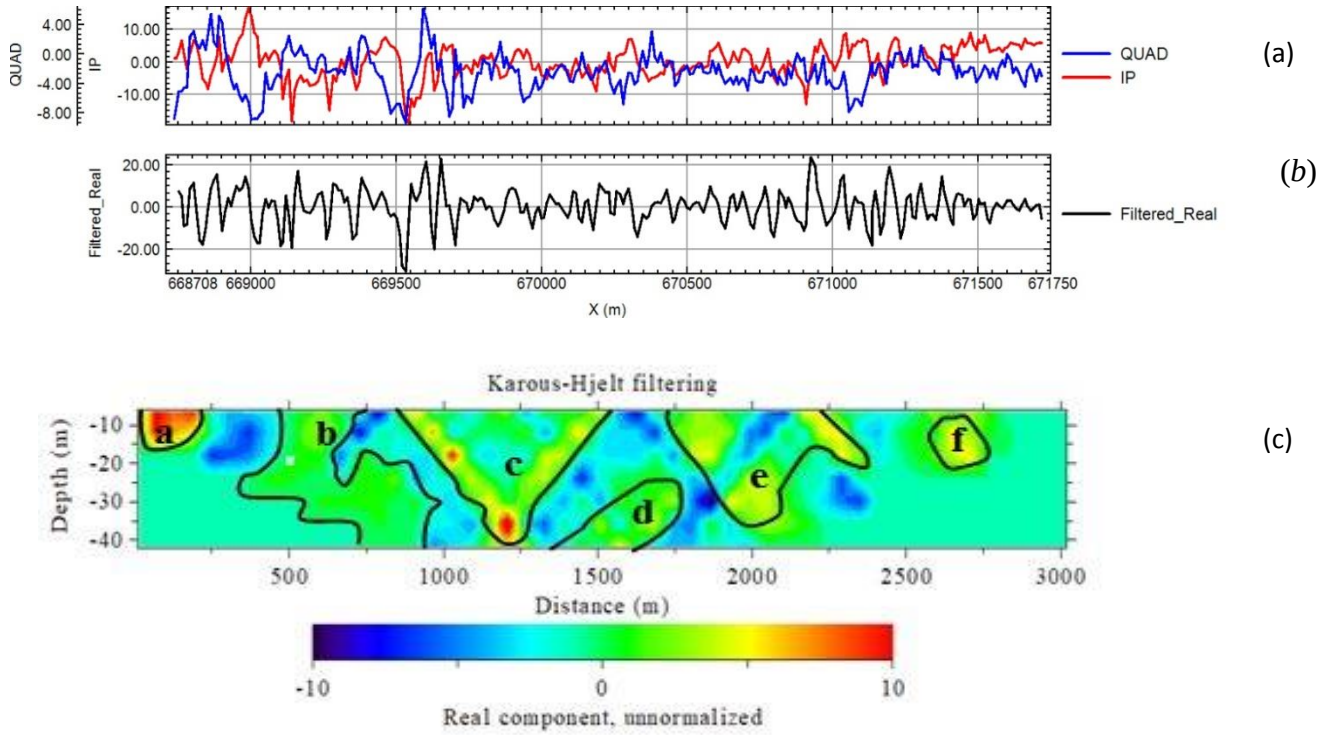

Figure 4.34: VLF of Profile 1 (*a*) Raw in-phase and quadrature plot (*b*) Frasier filter plot (*c*) Karous-Hjelt filter model section

4.1.4.2 Profile Line 2

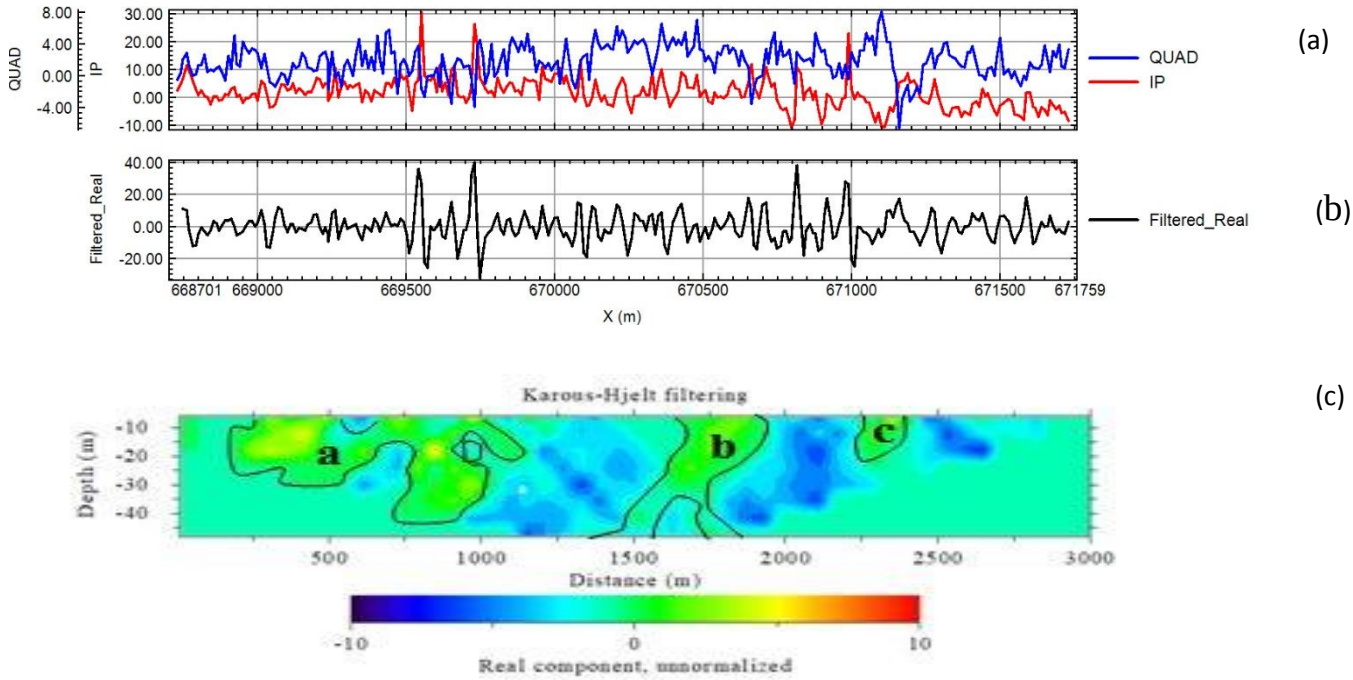

Figure 4.35: Interpreted VLF of Profile 2 (*a*) Raw in-phase and quadrature plot (*b*) Frasier filter plot (*c*) Karous-Hjelt filter model section

4.1.4.3 Profile Line 3

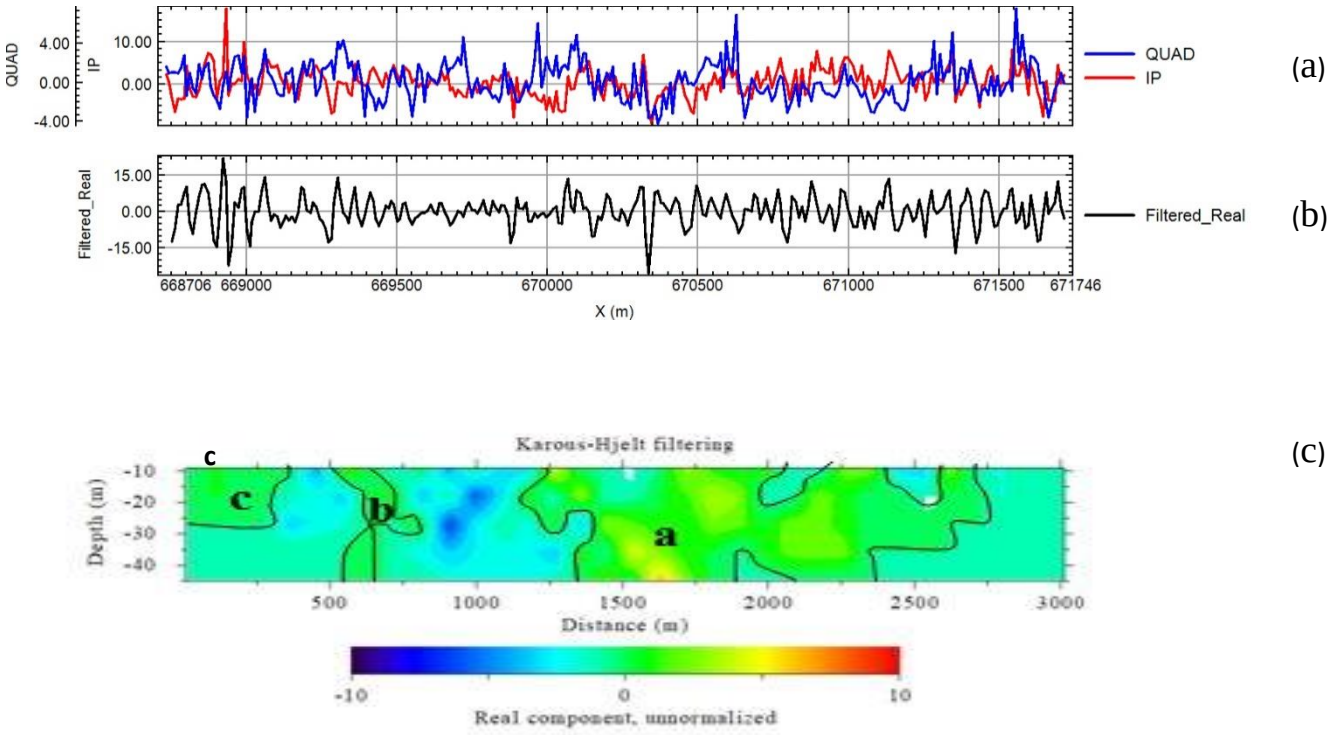

Figure 4.36: VLF of Profile 3 (*a*) Raw in-phase and quadrature plot (*b*) Frasier filter plot (*c*) Karous-Hjelt filter model section

4.1.4.4 Profile Line 4

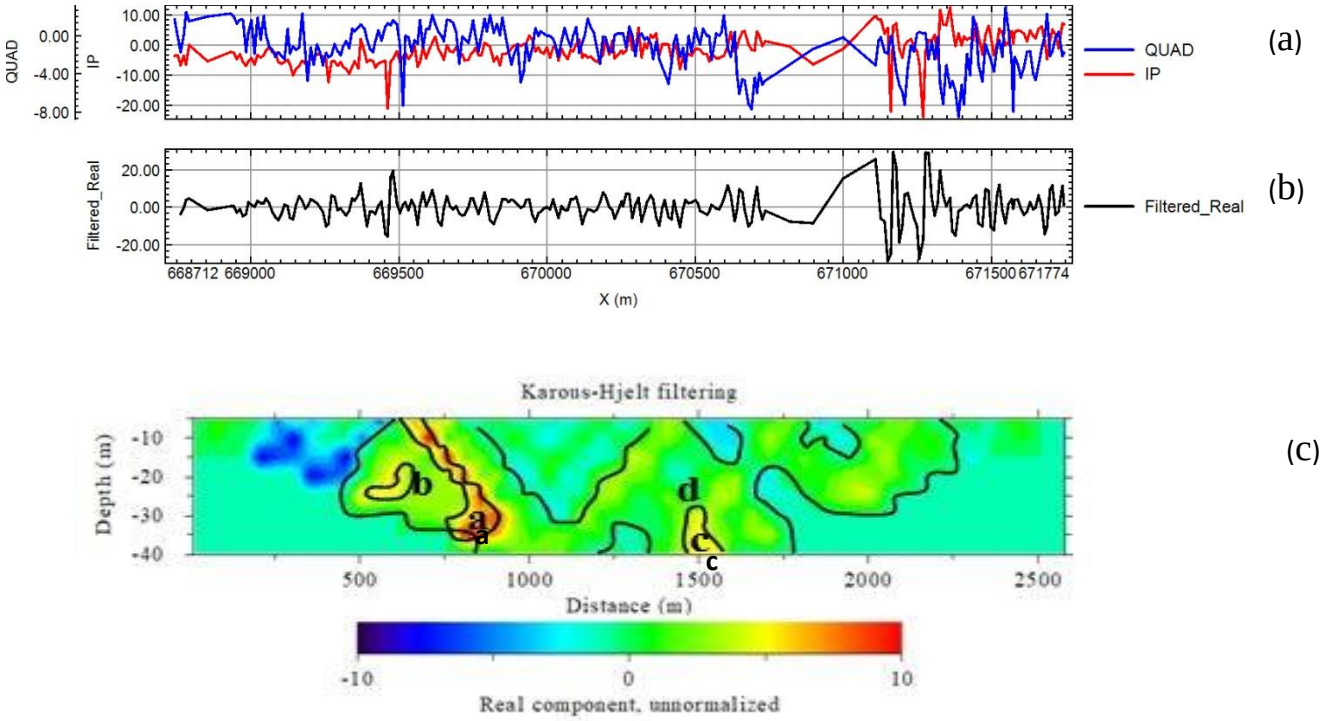

Figure 4.37: VLF of Profile 4 (*a*) Raw in-phase and quadrature plot (*b*) Frasier filter plot (*c*) Karous-Hjelt filter model section

4.1.4.5 Profile Line 5

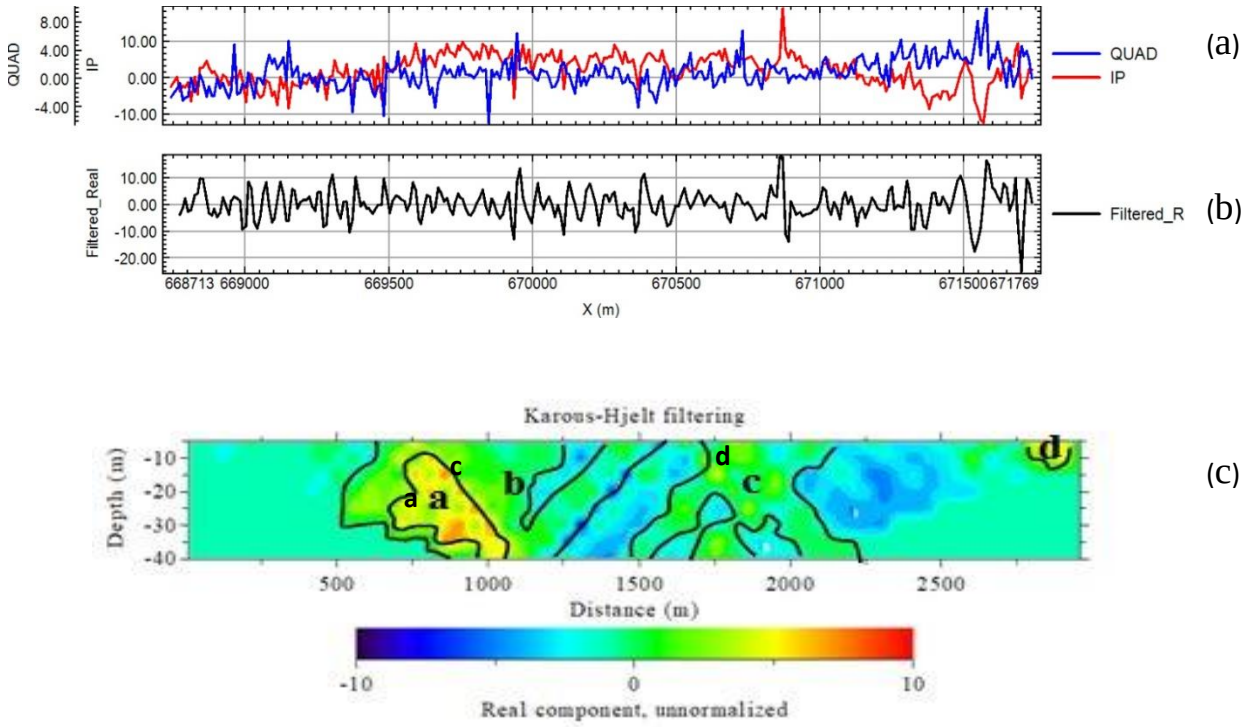

Figure 4.38: Interpreted VLF of Profile 5 (*a*) Raw in-phase and quadrature plot (*b*) Frasier filter plot (*c*) Karous-Hjelt filter model section

4.1.4.6 Profile Line 6

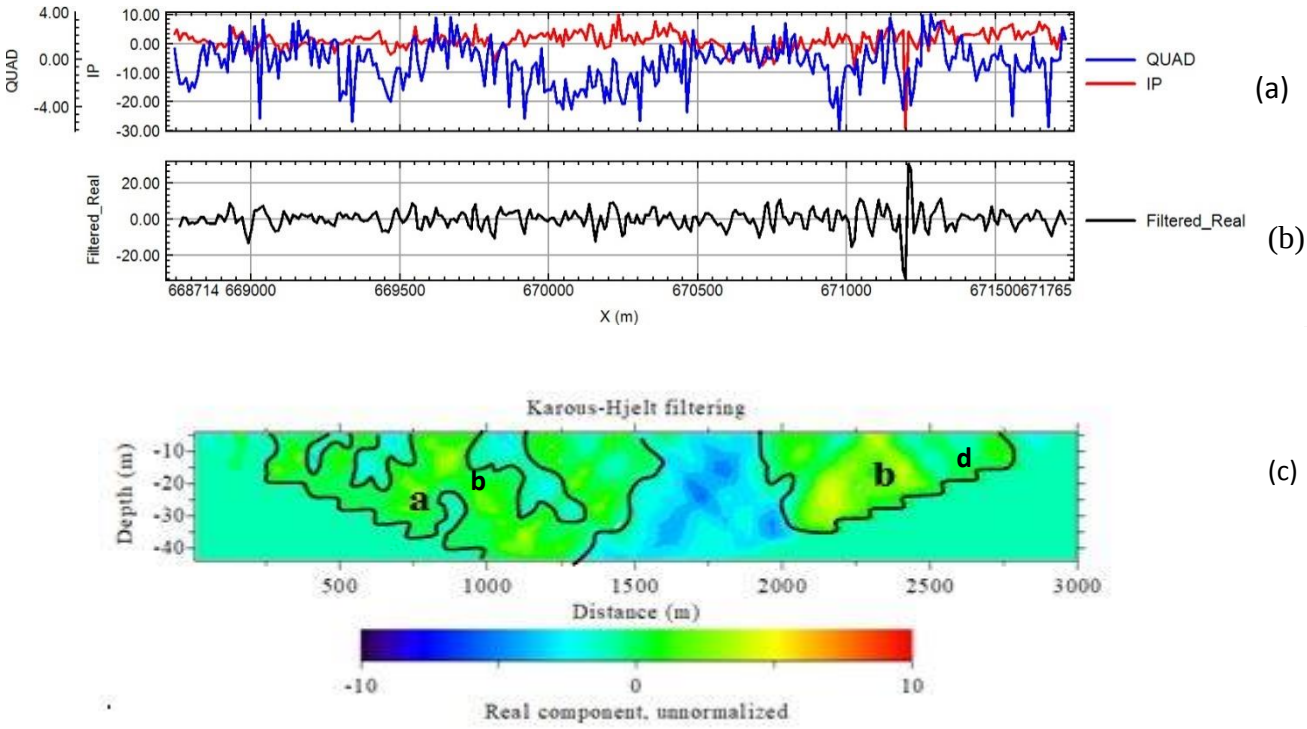

Figure 4.39: VLF of Profile 6 (*a*) Raw in-phase and quadrature plot (*b*) Frasier filter plot (*c*) Karous-Hjelt filter model section

4.1.4.7 Profile Line 7

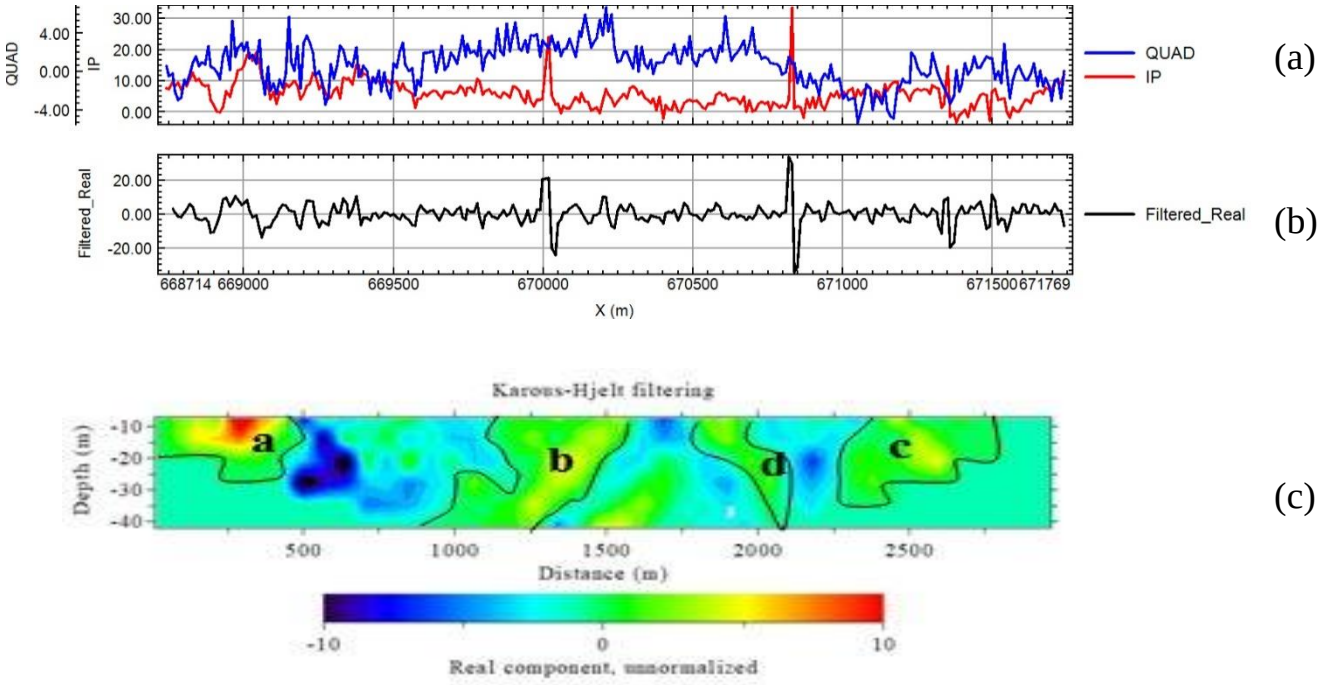

Figure 4.40: VLF of Profile 7 (*a*) Raw in-phase and quadrature plot (*b*) Frasier filter plot (*c*) Karous-Hjelt filter model section

Plate 4.0: faulted shale observed between station 0 and 1000 (Coordinate UTM zone 32N: 669459.7, 1024716.5)

4.1.4.8 Profile Line 8

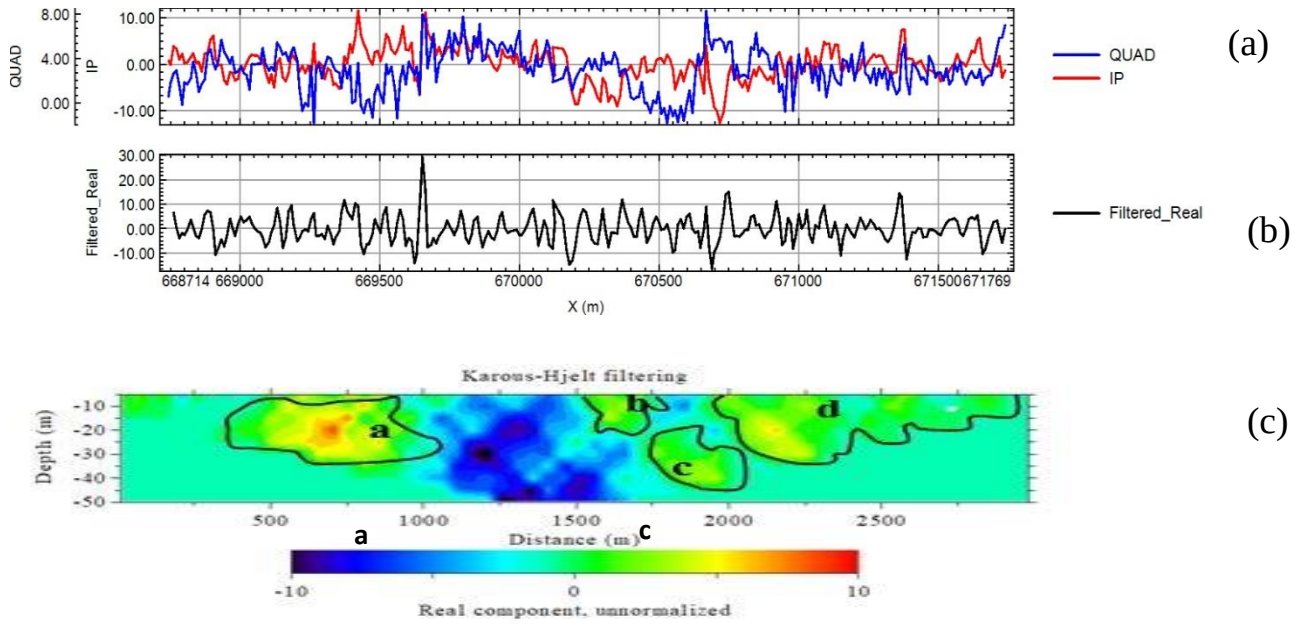

Figure 4.41: Interpreted VLF of Profile 8 (*a*) Raw in-phase and quadrature plot (*b*) Frasier filter plot (*c*) Karous-Hjelt filter model section

4.1.4.9 Result of Frasier Filter 2D Map

To determine the behavior of the overall conductivity variation of the survey area at depths horizontally, a stacked map of the Frasier filter of each profile. The computed Frasier filter values was computed using the Geosoft Oasis Montaj channel math tool and the parameters used to calculate the Frasier result is the in-phase dataset. The computed Frasier filter result of current density (conductivity) was used to create 2-dimentional maps. Gridding of the Frasier filter values was based on the non-directional kriging algorithm. The grid cell was set to 80m and the maximum interpolation distance to 400 m. The results are presented as colour contours maps at a 1/10000 scale.

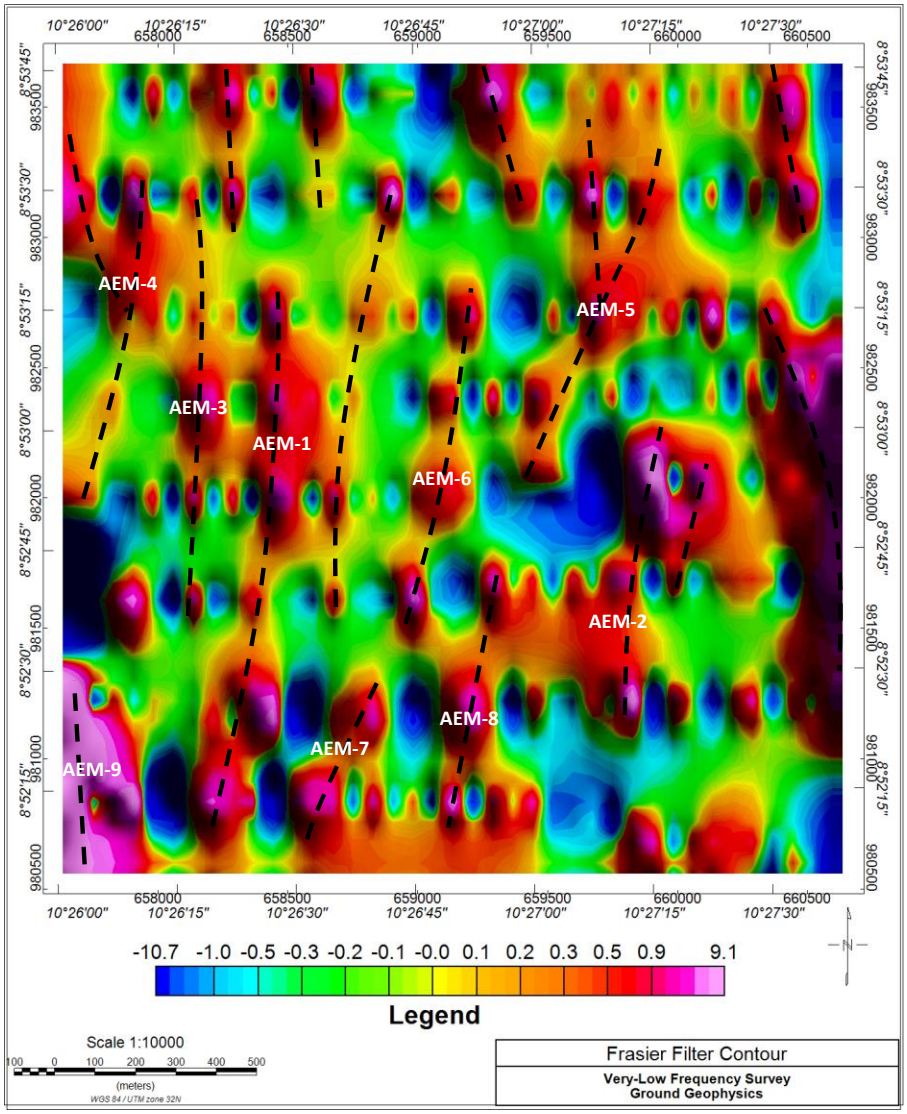

Figure 4.42: 2-Dimentional Frasier Filter Map of the study area.

Based on the interpretation of the VLF-EM survey, a sub-block of the ground magnetic and VLF-EM survey block was selected for ground resistivity and IP survey (Figure 4.43).The choice was made based on the interpreted magnetic structures and conductive structures interpreted from the ground survey. AEM-1 and AEM-3 was both the target of the electrical resistivity and induced polarization survey because they both recorded high anomaly when Frasier and Karous-Hjelt filter, especially between profile-line 4 and 5.

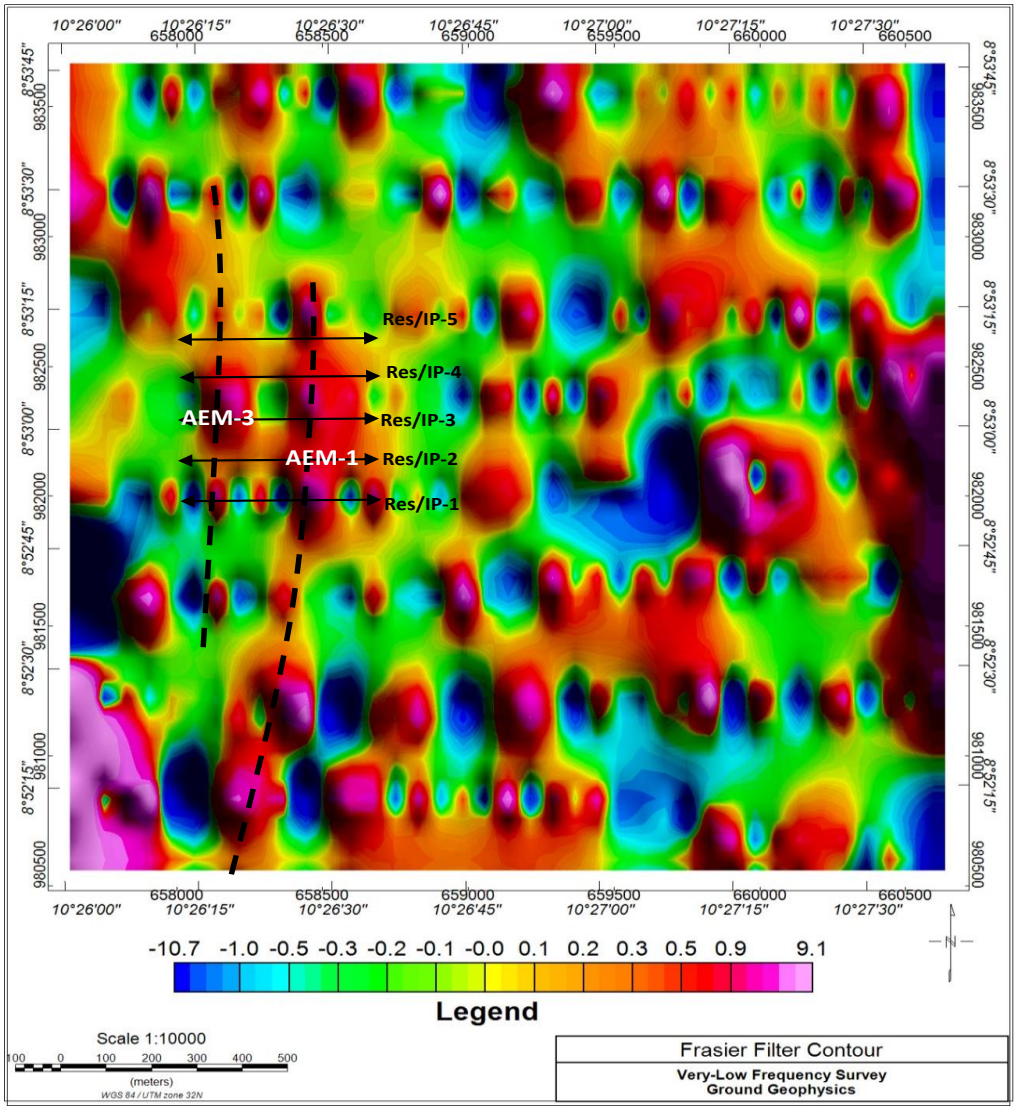

Figure 4.43: 2-Dimentional Frasier Filter Map of the study area showing selected Electrical Survey Sub-Block

4.1.5 Ground Electrical Geophysical Results (Zone 1)

The electrical resistivity method investigates subsurface conditions by passing an electric current (I) into the ground through a pair of electrodes called current electrodes while the resulting potential difference (Δv) arising from the current flow is measured through a pair of electrode called potential electrodes which may or may not be located within the current electrode pair. The ground resistivity value is obtained from parameter I, Δv and the geometric factors of the electrode array used. In this study, lateral profiling using dipole - dipole arrays were adopted (Appendix iii and iv).

Direct current (DC) resistivity and chargeability method was used in carrying out the lateral profiling in the study area in order to investigate the electrical properties of the subsurface using Abem SAS1000 resistivity meter.

1. **Resistivity/IP Data Processing**

On a daily basis, the data quality was checked and related information saved in separate database for each of the survey lines in Microsoft excel format. In order to help with the quality control as well as the flagging of erroneous data, most of the readings were in fact repeated 3 times in the field. Part of the information contained in these databases was subsequently exported to RES2DINV (Software developed by M.H. Loke) compatible file formats in order to carry out the inversions. The 2D models used by the inversion process, consists of a number of blocks having their distribution and size automatically generated by the program using the distribution of the points in the pseudo sections, which is a function of the electrode array. The depth of the bottom row of blocks is set to be approximately equal to equivalent depth of investigation (Edwards, 1977). During the initial loading of the files, a correction is applied on the RES/IP data for surface topography effects.

2. Resistivity/IP Data Interpretation

The results of the Res/IP measurements taken along each of the (5) IP-lines that were surveyed were initially shown as interpreted colour pseudo-sections. On each of these pseudo-sections, a 2D inversion model illustrating the apparent resistivity and chargeability values with the surface topography and vertical depth in meters is shown.

The inversion values of resistivity/chargeability extracted at 12, 18, 24 and 39 meters of vertical depth were used to create 2-dimentional maps. Gridding of the IP-RES values was based on the non-directional kriging algorithm. The grid cell was set to 12.5 m and the maximum interpolation distance to 250 m. The results are presented as colour contours maps at a 1/7000 scale.

Based on the available information, the signature of the lead bearing structures will be a function of their percentage content of certain accessory minerals such as pyrite, zinc, lead and copper. Otherwise the percentage contents of other minerals such as quartz, pyrrhotite, chalcopyrite or magnetite if presents, will also help in the indirect delineation of the mineralized structures, layers or bodies. The percentage content of sulphides, thickness as well as lateral and depth extent of the mineralized structures will ultimately determine the strength of the anomaly. Based on the fact that the mineralization's will be found in altered and associated silicified rocks, the chargeability anomalies indicative of these mineralization's should also be associated with moderate to high resistivity.

4.1.5.1 Res/IP Line-1

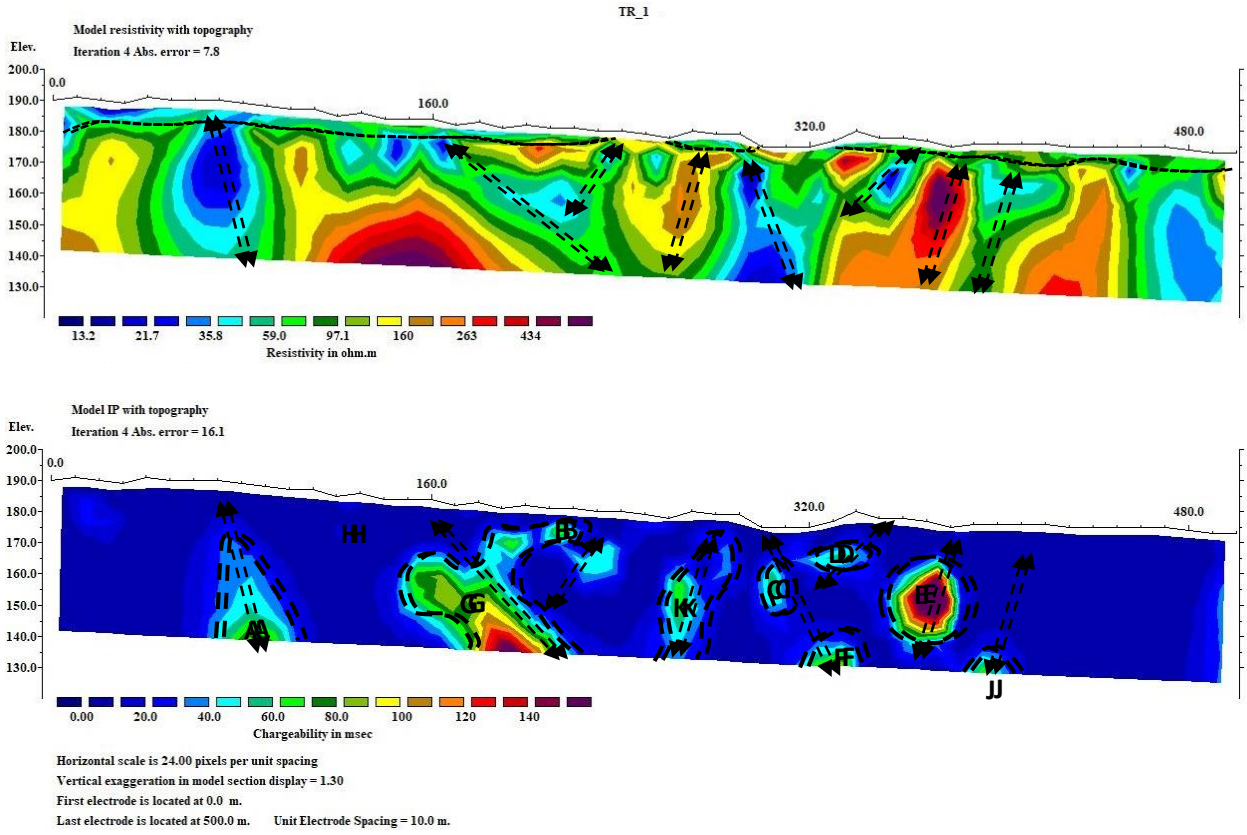

Figure 4.44: Electrical resistivity and chargeability model of Res/IP Line-1

4.1.5.2 Res/IP Line-2

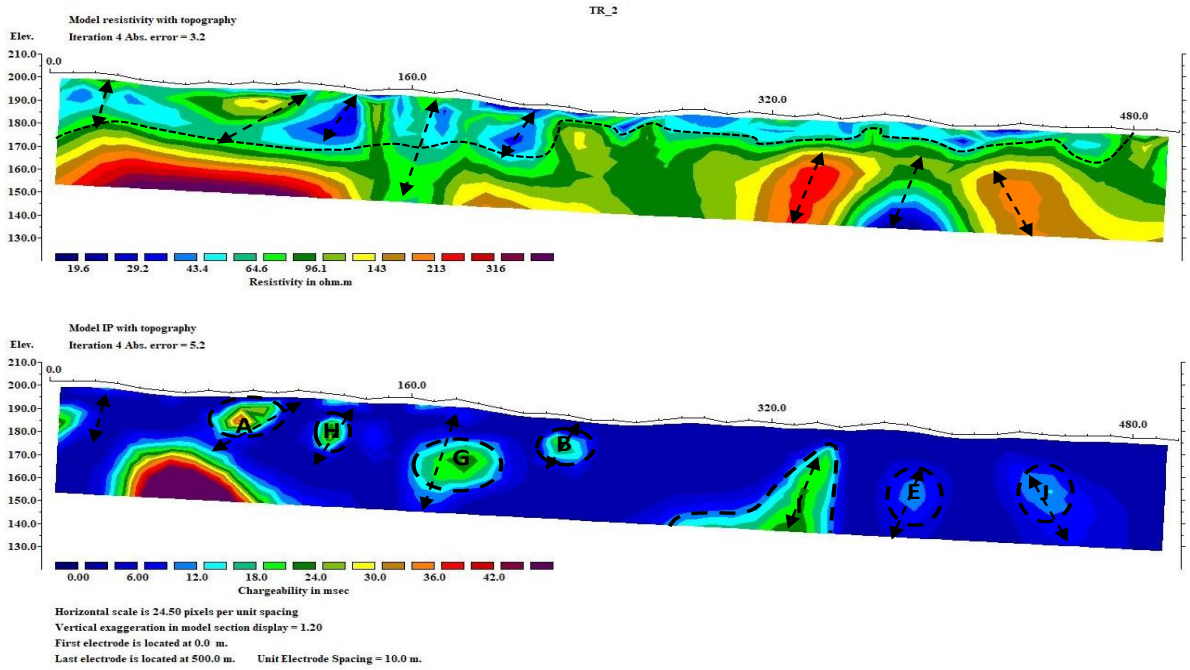

Figure 4.45: Electrical resistivity and chargeability model of Res/IP Line-2

4.1.5.3 Res/IP Line- 3

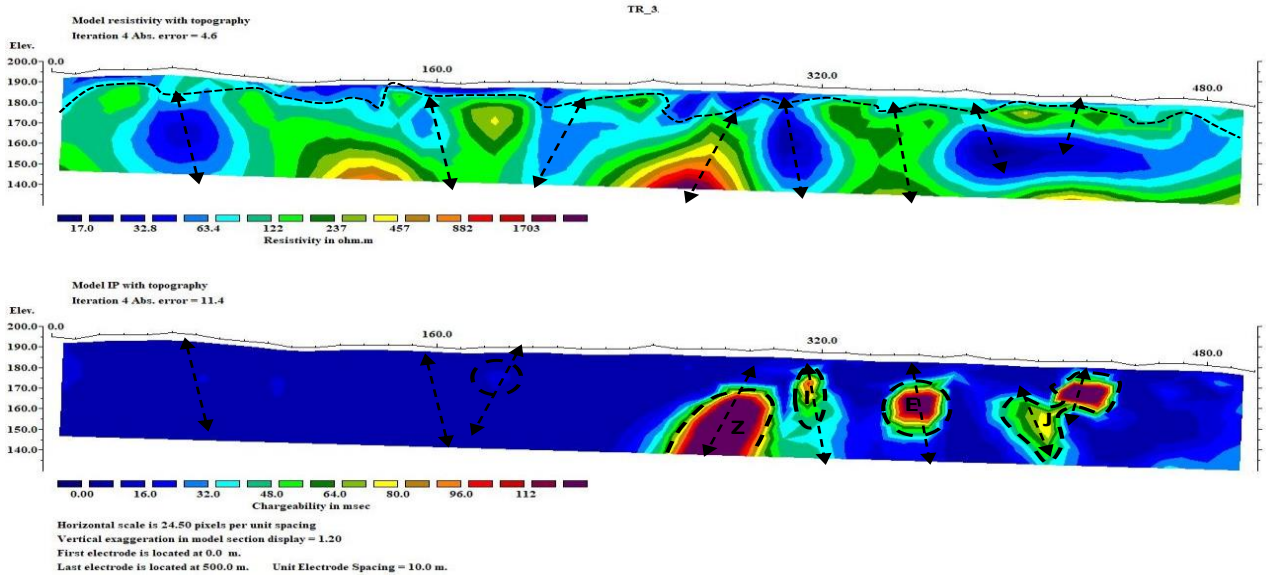

Figure 4.46: Electrical resistivity and chargeability model of Res/IP Line-3

4.1.5.4 Res/IP Line-4

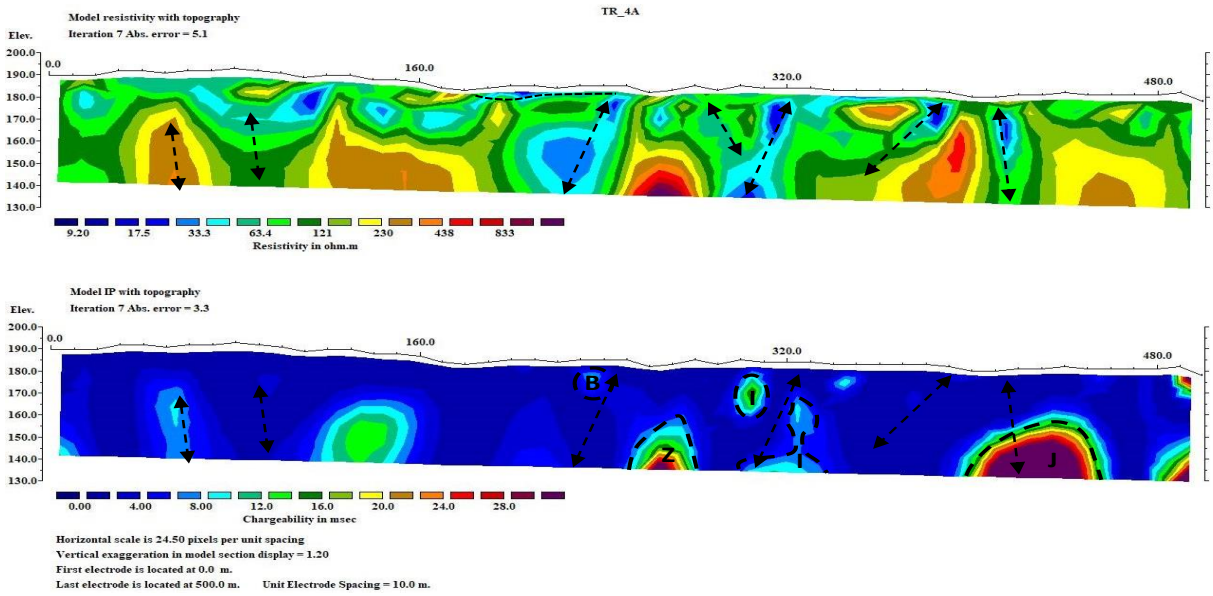

Figure 4.47: Electrical resistivity and chargeability model of Res/IP Line-4

4.1.5.5 Res/IP Line-5

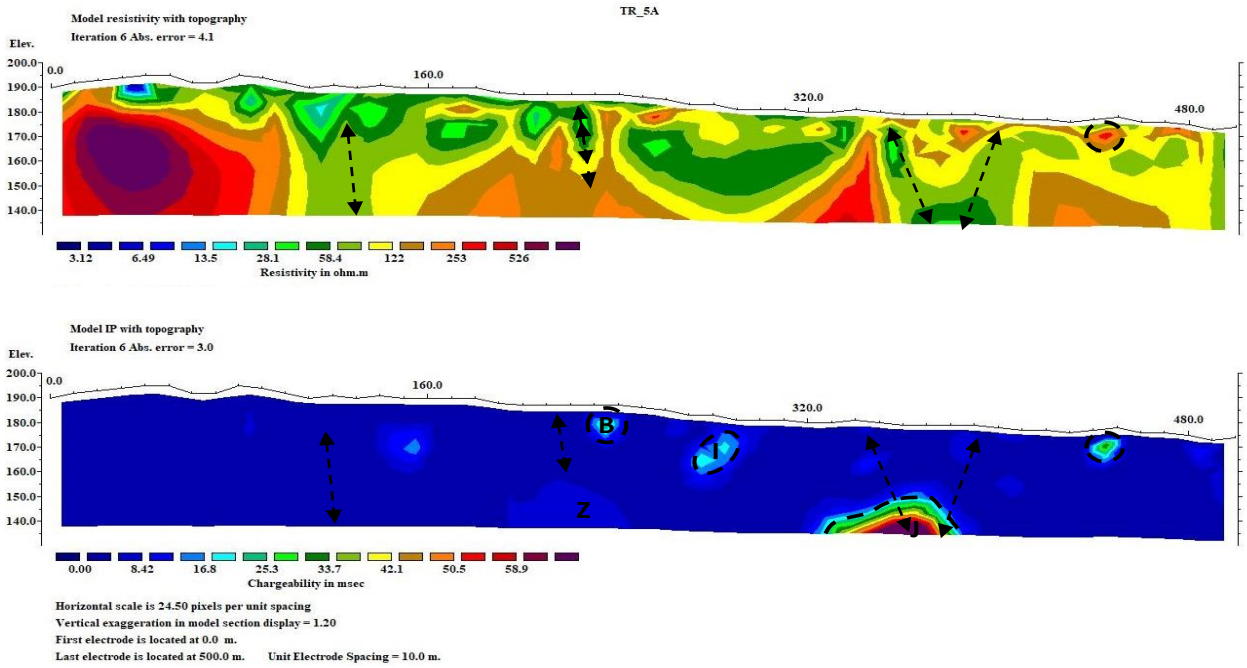

Figure 4.48: Electrical resistivity and chargeability model of Res/IP Line-5

4.1.5.6 Stacked Maps of Resistivity Imaging

To determine the behavior of the overall resistivity variation of the survey area at different depths as well as horizontally, a stacked map of the resistivity imaging sections is prepared at different depths (12m, 18m, 24m, 39m and 48m). The resistivity values and the depths are determined from the inversion process in Res2Dinv software and exported to Oasis Montaj for gridding and map production. Therefore, the parameters used to obtain these stacked plots are the inverted resistivity and chargeability depths.

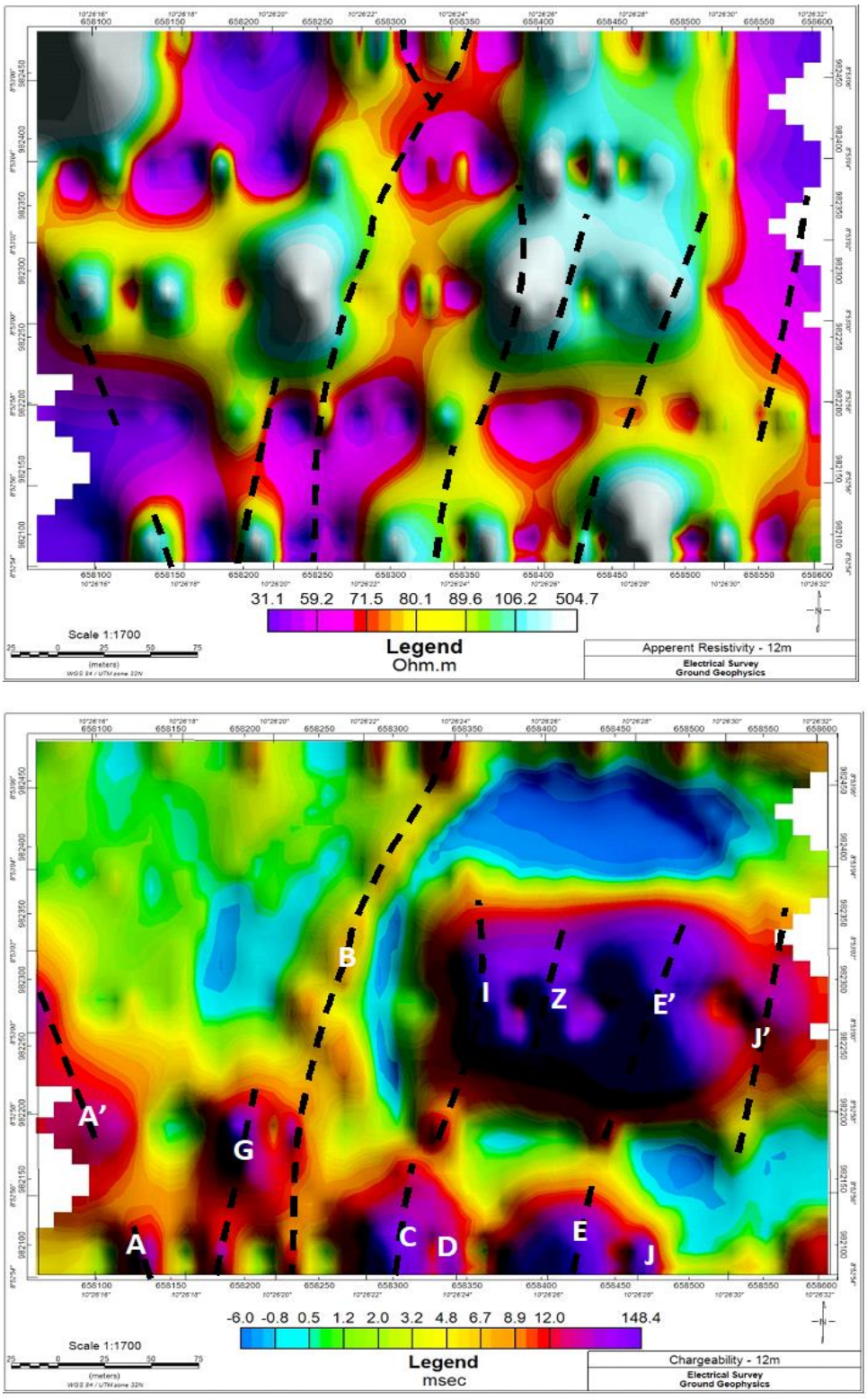

Figure 4.49: Chargeability variation and Resistivity variation at depth of 12m

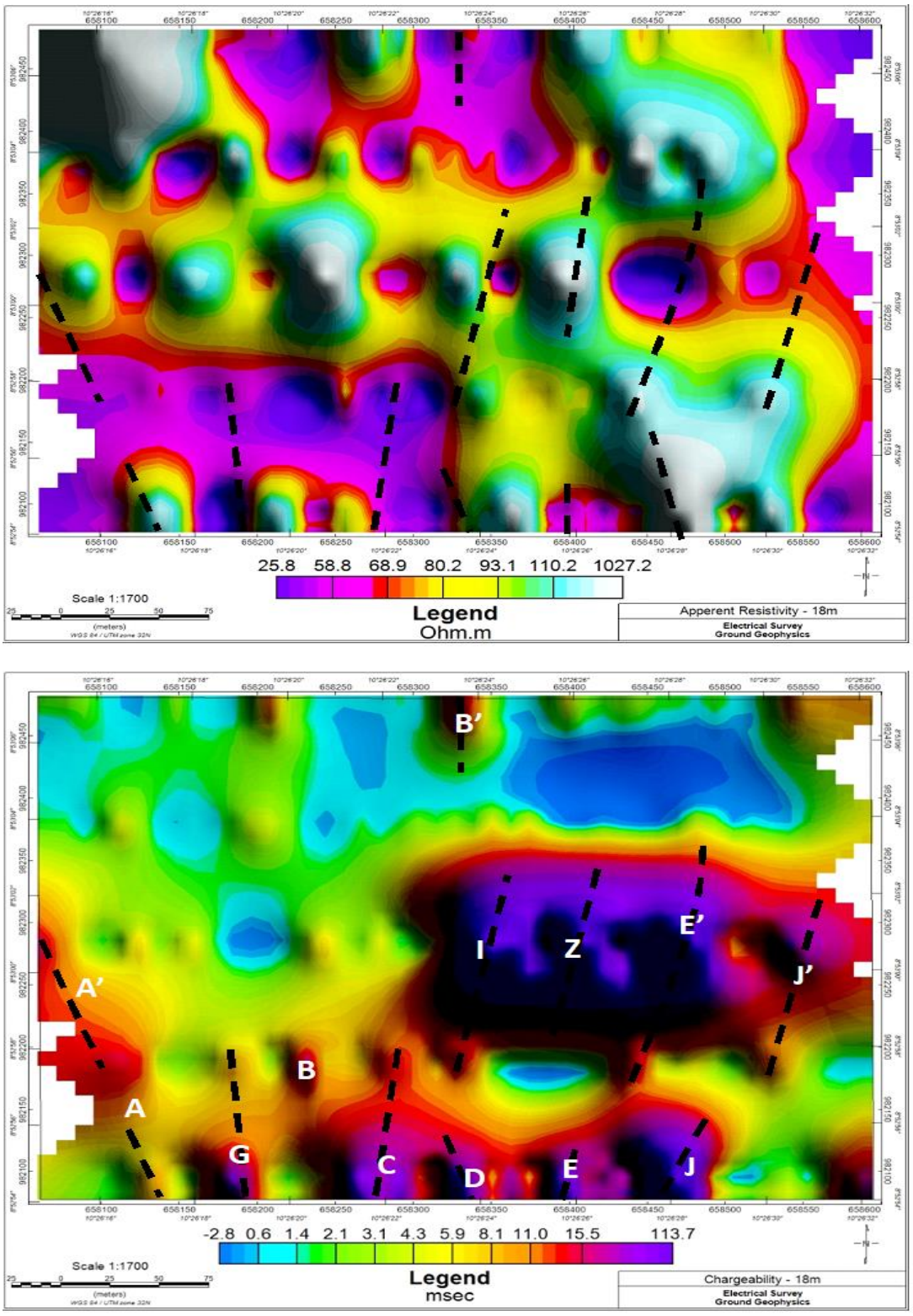

Figure 4.50: Resistivity and chargeability variation at depth of 18m

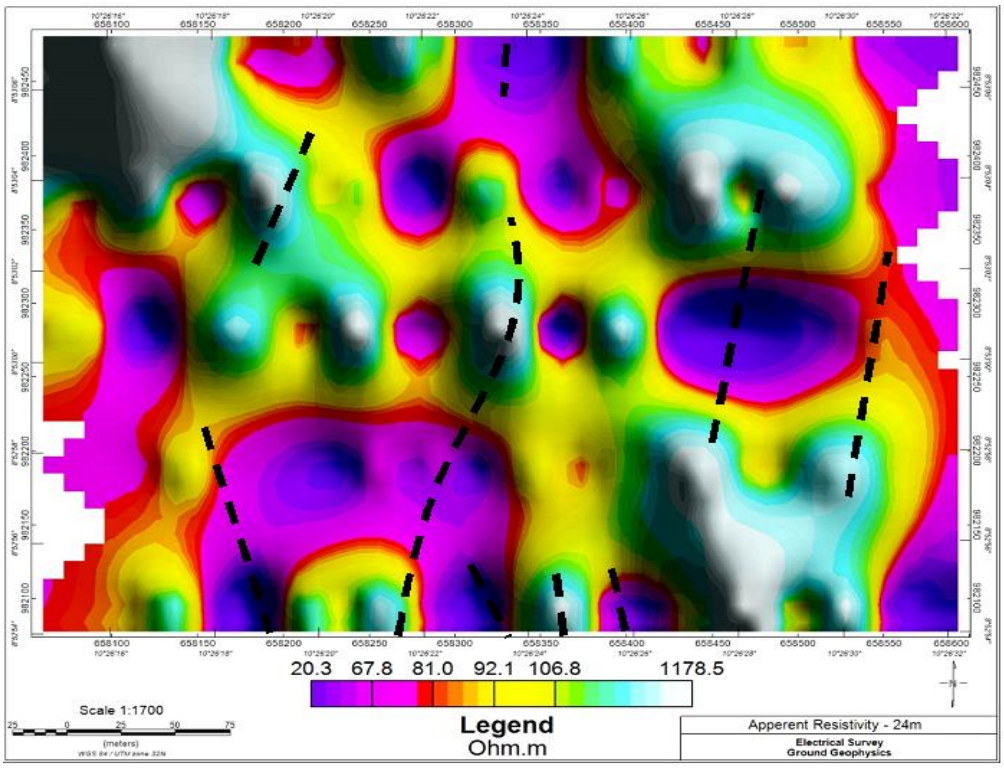

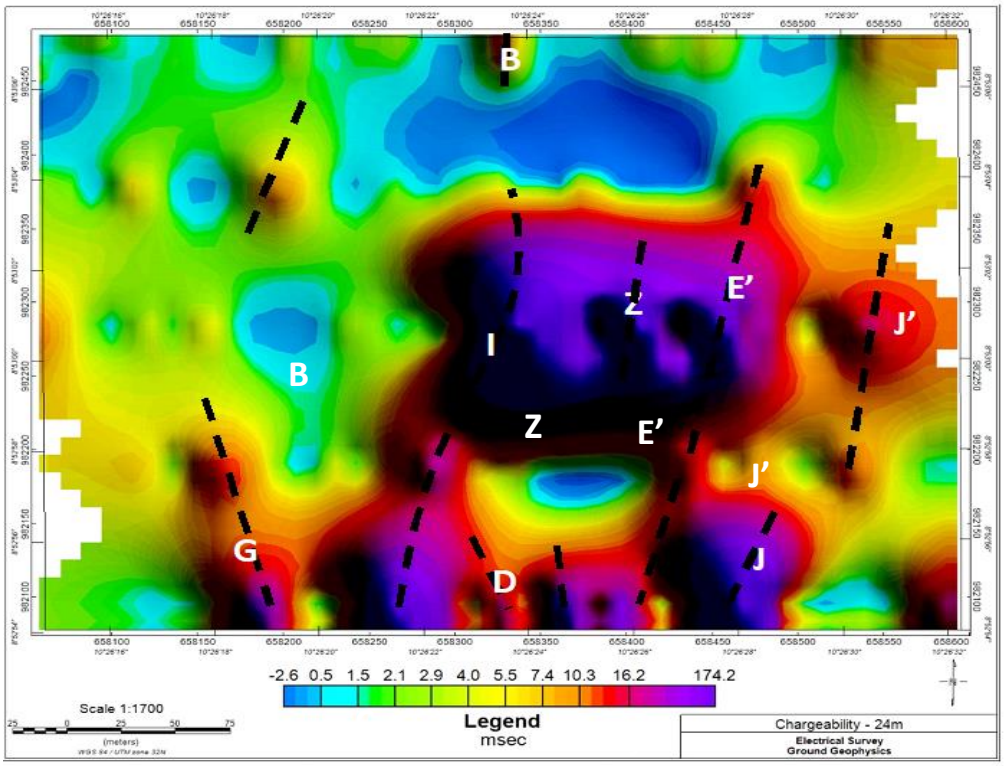

Figure 4.51: Resistivity and chargeability variation at depth of 24m

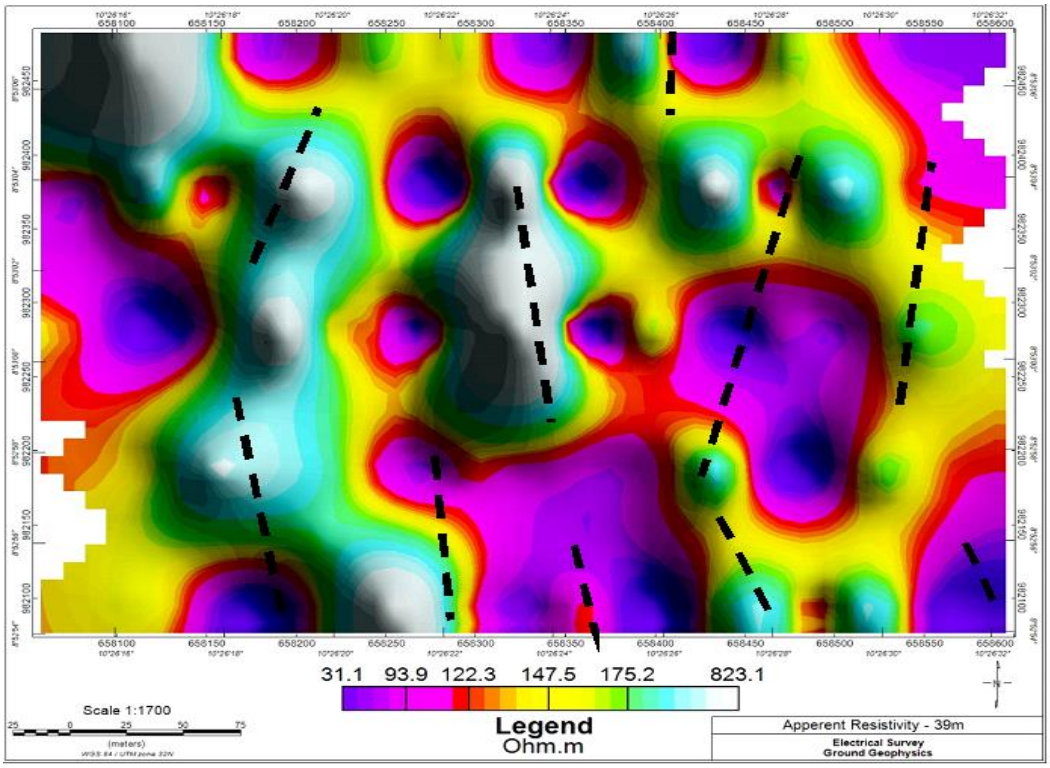

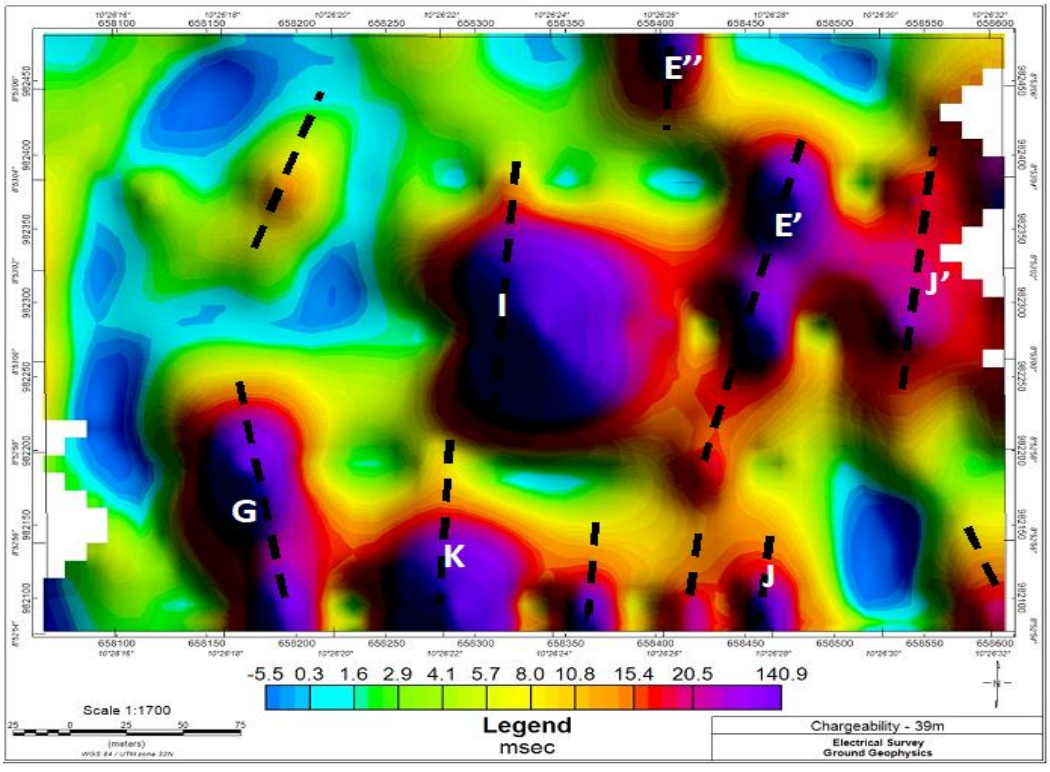

Figure 4.52: Resistivity and chargeability variation at depth of 39m

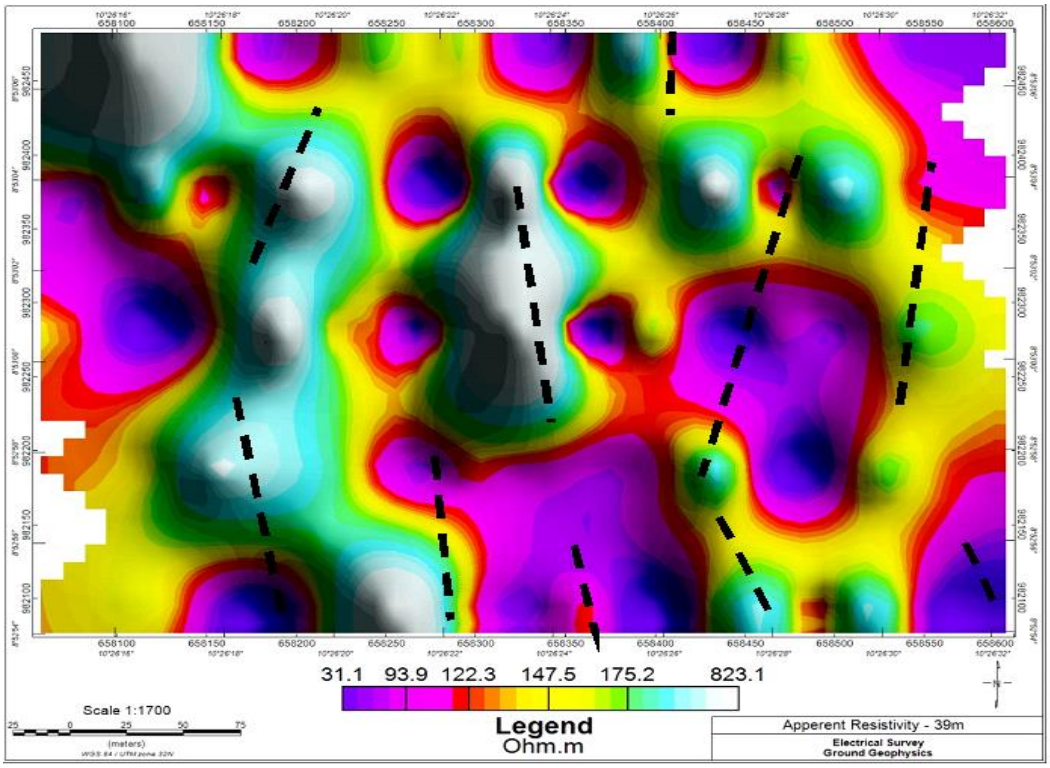

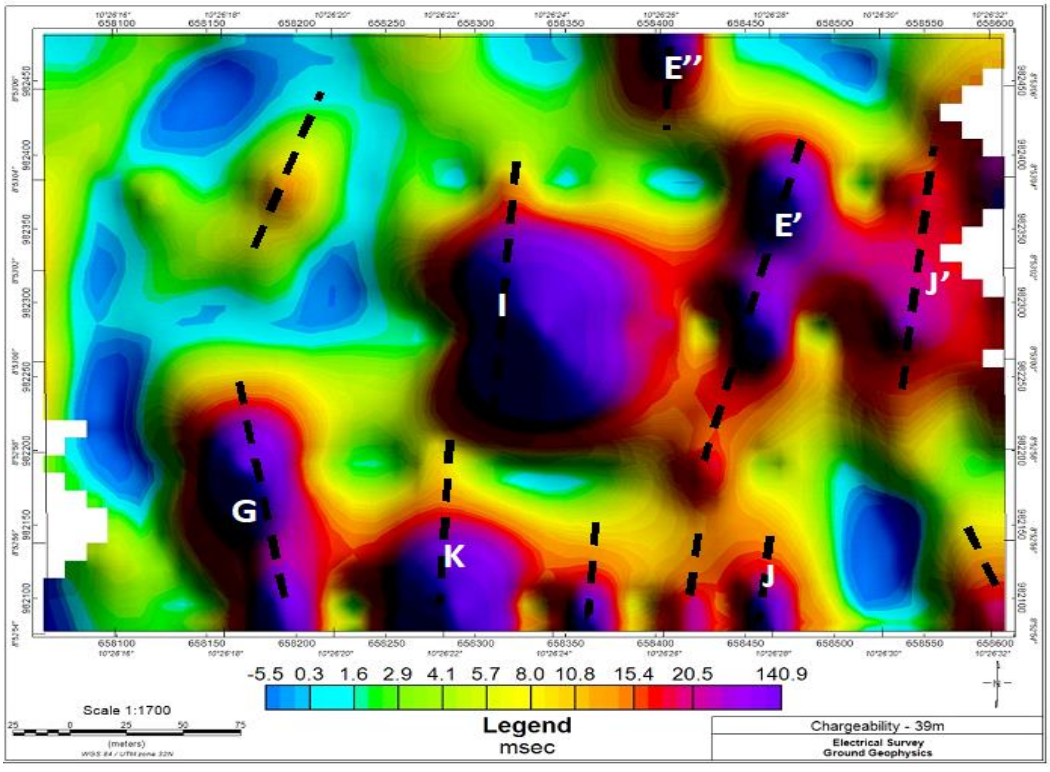

Figure 4.52: Resistivity and chargeability variation at depth of 39m

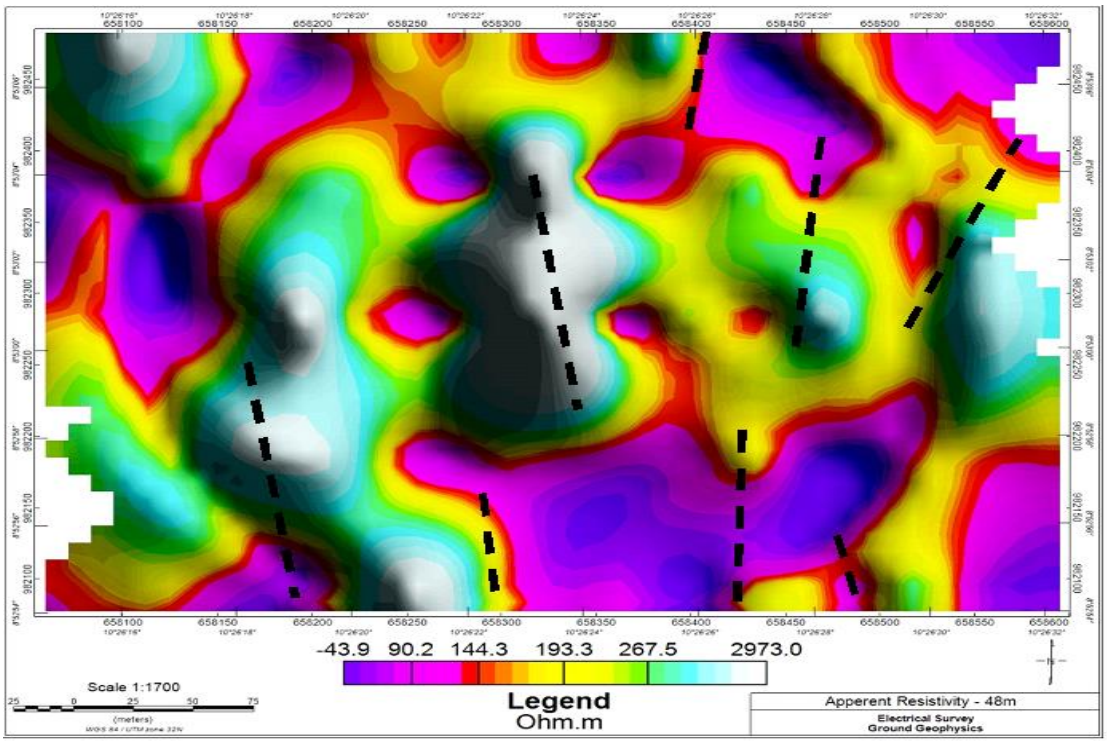

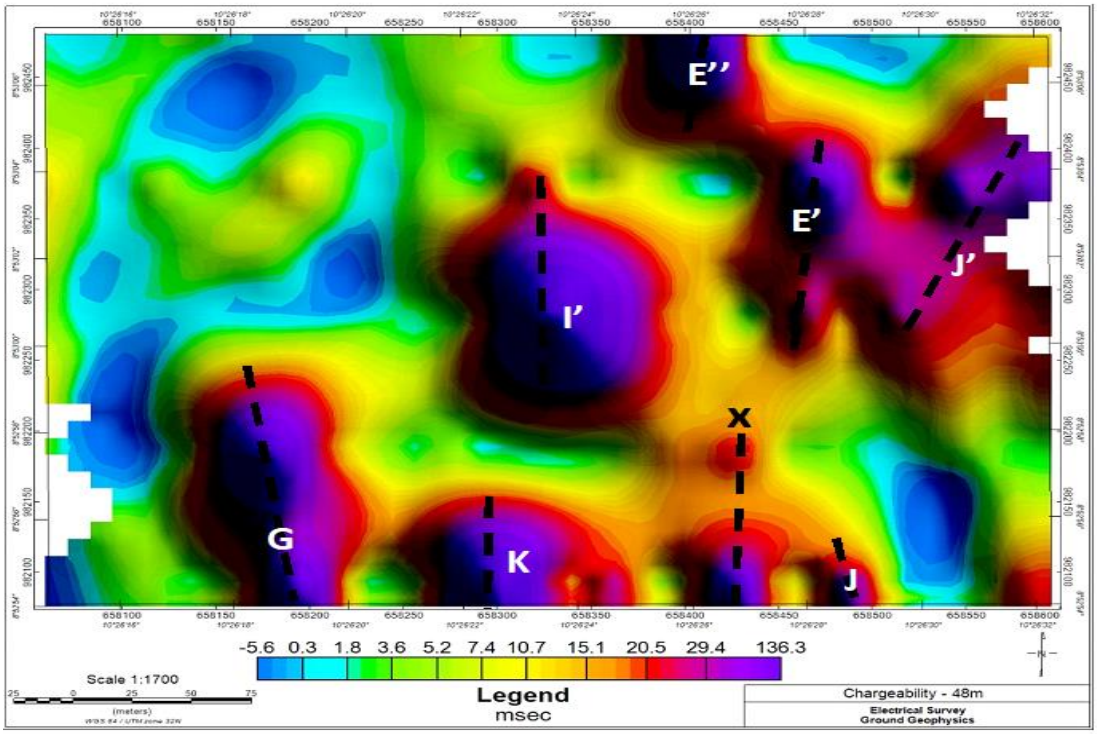

Figure 4.53: Resistivity and chargeability variation at depth of 48m

4.1.6 Core drills result (Zone 1)

Two core drills were done within the two-site studied in these works. Site one drill was carried out along RES/IP Line 2 and RES/IP Line 3 in zone 1. Drill point one was carried out to test anomalous body **C** which is characterized by high resistivity and chargeability response.

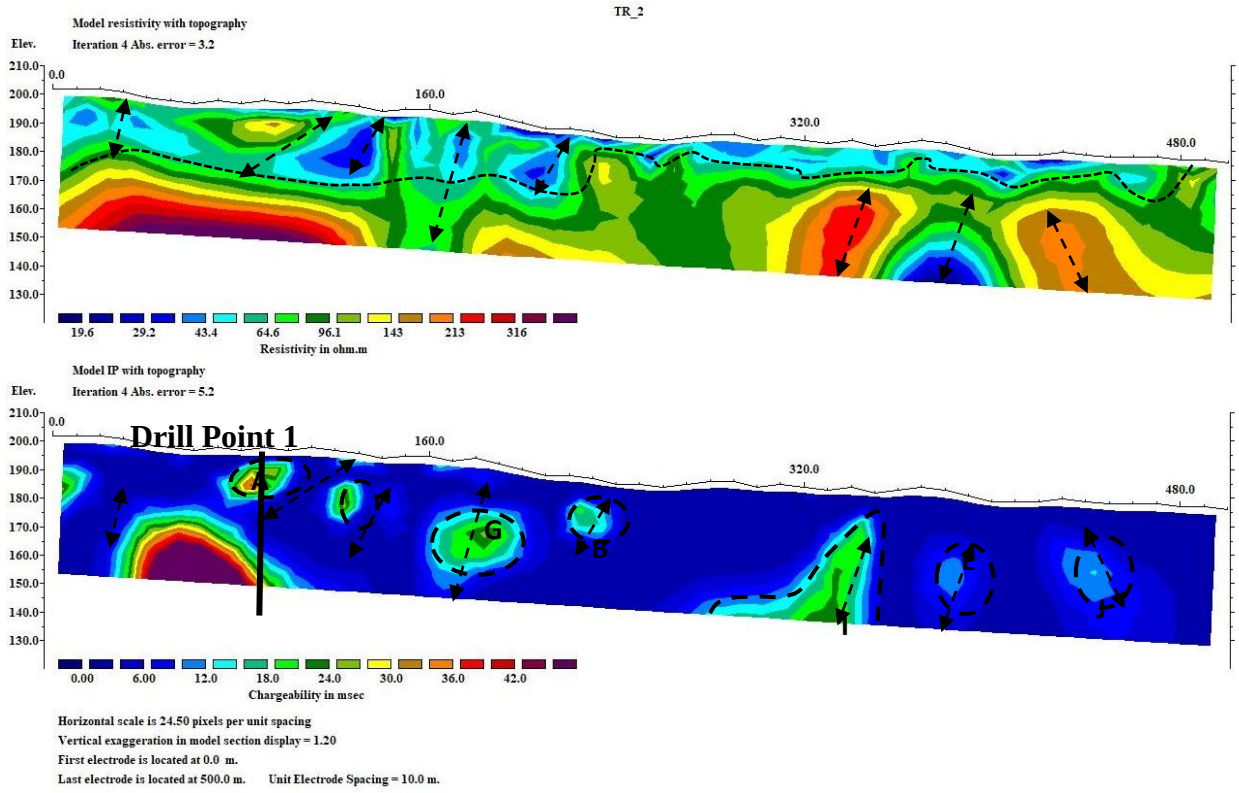

Figure 4.54: Electrical resistivity and chargeability model of Res/IP Line-2 in zone 1, showing drill point 1

Plate 4.1: Mineralised core length 5m from zone 1 showing excellent recovery

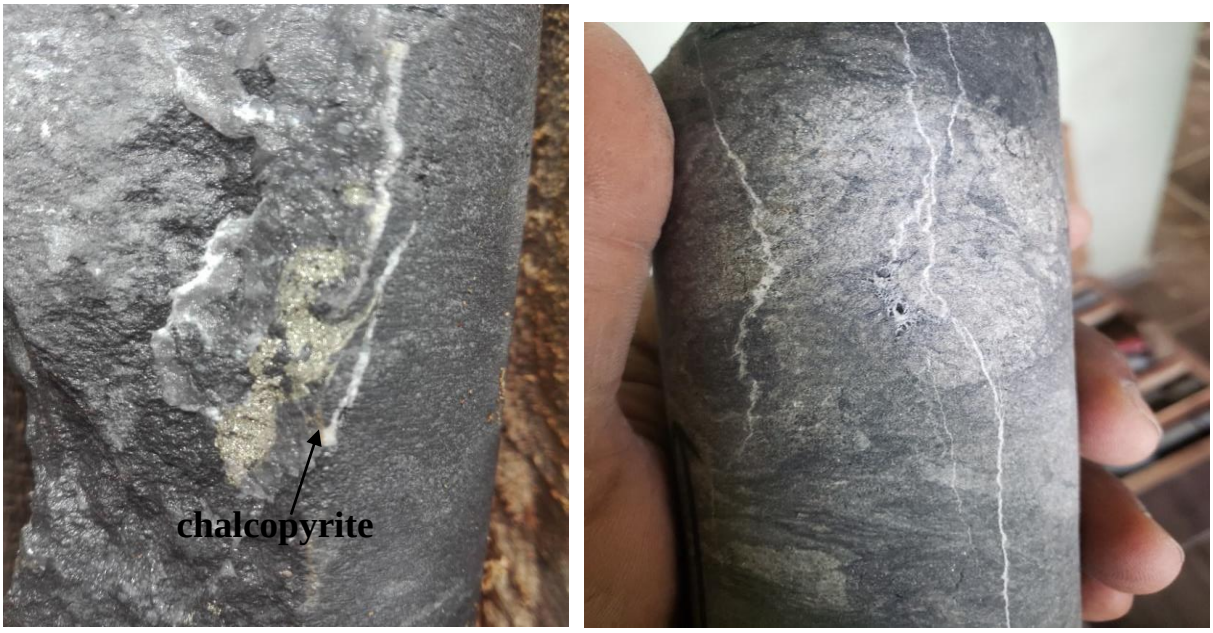

Plate 4.2:Quartz filled Fault from target

Plate 4.3: Lead Sample from crashed quartz from drill

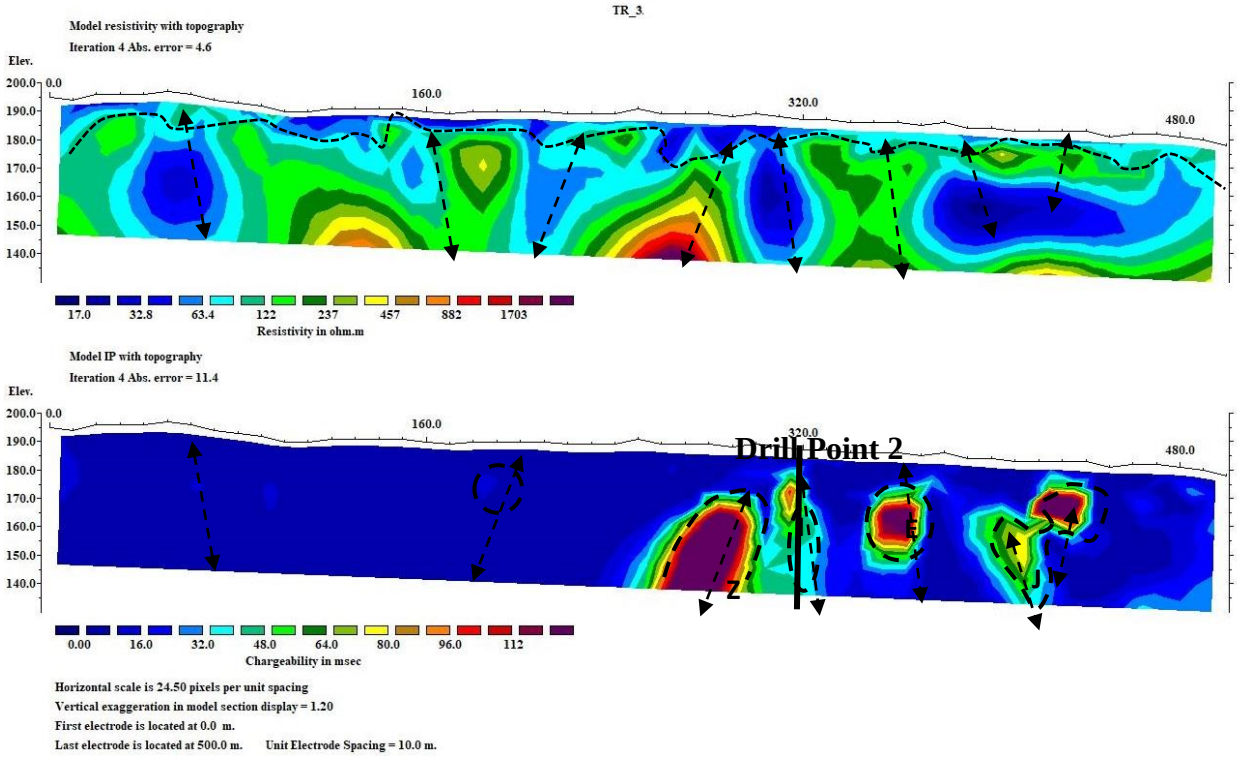

Figure 4.55: Electrical resistivity and chargeability model of Res/IP Line-3 in zone 1, showing drill point 2

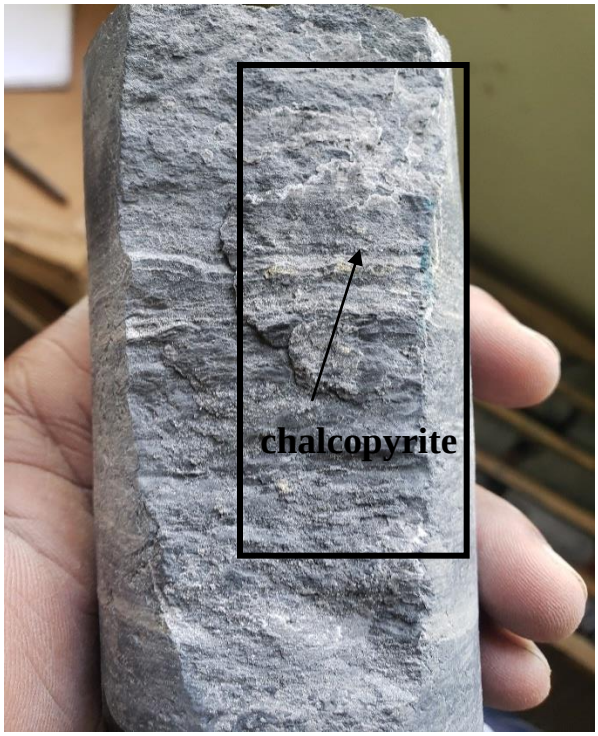

Plate 4.4: Fault Plan from target (Zone 1-drill point 2)

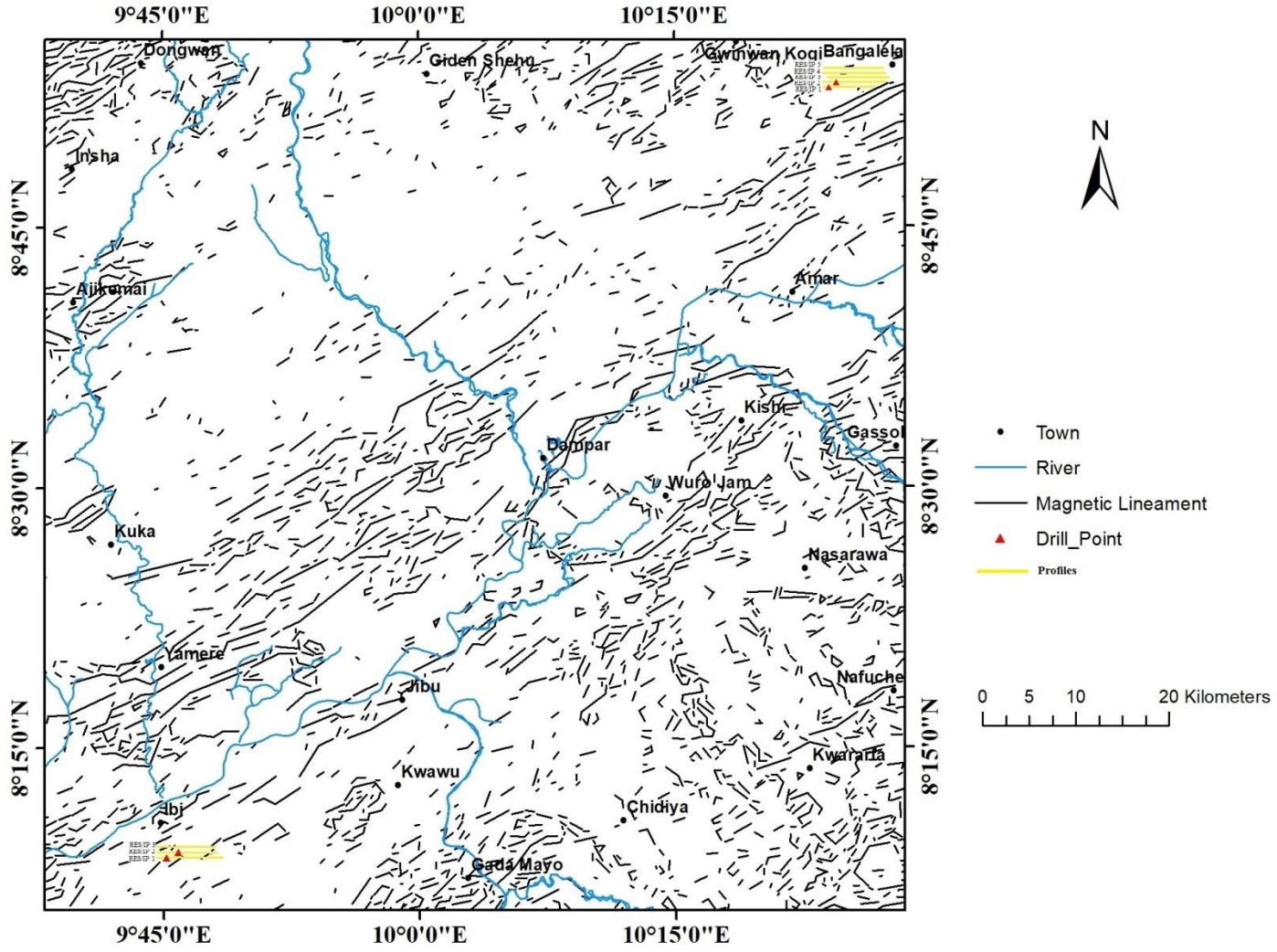

Figure 4.55a: Superimposed Lineament map and ground survey area showing selected Electrical Survey Sub-Block core drill point. (Zone1 and 2)

4.1.7 Voxel Modeling for Probable Reserve Estimation and Value Evaluation (Zone 1)

The chargeability values obtained from the 2D inversion of the chargeability data was inserted into two separate database matrixes where each value is associated with its X, Y and Z coordinate. The three-dimensional gridding of the data was subsequently done by using an algorithm called kriging. This algorithm determines the weight of each cell, and ultimately the preferential interpolation direction, based on a geo statistical analysis of all data. The 3D voxel images that were obtained contain the information associated with each cell along with its coordinates. The resolution of the images is a function of the grid cell size, which has been set during this process to 12.5 m.

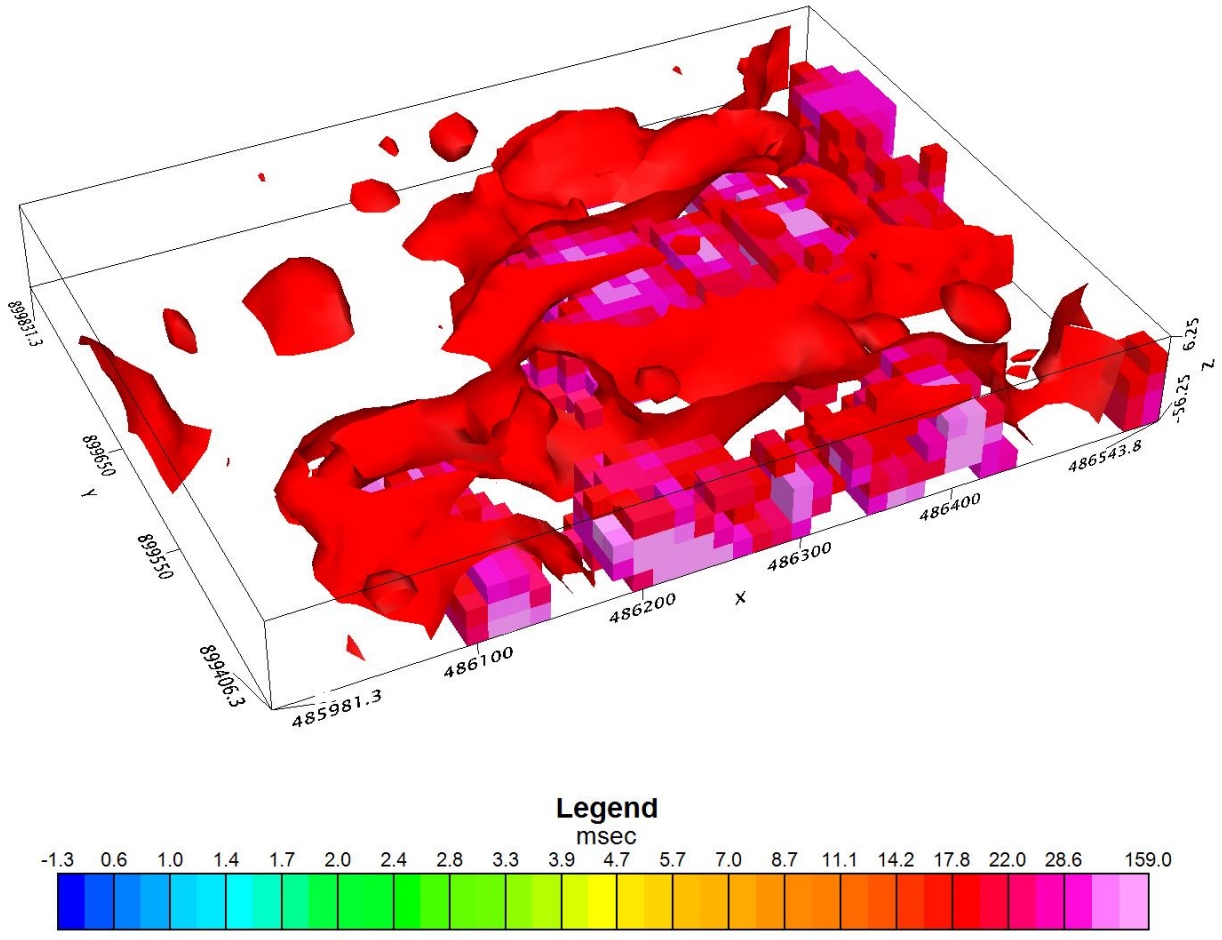

Figure 4.56: Chargeability Voxel Model (Zone 1)

4.1.8 Ground Magnetic Survey Results (Zone 2)

4.1.8.1 Digital Elevation Map

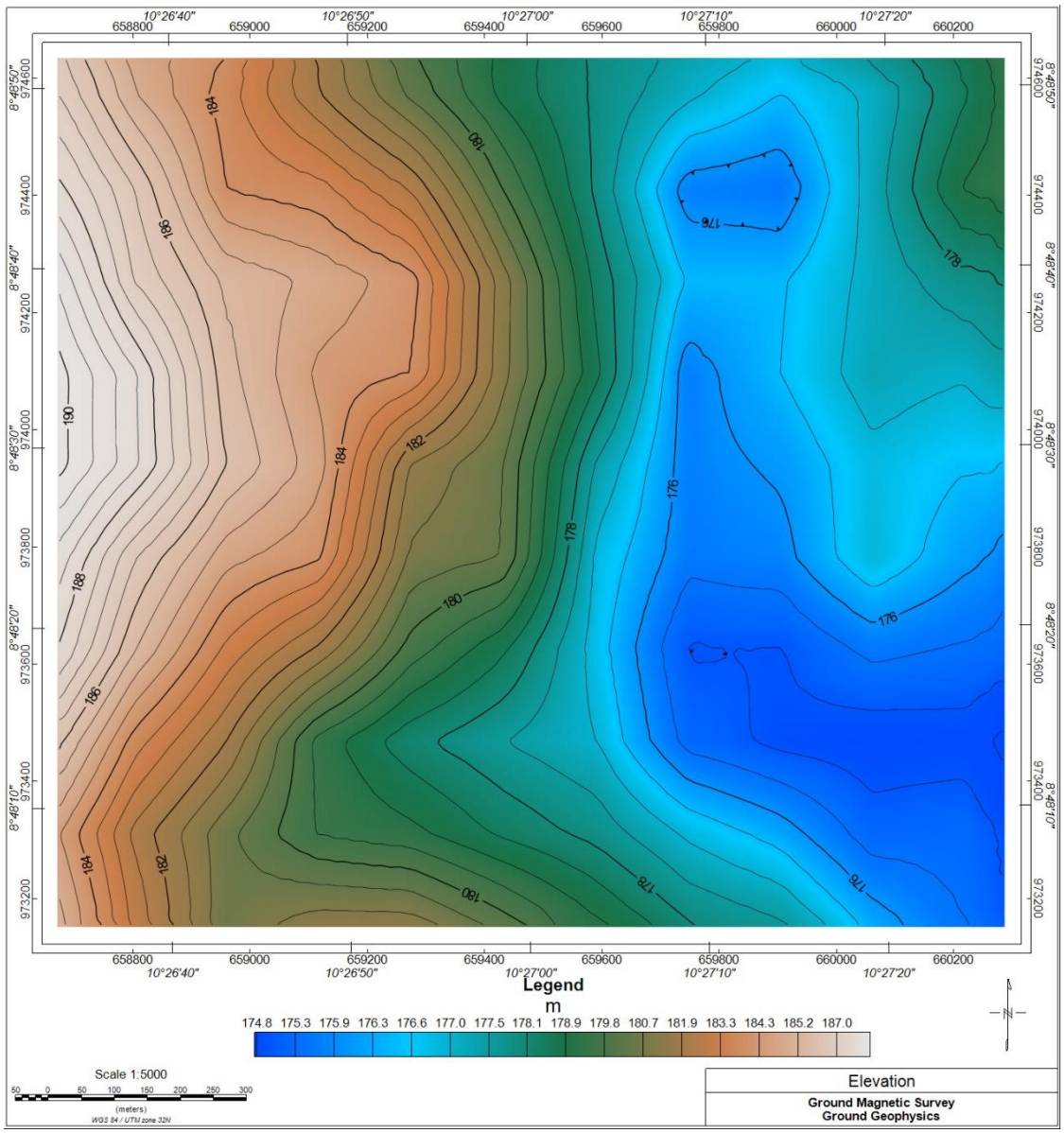

Figure 4.57: 3D surface DEM of study area

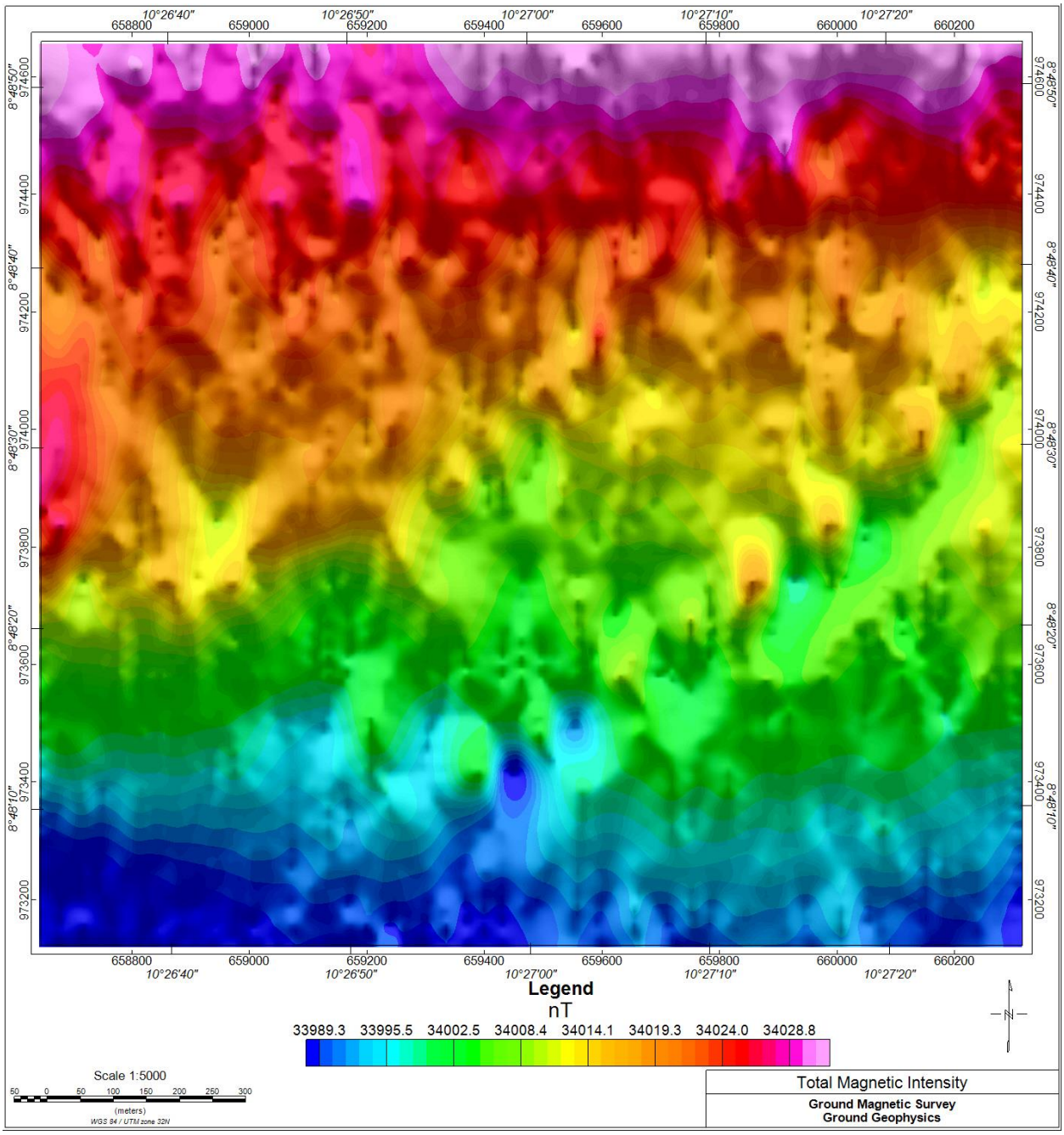

Figure 4.58: Observed magnetic intensity map from ground magnetic survey

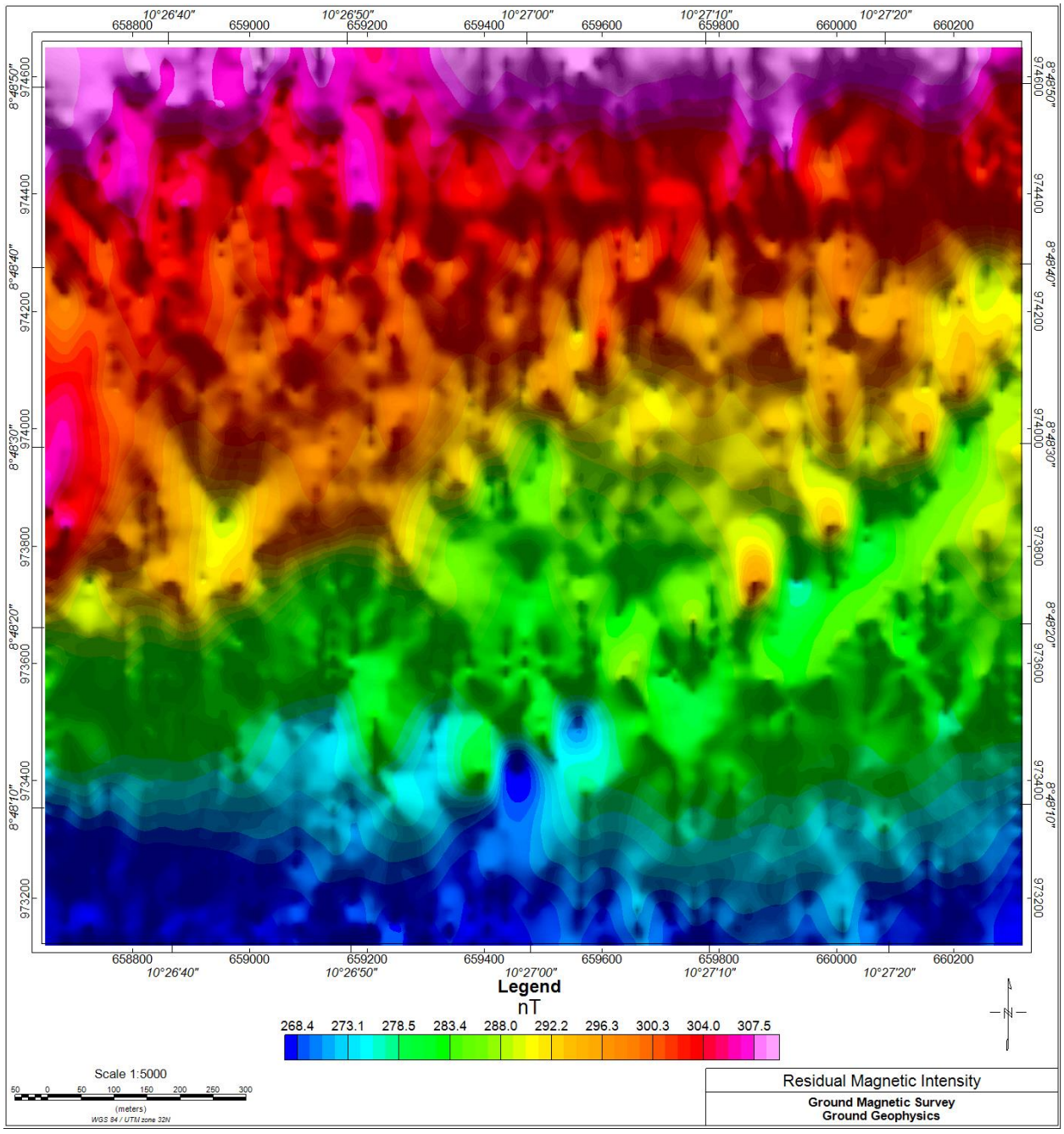

Figure 4.59: Residual Reduced to Equator magnetic intensity map from ground magnetic survey

4.1.8.2 Analytic Signal Map

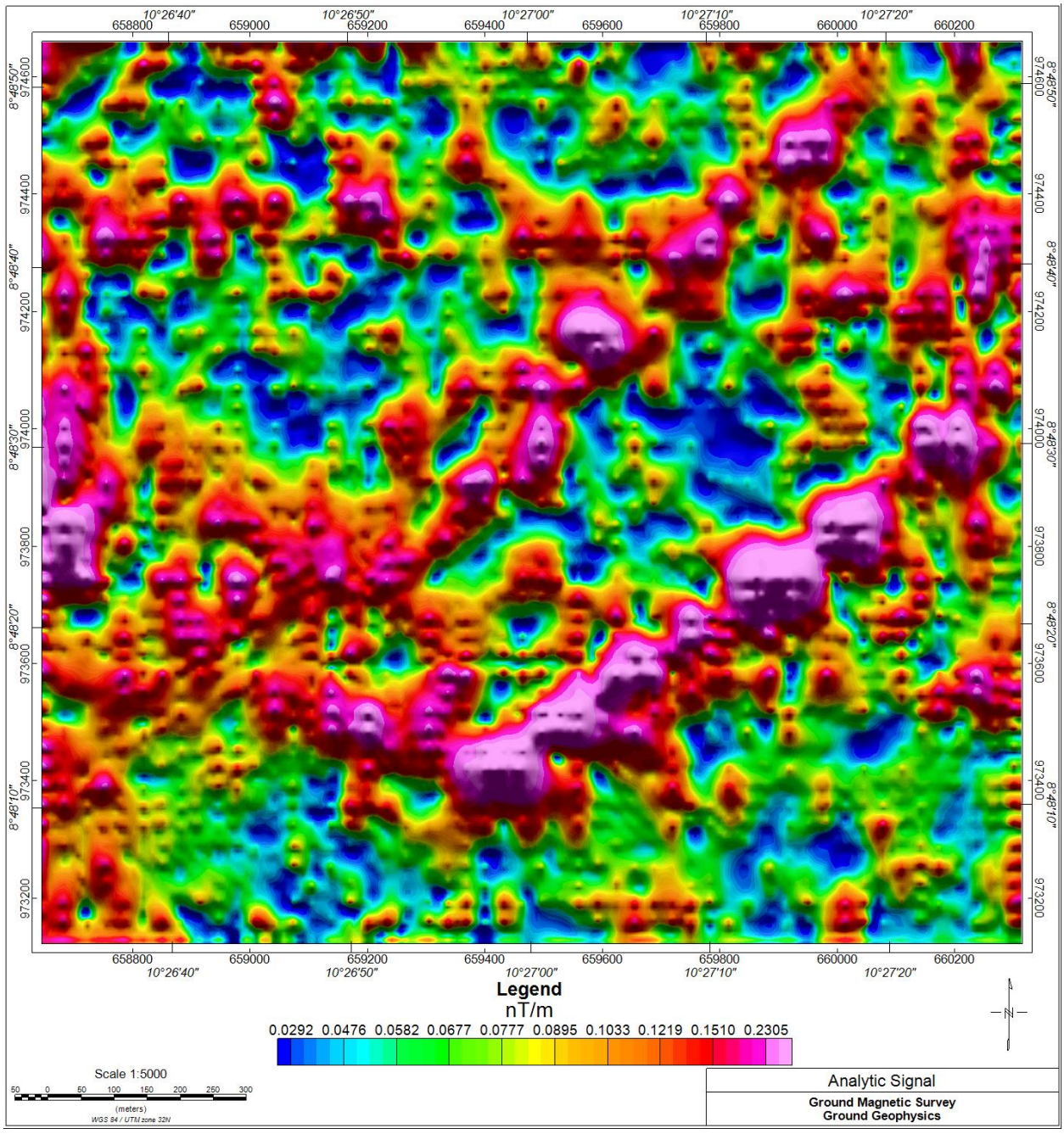

Figure 4.61: Analytic signal map from ground magnetic survey

4.1.8.3 First Vertical Derivative Map

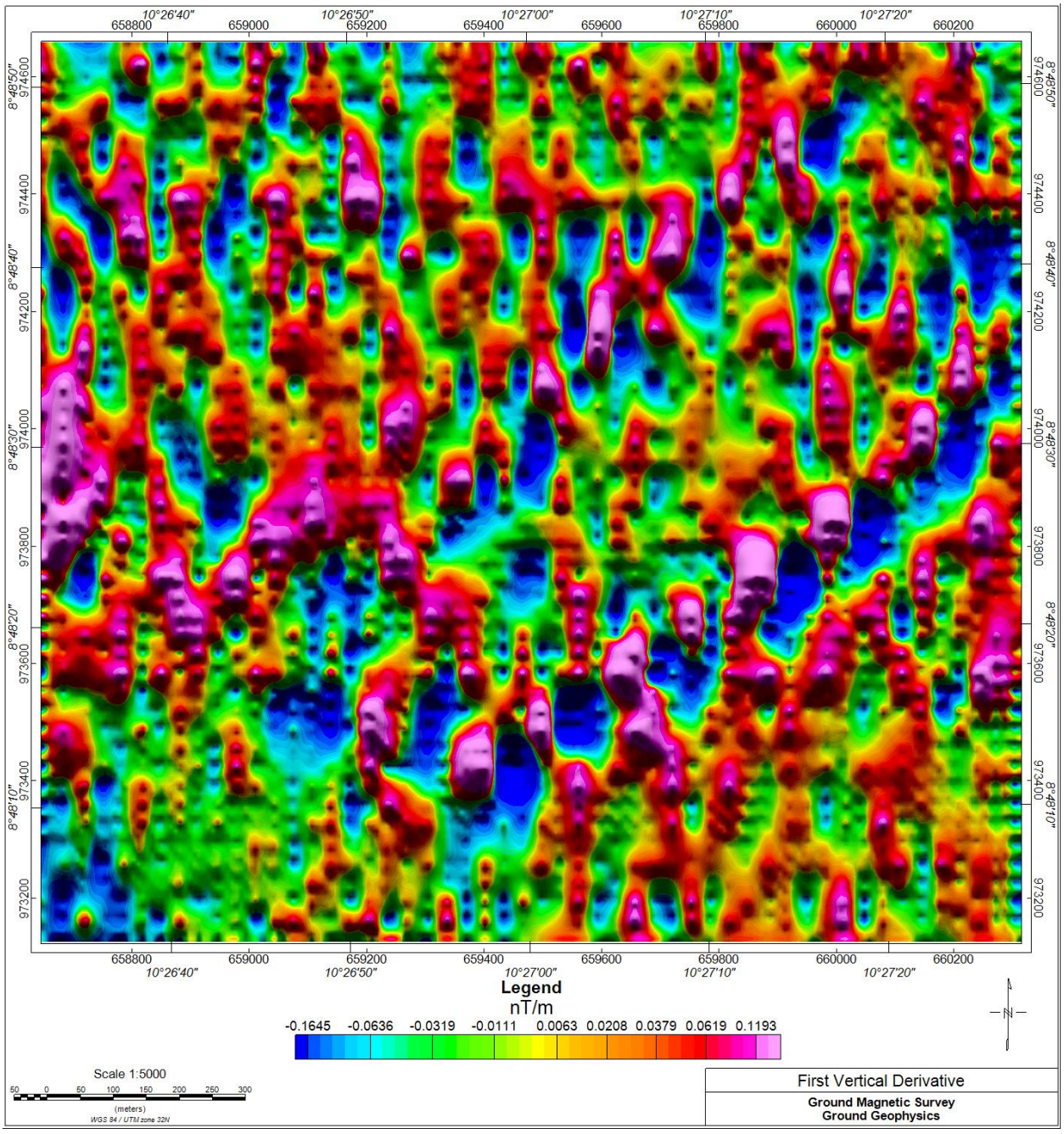

Figure 4.62: First Vertical Derivative map

4.1.8.4 Apparent Susceptibility Analysis

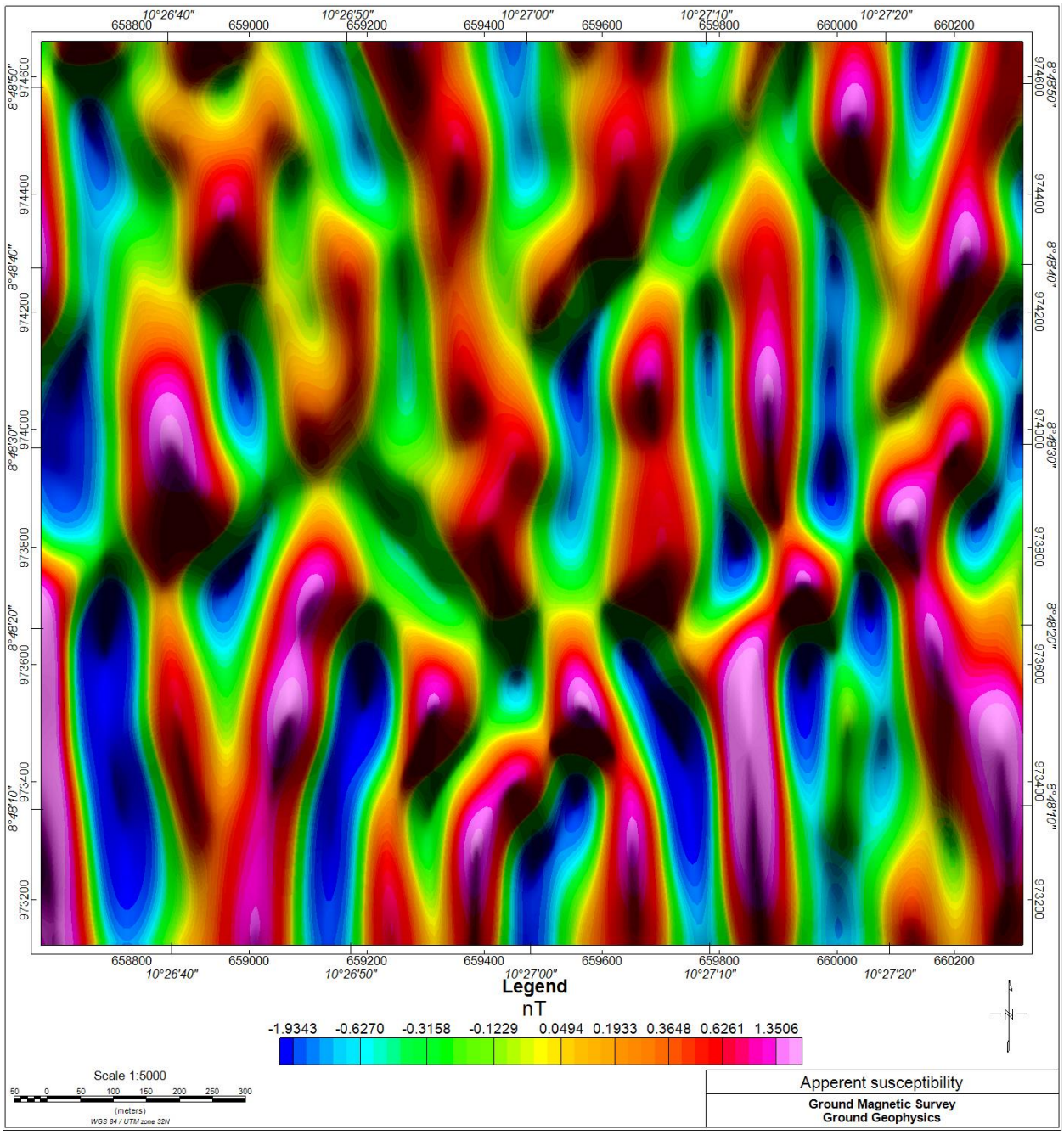

Figure 4.63: Apparent Susceptibility map

4.1.9 Results of VLF-EM (Zone 2)

4.1.9.1 Profile Line 1

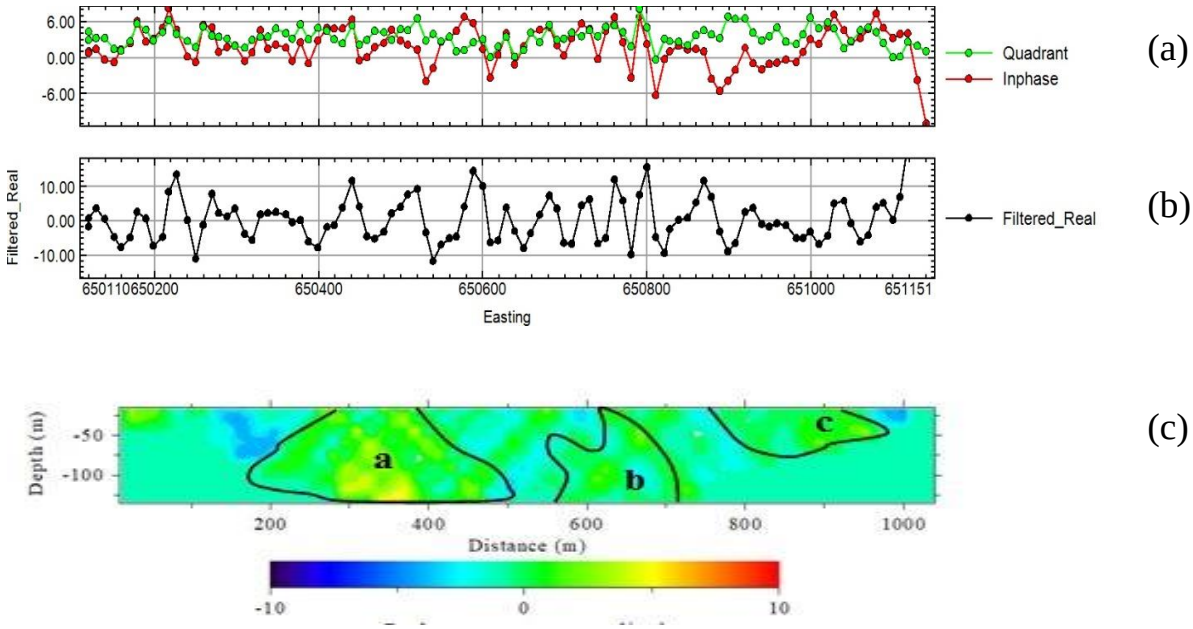

Figure 4.64: Interpreted VLF of Profile 1 (*a*) Raw in-phase and quadrature plot (*b*) Frasier filter plot (*c*) Karous-Hjelt filter model section

4.1.9.2 Profile Line 2

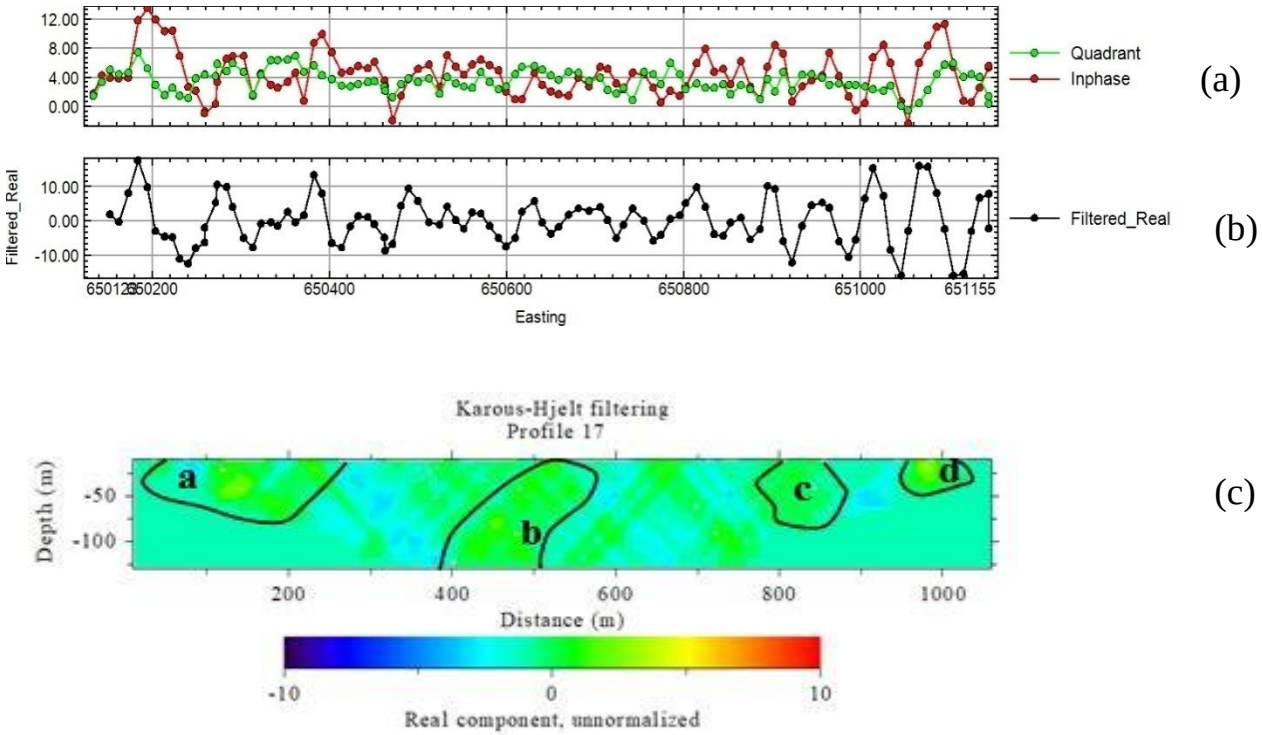

Figure 4.65: Interpreted VLF of Profile 2 (*a*) Raw in-phase and quadrature plot (*b*) Frasier filter plot (*c*) Karous-Hjelt filter model section

4.1.9.3 Profile Line 3

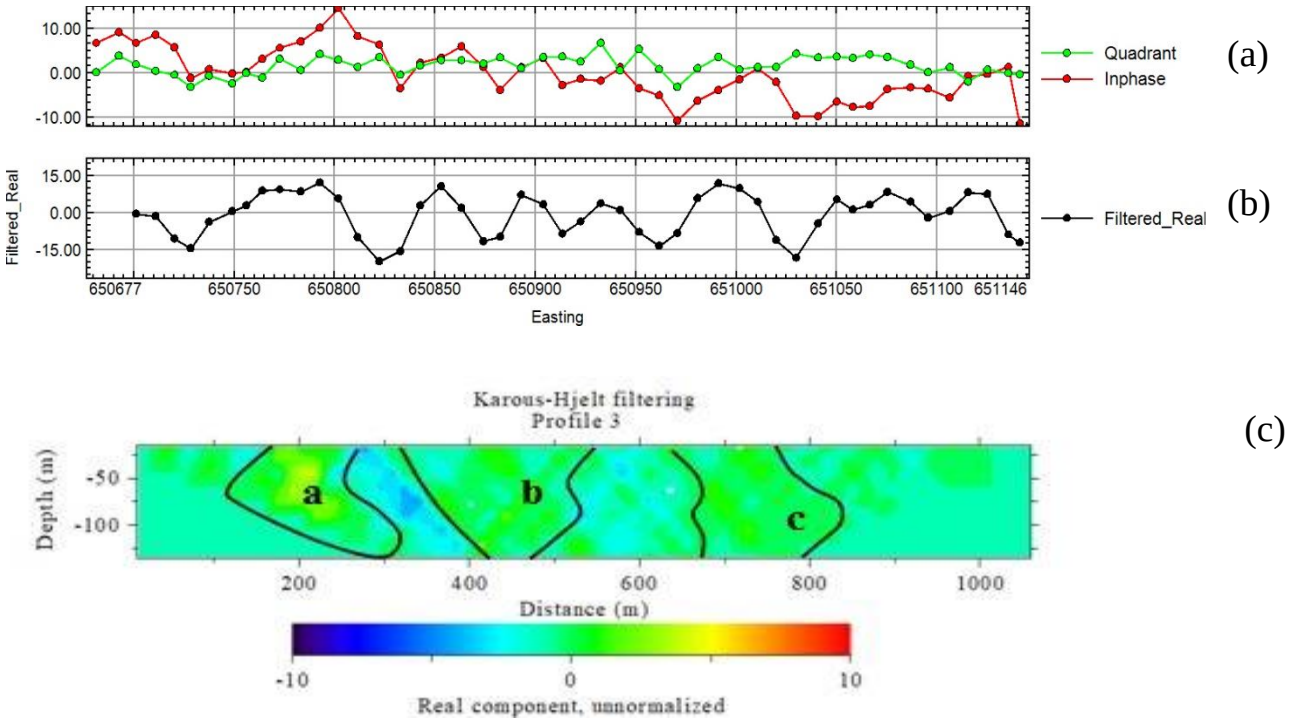

Figure 4.66: Interpreted VLF of Profile 3 (*a*) Raw in-phase and quadrature plot (*b*) Frasier filter plot (*c*) Karous-Hjelt filter model section

4.2.9.4 Profile Line 4

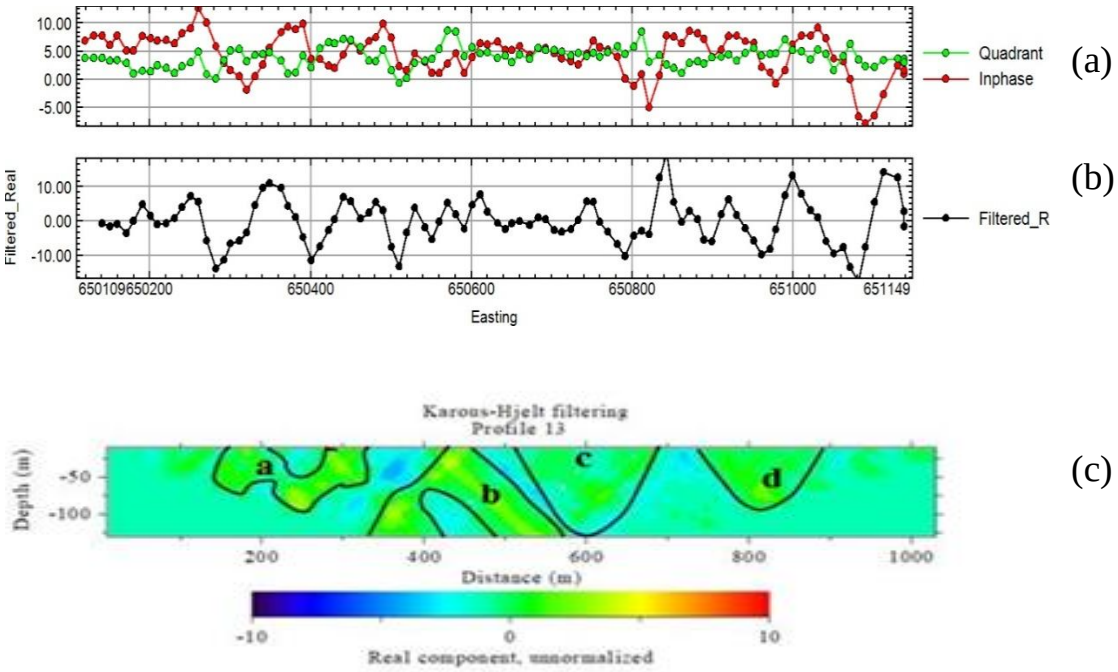

Figure 4.67: Interpreted VLF of Profile 4 (*a*) Raw in-phase and quadrature plot (*b*) Frasier filter plot (*c*) Karous-Hjelt filter model section

4.1.9.5 Profile Line 5

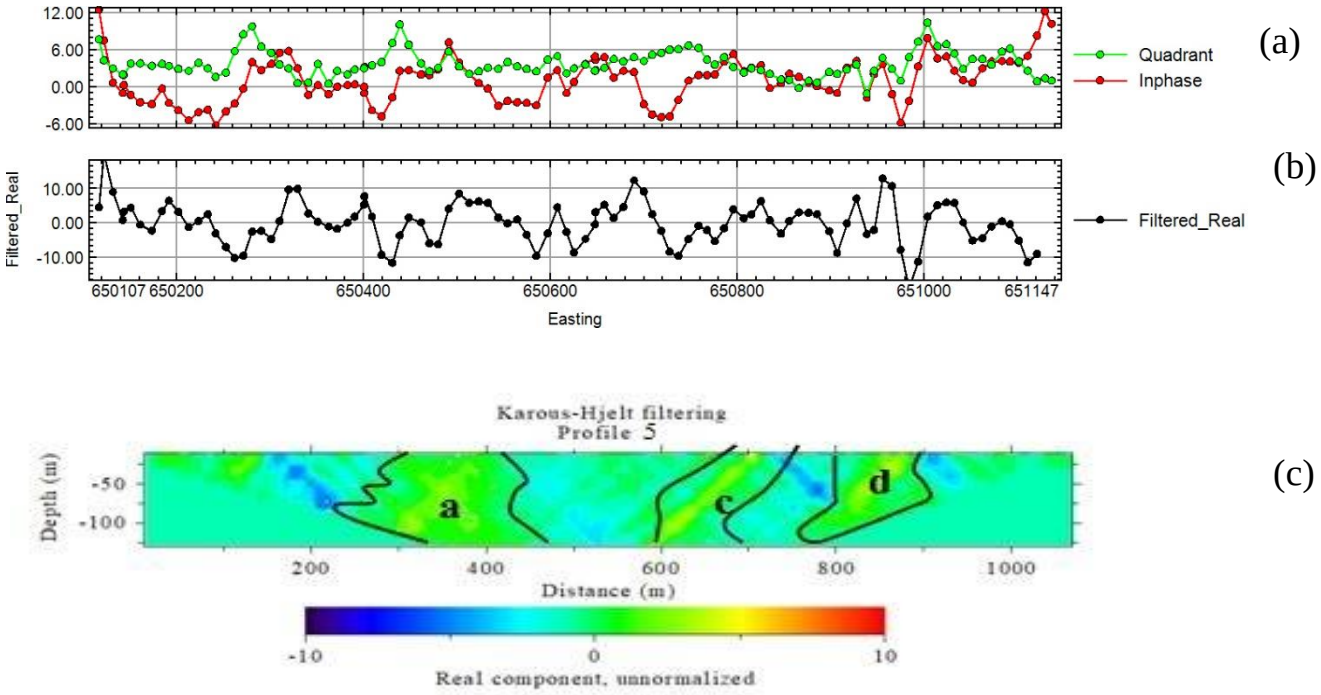

Figure 4.68: Interpreted VLF of Profile 5 (*a*) Raw in-phase and quadrature plot (*b*) Frasier filter plot (*c*) Karous-Hjelt filter model section.

4.1.9.6 Frasier Filter 2D Map (Zone 2)

Figure 4.69 represent the variations of conductivity across the survey block. The conductive and none-conductive bodies as seen to align N-S, with N-S contact just like the Apparent Susceptibility Magnetic map. The VLF and magnetic map is seen to be in agreement with conductive structures sitting within in low magnetic zone. The conductivity values range from -17.9 to 22.2.

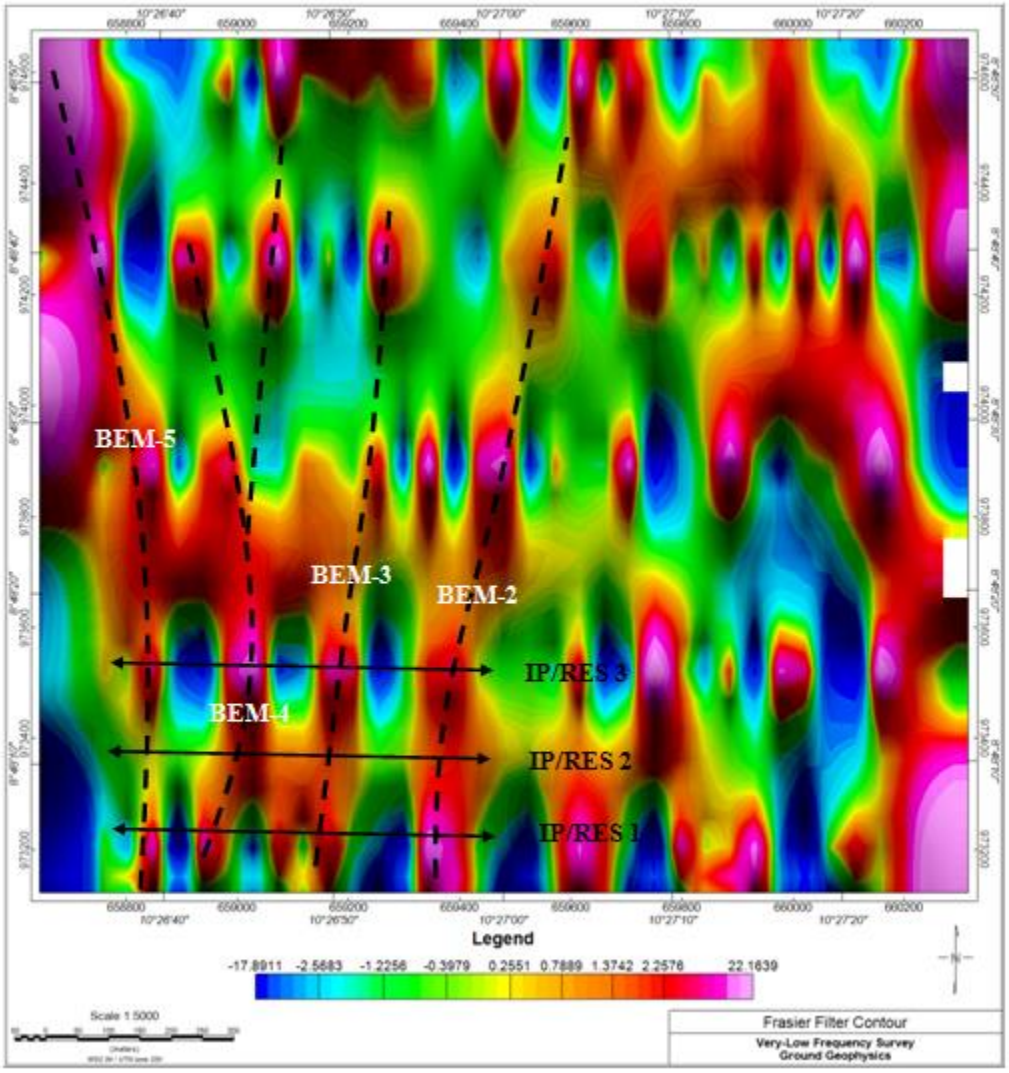

Figure 4.69: 2-Dimentional Frasier Filter Map of the study area showing selected Electrical Survey Sub-Block

4.1.10 Results of Ground Electrical and Induced polarization Survey (Zone 2)

4.1.10.1 Res/IP Line-1

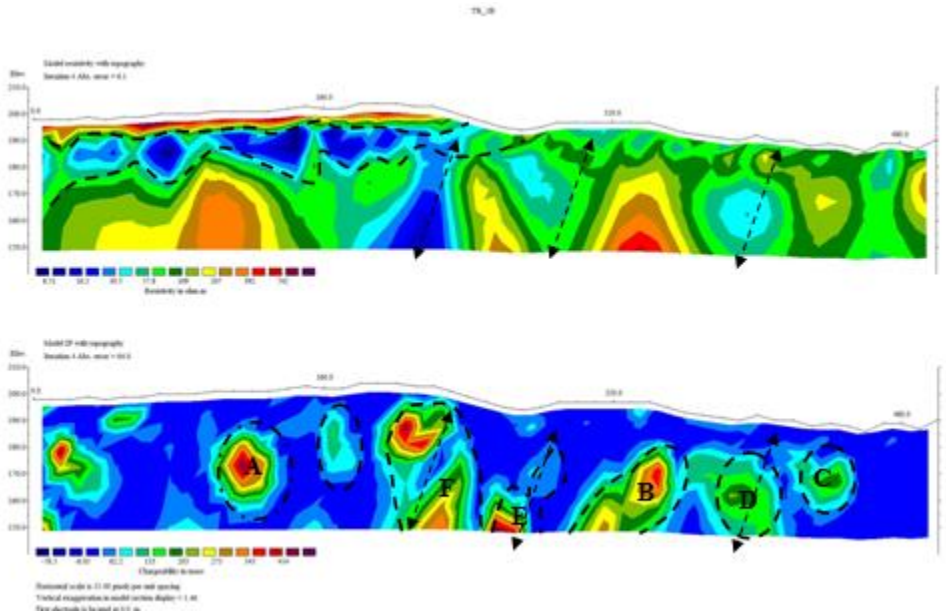

Figure 4.71: Electrical resistivity and chargeability model of Res/IP Line-1

4.1.10.2 Res/IP Line-2

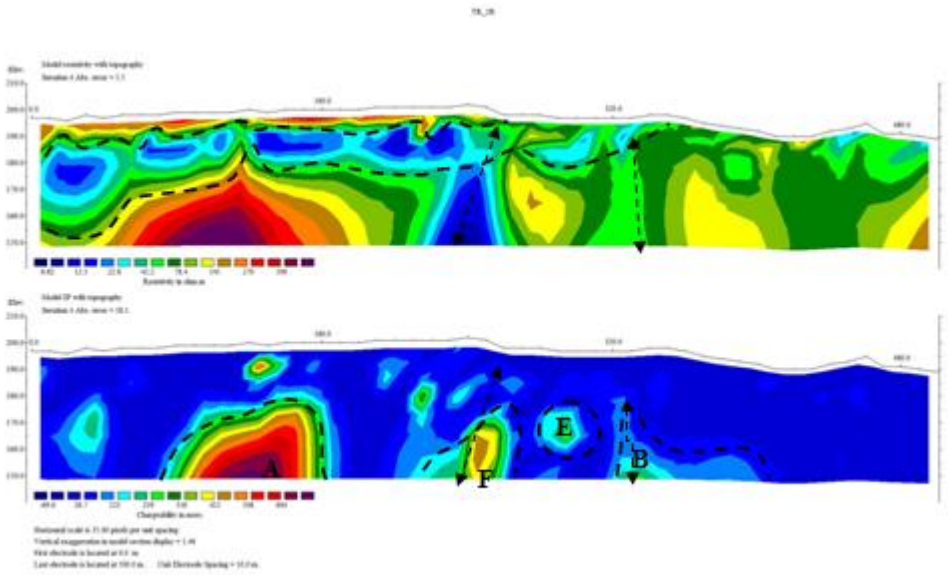

Figure 4.72: Electrical resistivity and chargeability model of Res/IP Line-2

4.1.10.3 Res/IP Line-3

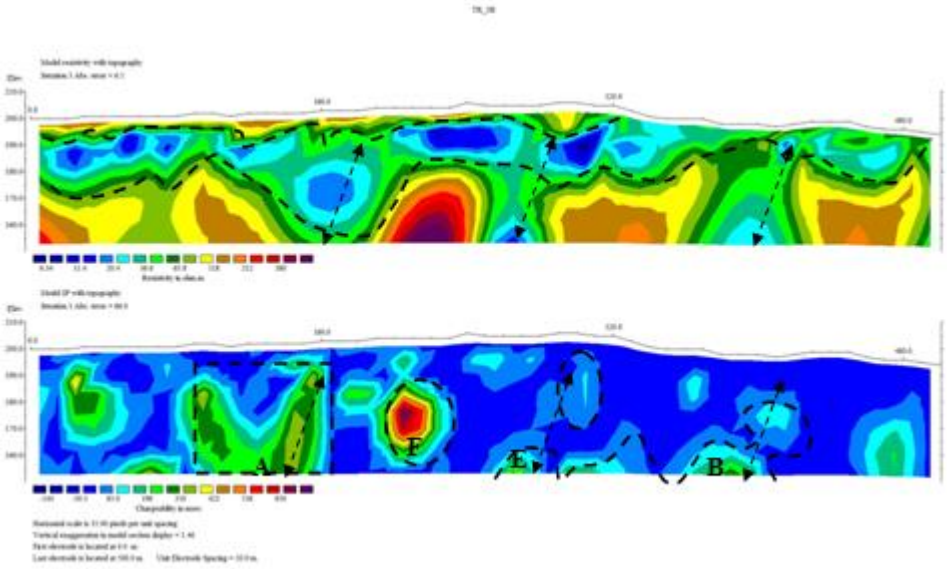

Figure 4.73: Electrical resistivity and chargeability model of Res/IP Line-3

4.1.11 Core drill results (Zone 2)

The drill (Zone 2) was done along RES/IP Line 1 and RES/IP Line 2. The target anomaly is characterized by high resistivity and high chargeability. Drill point three (3) was carried out along RES/IP Line 1 in Zone 2.

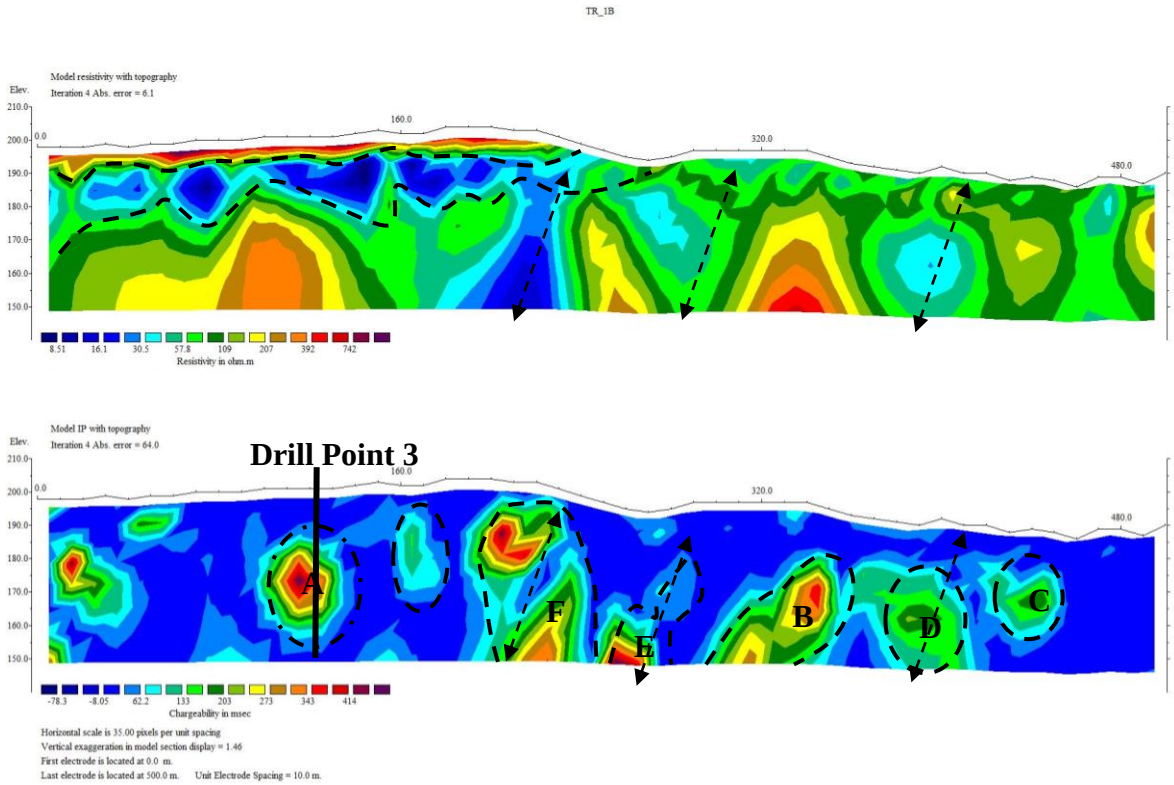

Figure 4.74: Electrical resistivity and chargeability model of Res/IP Line-1 point 3

Plate 4.5: Chalcopyrite was observed within the quartz observed at point 3

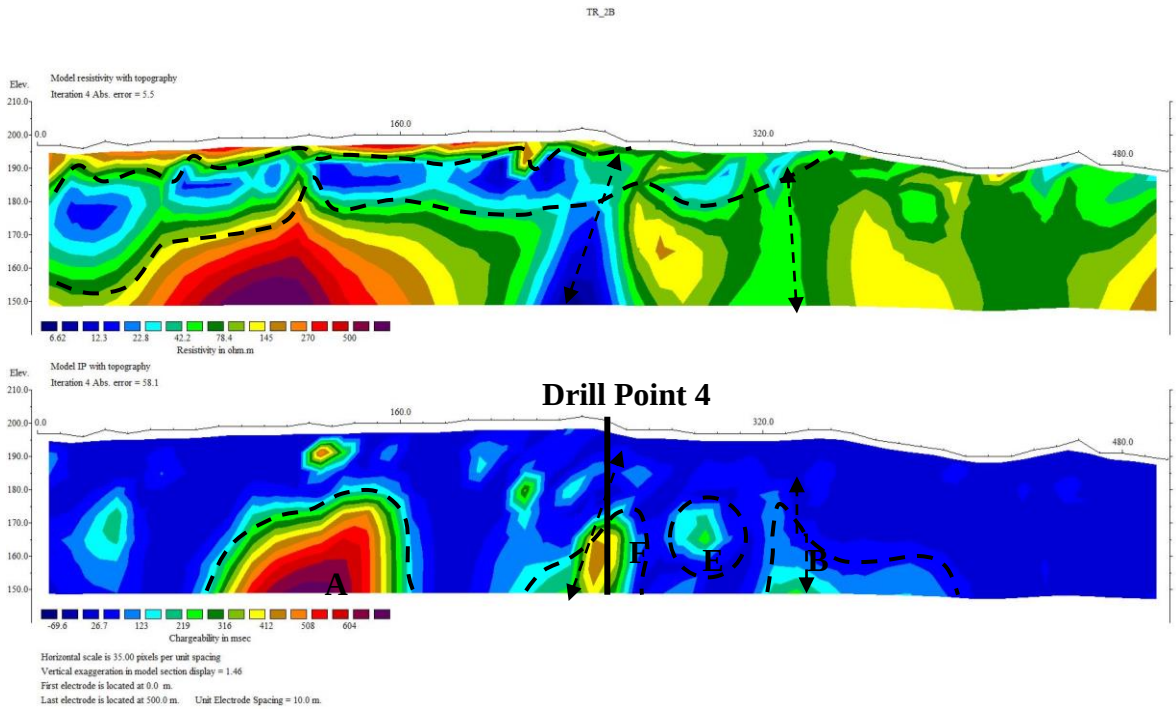

Figure 4.75: Electrical resistivity and chargeability model of Res/IP Line-2 point 4

Plate 4.6: Sulphide mineral was observed within the quartz observed at point 4

4.2 Discussion

4.2.1 Discussion of Landsat 8 OLI Results

4.2.1.1 Single Band Combinations

In Figure 4.1 a true colour image was produced with Landsat 8 visible bands 4, 3 and 2 (Red, Green and Blue, respectively). With this band combination, it is possible to do an exploratory analysis of the area, identifying rock exposure areas (brown), vegetation areas (green), rivers and lakes (blue) and urbanized areas represented by light blue. In addition, some structural features such as faults and fractures were identified. Geoloigically, Rock exposures were observed around Bangalala, Giden Shehu, Amar, Dongwan, Garkawa, Ajikemai, Kishr, Dampar, Kuka, Yamere, Shamankar, Bembem, Janka, Akiri, Yalwa, Shandam, JauroGarmaho, Adi, Apar, Hundu, Fiyayi, Kwana, Ugba, ZakiBiam, Sankara, Chonku, Wukari,Gidan Idi, Ngbebe, Donga, Avermun, Akume, Dooga, Gankol, Kurgwi, Kande and BakinChiwe.

Figure 4.2 a False Colour image was created, using bands 5, 4 and 3 (R, G, B) (Figure 4.2). This band combination allows a better differentiation between vegetated areas (red areas) and good exposure outcrops (greyish colours). Light blue colour represents urbanized areas.

For a preliminary geological study, a contrast-enhanced RGB combination (SWIR, NIR, and Visible) was created. The most contrasting band combination for lithological features and that provide more detail without additional enhancement should include one visible (2, 3 and 4), one NIR (5) and one SWIR (6 or 7) band (USGS, 2015a; USGS, 2015b). Based on this assumption, a composite using the bands 7, 5, 2 (RGB) was created (Figure 4.3) where it is possible identify outcrops as shades of orange and red, vegetation in light green and water in black (Figure 4.3).

A band combination with a NIR band (band 5) and two SWIR bands (band 6 and band 7) was created, allowing a regional scale detection of geological features like faults, and differentiation of rock outcrops from vegetation (Figure 4.4). In this image, outcrops show a light blue colour, while vegetated areas an orange colour and water bodies appear black. Some hydrothermal alterations in outcrop areas were identified as blue observed around Bangalala, Giden Shehu, Ajikeman. Kuka, Gessol, Akiri, Janka, Bembem, Wukari and Akwana. They are potential mineralized zones (Figure 4.4)

4.2.1.2 Band Ratio

Figure 4.5: Landsat 8 band ratio 4/2 image reveals areas where iron minerals (hematite, goethite, limonite, etc.) are abundant as shown in bright tones.

Ratio of Band 6 over band 5 discriminate ferrous minerals in bright tone (Figure 4.6). Clay minerals, as illite, kaolinite, and montmorillonite are discriminated with the ratio image of band 7 over band 5 as bright pixels (Figure 4.7). The ratio image of band 6 over band 7 distinguishes altered rocks containing clays and alunite from unaltered rocks, where pixels are bright (Figure 4.8). Pronounced alteration mapping interpreted by the occurrence of iron oxide bearing minerals as observed in ratio band 4 over band 5, Clay minerals, as illite, kaolinite, and montmorillonite in ratio of band 7 over band 5 and clays; and alunite in ratio of band 6 over band 7, indicated major anomalous alteration at Gidan Shehu, east of Wukari, Kuka, Bambam, Uzam, Agor and minor anomalous alteration at Bangalala, Akwana and Dongwan indicated as potential areas for further investigations.

An image incorporating these band ratios will discriminate altered from unaltered outcrop and highlight areas where concentration of these minerals occurs. An image using Sabin's ratio (4/2, 6/7 and 6/5 as RGB) was produced for lithological mapping and hydrothermal alteration zones (Figure

4.9). The ratio 4/2 was used for mapping iron oxides as hematite, limonite and jarosite, and has high reflectance in red region. The ratio 6/7 was used to map clay minerals as kaolinite, illite and montmorillonite (Figure 4.8). The ratio 6/5 shows high reflectance in presence of ferrous minerals. In Figure 4.9, light blue yellow- colour represents outcrops and blue areas represent vegetation. Light green areas highlight hydrothermal alteration in outcrop rocks.

4.2.1.3 Principal Component Analysis (PCA)

Vegetation density is a limiting factor when detecting and mapping hydrothermal altered rocks by band rationing. In order to minimize this limitation a spectral unmixing technique, as Principal Component Analysis (PCA) was applied.

PC1 explains 94.5% of the total variance of the data, as shown in Table 4.1. This PC is composed of positive values of all 6 bands and is being responsible for the overall scene brightness. PC2 contains 3.9% of the original data variance and PC3 represents just 1.4%. The firsts three PC that contain the most data variance was combined in an RGB composite (Figure 4.11) and it is useful for lithological mapping purposes. Green-yellow colours represent granite outcrops, while blue colour represents metasediments; purple represents vegetation and light blue colouration represents water bodies. Light green areas highlight hydrothermally altered rocks.

4.2.2 Discussion of Aeromagnetic Results

4.2.2.1 Total Magnetic Intensity (TMI) Map

The total magnetic field intensity map is presented as total field intensity. From these Figures, magnetic anomalies both short and long wavelengths were interpreted within the study area. These interpreted anomalies are represented by magnetic highs and lows respectively (Figure 4.12).

4.2.2.2 Residual Magnetic Intensity, RMI

Residual Magnetic Intensity (RMI) level in the study area ranges from -122.6 to 57.7 nT with the mean value of -32.45 nT. Negative anomalies were observed in the area which may be due to the present of low magnetic rocks (e.g. shale, sandstone, limestone) in the area, that are noted for low magnetic signatures or magnetic rocks at great depth. By removing the regional magnetic anomaly (Figure 4.14) from the measured anomaly, negative RMI values were obtained. The residual magnetic field intensity data was gridded using the minimum curvature method to highlight near surface anomalies. The residual magnetic image (Total Magnetic Intensity (TMI) -IGRF) showed the difference in locations of high and low magnetic intensities and many crustal magnetization patterns (Figure. 4.14).

The Residual Magnetic Intensity (RMI) map (Figure 4.14) emphasizes the intensity and the wavelengths of local anomalies. The rock formations at low magnetic latitude are magnetized parallel to the Earth's magnetic field; the area around Kopar, JauroGarmaho, Peshiep, Kopbepand, Kurgwi, Shandam, Yalwa, Kwande and Namu is characterized by high magnetic susceptibility and short wavelength anomalies, this signature is commonly associated with basement rocks. Area around Anzwa, Ugba, ZakiBiam, Sankara, Chonku, Ngbebe, Toskundi, Tunari, Bayawal and Nwarara are characterized by low magnetic susceptibility and both long and short wavelength anomalies. Donga,

Mbusa, AbakoAvermum, Sankara, Dooga, NorjjoGankoi, and Zaga areas are characterized by moderate magnetic susceptibility and short wavelength anomalies. Akwana and Fiyayi is also characterized by high magnetic susceptibility bodies and short wavelength anomalies, while nearby Hawe, Hundu, Apar, Wukari and Chonku is characterized by high magnetic susceptibility and long wavelength anomalies. A NE-SW trending low magnetic susceptibility is observed at Akahana, Tunga, Keffin, Awe, Adawa, Amafan through Ibi, Shinye, Yamere to Dampar, Kishr, Wuro Jam; Gassol. Bangalala and Giden Shehu is characterized by both long and short wavelength with high magnetic susceptibility, while Gidan Tata, BakinChiawa, Bembem, Shamanajar and Ajikemai is characterized by moderate to low magnetic susceptibility.

Gidan Tata, Bakin Chiawa, Bembem, Shamanajar and Ajikemai areas are interpreted to be sedimentary environment that has undergone mobilization of magnetic minerals such as magnetite and hematite. Akahana, Tunga, Keffin, Awe, Adawa, Amafan through Ibi, Shinye, Yamere to Dampar, Kishr, Wuro Jam and Gassol. Bangalala and Giden Shehu are interpreted to be area of igneous intrusive rocks that has undergone tectonism leading to the destruction of magnetic minerals and emplacement of intrusive rocks. Akwana, FiyayiHawe, Hundu, Apar, Wukari and Chonku are interpreted as areas of intense structural activities with intrusive rocks and occurrence of feroginized sandstone; Hawe, Hundu, Apar, Wukari and Chonku have thicker sedimentary cover when compared to Akwana and FiyayiHawe. The NE-SW stretching low magnetic amplitude is interpreted as Akahana, Tunga, Keffin, Awe, Adawa, Amafan through Ibi, Shinye, Yamere to Dampar, Kishr, Wuro Jam and Gassol. Bangalala and Giden Shehu are interpreted as zone of thick sediment cover is high faulting and fracturing and thermal activities during the santonian orogeny. Kopar, JauroGarmaho, Peshiep, Kopbep and, Kurgwi, Shandam, Yalwa, Kwande and Namu are interpreted to be zones igneous environment (Basement Complex). Jangwa, Agana, Madakin, Azaza, GidanShahu and

Bangalala and Akiri are interpreted to be areas of thick sediment cover and ferruginized sandstone (iron oxide element is present in them), but Gindan Shehu and Bangalala is interpreted to as having shallow magnetic sources and intense fracturing and faulting.

4.2.2.3 Reduction to the Equator (RTE)

The RTE magnetic anomaly map (Figure 4.15) shows both low and high magnetic frequencies representing points of low and high magnetic signatures respectively in the area. Both RMI (Figure 4.15) and the reduction to the Equator (RTE) image (Figure 4.16) display similar magnetic features, but there is a shift in orientation of the anomalies as observed around Chidiya, Mayo, Kwawu, Nafuche (RM in Figure 4.15), there is also a reduction in magnetic susceptibility as observed around Akiri, Azara, Agana, Jangwa and Uzam. The RTE map shows more significant features such as structures and lithology in the magnetic signature than the residual magnetic intensity map. At the central zone (CB in Figure 4.15) some features observed in the RMI at Yamere, Shinye, Dampar, Wuro Jam, Kuka, Adawa, Awe, Akete, Tunga, Akahana and Abuni are now seen as linear features trending in the NE - SW. Moreover, other features (e.g. the low magnetic signature (CB1 in Fig. 4.15) and high magnetic signature (CB2, CB3, CB4 and CB5 in Figure 4.15) which are not clearly seen in the RMI image (Figure 4.14) are seen in the RTE. Another clear example is the linear magnetic signature (LM in Figure 4.15) at the south eastern part of the area, around Ibi, Wurbo, Bako, Gondo, Adugu, Maikarfi, Zaga and Jimeta.

The RTE image displays the highest magnetic intensity within the Central Benue Trough trending NE SW from Hawe, Akwana, Fiyayi through Apa, Gindan Kagwa, to Nasarawa, Nafuche Kwararfa. It has an average peak of about 309.2 nT. Clear lithological boundaries are also observed in the image. These boundaries are observed from the sharp contrast in the magnetic signature on adjacent magnetic bodies. The high frequency magnetic anomaly at the western part of the area was

interpreted as the magnetite-rich formation and was delineated as the volcanic rocks (Nigerian Geological Survey, 2005). Numerous NE SW geologic contacts (C1 to C6 in Figure 4.15) are defined within the Central Benue Trough, and are interpreted to be structurally controlled by fault systems that formed during the basin forming processes. Contact C1 and C6 are interpreted to be the contact between the Central Benue Trough and Eastern Nigerian Massif and Northern Nigerian Massif. Three major fault systems are observed within the RTE map (F1 to F3 in Figure 4.15). Fault F1 extends from Bambem to Shinye with a NW – SE trending fault plain. This fault is interpreted to have formed during the late phase of basin forming tectonic activities. Fault F2 and F3 are interpreted to be have resulted from post basin tectonics. The RTE map was draped on a 3D topographic map. Draping the RTE image over the digital elevation map (DEM) and viewing it in 3D helped to visualize the relation between the sandstone and the elevation of the area.

Within the Central Benue Trough, the highest elevated area is observed to have the highest magnetic susceptibility values ranging from 14.6 to 570.8 nT (Figure 4.16), these high elevated and magnetic amplitude is interpreted to have resulted from the porphyritic granite and new basalt rocks know to occur around the contact between the Central Benue Trough and the Eastern Nigerian Massif, they are aligned in a NE – SW directional trend. The intermediate magnetic amplitude has an average topographic value range of 130.5 to 181.8 m, these areas is interpreted to be thick sediment units that's made up of thick layers of ferruginized sandstone. The central part of the basin has the lowest topographic values (<130 m) and also recorded low magnetic amplitude, this is interpreted to a thick sediment zone that's highly fractured forming the major control of the river Benue.

4.2.2.4 Analytic Signal

Folds and sills are observed around Yamere, Shinye (FD2 in Figure. 4.17), Dampar, Auro, Nasarawa Dundewa, Kishr and Gassol (FD1 in Figure 4.17). Numerous longitudinal bodies trending NE-SW is also observed at Bangalala and Giden Shehu. Akwana and Fiyayi, Akahana, Tunga, Keffin, Awe, Adiere areas is seen to have numerous magnetic bodies indicative to igneous rocks such as porphyritic granite. NW-SE trending structures is observed at Chonku, Mbusa, Agbemda, Sankara, Wukari and ZakiBiam (ST in Figure 4.17); while, Kopar, Jauro Garmaho, Peshiep, Kopbepand, Kurgwi, Shandam, Yalwa, Kwande, Namu, Anzwa, Chan Gasuwa, Wurbo, Bako, Gidan Idi, Tunari, YerimaBaya, Bako, Gbakpo, Ugba, Maikarfi, Zaga, Mindi, Mbusa, ZakiBiam, Avermun, Dooga, Mararaba and GidanUsumanu is interpreted to be characterized my high amplitude magnetic bodies. High amplitude magnetic body trending NE-SW is also observed stretching from Janka to Bembem. The high amplitude magnetic zone CB if Figure 4.16 above is seen be better interpreted in the analytic signal map, which highlights GindanKagwa, Gada Mayo, Anzwa, Gidan Idi (IG1); Nafuche, Kwararfa (IG2); Apar, Hundu, Fiyayi, Akwana, Tunga, Akahana, Ayere, Adawa and Hawa (IG3 in Figure 4.17).

The low magnetic signature was delineated to be the thick sediment while the intermediate is interpreted as ferruginous sandstone. In general, the analytic signal image (Figure 4.17) revealed the different lithological units and geological structures in the area. Analytic signal image was draped over the digital elevation map (DEM) (Figure 4.17) and there appears to be a greater correlation between the highlands in the area and the high magnetic signature observed. These relatively high magnetic amplitude observed to be associated with the highlands are interpreted as the basement rocks, intermediate magnetic amplitude is observed to be associate with moderate elevations and is

interpreted as sandstone and magnetic mineral (magnetite and hematite) enrichment areas; while low magnetic amplitude is associated with lowlands.

4.2.2.5 First Vertical Derivative (FVD)

The colour and grey scale vertical gradient images of the residual magnetic intensity (Figure 4.18a & b) enhanced the image by showing major structural and lithological detail which was not obvious in RMI image (Figure 4.14). Thus, the colour and grey-scale images complement each other.

Prominent regional faults and fracture systems were observed at Anzwa, Chan Gasuwa, Wurbo, Bako, Gidan Idi, Tunari, Yerima Baya, Bako, Gbakpo, Ugba, Maikarfi, Zaga, Mindi, Chonku, Mbusa, ZakiBiam, Avermun, Dooga, Mararaba and GidanUsumanu, all located at the southeastern part of the study area; these areas is characterized by clusters of high frequency bi-polar bodies and its interpreted to have resulted from basement rocks of the Eastern Nigerian Massif. Similer structure is observed at the southwestern part of the study area, around Kopar, JauroGarmaho, Kopbep and, Kurgwi, Shandam, Yalwa, Kwande and Namu; these signatures were interpreted to have resulted from the basement rocks of the Northern Nigerian Massif. The central part of the study area is characterized by both long and short wavelength bodies, these bodies are characterized by both high and low magnetic susceptibility; this area is interpreted as to fall within the Central Benue Trough. The areas around Akwana, Fiyayi, Akahana, Keffin, Tunga, Adawa, Adiere and Ugba is characterized by high frequency anomalies and is interpreted to have resulted from volcanic rocks know to outcrop around the area (Akande *et al.*, 1988).

The FVD map helped to attenuate broad, more regional anomalies and enhance local, more subtle magnetic responses because of their sensitive to shallow magnetic source bodies and contacts (Gunn, 1997). These is observed within Central Benue Trough where shallow magnetic bodies area

interpreted around Bangalala, Giden Shehu, Amar, Kishr, Dampar, Wuro Jam, Nasarawa Dundewa, Chidiya, Wukari, Chonku, Hundur, Apar, Ibi, Kukq, Janka, Ajikami, Azara, Jangwa and Agor, these areas is interpreted to host shear zones and intrusive rocks emplaced during the satonian orogeny. Major faults/fractures within the study area were interpreted stretching NE-SW from Kuka to Bangalala, numerous faults are observed stretching from Giden Shehu to Bangalala. NE-SW trending faults are interpreted stretching from Uzam to Janka and another from Janka to Ajikemai. There is also a major fault stretching from Shinye to Dampar; these regional faults systems in interpreted to have formed during the opening of Gondwana Supercontinent.

The contact Northern Nigerian Massif - Central Benue Trough, and the contact Central Benue Trough – Eastern Nigerian Massif is also well defined in the FVD map. The contact between Northern Nigerian Massif and Central Benue Trough within the study area extends from Namu, through Kwande, Damshin, Yalwa, Gongwan and ended at Garkawa; while the contact between Central Benue Trough and Eastern Nigerian Massif within the study area extends from Sankara, Mbusa, Ngbebe, Tunari, Chan Gasuwa, Wurbo down to Bako. The structures ST1 as observed at Chonku, Wukari, Mbusa, Sankara, Agbemda is also observed at Chidiya, Gada Mayo, Wurbo, Bako and Chan Gasuwa (ST2); thus, indicating that the contact between the Central Benue Trough and Eastern Nigerian Massif is characterized by NW – SE trending structures.

4.2.2.6 Upward Continuation

Figures 4.19a to c show the continued upward to 100 m, 500 m and 800 m, respectively. They show images of the magnetic intensity that would be obtained assuming the data were recorded at heights of 100 m, 500 m and 800 m higher than the original datum the data was collected. In physical terms, as the continuation distance is increased, the effects of smaller, narrower and thinner magnetic

bodies progressively disappear relative to the effects of larger magnetic bodies of considerable depth extent. As a result, upward-continuation maps give the indications of the main tectonic and crustal blocks in an area.

Comparing the figures, the 100 m upward continuation for the RTE image (Figure 14.19a) shows similar features as seen in the RTE image (Figure 14.19b). Thus, the magnetic body producing the anomaly may be at a deeper depth other than the 100 m depth. Moreover, comparing the 500 m and 800 m upward continuation images (Figure 14.19c) with the RTE image and 100m upward continuation image (Figure 14.19a and 14.18b respectively) it is seen that most sharp features in figure 14.19a & b are not seen in Figure 14.19c. Prominent is the sharp linear feature (L and L3 in figure14.18a & b) at the north eastern part; around Bangalala, Giden Shehu and Amar is not visible in upward continued maps of 500m and 800m. This is also observed at Abuni, Adawa, Adiere, Tunga, Akwana area (L2 in Figure 14.19a to c); Yamere and Shinye (L2 in Figure 14.19a to c); Ajikemai (L6 in Figure 14.19a to c); Anzwa, Gidan Idi, Wukari (L5 in figure 14.19a to c) and in Jibu and Wuro Jam (L4 in Figure 14.19a to c). This may indicate that the signature is coming from a magnetic body at shallow depth than the 500 or 800 m.

Prominent bodies believed to be situated at a deeper depth other that the 800 m is also observed in the images. A clear example is the dome shaped body labeled DJ in Figure 4.19a to c as seen in all the images and others indicating that the causative bodies are deep seated.

4.2.2.7 Tilt Derivative

It is observed that the zero contours estimate the location of abrupt changes in magnetic susceptibility values. The zero contour lines in this grid (Figure 4.20) are represented by a yellow colour interpreted as faults, folds are indicated by red lines, contacts as blue lines and polygon and

thrust fault are indicated by green lines. The FVD map of the study area was also used to map additional structures.

TDR derived from RTE Figure 4.20a displays most structural feature of the area such as the faults, contacts and to some extent the shape of some lithology. Some structural lineaments (faults) e.g. were delineated by observing the abrupt change between the positive and negative magnetic anomalies (Figure 4.20b), the maps better enhanced the faults within the study area. The NW – SE trending fault systems that characterized the Benue Trough and Eastern Nigerian Massif is better enhanced. The thrust fault at the central part of the Trough (green lines) mapped is interpreted to have formed during the opening of Godwana that resulted in the forming of the Benue Trough while the fold (red lines) are interpreted to have formed during the santonian orogeny that resulted in the deformation of the basin and emplacement of mineral forming hydrothermal fluids in faults and displacements. The FVD of RTE enhanced folds which were not seen in the TDR map. The qualitative and quantitative interpretation of the magnetic data was also used to map geologic contacts and lithologies based on their magnetic response, the resulting interpreted lithologies was then correlated with the regional geologic map of the study area so as to produce an integrated geologic map. The lithologies (e.g. GG, b, bb, M, OGp, bG and seen in Figure 4.20a) in the area are accentuated. Prominent of these features are the ones marked with blue polygon, OGp (Figure 14.20a) at the south-eastern part of the area and this is interpreted as the basalt with some associated volcanic rocks.

In attempt to identify the structures and geology of the area, recognizable patterns from the RMI and enhanced maps were first observed and related to their possible physical causes. Furthermore, the geophysical interpretations were properly correlated with available geological publications, topography and geological data of the area to actually confirm the interpreted structures. From the results of enhanced aeromagnetic maps, we were able to distinguish the magnetic responses

in the geology due to the difference in magnetic susceptibilities, structures and deformation styles of the magnetic units in the area. The area was divided into magnetic domains (regions) based upon the magnetic intensities, structural styles, and geological features. Boundaries of the individual lithological domains coincide with the abrupt changes in the magnetic intensities and orientations were delineated. The division was also on the basis of interpreted subsurface geology and structure, lineament patterns, and circular/curve features described in the previous figures.

Figure 4.20c shows the interpreted geological structures in the area delineated from the magnetic dataset and superimposed on the TDR image. This map gives a rough idea about the geological structural and lithology deformation of the area. Figure 4.21 reveals enhanced structural features that include faults, folds, lithological contacts and fracture systems in the study area.

Lineaments were extracted from the FVD map to add structural interpretation and evaluate lineament density. The lineaments are marked in black ticks while dykes and sills are marked in arched curves and Figure 4.22b shows the superimposed lineament, mineral and location map. The orientation and length of the lineament extracted from the Vectorization lineament map (Figure 4.22a) were displayed in a rose diagram to analyze the spatial distribution of lineaments. This was done to enhance smaller structures that are difficult to map by qualitative interpretation.

The rose diagram (Figure 4.23) shows that the structures within the study area trend majorly NE-SW and EW with minor NW-SE trend. The analysis shows that the Massif of the study area is characterized by NE-SW and EW trending structures, while the Central Benue Trough is characterized by NE-SW and NW-SE structures.

Intensity of deformation is evaluated using the lineament density map (Figure 4.24). Areas that have high lineament density indicates high deformation and closer to basement rocks, while

areas with less lineament density indicate low deformation with plane grounds mainly composed of sediments. Areas of intense deformation are seen within the Eastern and Northern Nigerian Massif. The area around Akwana, Hawa, Ugba, Tunga, Akahana, AdawaAyere and Abuni also reflects high deformation. Areas of moderate structural deformation include Gidan Shehu, Bangalala, Yamere, Shinye, Ibi, Wuro Jam, Kishr, Jibu, Ajikemai, Bembem and Janka; while areas of low structural deformation are observed at Amar, Kuka, Kwawu, GidanKagwamJangwa, Gidan Tata, BakinChiawa, Uzam, Azara, Akiri, Adi, Amar, Hundu and ZakiBiam.

Structural complexity is important in the formation of traps for mineralization. High deformed sediments could lead to the destruction of stratigraphic traps and enhance the occurrence of structural traps but due to its intensity it could yield leakage of traps due to micro faults or total destruction of structural trap, hence, moderately deformed areas host better structural traps. Gidan Shehu, Bangalala, Yamere, Shinye, Ibi, Wuro Jam, Kishr, Jibu, Ajikemai, Bembem and Janka, Kuka, Kwawu, GidanKagwamJangwa, Gidan Tata, BakinChiawa, Uzam, Azara, Akiri, Adi, Amar, Hundu and ZakiBiam show structural complexity suitable for the formation of structural traps within the study area, while areas of high to moderate deformation within the Central Benue Trough is interpreted to serve as good conduit for hydrothermal fluids forming mineralization, hence is recommended for ground-truthing. The areas of high structural complexity (lineament density) within the Central Benue Trough were mapped as areas of great potential to host mineralization.

4.2.3 Discussion of Ground Magnetic Results (Zone 1)

4.2.3.1 Digital Elevation Map

Elevation column extracted from the ground magnetic datasets was used to create a digital elevation map using Oasis Montaj software. Figure 4.27 shows the digital elevation model, representing the

elevation of the study area; it is described to be relatively flat with small ridges at the western and eastern part of the study area. The terrain ranges from 178 m to 217 m above mean sea level. The high-lands trends NE-SW and NW-SE being truncated by a valley at the central part of the study area. The lowlands have an average elevation of 188 m above mean sea level and are occupied by fractured shales.

Figure 4.28 is the observed magnetic intensity anomaly map obtained after diurnal variation correction was removed from the measured field during the ground survey. The observed magnetic intensity ranges from 33851 nT to 33865 nT. The northern part of the study area is characterized by high magnetic intensity variation, while the southern part is characterized by low magnetic intensity variation. To obtain the residual field reduced to equator, IGRF model magnetic field was removed from the observed magnetic intensity and gridded using the minimum curvature algorithm.

Residual field Reduced to equator map (Figure 4.29) was used to delineate lithological units exclusively and three responses were identified; low, intermediate and high magnetic responses. The magnetic signature also be grouped further into very low (116 to 119 nT), fairly smooth positive (119 to 120 nT) and high positive (120 to 126 nT) susceptibilities. The conglomerate ironstone shows higher magnetic response, while the shale units show lower magnetic response. The general high magnetic response within the study area is interpreted as enrichment of magnetic minerals (magnetite and hematite) by action of hydrothermal fluid that lead to the emplacement of mineral deposits.

4.2.3.2 Analytic Signal Map

Figure 4.30 is the analytic signal map which shows well-defined and positioned magnetic signatures as compared to the TMI and RTP maps. The effect of remanence (RM) in the residual reduced to equator map (Figure 4.29) has been corrected by putting a high over the top of any magnetic anomaly (high or low) regardless of the direction of magnetization. Three magnetic signatures have been

mapped from the analytic signal map. High magnetic amplitude (CI) correlates to a conglomeratic ironstone. Intermediate magnetic amplitude (SL) is correlated to the silica rich and altered limestone. Low magnetic signature (IS) which is bounded by the intermediate magnetic signature is also correlated to the altered indurated shale unit.

4.2.3.3 First Vertical Derivative Map

Figure 4.31 is the First Vertical Derivative (FVD) map of the RTP which is displayed in raster colour to enhance interpretation. The FVD filter has been useful in sharpening short wavelength magnetic anomalies at the expense of high wavelength magnetic anomalies making it useful in elevating textural variation in the data. The FVD sharpen both deep and shallow structures and it is best in characterizing the regional structures within the study area. A major regional NE-SW fault (F1) is mapped at the southern part of the study area; this fault is also visible in the airborne magnetic interpretation. The structures within the area have a NE-SW regional trend, with minor NW-SE and NS structures. The NE-SW structures are interpreted as deeper structures, while the NW-SE and N-S structures are interpreted as shallow structures of interest.

4.2.3.4 Apparent Susceptibility Analysis

The apparent susceptibility analysis of the residual field reduced to equator was carried out so as to highlight shallow magnetic variation which is indicative of thermal alteration. As temperature increases, magnetic minerals are destroyed, therefore shallow magnetic lows are indicative of thermally altered regions.

The interpretation of the apparent susceptibility map (Figure 4.32) shows numerous thermally altered zones (depletion in magnetism). These altered zones result from an increase in temperature that results from hydrothermal fluids that deposit lead-zinc ores. The temperature increase destroys the magnetic minerals in rocks and these minerals are usually aligned in the direction/trend of the

associated mineralization, and demagnetize structures where delineated within the depleted magnetic zones. The regional structures are interpreted to trend NE-SW, while the shallow structures of interest align N-S, NW-SE and NNE-SSW. The structures within the magnetic depleted zones MD at the western part of the study area is of major interest as this area shows magnetic depletion and host structures which trending N-S. These structures are also evident at the surface where the exposed shale rocks are highly fractured (Figure 4.33). The VLF interpretation was carried up to majorly target conductive structures within these areas.

4.2.4 Discussion of Ground Electromagnetic Very-Low Frequency (EM-VLF) Results (Zone 1)

4.2.4.1 Profile Line 1

Profile Line-1 has a total length of 3000 m and has E to W orientation straddling the alteration and interpreted structures from magnetic dataset. A total of 300 data points were used for the inversion and has produced current density (conductivity) ranges of -10 to +10 % with optimum depths of around 45 m. Interpreted 2D model section for this line is given in Figure 4.34.

The section can be separated as zones and is interpreted as the first zone >7.5 % (Figure 4.34) representing zone of high conductivity (current density), interpreted as zone of great potential of hosting conductive minerals as the host rock (shale) is not conductive. This anomalous zone is divided into two (2) subzones, the first (**a** in Figure 4.34) extend from the surface to a depth of 18m and is located between station 0 and station 250 (between 0m and 250m on the surface, where the measurement of survey line starts). The second anomalous subzone (**b** in Figure 4.34) extends from the surface to a depth of 40m and is located between station 875 and station 1500, this zone has a

horizontal thickness of 625m. The high of these zones is interpreted to have resulted from conductive bodies at depth.

The second zone with current density range of 2.5 to 7.5% with three anomalous subzones **c**, **d** and **e** (Figure 4.34). Anomalous subzone **c** has a depth to top of about 30m and extends to depth >40m, it is located between station 1500 and station 1750 and has a horizontal thickness of 250m. Anomalous subzone **d** occurs between station 1750 and station 2375 and it extends from the surface to a depth of about 30m within a thickness of about 250m. Based on the signal its source is interpreted to be truncated (highly fractured). Anomalous subzone **e** is located between station 2500 and station 2750, it has a thickness of about 250m and extends from the depth of 10m and terminates at a depth of 20m.

The third zone has current density ranges of 0 to 2.5% (**f** in Figure 4.34). It has a relative thickness of about 500m and is observed between station 375 and 875. The zone is interpreted as indurated shale that is highly affected by alteration as a result of the hydrothermal fluids and could consist of veinlets. This result is also supported by the magnetic profiles which show numerous faults across the study area.

4.2.4.2 Profile Line 2

Profile Line-2 has a total length of 3000 m. A total of 300 data points were used for the inversion and has produced current density (conductivity) ranges of -10 to +10 % with optimum depths of around 48m. Interpreted 2D model section for this line is given in Figure 4.35.

The first interpreted zone >7.5 % (**a** in Figure 4.35) representing zone of high conductivity (current density), is observed between station 750 and station 1000. It has an approximate thickness of 50m and is located at a depth of 20m. This zone is interpreted to be surrounded by highly indurated shale

that has imprints of associate minerals such as pyrite, siderite and chalcopyrite, along with veinlet of lead and quartz.

The second zone (**b** in Figure 4.35) with current density range of 2.5 to 7.5%, is located between station 250 and 500 and has an approximate thickness of 200m. Its depth to top and bottom is approximately 10m and 20m respectively. This zone is interpreted as conductive zone with relatively high amount of gange mineral (e.g. quartz).

The third layer has current density ranges of 0 to 2.5% (**c** in Figure 4.35), it is observed surrounding zone **a** and **b**, and between station 1500 and 2000, extending from the surface to depth greater than 48m. The zone is interpreted as altered shale and could consist associate minerals of lead deposits and veinlets. The low current density zone (<0%) is interpreted as fresh shale units, this zone is defined by blue in Figure 4.35.

4.2.4.3 Profile Line 3

Profile Line-3 has a total length of 3000 m. A total of 300 data points was used for the inversion and has produced current density (conductivity) ranges of -10 to 10 % with optimum depths of around 45m. Interpreted 2D model section for this line is given in Figure 4.36.

The first interpreted zone >7.5 % (**a** in Figure 4.36) representing zone of high conductivity (current density), is observed between station 1500 and station 1750. It has an approximate thickness of 125m and its depth to top is 30m and it extends above 45m. This zone is surrounded by a broad zone (**b** in Figure 4.36) with current density ranging from 2.5 to 7.5%, this zone is interpreted as an indurated shale with associate minerals such as pyrite, siderite and chalcopyrite, along with veinlet of lead and quartz.

The second zone has current density ranges of 0 to 2.5% (c and d in Figure 4.36), it is observed at station 0 and 125 and between station 500 and 875, extending from the surface to depth greater than 45m. The zone is interpreted as altered shale and could consist of low percentage of associate minerals of lead deposits and veinlets and high concentration of gange mineral. The low current density zone (<0%) is interpreted as fresh shale units, this zone is defined by blue in Figure 4.36.

4.2.4.4 Profile Line 4

Profile Line-4 has a total length of 2580 m. A total of 258 data points was used for the inversion and has produced current density (conductivity) ranges of -10 to +10 % with optimum depths of around 40m. Interpreted 2D model section for this line is given in Figure 4.37.

The first interpreted zone >7.5 % (**a** in Figure 4.37) is representing zone of high conductivity (current density) observed between station 625 and 875 and extends from the surface to a depth of about 35m. This zone is surrounded by a broad zone (**d** in Figure 4.37) with current density ranging from 2.5 to 7.5%, this zone is interpreted as an indurated shale with associate minerals such as pyrite, siderite and chalcopyrite, along with veinlet of lead and quartz.

The second zone (**b** and **c** in Figure 4.37) with current density range of 2.5 to 7.5%, anomalous zone **b** is located between station 500 and 625 and has a depth to top and bottom is approximately 18m and 25m respectively. Anomalous zone **c** is located between station 1500 and station 1600 along profile 4. It has a depth to top of about 28m and bottom greater than 40m. This zone is interpreted as conductive zone with relatively higher amount of conductive body than gange mineral.

4.2.4.5 Profile Line 5

Profile Line-5 has a total length of 2960 m. A total of 296 data points was used for the inversion and has produced current density (conductivity) ranges of -10 to +10 % with optimum depths of around 40m. Interpreted 2D model section for this line is given in Figure 4.38.

The first interpreted zone >7.5 % (**a** and **b** in Figure 4.38) represents zone of high conductivity (current density). Anomaly **a** is located between station 750 and station 1100 and has a depth to top 10m and bottom extending beyond 40m. It has a relative thickness of about 250m therefore, is interpreted as having a thick conductive body at depth. Anomaly **a** is also interpreted as continues from Profile-Line 5 (**a** in Figure 4.38). Anomaly **a** is surrounded by a broa in Figure 4.38) with current density ranging from 2.5 to 7.5%, this zone is interpreted as an indurated shale with associate minerals such as pyrite, siderite and chalcopyrite, along with veinlet of lead and quartz. Zone **d** also has similar signature and interpretation as zone **c**.

Anomaly zone (**b** in Figure 4.38) with current density range of 5 to 7.5%, is located between station 2750 and station 2950 and has an estimated thickness of about 150m. Anomaly **b** has a depth to top of 0m and an approximately depth to bottom of 15m respectively. This zone is interpreted as conductive zone with relatively higher amount of conductive body than gange mineral. The low current density zone (<0%) is interpreted as fresh shale units, this zone is defined by blue in Figure 4.38.

4.2.4.6 Profile Line 6

Profile Line-6 has a total length of 3000 m. A total of 300 data points was used for the inversion and has produced current density (conductivity) ranges of -10 to +10 % with optimum depths of around 45m. Interpreted 2D model section for this line is given in Figure 4.39.

The first interpreted zone has a current density range of 2.5 to 7.5% (**a** and **b** in Figure 4.39). Anomaly **a** is located between station 2125 and station 2500 and extends from the surface to a depth of about 30m. It has an estimated thickness of about 625m with its high thickness observed at depth. Anomaly **b** is located between station 750 and 1000 with depth to top and bottom of 10m and 25m respectively. These anomalies (**a** and **b**) is interpreted as an indurated shale with conductive bodies associated with minerals such as pyrite, siderite and chalcopyrite, along with veinlet of lead and quartz.The low current density zone (<0%) is interpreted as fresh shale units, this zone is defined by blue in Figure 4.39.

4.2.4.7 Profile Line 7

Profile Line-7 has a total length of 2970 m. A total of 297 data points was used for the inversion and has produced current density (conductivity) ranges of -10 to +10 % with optimum depths of around 45m. Interpreted 2D model section for this line is given in Figure 4.40.

The first interpreted zone >7.5 % (**a** in figure 4.40) represents zone of high conductivity (current density). Anomaly **a** is located between station 250 and station 500. It extends from the surface to a depth of about 15m, having a thickness of about 150m. This zone is interpreted to be highly conductive and could have resulted from conductive minerals and/or water that percolate to the subsurface through surface fault systems observed around that area (Plate 4.0).

The second interpreted zone has a current density range of 5 to 7.5% (**b**, **c** and **d** in Figure 4.40a). Anomaly **b** is located between station 1250 and station 1500 and extends from a depth of about 15m to a depth of 35m and having a thickness of about 100m. Anomaly **c** is located between station 1500 and 1750 with an estimated thickness of 100m and depth to top of 30m. Anomaly **d** is located between station 2500 and 2750, having an approximate thickness if 100m and depth to top of 15m

with bottom depth of 25m. This zone is interpreted as conductive zone with relatively higher amount of conductive body than gange mineral. Zone **a**, **b**, **c** and **d** (Figure 4.40) is surrounded by current density range of 0 to 2.5%. This surrounding zone is interpreted as the contact aureole formed by the hydrothermal fluid that filled the faults and fractures. They may consist of associate minerals. The low current density zone (<0%) is interpreted as fresh shale units, this zone is defined by blue in Figure 4.40.

4.2.4.8 Profile Line 8

Profile Line-8 has a total length of 2980 m. A total of 298 data points was used for the inversion and has produced current density (conductivity) ranges of -10 to 10 % with optimum depths of around 45m. Interpreted 2D model section for this line is given in Figure 4.41.

Zone with >7.5 % (**a** in Figure 4.41) represents zone of high conductivity (current density). Anomaly **a** is located between station 500 and station 1000. It extends from a depth of 10m to a depth of 30m, having a thickness of about 625m. This zone is interpreted to be highly conductive.

The second interpreted zone has a current density range of 2.5 to 7.5% (**b**, **c** and **d** in Figure 4.41). Anomaly **b** is located between station 1500 and station 1750 and extends from the surface to a depth of about 25m. It has a thickness of about 250m. Anomaly **c** is located between station 1750 and 2000 with an estimated thickness of 100m and depth to top of 30m. Anomaly d is located between station 2000 and 2250, having an approximate thickness if 250m and depth to top of 15m and bottom depth of 30m. This zone is interpreted as conductive zone with relatively higher amount of conductive body than gange mineral. Zone **a**, **b**, **c** and **d** (Figure 4.41) is surrounded by current density range of 0 to 2.5%. This surrounding zone is interpreted as the contact aureole formed by the hydrothermal fluid

that filled the faults and fractures. The low current density zone (<0%) is interpreted as fresh shale units, this zone is defined by blue in Figure 4.41.

4.2.4.9 Discussion of Frasier Filter 2D Map

Figure 4.42 represent the variations of conductivity across the survey block. The conductivity values range from -10.7 to 9.1 numerous conductive fault systems were mapped within the surveyed block, major anomalies of interest are labeled AEM-1 to AEM-9. The choice of major was made by comparing structures within the Frasier filter 2D section and the Karous-Hjelt filter model section. The conductive structures trends majorly in the NE-SW direction, with minor N-S and NW-SE trends. The longest conductive fault (AEM-1) has a length of about 2330m, trending NE-SW and stretches from profile-line 1 to profile-line 6. AEM-1 has a very strong conductive response (>0.9 to 9.1), and it's also observed within the Karous-Hjelt filter model section of profile-line 1, 4, 5 and 6. AEM-1 is interpreted as the most potential mineralized target.

AEM-2 conductive structure cuts across profile-line 2, 3 and 4 and has a length of about 1080m. AEM-2 trends NE-SW and has a broad conductive anomaly at its northern end, this is also observed along the Karous-Hjelt filter model section of profile-line 4. AEM-3 is located east of AEM-1, it has a length of 1500m and extends across profile-line 3, 4, 5, 6 and 7. AEM-4 is a Y-shaped conductive fault system, it has a length of 1300m and cuts across profile-line 4, 5, 6 and 7. AEM-4 is visible is profile-line 7 in the Karous-Hjelt filter model section. Another Y-shaped conductive structure is AEM-5, it has a higher conductivity level than AEM-4. AEM-5 has a length of about 1400m and cuts across profile-line 5, 6 and 7. AEM-5 also shows a strong current density within Karous-Hjelt filter model section of profile-line 5, 6 and 7.

AEM-6 has a length of 1320m and cuts across profile-line 3, 4, 5 and 6. The conductivity across this fault is interpreted as truncated, hence forming some sought of a pinch and swell structure. Similar conductive structure is AEM-7 and AEM-8 which has lengths of 612m and 1000m respectively. AEM-7 cuts across profile-line 1 and 2, while, AEM-8 cuts across profile-line 1, 2 and 3. They are both located south of AEM-6 and also reflect high to moderate current density with Karous-Hjelt filter model section. AEM-9 has a broad anomaly with length of about 500m. It is also reflect high current density within profile-line 1 of Karous-Hjelt filter model section.

4.2.5 Discussion of Ground Electrical Geophysical Results (Zone 1)

4.2.5.1 Res/IP Line-1

Res/IP Line-1 has a total length of 500 m and, as indicated in the discussion of the previous chapter, it has W to E orientation straddling interpreted conductive structures. An interpreted 2D inverse resistivity and chargeability model section for this line is given in figure 4.44. A total of 234 data points was used for the inversion and has produced resistivity ranges of 13.2 to >434 Ohm.m and chargeability ranges of 0 to >140 msec, with optimum depths of around 48 m. The aim of the survey was to use the resistivity data to map the presence of fractures (weak zones) that could potentially act as conduits for hydrothermal fluids and to use the chargeability data to map chargeable responses indicative of sulphide mineralization.

It is clear from the Figure that the subsurface shows regions of low resistivity zones at shallow depth followed by regions of relatively medium and higher resistivity at depth. The resistivity section can be separated as layers and are interpreted as the first layer (top layer) with resistivity range of 13.2 to <97.1 Ohm.m resistivity representing the response of the top soil cover. This layer extends to a depth of 10m at the first electrodes (at 0m on the surface, where the measurement of imaging line starts)

and fades out around 200 to 220m along the survey line towards the E. The low resistivity of this layer is due to the salinity and high moisture content of the soil, this condition is justified by surface manifestations and its average thickness are determined as 10m.

The second layer has resistivity ranges of 21.7 to >434 Ohm.m, relatively higher resistivity; it starts from depths of >10m to 48m (maximum depth of this section). The high resistivity bodies with range 160 to >434 Ohm.m, within this layer in interpreted as highly indurated shale. At surface horizontal distances of 70, between 170 and 240, 270, 290, 340, 380 and 410m, the layer shows discontinuities along the profile and the layer is highly affected by alteration (defined by sharp contact between high and low resistivity body) as a result of the hydrothermal fluids, these discontinuities could be interpreted as faults.

Numerous chargeable bodies where mapped across Res/IP Line-1, they are ground into high chargeability – high resistivity anomalies and high chargeability – low resistivity anomalies, it is observed that the anomalies with high resistivity generally have higher chargeability values.

Chargeable anomalies **A**, **B**, **C**, **D**, **E**, **F**, **G** and **H** are areas with high chargeability and varying resistivity. Chargeable bodies **A**, **C**, **F**, **G** and H are characterized by low resistivity (ranging from 21.7 to 59 Ohm.m) and high chargeability signature (ranging from 40 to <100 msec); while, chargeable bodies **B**, **D**, **E** and **K** and characterized by moderate to high resistivity (ranging from 80–263 Ohm·m) and high chargeability (range >100 msec). Mineralization is generally characterized by high chargeability with low resistivity bodies in electrical imaging survey, therefore anomalous bodies **A**, **C**, **F**, **G** and **H** is of major interest. Geological lead-zinc ore occur with associate minerals such as quartz, siderite etc., these minerals are generally highly resistive, therefore bodies **B**, **D**, **E** and **K** are equally of interest as the high chargeability signature of the bodies could be as a result of

mineralization while the corresponding moderate to high resistivity could be as a result of its associate minerals.

4.2.5.2 Res/IP Line-2

Figure 4.44 gives the geo-electrical section of the ground beneath Res/IP Line-2, targeting interpreted conductive structures. The interpreted 2D inverse resistivity and chargeability model section for this line is given in Figure 4.45. A total of 269 data points was used for the inversion and has produced resistivity ranges of 19.6 to >316 Ohm.m and chargeability ranges of 0 to >42 msec, with optimum depths of around 48 m. As in the above section for Line 1, the true resistivity model section can be seen to exhibit two distinct resistivity zones, each segregated by a relatively flat boundary. In general, two zones are mapped: the relatively low resistivity of (19.6 to 64.6 Ohm-m) top layer and a resistive layer of resistivity >19.6 Ohm-m forming the bottom stratum mapped by the survey depth. The geological interpretation of the above layers is the top layer comprises of top soil cover of thickness of about 25 m at the western end of about 12.8m at the eastern end of the survey line. This layer as in above section (Res/IP Line-1) is affected by salinity and is with moisture content as a result of which it gives low resistivity response. Within this layer and at its bottom, at a distance of between 270 to 480 m along the profile, is a very low resistivity zone possibly the direct effect of seeping water down slope (elevation variation across the profile).

From the inverted sections, six zones of subsurface weakness (faults) are clearly apparent within the second layer of resistivity. The second layer has resistivity ranges of 96.1 to >316 Ohm.m, relatively higher resistivity; it starts from depths of 15m to 48m (maximum depth of this section). The high resistivity bodies with range >213 Ohm.m, within this layer in interpreted as indurated shale. The discontinuities (fault) across this survey line is observed at 30m, 110m, 170m, 210m, 340m, 380m

and 420m of horizontal distance starting from the first electrode. This fault zones have resistivity value range of 29.2 60 143 Ohm.m.

From the chargeability section, chargeable bodies **A, B**, **E**, **G** and **H** is interpreted to be continuous from Res/IP Line-1 as it also occurs in Res/IP Line-2 (Figure 4.45). Chargeable bodies **E**, **G**, **H** is characterized by high chargeability with low resistivity; while, chargeable bodies **A**, **B**, **I** and **J** is characterized by moderate to high resistivity and high chargeability. Chargeable bodies **D**, **C**, **F**, **K** is interpreted to have combined to form chargeable body I along Res/IP Line-2; while, a new chargeable body **J** appear to becomes larger and closer to the surface than in Res/IP Line-1. The increase in resistivity of bodies **A** and **I** is interpreted to be as a result of an increase in associate minerals (gange e.g. quartz).

4.2.5.3 Res/IP Line-3

Figure 4.46 show the geo-electrical section of Res/IP Line-3 across the targeted interpreted conductive structures. The interpreted 2D inverse resistivity and chargeability model section for this line is given in Figure 4.46. A total of 269 data points was used for the inversion and has produced resistivity ranges of 17.0 to >1703.0 Ohm.m and chargeability ranges of 0.0 to >112.0 msec, with optimum depths of around 48 m. The true resistivity model section also exhibits two distinct resistivity zones. The relatively low resistivity (17.0 to 64.3 Ohm.m) from top layer and a resistive layer of resistivity >64.3 to 1703.0 Ohm-m forming the bottom horizon mapped by the surveyed depth. The geological interpretation of the above layers is the top layer comprises of top soil cover of thickness of about 12.8m at the western end of about 7.0m at the eastern end of the survey line. This layer as in above sections is affected by salinity and is with moisture content as a result of which it gives low resistivity response.

From the inverted sections, the second layer has eight zones of weakness (Faults) which are highlighted in Figure 4.46. The second layer has resistivity ranges from 63.4 to 1703.0 Ohm.m, with the lower values found within the zone of weakness and the high resistivity values are interpreted as highly indurated shale with presence of highly resistive quartz veins running through it. The discontinuities (Fault) across this survey line is observed at 60m, 160m, 220m, 290m, 310m, 350m 370m and 420m of horizontal distance starting from the first electrode at the western end of the profile. This fault zones have resistivity value range of 63.4 60 237.0 Ohm.m.

Along Res/IP Line-3, chargeable bodies **I**, **J** and **E** is observed to be continuous from Res/IP Line-2. Chargeable bodies B is also observed but reflects low mineralization (low chargeability hen compared to other bodies across the Res/IP Line-3). Chargeable bodies **I** and **J** reflect low resistivity and high chargeability; while, chargeable body **E** reflects moderate resistivity and high chargeability. A new chargeable body of interest **Z** in interpreted across Res/IP Line-3, it has a very high resistivity value (>882.0 Ohm.m) and high chargeability (>96.0 msec), it is interpreted as potential mineralized zone with high percentage of highly resistive gange minerals.

4.2.5.4 Res/IP Line-4

Figure 4.47show the geo-electrical section of Res/IP Line-4 across the targeted interpreted conductive structures. The interpreted 2D inverse resistivity and chargeability model section for this line is given in Figure 4.46. A total of 269 data points was used for the inversion and has produced resistivity ranges of 9.2 to >833.0 Ohm.m and chargeability ranges of 0.0 to >28.0 msec, with optimum depths of around 48 m.

The top soil as observed in Res/IP Line-1, 2 and 3 is generally absent in Res/IP Line-4, this is in agreement with local geology as the surface across Res/IP Line-4 is an exposure of baked shale. Six

zones of weakness (Faults) interpreted in the resistivity section across Res/IP Line-4. The faulted zone has resistivity range of 9.2 to 121.0 Ohm.m and the fresh to baked to indurated shale unit has resistivity >121.0 Ohm.m. The discontinuities (fault) across this survey line is observed at 80m, 240m, 320m, 380m and 410m of horizontal distance starting from the first electrode.

From the chargeability section, chargeable bodies **B**, **I**, **J** and **Z** is interpreted to be continuous from Res/IP Line-3. Chargeable bodies **B**, **I** and **J** is characterized by high chargeability with low to moderate resistivity; while, chargeable bodies **Z** just like it is along Res/IP Line-3 has high chargeability and very high resistivity. Chargeable bodies at the western part of the Res/IP Line-4, at 50m and 150m were not highlighted as they have chargeability <12msec.

4.2.5.5 Res/IP Line-5

Figure 4.48 show the geo-electrical section of Res/IP Line-5 across the targeted interpreted conductive structures. The interpreted 2D inverse resistivity and chargeability model section for this line is given in Figure 15. A total of 268 data points was used for the inversion and has produced resistivity ranges of 3.1 to >536.0 Ohm.m and chargeability ranges of 0.0 to >58.9 msec, with optimum depths of around 48 m. This profile cuts across the northern end of the interpreted conductive structure AEM-1 and AEM-3.

The top soil as is absent in Res/IP Line-5 just as in Res/IP Line-4, this is also in agreement with local geology as the surface across both profiles falls within an exposure of baked shale. Six zones of weakness (faults) interpreted in the resistivity section across Res/IP Line-5. The faulted zone has resistivity range of 28.1 to 122.0 Ohm.m and the fresh to baked to indurated shale unit has resistivity >122 Ohm.m. A broad high resistivity body is observed at the western end of Res/IP Line-5. The

discontinuities (fault) across this survey line is observed at 140m, 220m, 360m and 400m of horizontal distance starting from the first electrode.

From the chargeability section, chargeable bodies **B**, **I**, **J** and **Z** is interpreted to be continuous from Res/IP Line-4. Chargeable bodies **B**, **I** and **J** is characterized by moderate chargeability with low to moderate resistivity; while, chargeable bodies **Z** which recorded high chargeability and very high resistivity across Res/IP Line-3 and 4 now record moderate chargeability of about 16.8msec and moderate resistivity of about 256.0 Ohm.m. The reduction is chargeability response is as a result of a decrease in chargeable minerals within the interpreted faults.

4.2.5.6 Discussion of Stacked Maps of Resistivity Imaging

Figure4.49 to 4.53 represents the variations of resistivity and chargeability from shallower level (depth of 12m) down to deeper horizons (depth of 48m) as attained by the imaging survey. This stacked plot sketched using data of selected depths, shows the relative variation of the resistivity and chargeability value of the whole area both laterally as well as vertically. As a general overview the area has low resistivity values with resistivity ranges of -43.9 to 2973.2 Ohm.m and chargeability with range -0.6 to 174msec. The maximum depth of penetration is 48m. The eastern part of the surveyed area is defined as the major chargeable axis (area with high concentration and volume of chargeable body), this is in agreement with the interpreted conductivity map from VLF-EM which shows that the major targeted conductive bodied (AEM-1 in figure 4.43) is at the eastern part resistivity/induced polarization survey area.

At depth of 12m (Figure 4.48), the volume of vein **I** is moderate with length and width of vein **I** being 87m and 28m respectively. The vein **G** has thinned out at depth of 18m while its daughter vein B is interpreted to have cut across the study area with a NE-SW trend. There is a reduction in the

volume of chargeable body **C** and **D**, which formed from **I.** The concentration of Chargeable body in **A** is generally higher. The orientation of **G** change from NW-SE to NE-SW, this is interpreted to have resulted from late phase of deformation, after the fault has been filled by hydrothermal fluid.

There are varying resistivity levels across the interpreted chargeable bodies, meaning once chargeable target is seen to show both high and low resistivity, this is interpreted to have resulted from segregation of hydrothermal fluid, leading to the separation of chargeable bodies of associated minerals (e.g. lead, quartze.t.c).

At the depth of 18m (Figure 4.50), vein **I** split forming vein **C** and **D**. vein **G** formed vein **A** and vein **B** by fluid flowing into shallow fault. Concentration of chargeable body slightly increase in **J'** but it has a reduced volume same as vein **J**. The connection between vein **E** and **E**' is discontinues. The length and width of vein **Z** looks to increase at depth of 18m when compared to its size at 24m.

At depth of 24m (Figure 4.51), Vein **I'** became more extensive, it joined with vein **K** forming vein **I** and also split forming vein **Z**. Vein **E'** became very extensive forming vein **E**, it also became thicker as then sits very close to vein **Z**. The concentration of chargeable body dropped massively in vein **J'**, while vein **J** increase in volume as it links up with vein **E'**. Vein **G** decrease in volume, with hydrothermal fluid flowing from **G** to a shallower fault zone west of it. This shallow fault zone forms the bottom of vein **A** which shows high concentration of chargeable body at depth 18m (Figure 4.49) and vanishes at 24m depth (Figure 4.51). At the depth of 24m, vein E'' continues, hence it has a depth to about 39m or more.

At depth of 39m (Figure 4.52), there is a reduction in the volume of **I**', **G**, **J'** and **E'**. The fault linking **J'** and **E'** reduced significantly in size. Vein **K** increased in sized and looks to form a small daughter vein east of itself. While, vein **Z** vanishes completely.

There are five major chargeable veins within the study area (**E, J, I, K** and **G** - Figure 4.53). These veins are named the mother veins as they are the source of chargeable body that's distributed within the study area. Vein **I** is observed at depth 48m with a trend of NNE-SSW, it has a length of 175m and width of 90m. Vein **K** is observed at the southern part of the study area, trending NNE-SSW with an estimated length of 80m and width of 60m. Vein **E'** has an estimated length of 151m and width of 51m, with a NE-SW trend. Vein **J'** has a length of 210m and width of 61m, with a NE-SW trend. Vein **E'** is interpreted to have been filed by hydrothermal fluid flow from **J'**. Vein **E', I, J'** and **K** is linked by a low chargeability zone (**X** in Figure 4.52) which lead to the formation of vein **J** as hydrothermal fluid filed a fault which in visible in the resistivity map. Vein **G** has an estimated length of 174m and a width of 58m, with a NW-SE trend. Vein **E''** looks to have formed from vein **E'**.

4.2.6 Discussion of Core drill results (Zone 1)

The result revealed numerous faulting within target depth. The fault is filled with quartz and there is an occurrence of chalcopyrite. When the quartz was broken, there are some amounts of lead zinc within the rock (Figure 4.54)

Drill point two (2) is located along RES/IP Line 3 in zone 1 (Figure 4.55), the target anomaly is a high chargeability with low resistivity anomaly/ highly indurate shale that's faulted is observed at target depth (Figure 4.55). The fault plan has no fill a small spec of chalcopyrite is seen (Plate 4.2).

4.2.7 Discussion of Voxel Modeling for Probable Reserve Estimation and Value Evaluation (Zone 1)

The three-dimensional voxel model was used to isolate chargeable bodies (Potential Mineralization) with chargeability >15msec which is regarded as anomalies of interest (Figure 4.57). The volume of the chargeable voxel was then computed and used for the reserve estimation. The advance windows-based Oasis Montaj target was used for the modeling.

The estimated volume of chargeable body is given as 853,250m^3. Correlating the regional and local geological studies with geophysics, the chargeable body is named as lead mineralization. In other to keep error to a minimum, a density of 6.4 g/cm^3 was used to compute the tonnage of the mineral deposit.

$$Volume\ of chargeable\ body\ =\ 853{,}250\ m3$$

$$Density\ of\ Galena\ mineral\ =\ 6.4\ g/cm3$$

$$Tonnage = V\rho$$

$$Tonnage = 853{,}250 \times 6.4$$

$$= 5{,}460{,}800\ tonnes$$

Loke and Baker, 1996; Marescot, et al., 2003 stated that the size of a chargeable anomaly is generally about half of the causative structure/bodies, therefore, half of the computed tonnage is the nearest estimate to the true tonnage of the interpreted mineralization. This is given as;

$$Nearest\ estimate = \frac{5{,}460{,}800}{2}\ tonnes$$

$$= 2{,}730{,}400\ tonnes$$

As at the time of writing this research, the price of lead at Indiamart is $467.1, therefore the estimated value of the surveyed area is calculated as;

$$Estimated\ value = 467.1 \times 2{,}730{,}400$$

$$= \$1.3\text{B}$$

4.2.8 Discussion of Ground Magnetic Interpretation (Zone 2)

4.2.8.1 Digital Elevation Map

Elevation column extracted from the ground magnetic datasets was used to create a digital elevation map using Oasis Montaj software. Figure 4.58 shows the digital elevation model, representing the elevation of the study area; it's described to be described as a gentle slope, dipping to the eastern part of the study area. The terrain ranges from 178 m to 217 m above mean sea level. The lowlands have an elevation average of 187 m above mean sea level and are occupied by shales and limestone.

Figure 4.58 is the observed magnetic intensity anomaly map obtained after diurnal variation correction was removed from the measure field during the ground survey. The observed magnetic intensity ranges from 33989.3nT to 34038.8nT. The northern part of the study area is characterized by high magnetic intensity variation, while the southern part is characterized by low magnetic intensity variation; hence there is a gradient decrease in magnetic intensity southward.

Residual field Reduced to equator map was used to delineate lithological units. The magnetic signature is grouped into low (<278.5nT), moderate positive (278.5 to 296.3nT) and high positive (>307.5nT) susceptibilities (Figure 4.60). The general high magnetic response within the study area is interpreted as an enrichment of magnetic minerals (magnetite and hematite) by action of hydrothermal fluid that lead to the emplacement of mineral deposits. A major NE-SW trending fault

(F1) is observed in the residual magnetic intensity map; this fault is interpreted as a deep fault and is also observed in the regional interpreted magnetic dataset.

4.2.8.2 Analytic Signal Map

Figure 4.61 is the analytic signal map (Zone 2); it shows two major high magnetic intensity structures with a NE-SW trend. This location of these structures coincides with that of the outcropping conglomerate ironstone bodies. The moderate magnetic intensity regions correspond to the highly indurated regions, especially at the western part of the study area and northeastern part of the study area, where the indurated nature result to the high resistance to weathering, causing the topographic highs. The moderate intensity count is as a result of magnetic mineral enrichment.

The low magnetic region at the central, northern and southern part of the study area is interpreted as magnetic depleted regions.

4.2.8.3 First Vertical Derivative Map

Figure 4.61is the First Vertical Derivative (FVD) map of the RTE residual magnetic intensity map (Zone 2). The FVD map shows a major NE-SW and N-S trending structures. The N-S structures are interpreted as shallow structures, while the deeper structures are NE-SE. the cross-cutting relationship between the NE-SW trending structures and N-S trending structures shows that the NE-SW structures are older and defined as structures forming during the opening of Gondwana Super continent, which resulted in the formation of the Benue Trough. The N-S structures formed during Santonian Orogeny.

4.2.8.4 Apparent Susceptibility Analysis

The interpretation of the apparent susceptibility map (Figure 4.63) shows numerous thermally altered zones (depletion in magnetism), these altered zones results from an increase in temperature that results from hydrothermal fluids that deposits lead-zinc ores. The maps show a major NNE-SSW with minor NNW-SSE contact. Higher intensity contacts are observed at the northern part of the study

area, than at the southern part. This is indicative of higher depletion of magnetism at the southern part of the study area. The VLF interpretation was carried up to majorly target conductive structures within these areas.

4.2.9 Discussion of VLF-EM Results (Zone 2)

4.2.9.1 Profile Line 1

Profile Line-1 has a total length of 1000 m and has E to W orientation straddling the alteration and interpreted structures from magnetic dataset. A total of 104 data points was used for the inversion and has produced current density (conductivity) ranges of -10 to +10 % with optimum depths of around 100 m. Interpreted 2D model section for this line is given in Figure 4.64

The section can be separated as zones and is interpreted as the first zone >5 % (Figure 4.64) representing zone of high conductivity (current density), interpreted as zone of great potential of hosting conductive minerals. Three anomalous subzones occur along the profile. The first **a** occur extends from the surface to a depth of 60m and is located between station 300 and station 400. The anomaly has an estimated width of 100m and is broad at depth.

The second **b** subzone with current density range of 0 to 2.5%, occur between station 600m and 700m with an estimated depth to top of 30m. The third **c** occurs between station 850m and 950m, it extends from the surface to a depth of 50m. The generally weak conductive response is interpreted as deep sited conductive structures within the study area.

4.2.9.2 Profile Line 2

Profile Line-2 has a total length of 1050 m. A total of 106 data points was used for the inversion and has produced current density (conductivity) ranges of -10 to +10 % with optimum depths of around 100m. Interpreted 2D model section for this line is given in Figure 4.65.

The conductive structures within this profile are generally weak with range of 0 to 2.5 %, this is indicative of deep sited conductive structures and high occurrence of gauge minerals. The first **a** occurs between station 100m and 250m while extending from the surface to a depth of 50m. The second **b** occurs between station 400m and 550m with a depth to top of 25m. The third **c** occurs between station 800m and 850m, it extends from the surface to a depth of 75m.

The fourth **d** anomaly has an average of 5 % current density. Extends from the surface to a depth of 50m and occurs between station 950m to 1000m.

4.2.9.3 Profile Line 3

Profile Line-3 has a total length of 1050 m. A total of 106 data points was used for the inversion and has produced current density (conductivity) ranges of -10 to +10 % with optimum depths of around 100m. Interpreted 2D model section for this line is given in Figure 4.66.

The profile has three major conductive zones, the first **a** has current density >5%, it is seen between station 150 and 250, extending from the surface to a depth of about 70m. The second conductive zone extends from the surface to about 100m, it has a current density range of 0 to 5%. The second **b** zone has an approximate with of 200m and occurs between station 300m and 500m.

The third **c** zone has the same extension as the second but a lower current density range of 0 to 2.5%, it occurs between station 600 and 800m.

4.2.9.4 Profile Line 4

Profile Line-4 has a total length of 1000 m. A total of 102 data points was used for the inversion and has produced current density (conductivity) ranges of -10 to +10 % with optimum depths of around 100m. Interpreted 2D model section for this line is given in Figure 4.67.

The first **a** interpreted zone 2.5 to 5 % representing zone of high conductivity (current density) is observed between station 200 and station 300 and extends from the surface to a depth of about 75m. This zone is interpreted as a indurated shale with associate minerals such as pyrite, siderite and chalcopyrite, along with veinlet of lead and quartz.

The second **b** zone with current density range of 2.5 to 5%is located between station 300 and station 600 and has a depth to top and bottom is approximately 20m and 100m respectively. The third **c** anomalous zone is located between station 520 and 650m which the fourth **d** anomalous zone is 750 and station 850 along profile 4, it has a depth to top at the surface and bottom greater than 50m. This zone is interpreted as conductive zone with relatively higher amount of gange mineral.

4.2.9.5 Profile Line 5

Profile Line-5 has a total length of 1060 m. A total of 107 data points was used for the inversion and has produced current density (conductivity) ranges of -10 to +10 % with optimum depths of around 100m. Interpreted 2D model section for this line is given in Figure 4.68.

There are three major conductive zones along profile 5 all has a current density range of 2.5 to 5 %. The first **a** is located between station 300 and 400, it extends from the surface to high depth with an estimated width of 100m. The second **c** with a width of 100m and is located between station 600 and 700. The third **d** conductive zone is located between station 790 and 900, it extends from the surface to a depth of about 75m. The conductive zones within this profile are interpreted as high conductive minerals with moderate occurrence of gange mineral.

4.2.9.6 Discussion of Frasier Filter 2D Map (Zone 2)

Numerous conductive fault systems were mapped within the surveyed block, major anomalies of interest are labeled BEM-1 to BEM-6. The choice of major was made by comparing structures within the Frasier filter 2D section and the Karous-Hjelt filter model section. The conductive structures trend majorly in N-S direction, with minor NE-SW and NW-SE trend. The longest conductive fault (BEM-1) has a length of about 600m, trending NW-SE and stretches from profile-line 1 to profile-line 4 and has a broad conductive anomaly. BEM-1 has a very strong conductive response (>2.3 to 22.2), BEM-2 conductive structure cuts across profile-line 1, 2, 3 and 4 and has a length of about 580m. BEM-2 trends NE-SW. BEM-3 is located west of BEM-2, it has a length of 600m and extends across profile-line, 2, 3 and 4. BEM-3 looks to be discontinues as it stretches northward, this may be due to variable increase in gange mineral or the filled fault is a pinch and swell structure. BEM-4 is a Y-shaped conductive fault system, it has a length of 600m and cuts across profile-line 1, 2, 3 and 4, it's also notably discontinues like BEM-3. BEM-5 trends NW-SE and is broad at its northern end. It has a length of about 800m and is very visible in the Karous-Hjelt filter model section.

Based on the interpretation of the VLF-EM survey, a sub-block of the ground magnetic and VLF-EM survey block was selected for ground resistivity and magnetic survey (Figure 4.69). The choice was made based on the interpreted magnetic structures and conductive structures interpreted from the ground survey. BEM-1 and BEM-3 was both the target of the electrical resistivity and induced polarization survey because they both recorded high anomaly when Frasier and Karous-Hjelt filter, especially between profile-line 4 and 5.

4.2.10 Discussion of Ground Electrical and Induced polarization Survey

(Zone 2)

4.2.10.1 Res/IP Line-1

Res/IP Line-1 has a total length of 500 m and it has W to E orientation straddling interpreted conductive structures. An interpreted 2D inverse resistivity and chargeability model section for this line is given in Figure 4.71. A total of 240 data points was used for the inversion and has produced resistivity ranges of 8.51 to >746Ohm.m and chargeability ranges of -78.6 to >414msec, with optimum depths of around 48 m.

It is clear from the figure that the subsurface shows regions of high resistivity zones at shallow depth followed by regions of relatively low and higher resistivity at depth. The resistivity section can be separated as layers and are interpreted as the first layer (top layer) with resistivity range of >392Ohm.m resistivity representing the response of the top soil cover. This layer extends to a depth of 7m occur from the first electrodes (at 0m on the surface, where the measurement of imaging line starts) and fades out around 230m along the survey line towards the E. this reflects the contacts as observed in both the magnetic and VLF interpretation.

The second layer has resistivity ranges of 8.75 to >106Ohm.m, relatively low resistivity; it starts from depths of >7m to 24m. The third layer has resistivity variation and reflects numerous faulting. The third layer shows discontinuities along the profile and the layer is highly affected by alteration (defined by sharp contact between high and low resistivity body) as a result of the hydrothermal fluids, these discontinuities could be interpreted as faults.

Chargeable anomalies **A, B** and **C** are areas with high chargeability and high to moderate resistivity. Chargeable bodies **D**, **E** and **F** are characterized by low resistivity (ranging from 8.51 to 57.8 Ohm.m)

and high chargeability signature (ranging from >203msec). Anomaly **A** and **B** is interpreted as bodies with high chargeable mineral and high occurrence of gange mineral, anomaly **C** has a moderate concentration on gange and chargeable mineral. **D, E** and **F** are interpreted as having high chargeable mineral with low concentration of gange mineral.

4.2.10.2 Res/IP Line-2

Figure 4.72 gives the geo-electrical section of the ground beneath Res/IP Line-2, targeting interpreted conductive structures. The interpreted 2D inverse resistivity and chargeability model section for this line is given in Figure 4.71. A total of 274 data points was used for the inversion and has produced resistivity ranges of 19.6 to >316 Ohm.m and chargeability ranges of 0 to >42 msec, with optimum depths of around 48 m. As in the above section for Line 1, the true resistivity model section can be seen to exhibit two distinct resistivity zones, each segregated by a relatively flat boundary. In general, two zones are mapped: the relatively low resistivity of (6.63 to 500 Ohm-m) top layer and a resistive layer of resistivity >145 Ohm-m.

From the inverted sections, two zones of subsurface weakness (faults) are clearly apparent within the third layer of resistivity. The second layer has resistivity ranges of 6.62 to 78.2Ohm.m; it starts from depths of 12.8m to 31m.

From the chargeability section, chargeable bodies **A**, **B**, **E** and **F** are interpreted to be continuous from Res/IP Line-1 as it also occurs in Res/IP Line-2 (Figure 4.72). All the bodies have similar signature as observed in Res/IP Line-1 except for **E**. The increase in resistivity of bodies E is interpreted to be as a result of an increase in associate minerals (gange e.g. quartz).

4.2.10.3 Res/IP Line-3

Figure 4.73 show the geo-electrical section of Res/IP Line-3 across the targeted interpreted conductive structures. The interpreted 2D inverse resistivity and chargeability model section for this line is given in Figure 4.73. Total of 270 data points were used for the inversion and has produced resistivity ranges of 6.38 to >380Ohm.m, with maximum depths of around 48 m. From the inverted sections, the second layer has three zones of weakness (faults) which are highlighted in Figure 4.73.

Along Res/IP Line-3, chargeable bodies **A**, **B**, **E** and **F** is observed to be continuous from Res/IP Line-2. Chargeable bodies **A** reflects low mineralization (low chargeability when compared to Res/IP Line-2). Chargeable bodies **F** reflects high resistivity and high chargeability indicative of an increase in gange/associate minerals; while, **B** indicate show is decrease in gange minerals as indicated by the decrease in resistivity.

4.2.11 Discussion of Core drill results (Zone 2)

The result from the drilling reveals numerous faulting with quartz filling the fault plane. Chalcopyrite was observed within the quartz observed at target depth (Figure 4.74).

Drill point four (4) was carried out along RES/IP Line 2 in zone 2. The target anomaly is characterized by high chargeability with low resistivity **F**. The result from the drilling (Point four 4) reveal numerous faulting with no fill along the fault plane. Small sample of sulphide mineral was observed around target depth (Figure 4.75).

4.2.12 Voxel Modeling for Probable Reserve Estimation and Value Evaluation (Zone 2)

The estimated volume of chargeable body is given as 502,310 m^3. Correlating the regional and local geological studies with geophysics, the chargeable body is named as potential lead mineralization. In

other to keep error to a minimum, a density of 6.4 g/cm^3 was used to compute the tonnage of the mineral deposit of lead (chargeable mineral).

$$Volume\ of chargeable\ body\ =\ 502{,}310\ \mathrm{m}^3$$

$$Density\ of\ Galena\ mineral\ =\ 6.4 g/\mathrm{cm}^3$$

$$Tonnage = V\rho$$

$$Tonnage = 502{,}310\ \times 6.4$$

$$= 3{,}214{,}784\ tonnes$$

Loke & Baker, 1996 and Marescot *et al*., 2003 stated that the size of a chargeable anomaly is generally about half of the causative structure/bodies, therefore, half of the computed tonnage is the nearest estimate to the true tonnage of the interpreted mineralization. This is given as;

$$Nearest\ estimate = \frac{3{,}214{,}784}{2}\ tonnes$$

$$= 1{,}607{,}392\ tonnes$$

As at the time of writing this research, the price of lead at Indiamart is $467.1, therefore the estimated value of the surveyed area is calculated as;

$$Estimated\ value = 467.1 \times 1{,}607{,}392 = \$750\mathrm{M}$$

CHAPTER FIVE

CONCLUSION AND RECOMMENDATIONS

5.1 CONCLUSION

Integration of airborne magnetic, satellite imagery analysis and ground geophysical survey was carried out to unravel the mineral potential of the study area which falls geologically within the Central Benue Trough. The desk study stage involved the acquisition of Landsat 8 imagery, processing of the imagery using geometric calibration, radiometric calibration and dark object extract, the images was also enhanced by the application of linear filters. Band combination, rationing and principal component analysis was then carried out in other to highlight altered rocks within the study area. These techniques highlight areas where concentration of minerals and assemblage of alteration minerals, as iron-bearing minerals, hydroxyl-bearing minerals and hydrated sulphates occur, discriminating altered from unaltered rocks. The altered rocks where mapped around Bangalala, Giden Shehu, Ajikeman. Kuka, Gessol, Akiri, Janka, Bembem, Wukari and Akwana. Band rationing was also used to map some major anomalous alteration at Gidan Shehu, east of Wukari, Kuka, Bambam, Uzam, Agor and minor anomalous alteration at Bangalala, Akwana and Dongwan. These areas where occurred hydrothermal alteration of the adjacent country rocks can be an indication of vein deposits, but not all ore bodies are accompanied by alteration. In way to validate this information, airborne magnetic interpretation was carried out to map structures of interest within these altered areas.

Airborne magnetic dataset was acquired from Nigerian Geological Survey agency, it was processed and filtered using tilt derivative, analytic signal, upward continuation, first vertical derivative, reduction to equator as an enhancement tools for delineation of the structural trends within the study

area. Results of the enhanced aeromagnetic maps, distinguished the magnetic responses in the geology due to the difference in magnetic susceptibilities, structures and deformation styles of the magnetic units in the area. The area was divided into magnetic domains (regions) based upon the magnetic intensities, structural styles, and geological features. Boundaries of the individual lithological domains coincide with the abrupt changes in the magnetic intensities and orientations were delineated. The division was also on the basis on interpreted subsurface geology and structure, lineament patterns, and circular/curve features described in the previous sections.

The area around Kopar, JauroGarmaho, Peshiep, Kopbepand, Kurgwi, Shandam, Yalwa, Kwande and Namu is characterized by high magnetic susceptibility and short wavelength anomalies, this signature is commonly associated with basement rocks. Anzwa, Ugba, ZakiBiam, Sankara, Chonku, Ngbebe, Toskundi, Tunari, Bayawal and Nwarara is characterized by low magnetic susceptibility with both long and short wavelength anomalies. Donga, Mbusa, Abako Avermum, Sankara, Dooga, Norjjo Gankoi, and Zaga are characterized moderate magnetic susceptibility and short wavelength anomalies. Akwana and Fiyayi is also characterized by high magnetic susceptibility bodies and short wavelength anomalies, while nearby Hawe, Hundu, Apar, Wukari and Chonku is characterized by high magnetic susceptibility and long wavelength anomalies. A NE-SW trending low magnetic susceptibility was observed at Akahana, Tunga, Keffin, Awe, Adawa, Amafan through Ibi, Shinye, Yamere to Dampar, Kishr, Wuro Jam; Gassol. Bangalala and Giden Shehu is characterized by both long and short wavelength with high magnetic susceptibility, while Gidan Tata, BakinChiawa, Bembem, Shamanajar and Ajikemai is characterized by moderate to low magnetic susceptibility.

Gidan Tata, BakinChiawa, Bembem, Shamanajar and Ajikemaiare interpreted to be area sedimentary environment that has undergone mobilization of magnetic minerals such as magnetite and hematite. Akahana, Tunga, Keffin, Awe, Adawa, Amafan through Ibi, Shinye, Yamere to Dampar, Kishr, Wuro

Jam and Gassol. Bangalala and Giden Shehu are interpreted to be area of igneous intrusive rocks that has undergone tectonism leading to the destruction of magnetic minerals and emplacement of intrusive rocks. Akwana, FiyayiHawe, Hundu, Apar, Wukari and Chonkuare interpreted as areas of intense structural activities with intrusive rocks and occurrence of feroginized sandstone; Hawe, Hundu, Apar, Wukari and Chonku has thicker sedimentary cover when compared to Akwana and FiyayiHawe. The NE-SW stretching low magnetic amplitude is interpreted as Akahana, Tunga, Keffin, Awe, Adawa, Amafan through Ibi, Shinye, Yamere to Dampar, Kishr, Wuro Jam and Gassol. Bangalala and Giden Shehu are interpreted as zone of thick sediment cover is high faulting and fracturing and thermal activities during the santonian orogeny. Kopar, JauroGarmaho, Peshiep, Kopbepand, Kurgwi, Shandam, Yalwa, Kwande and Namu is interpreted to beigneous environment (Basement Complex). Jangwa, Agana, Madakin, Azaza, GidanShahu and Bangalala and Akiri is interpreted to be areas of thick sediment cover and ferruginized sandstone (iron oxide element is present in them), but Gindan Shehu and Bangalala is interpreted to as having shallow magnetic sources and intense fracturing and faulting.

Clear lithological boundaries were also observed in the image. These boundaries were observed from the sharp contrast in the magnetic signature on adjacent magnetic bodies. The high frequency magnetic anomaly at the western part of the area was interpreted as the magnetite-rich formation and was delineated as the volcanic rocks (Nigerian Geological Survey, 2005). Numerous NE-SW geologic contacts are defined within the Central Benue Trough, and are interpreted to be structurally controlled by fault systems that formed during the basin forming processes (Akande et al.1988).

Prominent regional faults and fractures system were observed at Anzwa, Chan Gasuwa, Wurbo, Bako, Gidan Idi, Tunari, YerimaBaya, Bako, Gbakpo, Ugba, Maikarfi, Zaga, Mindi, Chonku, Mbusa, ZakiBiam, Avermun, Dooga, Mararaba and GidanUsumanu, all located at the southeastern

part of the study area; these areas is characterized by clusters of high frequency bi-polar bodies and its interpreted to have resulted from basement rocks of the Eastern Nigerian Massif. Similar structure are observed at the southwestern part of the study area, around Kopar, JauroGarmaho, Kopbepand, Kurgwi, Shandam, Yalwa, Kwande and Namu; these signatures were interpreted to have resulted from the basement rocks of the Northern Nigerian Massif. The central part of the study area is characterized by both long and short wavelength bodies, these bodies are characterized by both high and low magnetic susceptibility; this area is interpreted as to fall within the Central Benue Trough. The areas around Akwana, Fiyayi, Akahana, Keffin, Tunga, Adawa, Adiere and Ugba is characterized by high frequency anomalies and is interpreted to have resulted from volcanic rocks know to outcrop around the area.

Two zones (Zone 1 and Zone 2) were selected for further investigation based on the anomalous attributes of the zones and varying resistivity levels across the interpreted chargeable bodies resulting from segregation of hydrothermal fluid, leading to the separation of chargeable bodies of associated minerals (e.g. lead, quartz e.t.c). Core drilling confirmed the chargeable body to be Galena and chalcopyrite.The three-dimensional voxel model was used to isolate chargeable bodies (potential mineralization) with chargeability >15msec which is regarded as anomalies of interest. The volume of the chargeable voxel was then computed and used for the reserve estimation. The estimated volume of chargeable body in zone 1 is given as 853,250 m^3 with nearest estimate of 2,730,400 tonnes and estimated value of $1.3Billion. While, the estimated volume of chargeable body in zone 2 is given as 502,310 $m^3$with nearest estimated of 1,607,392 tonnes and estimated values of $750Million.

5.2 RECOMMENDATION

1. Ground gravity study should be carried out within the vicinity of the mineralized veins using high precision gravimeter for localized vein delineation
2. Geochemical analysis should be carried out on core samples in order to ascertain the ore grade for Proven Reserve Estimation (PRE).

6.1 CONTRIBUTION TO KNOWLEDGE

1. This study has substantially proven that the concept of chargeability can be used to make educated guess on mode of occurrence (veinlet or disseminated) of the mineralized body.
2. There is an extension of the occurrence of the cretaceous Middle–Benue Trough veins to Gidan Shehu, Bangalala, Yamere, Shinye, Ibi, Wuro Jam, Kishr, Jibu, Ajikemai, Bembem and Janka other than the previously known restricted localized occurrence at Zurak, Azara, Akwana and Arufu alone.

REFERENCE

Ajakaiye, D. E. (1981). Geophysical investigation in the Benue-Trough. A review; Earth Evolution. Arbitrary shape; In Computers in the Minerals industries. Part 1(ed.) Parks G A, Stanford University Publisher. *Geological Sciences*, (9) 464–480.

Akande, S. O., Horn, E. E., & Reutel, C. (1988). Minerology, fluid inclusion and genesis of the Arufu and Akwana Pb-Zn mineralization, middle Benue Trough, Nigeria. *Journal of African Earth Sciences (and the Middle East)*, 7(1), 167–180.

Ali, A., & Pour, A.B. (2014). Lithological mapping and hydrothermal alteration using Landsat 8 data: a case study in Ariab mining district, Red Sea Hills, Sudan. *International Journal of Basic and Applied Sciences*, (3),199–208.

Al-Zoubi, A.S., Awni, T.B., & Ziad S.H. (2003). Integrated Geophysical Methods Approach to Mineral Exploration in the Wadi Araba Area, Southern Jordan. *Pakistan Journal of Applied Science*s 3(2), 133-141.

Ananaba, S. E., & Ajakaiye, D. E. (1987). Evidence of tectonic control of mineralization of Nigeria from lineament density analysis: A Landsat study; *International Journal of Remote Sensing*, 1(10), 1445-1453

Appiah, H. (1991). Geology and mine exploration trends of Prestea Goldfields, Ghana. *Journal of African Earth Sciences (and the Middle East)*, 13(2), 235–241.

Araffa, S.A. (2021). Geophysical Data for Mapping Structural Features andHydrothermal Alteration Zones in Basement Rock of Egypt. In: Hamimi Z., Arai S., Fowler AR., & El-Bialy M.Z. (eds).The Geology of the Egyptian Nubian Shield. *Regional Geology Reviews. Springer,Cham.*

Asadi, H., & Hale,V. (1999). Integrated analysis of aeromagnetic, Landsat-TM and mineral occurrence data for epithermal gold exploration in northwest Iran. *Thirteenth International Conference* on Applied Geologic Remote Sensing, Vancouver, British Columbia, Canada, 1-3 March, p. 8.

Anudu, G., Onuba, L., Onwuemesi, A., & Awajiokan, I.(2012). Analysis of aeromagnetic data over Wamba and its adjoining areas in north-central Nigeria. *Earth Sciences Research Journal,*16, 25-33.

Baranwal, V. C., Rønning,, J. S., Gautneb H., Larsen B. E., Ofstad, F., & Brönner, M. (2018). Integrated interpretation of airborne and ground geophysical data for graphite exploration in Northern Norway. *Abstract, 24th EM Induction Workshop,* Helsingør, Denmark, 12-19.

Bath, M. (1974). Spectral Analysis in Geophysics, *Elsevier Scientific Publishing company* Amsterdam.

Beard, L. P., & Goitom, B. (2000). Some problems in interpreting low latitude magnetic surveys .6th EAGE/EEGS Meeting.

Becken, Michael & Pedersen, Laust. (2003). Transformation of VLF anomaly maps into apparent resistivity and phase. *Geophysics*. 68. 10.1190/1.1567218.

Benkhelil, J. (1989). The origin and evolution of the Cretaceous Benue Trough (Nigeria). *Journal African Earth Sciences,*8, 251–282.

Bhattacharrya, B.K. (1976). Continuous Spectrum of the totals magnetic field anomaly due to rectangular prismatic body. *Geophysics*, 31, 97 - 121.

Bhattacharyya, B.K., & Leu, L.K. (1975).Spectral analysis of gravity and magnetic anomalies due to two-dimensional structures. *Geophysics*, 40, 993–1013

Bhattacharyya, B.K., & Leu L.K. (1977). Spectral analysis of gravity and magnetic anomalies due to rectangular prismatic bodies. *Geophysics*, 42, 41–50.

Bolouki, Seyed., Ramazi, Hamidreza., Maghsoudi, Abbas., & Sohrabi, Ghahraman. (2019). A Remote Sensing-Based Application of Bayesian Networks for Epithermal Gold Potential Mapping in Ahar-Arasbaran Area, NW Iran. *Remote Sensing*. 12. 10.3390/rs12010105.

Brigo Mining Company Ltd. (2015). Electromagnetic and Induced Polarization Exploration. Geophysical Exploration Report of 18282EL, Safiyo, Wase LGA, Plateau State.

Burke, K. C., & Dewey, J. F. (1974). Two plates in Africa during the Cretaceous. *Nature*, Lond., 249, 313–316.

Campbell, J. B. (2007). Introduction to Remote Sensing, 4th ed. New York: Guilford Press.

Chaturvedi, A.K., Kovac, P., Chawla, A.S., Wiseman, R., Markandeyulu, A., Hope, J., Sridhar, M., Carey, H., Sharp, B., & Rai, A.K. (2012).Geological interpretation of heliborne geophysical data from the Kaladgi Basin; southern India.

Chaturvedi, A.K., Lo¨tter, C., Jagannadha, R.K., Maurya, A.K., Patra, I., & Chaki, A. (2010). Quantitative appraisal of heliborne and ground-based time domain electromagnetic surveys for uranium exploration: a case study from Rajasthan, India..

Chukwuka, C. (2016). Intergrated Landsat ETM and Aeromagnetic Survey for Enchanced Structural and Geothermal Interpretation of part of Calabar Flank Unpubl. Thesis, 113p

Clark, D. A. (1997). Magnetic properties of rocks and minerals. *AGSO Journal of Australian Geology and Geophysics*, 17(2), 83-104.

Clark, D. A., & Emerson, D. W. (1991). Notes on rock magnetic characteristics in applied Geophysical studies. *Exploration Geophysics*, 22, 547–555.

Colwell, R. N. (1997). History and place of photographic interpretation. In Manual of Photographic Interpretation, 2nd ed., edited by W. R. Philipson. Bethesda, MD: American Association of Photogrammetry and Remote Sensing.

Combrinck, M., Botha, W.J., Hutchins, D. (2009b).The use of VTEM data in geological mapping and mineral exploration in north-eastern Namibia. *11th South African Geophysical Association biennial technology meeting and exhibition,* Swaziland, 16–18, 352–355.

Crosta, A. P., & Moore, J. (1989). Enhancement of Landsat Thematic Mapper Imagery for Residual Soil Mapping in SW Minais Gerais State, Brazil: A Prospecting Case History in Greenstone Belt Terrain. *Proceedings of the 7th (ERIM) Thematic Conference*: Remote Sensing for exploration geology. Calgary, 2-6 , 1173-1187.

Cyril, C.O. (2019). Delineation of High-Resolution Aeromagnetic Survey of Lower Benue Trough for Lineaments and Mineralization: Case Study of Abakikili Sheet 303. *Malaysian Journal of Geosciences*, 3(1), 51-60.

Dearing, J.A.(1994).Environmental magnetic susceptibility, using the Bartington MS2 system. Chi Publisher.

Dobrin, M., & Savit, C. (1988). Introduction to Geophysical Prospecting, McGraw Hill, 4th edn.

Dobrin, M. B. (1983). Introduction of Geophysical Prospecting. McGraw-Hill Book Co.; Tokyo, Japan.

Ducart, Diego., Silva, Adalene., Toledo, Catarina., & Assis, Luciano. (2016). Mapping iron oxides with Landsat-8/OLI and EO-1/Hyperion imagery from the Serra Norte iron deposits in the Carajás Mineral Province, Brazil. *Brazilian Journal of Geology*.46.331-349.10.1590/2317-48892016201600 23.

Edwards, L. S. (1977). A Modified Pseudosection for Resistivity and IP, *Geophysics*, 42, 1020- 1 0 36.https://doi.org/10.1190/1.1440762

Ehinola, O. A., Ekweozor, C. M., & Simoneit, B. R. T. (2000). Geological and geochemical evaluation of Lafia-Obi coal, Benue Trough, Nigeria. *NAPE Bulletin,* 15, 92–104.

Ernst, Schetselaarand Eric De Kemp. (2000). Image Classification from Landsat Tm, Airborne Magnetics and Dem Data For Mapping Paleoproterozoic Bedrock Units, Baffin Island, Nunavut, Canada. *International Archives of Photogrammetry and Remote Sensing,* 33, Part B7. Amsterdam.

Eze, C. L., & Adaora, A.G. (2018). Ground Magnetic Survey over Lead-Zinc Mineralization in Edor, Cross River State, Nigeria. *Advances in Physics Theories and Applications.* ISSN 2224-719X (Paper) ISSN 2225-063,70.

Finn, M., Cameron, B., & Hutchins, D.G (2010). Namibia AEM mapping: a case study of airborne EM data used as a geological mapping and interpretation tool. Australian Society of Exploration Geophysicist. Extended Abstract.

Flores, C., & Peralta-Ortega, S.A. (2009).Induced polarization with in-loop transient electromagnetic soundings: a case study of mineral discrimination at El Arco porphyry copper, Mexico. *Journal Applied Geophysics,*68, 423–436.

Fon, V., Che, V.B & Suh, C.E. (2012). Application of electrical resistivity and chargeability data on a GIS platform in delineating auriferous structures in a deeply weathered lateritic terrain, Easter Cameroon. *International Journal of Geoscience,* 3, 960 – 971.

Fraser, (1969). D.C. Fraser Contouring of VLF-EM data. *Geophysics,*34 , 958-967.

Grant, F. S. (1985). Aeromagnetic, geology of an ore environment, Magnetite in igneous, sedimentary and metamorphic rocks. *An overview of Geoexploration,* 23, 303–33.

Grant, F. S., & West, G. F. (1965). Interpretation theory in applied geophysics. McGraw-Hill, New York.

Grant, N. K. (1971). South Atlantic, Benue Trough and Gulf of Guinea Cretaceous triple junction. *Bulletin Geological Sciences*, 82, 2295–2298.

Gunn, P. J. (1997). Application of Aeromagnetic Survey to Sedimentary Basin Studies. *AGSO Journal of Australian Geology and Geophysics*, 17 (2),133-144.

Hahn, A., Kind, E. G., & Mishra, D. C. (1976). Depth estimation of Magnetic sources by means of Fourier amplitude spectra, *Geophysical Prospecting*, 24, 287-308.

Harrison, R. J., Dunin-Borkowski, R. E., Kasama, T., Simpson E. T., & Feinberg J. M (2007). Properties of rocks and minerals. Magnetic properties of rocks and mineral. University of Cambridge, Cambridge, UK.

Ikpokonte, A. E., & Ajayi, C. O. (2003). A preliminary Interpretation of the Shallow Regional Structures deduced from Ground Magnetic Data over the Eastern Part of the Lower Benue Trough (Confluence) area, Nigeria. *Journal of Earth Sciences,* 2, 57-69.

Inglis D.R. (1955). Theories of the Earth's Magnetism. *Rev. Mod. Physics*,27, 212–248

Isife, F.A., Obasi, R.A. & Balogun, O. (2000). Electrical Resistivity and self-potential investigations of lead-zinc mineralization at Enyigba area, Ebonyi. Sate,Nigeria. *Journal of Biological and Physical Sciences*, 1, 135-148.

Jackisch, R., Lorenz, S., Kirsch, M., Zimmermann, R., Tusa, L., Pirttijärvi, M., Saartenoja, A., Ugalde, H., Madriz, Y., & Savolainen, M.(2020). Integrated Geological and Geophysical Mapping of a Carbonatite-Hosting Outcrop in Siilinjärvi, Finland, Using Unmanned Aerial Systems. *Remote Sensing*, 12, 2998.

Jatau, B. S., & Nandom, A. (2013). Morphology of Parts of the Middle Benue Trough of Nigeria from Spectral Analysis of Aeromagnetic Data. *International Science Index, Geological and Environmental Engineering* , 7(9), 16703.

Jensen, J. R. (2005). Introductory Digital Image Processing: A Remote Sensing Perspective, 3rd ed. Upper Saddle River, NJ: Prentice-Hall.

Karous M, Hjelt SE (1983) Linear filtering of VLF dip-angle measurements. *Geophysics Prospect* ,31, 782–794

Kasidi, S & Lazarus, G. N. (2017). Analysis of Aeromagnetic Data Over Middle Benue Trough and Its Adjourning Basement Terrain, North Central Nigeria. *Journal of Applied Geology and Geophysics,*5,01-08.

Kearey, P., Brooks, M., & Hill, I . (2002). An introduction to geophysical Exploration third Edition. *TJ international.*,1, 2-160

King, L .C. (1950). Outline and disruption of Gondwanaland; Geol. Mag., 87, 353–359.

Koné, A.Y., Nasr, I.H., Traoré, B., Amiri, A., Inoubli, M.H., Sangaré, S & Qaysi, S. (2021). Geophysical Contributions to Gold Exploration in Western Mali According to Airborne Electromagnetic Data Interpretations. *Minerals*, *11*, 126.

Kono, M., & Schubert, G. (2007).Geomagnetism (Treatise on Geophysics) (5).

KPMG, (2017). Solid Minerals in Nigeria. Nigerian Mining Sector Brief. *Retrieve from https://home.kpmg/ng/en/home/insights/2017/03/nigerian-mining-sector-brief.html*

Langenheim, V.E., Duval, J.S., Laurie, W. & Ed, D. (2000). Preliminary Report on Geophysics of the Verde River headwaters region Arizona. Open-File Report 00-403.

Leandro, V.B., Cesar, M.A., Ariane, R & George, L.L. (2016). Geophysical modeling of the manganese deposit for induced polarization method in Itapira. *Geofísica internacional*,55,2

Likkason, O. K. Singh, G. P. & Samaila N. K . (2013). A Study of the Middle Benue Trough (Nigeria) Based on Geological Application and Analyses of Spectra of Aeromagnetic Data. *Energy Sources*, Part A, 35, 706–716.

Lillesand, T. M., Kiefer, R. W., & Chipman, J. W. (2008). Remote Sensing and Image Interpretation, 6th ed. New York: Wiley.

Lo, C. P., & Yeung, A. K. W. (2002). Concepts and Techniques of Geographic Information Systems. Upper Saddle River, NJ: Prentice-Hall.

Loke, M.H., & Barker, R.D. (1996). Rapid Least-Squares Inversion of Apparent Resistivity Pseudosections by a Quasi-Newton Method. *Geophysical Prospecting*, 44, 131-152.

Loughlin, W.P (1991). Principal component analysis for alteration mapping. Photogramm Eng. Remote Sens., 57(9), 1163–1169

MacLeod, I. N., Jones, K. & Dai, T. F. (1993).3-D analytic signal in the interpretation of total magnetic field data at low magnetic latitudes, Exploration Geophysics, 679–688.

Marescot, L., Loke, M.H., Chapellier, D., Delaloye, R., Lambiel, C., & Reynard, E. (2003). Assessing reliability of 2D resistivity imaging in mountain permafrost studies using the depth of investigation index method. Near Surface Geophysics, 1(2), 57–67.

Martín-Crespo, T., Gómez-Ortiz, D., & Martín-Velázquez, S. (2020). Geoenvironmental Characterization of Sulfide Mine Tailings. In Applied Geochemistry with Case Studies on Geological Formations, Exploration Techniques and Environmental Issues; Mazadiego, F.L., Barrio-Parra, F., Izquierdo-Díaz, M., Eds.; IntechOpen: London, UK, 1–26.

Mascle, J., Marinho, M., & Wannesson, J. (1986). The structure of the Guinean continental margins: Implications for the connection between the Central and the South Atlantic Oceans. *Geological Rundsch*, 75, 57–70.

Meyer, C., De Waele, B., & Monoury, S. (2010). Mapping and target generation in poorly exposed sub-tropical terrains: the application of heliborne VTEM and magnetic survey data in base metal exploration in the Central African Copperbelt. *Australian Society for Exploration Geophysicist Extended Abstract.*

Milligan, P.R. & Gunn, P.J. (1997). Enhancement and Presentation of Airborne Geophysical Data. *Journal of Australian Geology & Geophysics*, 17, 63-75.

Ministry of Mine and Steel Development, (2010). Lead-Zinc exploration opportunities in Nigeria. Retreived from https://www.a-mla.org/images/acts/Nigeria-Ministry-of-Solid-Minerals-Investment-BrochureV14

Nabighian, M.N., (1972). The analytic signal of two dimensional magnetic bodies with polygonal cross-section: Its properties and use for automated anomaly interpretation. *Geophysics,* 37, 507- 517.

Neville, R. A., Levesque, J., & Staene, K. (2003). Spectral unmixing of hyperspectral imagery for mineral exploration: Comparison of results from SFSI and AVinfraredIS. *Canadian Journal of Remote Sensing*, 29, 99–110.

Nigerian Geological Survey Agency. (2006). Lineament and Geological Map of Nigeria, Scale 1:100 000. Retreived from http://ngsa.gov.ng/wp-content/uploads/2019/11/List-of-Geological-Sheet-Maps-1-100000.pdf

Nndanduleni, M., & Abera, T. (2021). Identification of potential targets for kimberlite exploration using satellite imagery and map combination approach in the Lesotho Kimberlite Province, *Ore Geology Reviews,* Article 104001.

Nur, A (2000). Analysis of aeromagnetic data over the Yola arm of the Upper BenueTrough, Nigeria; *Journal Mining and Geology,* 36, 77–84.

Nurnberg, D., & Muller, R. D. (1991). The tectonic evolution of the South Atlantic from Late Jurassic to present. *Tectonophysics*,191, 27–53.

Nwosu, O.B., & Onuba, L.N., (2013). Evaluation of the Magnetic Basement Depth Over Parts Of Middle Benue Trough Nigeria by Empirical Depth Rule Based on Slope Techniques Using the Hram. *International Journal of Scientific & Technology Research* ,2,1-11.

O'Leary, D.W., Friedman, J.D., & Phn, H.A. (1976). Lineament, Linear, Lineation: Some proposed new standard for old terms. *Geological Society of America Bulletin*, 87, 1463-1469.

Obaje, N. G. (2000). Biomarker evaluation of the oil-generative potential of organic matter in Cretaceous strata from the Benue Trough, Nigeria. *NAPE Bulletin*, 15, 29–45.

Obi, D. A., Okereke C. S., Obei B. C., & George A. M. (2010). Aeromagnetic Modeling of Subsurface Intrusives and its Implication on Hydrocarbon Evaluation of the Lower Benue Trough, Nigeria. *European Journal of Scientific Research,* 47(3), 347 -361.

Offodile, M. E. (1976). The geology of the Middle Benue, Nigeria. Publications from the Palaeontological Inst. Of Univ. Uppsala, *Special Publication*, 4, 166-178.

Ofoegbu, C.O & Onuoha, K.M .(1991). Analysis of magnetic data over the Abakaliki Anticlinorium of the Lower Benue Trough, Nigeria; *Marine Petroleum Geology*,8, 174–183.

Ofoegbu, C .O., & Mohan, N.L. (1990). Interpretation of aeromagnetic anomalies over part of southeastern Nigeria using three-dimensional Hilbert transformation; *Journal of African Earth Sciences*, 134, 13–29.

Ofoegbu, C.O. (1984). Interpretation of aeromagnetic anomalies over the Lower and Middle Benue Trough of Nigeria; Geophysical Journal International, 79, 813–823.

Ofoegbu, C. O (1985). A review of the geology of the Benue Trough of Nigeria; *Journal of African Earth Sciences*,3, 283–291.

Ogah, V.E., & Jatau, B. S. (2014). Airborne Magnetic Study of Otukpo Area. *International Research Journal of Pure and Applied Physics*, 2(2), 15-24.

Ogunmola, J.K., Ayolabi, E.A., & Olobaniyi, S.B. (2014). Lineament extraction from spot 5 and Nigeriasat-X Imagery of the Upper Benue Trough, Nigeria. International Archives of the Photogrammetry, *Remote Sensing and Spatial Information Sciences* - ISPRS Archives, 323.

Oha, I. A, Onuoha, K. M., Nwegbu, A. N & Abba, A.U. (2014). Integration of geologic, remote sensing and airborne geophysical data for regional exploration of lead-zinc-barium mineralization in parts of the southern Benue Trough, south-east Nigeria"; Unpublished PhD Thesis, University of Nigeria, Nsukka, 201.

Ojonugwa, U.A., Ezeh, C.C., & Chinwuko,I.A. (2018). Integration of Aeromagnetic Interpretation and Induced Polarization Methods in Delineating Mineral Deposits and Basement Configuration within Southern Bida Basin, North-West Nigeria. *Journal of Geology and Geophysics*, 7, 449. doi: 10.4172/2381-8719.1000449

Okereke, C.N., Onu N.N., Ibe, K.K., Selemo, A.O.I., Opara, A.I., Ikoro, D.O., Ibeneme, S. I., & Oha I.A. (2012). Analysis of Landsat and Aeromagnetic Data for Mapping of Linear Structures: A

Case Study of Yola Area, Upper Benue Trough, Nigeria. *International Journal of Engineering Research and Applications (IJERA),* 2(3), 1968-1977.

Okereke, C. N., & Ananaba, S. E. (2006). Deep crustal Lineament inferred from aeromagnetic anomalies over the Niger Delta, Nigeria. *Journal of Mining and Geology*,42, 127-131

Okubo, Y., Graf, R.J., Hansen, R.O., Ogawa, K. & Tsu, H. (1985). Curie point depths of the Island of Kyushu and surrounding areas, Japan. *Geophysics* 53(3), 481–494

Okwesili, N.A., Johnson, U.A., & Igwe E.A. (2019). Spectral analysis and source parameter imaging of aeromagnetic data of Lafia and Akiri Areas, Middle Benue Trough, Nigeria. *International Journal of Physical Sciences.* 14(1), 1-14.

Olawale, O.O., Ahmed, G., & Moussa, I. (2021). Mapping hydrothermal alteration mineral deposits from Landsat 8 satellite data in Pala, Mayo Kebbi Region, Southwestern Chad. *Scientific African,* 11, Article e00687.

Onuba L. O., Chinwuko A. I., Onwuemesi A. G., Anakwuba E. K. and Nwokeabia N .C. (2012). Interpretation of Aeromagnetic Anomalies over parts of Upper Benue Trough and Southern Chad Basin, Nigeria. *Advances in Applied Science Research,* 3 (3), 1757-1766

Onwuegbuchulam, C.O., Ikoro, D. O., Nwugha, V.N., & Okereke, C. N. (2016). Application of Very Low Frequency- Electromagnetic (Vlf-Em) Method of Map Fractures/Conductive Zones InAuchi South Western Nigeria. *The International Journal of Engineering and Science (Ijes)* ,5, 07-13.

Onyedim, G. C., Awoyemi, M. O., Ariyibi, E. A. & Arubayi, J. B. (2006). Aeromagnetic imaging of the basement morphology in part of the Middle Benue Trough, Nigeria, *Journal of Mining and Geology*, 42 (2), 157-163.

Opara, A.I., Onyewuchi, R.A., Selemo, A.O.I., Onyekuru, S.O., Ubechu, B.O., Emberga, T.T., Ibim, D.F., & Nosiri, O.P. (2014b). Structural and tectonic features of Ugep and Environs, Calabar Flank,Southeastern Nigeria: Evidences from aeromagnetic and Landsat-ETM data; *Mitteilungen Klosterneuburg,* 64, (7), 33-54.

Opara, A. I., Odumosu, G. E., Akaolisa, C. Z., Onyekuru, S. O., Emberga, T. T. and Onu, N. N (2018). Basement Depth Re-Evaluation and Structural Kinematic Analysis of Part of the Middle Benue Trough using High Resolution Aeromagnetic Data. *Futo Journal Series*. 4(1), 409 – 436.

Osazuwa, I. B., Ajakaiye, D.E., & Verheijen, P.T. (1981). Analysis of the structure of part of the Upper Benue Rift Valley on the basis of new geophysical data; *Earth Evolution Science,* (2), 126–134.

Ouchchen, M., Said, B., Driss, E. A., Mohamed, A., Kevin, L.M., Abdelhalim, M., Fatima, Z.E., & Bouchra, D., (2021).Structural interpretation of the Igherm region (Western Anti Atlas, Morocco) from an aeromagnetic analysis: Implications for copper exploration. *Journal of African Earth Sciences,176,* 104140.

Pabalelo, Sono., Bokani, Nthaba., Elisha, M. Shemang., Boniface, Kgosidintsi & Thato, Seane .(2021).An integrated use of induced polarization and electrical resistivity imaging methods to delineate zones of potential gold mineralization in the Phitshane Molopo area, Southeast Botswana, *Journal of African Earth Sciences*,174, 104060.

Petersen, N. (1990). Curie temperature. In James, D. E. (ed.), The Encyclopedia of solid Earth Geophysics, 166–173. New York: Van Nostrand Reinhold.

Plummer, C. C., McGeary, D., & Carlson, D. H. (2001). Physical Geology.New York: McGraw Hill, 8th edition.

Pour, A., & Hashim, M. (2015). Hydrothermal alteration mapping from Landsat- 8 data, Sar Chesmeh copper mining district, south-eastern Islamic Republic of Iran. *Journal of Taibah University for Science*, 9,155–166.

Pour, A.B., Park, T.-Y., Park, Y., Hong, J.K., Muslim, A.M., Läufer, A., Crispini, L., Pradhan, B., Zoheir, B & Rahmani, O. (2019). Landsat-8, Advanced Spaceborne Thermal Emission and Reflection Radiometer, and WorldView-3 Multispectral Satellite Imagery for Prospecting Copper-Gold Mineralization in the Northeastern Inglefield Mobile Belt (IMB), Northwest Greenland. *Remote Sensing*, *11*, 2430.

Price, K. P., Guo, X., & Stiles, J. M. (2002).Optimal Landsat TM band combinations and vegetation indices for discrimination of six grassland types in eastern Kansas. *International Journal of Remote Sensing*, 23, 5031–5042.

Rajagopalan, S. (2003). Exploration Geophysics, 34 (4), 257–262.

Rashed, T., Weeks, J. R., Gadalla, M. S., & Hill, A. G. (2001). Revealing the anatomy of cities through spectral mixture analysis of multispectral satellite imagery: A case study of the greater Cairo region, Egypt. *Geocarto International*,16, 5–15.

Reeves, C. (2005). Aeromagnetic Survey: Principles, Practice and Interpretation.

Reeves, C. V. (1989). Aeromagnetic interpretation and rock magnetism. *First Break*,7, 275–286.

Reeves, C.V., Reford, S.W., & Millingan, P.R. (1997). Airborne geophysics: Old methods, new images. Geophysics and Geochemistry at the millennium. *Proceedings of the Fourth Decennial International Conference on Mineral Exploration*, 13-30.

Reford, M.S. (1964). Magnetic anomalies over thin sheets. *Geophysics*, 29, 523-536.

Reid, A.B., Allsop, J.M., Granser ,,A., Millett A.J., & Somertom, I.W. (1990). Magnetic interpretation in three dimensions using Euler deconvolution. *Geophysics*, 55, 80-91.

Remke, L., Van, D., Jan, M.H., Bruce, H., Brian, B., David, I.N., Samuel, N., Chris, J., Patrick, N., Robert, N., David, V., Lucas, C., & Janet, E.S. (2004). Spatial variability of magnetic soil properties. *The International Society for Optical Engineering*, 2004, 665-675.

Reynolds, J. M. (1997). An introduction to Applied and Environmental Geophysics, John Wiley & Ltd. Bans Lane, Chichester. 124-132.

Rivas, J. (2009). Gravity and Magnetic Methods.Retrieved from https://orkustofnun.is/gogn/unu-gtp-sc/UNU-GTP-SC-09-13a.pdf

Runge, (1996). Mining Economics and Strategy. Edited by Andrew Mular, Doug Halbe and Derek Barratt, Society for Mining, Metallurgy and Exploration Inc. (SME), Littleton, USA, New York, USA.

Sabins, F.F. (1999). Remote sensing for mineral exploration. *Ore Geology Review*, 14(3–4), 157–183.

Salem, Ahmed., Williams, Simon., Fairhead, Derek., Smith, Richard & Ravat, Dhananjay. (2008). Interpretation of magnetic data using tilt-angle derivatives. *The Leading Edge.* 73. 10.1190/1.2799992.

Sawuta, J.M., Ayanninuola, O.S., Udensi, E.E., & Ogwola, P. (2019). Estimation of Magnetic Depth to Source Using High Resolution of Aeromagnetic Data of Parts of Upper Benue Trough, North Eastern Nigeria. *Science World Journal*, 14(1).

Sekandari, M., Masoumi, I., Beiranvand Pour, A.M., Muslim, A., Rahmani, O., Hashim, M., Zoheir, B., Pradhan, B., Misra, A., & Aminpour, S.M. (2020). Application of Landsat-8,

Sentinel-2, ASTER and WorldView-3 Spectral Imagery for Exploration of Carbonate Hosted Pb-Zn Deposits in the Central Iranian Terrane (CIT). *Remote Sensing,* 12, 1239.

Shanks Pat W, C. (2010). Hydrothermal Alteration. Volcanogenic massive sulfide occurrence Model (Scientific Investigation Report). Retrieved from https://pubs.usgs.gov/sir /2010/ 5070/c/SIR10-5070-C.pdf

Shirmard, H., Farahbakhsh, E., Beiranvand, P. A., Muslim, A.M., Müller, R.D., & Chandra, R.(2020). Integration of Selective Dimensionality Reduction Techniques for Mineral Exploration Using ASTER Satellite Data. *Remote Sensing*, *12*, 1261.

Shirzaditabar, F., Bastani, M., & Oskooi., B. (2011). Imaging a 3D geological structure from HEM, airborne magnetic and ground ERT data in Kalat-e-Reshm area, Iran. *Journal of Applied Geophysics,* 75, 513–522.

Sillitoe, R. H. (1979). Some thoughts on gold-rich porphyry copper deposits. *Mineralium deposita*, 14, 161–1744.

Spector A. & Grant F.S., (1970). Statistical models for interpreting aeromagnetic Data; *Geophysics*, 25, 293-302.

Stephen, E. Ekwok., Anthony E. Akpan., & Ebenezer, A. Kudamnya (2020). Exploratory mapping of structures controlling mineralization in Southeast Nigeria using high resolution airborne magnetic data, *Journal of African Earth Sciences,*162,103700,ISSN 1464-343X.

Stoneley, R., (1966). The Niger Delta region in the light of the theory of continental drift; *Geological Magazine*, 103, 385–397.

Studemeister, P. A. (1983). The redox state of iron: a powerful indicator of hydrothermal alteration. *Geoscience Canada*, 10, 189–194.

Sun, L., Khan, S., & Shabestari, P (2019). Integrated Hyperspectral and Geochemical Study of Sediment-Hosted Disseminated Gold at the Goldstrike District, Utah. *Remote Sensing, 11*, 1987.

Telford, W. M., Geldart, L. P., & Sheriff, R. E. (1990). Applied geophysics. (Third Edition) Cambridge University Press.

Telford, W. M., Geldart, L.P., & Sheriff, R.E. (1998). *Geophysics,* (2nd Ed), Cambridge University Press, USA, 113 – 114.

Thiabaut, R. (2017). Application of Time-Domain Induced Polarization Technique to Characterize the Orman Gold Prospect in Mondulkiri Province, Cambodia. A thesis Submitted to University of Liege, Faculty of Applied Science.

Thiessen, R., Burke, K. C., & Kidd, W. S. F. (1979). African hotspots and their relation to the underlying mantle. *Geology*,7, 263–266.

Thompson, D. T. (1982). EULDPH: A new technique for making computer-assisted depth estimates from magnetic data. *Geophysics*, 47(1), 31-37.

Thurston, C. G., & Smith, R. (1999). Model-independent depth estimation with the SPITM method: 69th Annual International Meeting, *Society of Exploration Geophysicist*, 403–406.

Thurston, J. B., & Smith, R. S. (1997). Automatic conversion of magnetic data to depth, dip, and susceptibility contrast using the SPITM methods: *Geophysics*, 62 (3), 790-813.

Trifonova, P., Zheler Z., Petrova, T., & Bojadgieva, K. (2009). Curie point depths of the Bulgarian territory inferred from geomagnetic observations and its correlation with regional thermal structure and seismicity. *Tectonophysics*, 473, 362–374

Tsiboah, T., & Grant, T. (2009). Application of geophysics to gold exploration in Ghana: examples from Newmont projects. Aust ralian Society of Exploration Geophysicist Extended Abstract.

Tuşa, L., Khodadadzadeh, M., Contreras, C., Rafiezadeh Shahi, K., Fuchs, M., Gloaguen, R.,& Gutzmer, J. (2020). Drill-Core Mineral Abundance Estimation Using Hyperspectral and High-Resolution Mineralogical Data. *Remote Sensing*, 12, 1218.

USGS (2015a) M7.8-36 kmEofKhudi,Nepal. http://earthquake.usgs.gov /earthquakes / eventpage/ us 20002926#scientific_finitefault:us_us20002926

USGS(2015b).NetQuakes:StationKATNP_NQ_.http://earthquake.usgs.gov/ monitoring/ netquakes/ station/ KATNP_NQ_01/20150425061138/. Accessed SEP20 2015.

Victor, O.M., Onwuemesi, A.G., & Aniwetalu, E.U. (2015).Exploration of Lead-Zinc (Pb-Zn) Mineralization Using Very Low Frequency Electromagnetic (VLF-EM) in Ishiagu, Ebonyi State. *Journal of Geological Geosciences*, 4, 214.

Verduzco, Bruno., Fairhead, J., Green, Chris., & MacKenzie, Chris. (2004). New Insights into magnetic derivatives for structural imaging. *The Leading Edge*. 23. 116-119. 10.1190/1.1651454.

Vogley A. W. (1985). Economics of the Mineral Industries .American Institute of Mining, Metallurgical and Petroleum Engineers, Inc., New York. USA.

Wemegah, D. D., Menyeh, A., & Danuor, S. K. (2009). Magnetic Susceptibility Characterization of mineralized and non mineralized rocks of the Subenso Concession of Newmont Ghana Gold Limited. In Ghana Science Association Biennial Conference, UCC.

Whitehead, N., & Musselman, C. (2008). MontajGrav/Mag Interpretation: Processing, Analysis and Visualization System for 3D Inversion of Potential Field Data for Oasis montaj v6.3, Geosoft Incorporated, 85 Richmond St. W., Toronto, Ontario, M5H 2C9, Canada.

Whitham, K. (1960). Measurement of the geomagnetic elements. In Methods and techniques in Geophysics 1, *S. K. Runcorn*. 134–48.

Wijns, C. (2009). Structural mapping under cover with airborne EM. Australian Society of Exploration Geophysicist Extended Abstract.

Wright, J. B. (1968). South Atlantic continental drift and Benue Trough. *Tectonophysics*, 6(301–310), 464–480.

Yawsangratt, S. (2002). A gravity study of northern Botswana: a new perspective and its implications for regional geology. Thesis, International Institute for Aerospace Survey and Earth sciences, The Netherlands.

Zhang, R., Meng, Y & Sai, S. (2016). Application of geophysical methods to gold prospecting: An eample from Loulitou district, Jiaoding Peninsula Eastern China. *International conference on computational modeling, simulation and applied mathematics* (CMSAM 2016) ISBN:978 – 1 – 60595 – 385 –4.

Zhang, Z., Wang, G., Ding, Y & Carranza, E. J. M. (2020). 3D Mineral Exploration Targeting with Multi-dimensional Geoscience Datasets, Tongling Cu(au) District, China. *Journal of Geochemical Exploration,* 106702.

Zoheir, B., El-Wahed, M.A., Pour, A.B., & Abdelnasser, A.(2019). Orogenic Gold in Transpression and Transtension Zones: Field and Remote Sensing Studies of the Barramiya–Mueilha Sector, Egypt. *Remote Sensing, 11*, 2122.

Zoheir, B., Emam, A., Abdel-Wahed, M., & Soliman, N. (2019). Multispectral and Radar Data for the Setting of Gold Mineralization in the South Eastern Desert, Egypt. *Remote Sensing, 11*, 1450

APPENDIX

Apendix i: Measuring the dip and strike of an exposed outcrop (Limestone) in profile 2 zone 2

Appendix ii: Exposed Limestone

Appendix iii: Base station setup

Appendix iv:EM-VLF and Magnetic data acquisition (Mr. Onum Stephen Adikwu)

Appendix v: Setup for Electrical Resistivity/ Induce polarization (IP) survey

Appendix vi: Res/IP data acquisition